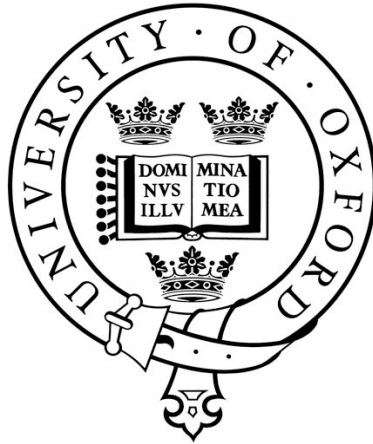


Towards Ultrafast Photoassociation of Ultracold Atoms

Duncan England
Wolfson College, Oxford



Submitted for the degree of Doctor of Philosophy
Trinity Term 2011

Supervised by
Prof. Ian A. Walmsley

Clarendon Laboratory
University of Oxford
United Kingdom

*“As the creeper that girdles the tree-trunk
the Law runneth forward and back –
For the strength of the Pack is the Wolf,
and the strength of the Wolf is the Pack. ”*

—Rudyard Kipling, The Jungle Book

Towards Ultrafast Photoassociation of Ultracold Atoms

Duncan England

Wolfson College, Oxford

Submitted for the degree of Doctor of Philosophy

Trinity Term 2011

Abstract

In the ultracold regime, where the interactions between atoms become quantum mechanical in nature, we can investigate the fundamental properties of matter. A natural progression from the catalogue of pioneering experiments using ultracold atoms is to extend the size of our quantum system by producing ultracold molecules in prescribed low-energy internal states. Techniques for cold molecule production are split into two methods: direct and indirect cooling. While direct cooling methods have yet to realize ultracold temperatures, collisional relaxation in the molecules leads to low internal energy states. By contrast, indirect cooling — the association of molecules from pre-cooled atoms — has produced a range of molecules at ultracold temperatures; the challenge with this technique is to control the internal state.

This thesis concentrates on a technique that is complementary to those already in existence: ultrafast photoassociation. Key to this technique is the formation of time non-stationary wavepackets in the excited-state in order to improve Franck-Condon overlap of the excited state with deeply bound ground-state vibrational levels. A pump-probe experiment was designed and built to demonstrate the formation of bound excited-state dimers. In this work we show that the initial state from which the wavepacket originates is of critical importance to the evolution of excited-state population. We find that the internuclear separation of the wavepacket produced in a rubidium magneto-optical trap is too large to observe coherent oscillations in the excited state. The implications of this are discussed along with recommendations for future ultrafast photoassociation experiments. Consequently, a new ultracold atom apparatus was built utilizing magnetic and dipole-force trapping to increase the density of the atomic sample; this apparatus will enable future experiments combining the exciting fields of ultracold matter and ultrafast light.

Acknowledgements

Firstly I must extend my sincerest thanks to my supervisor, Ian Walmsley who has fostered a group in which it is a true pleasure to work where everyone tries to contribute to everyone else's experiment and enjoys each other's successes. As a boss, Ian treats good and bad news from the lab with the same good humor and encouragement and always looks after his students. I must also thank Professor Chris Foot and his group for help and advice when constructing the new dipole trap apparatus.

As a great man once said, writing a thesis is like climbing a mountain. As I am reaching the summit of this mountain, I owe a huge debt of gratitude to my fellow mountaineers, especially my colleagues on the cold molecules experiment. Dave McCabe is a true warrior of light, his physics is like his cricket: Steady and methodical with occasional flashes of brilliance. It is tribute to an excellent working relationship that the only times I ever tried to kill him were in the nets. As a theorist, Hugo Martay was an experimentalist's dream; feed him enough taramasalata or pain au chocolat and he will solve any problem for you, however big or small. I must also thank him for making my job as quotemaster so easy. Jovana 'miniboss' Petrovic kept us in check in the lab, commanding respect both in the lab and on the basketball court, despite her diminutive stature. I also greatly enjoyed working, all to briefly, with Antoine Monmayrant, Alex Dicks, Melissa Friedman, Beatrice Chatel and 'General' Giuseppe Smirne.

I must also thank the quantum memorizers for welcoming an outsider into their group so kindly, I thoroughly enjoyed working with them all. The other students on the cesium memory experiment, Patrick Michelberger and Tessa Champion, provide an enjoyable mix of contrasting personalities; one offering optimism and enthusiasm, and the other exasperation and perspiration. I will leave it to those who know them to decide which is which. Josh Nunn was always on hand to offer advice or encouragement and is always kind enough to get half way through offering me a cup of tea before remembering I don't drink it. I also wish to thank the rest of the memories subgroup, Nathan Langford, KC Lee, Michael Sprague and Xian-Min Jin for many long, enjoyable group meetings.

Monty 'Phil' Bustard was always a great companion in the lab, office or friday evening pub session. Despite his acrimonious departure from the old library in 2008, his repeated laser thievery¹ and what will only be known as "the chocolate box

¹"I only need 4% of your laser"....."Ooops, I got my sums wrong"...."I needed the plug for something else" *etc.etc.*

incident”, we have somehow remained friends. Tim Bartley is, an excellent lunch-buddy and a great sounding-board for ideas (mostly on where to go for lunch). He is also a mean tennis player.....for a vegetarian. Ben Sussman is a mine of knowledge on everything from Van der Waals forces to Van Halen and from MCPs to MC Hammer. Brian Smith was a hero as a post-doc in our group and is now forging ahead with his own group, although I still struggle to think of him as the professor, to me he is still a very naughty boy. Klaus Reim is a bundle of energy and excitement and is equally as enthusiastic whether discussing memories or snackies, or indeed many other things ending in -ies. Dane Austin, Hendrik Coldenstrodt and KC Lee joined the group at the same time as me and together we have negotiated the trials and tribulations of graduate class, transfer of status and university administration. I wish Dane and Hendrik all the best in their new careers and hopefully KC and I will join you in the world of work soon! The group is too big for me to thank everyone so I apologize to those whom I have not mentioned by name, but if you are reading this, thanks for everything.

I am also very grateful to many of the excellent support staff in the department. Rob Harris, Simon Moulder and Bill Seager in the research workshop were always willing to help with my problems and discuss the weekend’s sporting action. Graham Quelch retains a huge amount of useful information in his brain, despite years of abuse in the 1960s and 70s. Alan Hodgson, George Dancer and Terry Fletcher manned the building services help desk expertly. Sue Gardner is my go-to-girl for navigating departmental bureaucracy and organized many great christmas parties. Alan Francis and Mohammed Cheddi were always extremely helpful in the stores. Unfortunately special stores — in which the push of a button reveals sliding shelves full of illicit goods — exists only in my imagination.

Last but not least I would like to thank my family. My Mum and Dad gave me the best possible start in life, and always encouraged me to do my best at everything I tried. My sisters, Hannah and Jennie mix encouragement and abuse in roughly equal proportions, I am sorry I never made you that lightsaber. And finally thanks to Lindsey, without whose distraction, I would have finished months ago, but without whose support, I might not have finished at all.

Contents

1	Introduction	1
1.1	Thesis Overview	4
1.2	Contribution of the Author	6
2	Background	9
2.1	A physical model of a diatomic molecule	10
2.2	Hund's coupling cases and molecular notation	14
2.2.1	Hund's case (a)	16
2.2.2	Hund's case (c)	17
2.2.3	Symmetry properties	18
2.2.4	Selection rules	18
2.2.5	Long-range behaviour	19
2.2.6	The Franck-Condon principle	22
2.2.7	The Rb ₂ molecule	27
2.3	Techniques for cold atoms	30
2.3.1	Laser cooling of atoms	31

2.3.2	Magnetic trapping	39
2.3.3	Dipole trapping	40
2.3.4	Evaporative cooling	42
2.4	Cold molecules	42
2.4.1	Direct cooling	43
2.4.2	Indirect cooling	45
2.4.3	Ultrafast photoassociation	57
3	MOT Experiment	64
3.1	MOT	65
3.1.1	Laser preparation	67
3.1.2	The vacuum chamber	69
3.2	Ultrafast lasers	73
3.2.1	NOPA	75
3.3	Detection of molecules	79
3.3.1	Time of Flight mass spectrometer	80
4	Pump-Probe Spectroscopy in a MOT	83
4.1	Initial state characterisation	84
4.1.1	REMPI spectroscopy of the <i>a</i> state	85
4.1.2	Pump-probe Experiments	91
4.1.3	Theoretical model of the pump-probe experiment	95
4.1.4	Demonstration of bound excited-state dimers	100

4.2	Conclusions	105
4.2.1	Outlook	107
5	Construction of the Dipole Trap Apparatus	110
5.1	Vacuum chamber	113
5.1.1	Bake-out	116
5.2	Computer control	117
5.3	Magnetic coils	119
5.3.1	MOSFET current control	121
5.4	Lasers	125
5.4.1	Diode lasers	125
5.4.2	The tapered amplifier	127
5.4.3	Dipole trap laser	129
5.5	MOT alignment and characterization	134
5.5.1	MOT alignment	135
5.5.2	MOT characterization	136
5.5.3	TOF temperature measurement	141
5.6	Experimental sequence	142
5.6.1	MOT	143
5.6.2	Compressed MOT	143
5.6.3	Optical molasses	145
5.6.4	Transfer of atoms into $F = 1$	148
5.6.5	Magnetic trap	149

5.6.6	Dipole trap	153
5.7	Time-of-flight mass spectrometer.	161
5.8	Summary	168
6	Conclusion	170
6.1	Outlook	175
7	Raman Quantum Memory	178
7.1	The Raman memory protocol	179
7.1.1	Raman memory theory	181
7.2	The cesium Raman memory	184
7.2.1	Experimental procedure	185
7.2.2	Previous results	189
7.3	Storage of polarization-encoded information	194
7.3.1	Quantum process tomography (QPT)	199
7.3.2	Results	201
7.4	Conclusions	210
7.5	Outlook	211
A	Atomic and Molecular Data of Rubidium	214
A.1	Atomic data	214
A.2	The D_2 line	215
A.3	Rb ₂ molecular potentials	216

B	The Position-Dependence of the Classical Oscillation Period.	220
C	Design of the Tapered Amplifier	224
C.1	Design of the mount	224
C.2	Alignment and collimation	226
D	UHV Construction	230
D.1	UHV bake-out	230
D.2	Light induced atomic desorption (LIAD)	231
E	Atomic Data of Cesium	236
E.1	Atomic data	236
E.2	The D_2 line	237

List of Figures

2.1	A simplified sketch of a diatomic molecule	11
2.2	The Lennard-Jones potential.	13
2.3	Examples of molecular potentials and vibrational wavefunctions . . .	15
2.4	Vector diagram of Hund's coupling cases (a) and (c)	17
2.5	An electric dipole	21
2.6	Differences in the long range behaviour of the Rb ₂ dimer	23
2.7	A semi-classical illustration of the Franck-Condon Principle	25
2.8	A Quantum-mechanical illustration of the Franck-Condon Principle .	28
2.9	The Sisyphus cooling	35
2.10	The magneto-optical trap (MOT)	37
2.11	Magnetic trapping	40
2.12	Continuous wave photoassociation	47
2.13	Optical cycling scheme demonstrated by Viteau <i>et al.</i> in Cs ₂	49
2.14	Feshbach resonances	52
2.15	Typical STIRAP energy levels, pulse timings and state transfer . . .	54

2.16	A schematic diagram of ultrafast photoassociation.	59
3.1	Hyperfine structure of the ^{85}Rb D1 and D2 lines	66
3.2	Beam diagram of MOT laser preparation	70
3.3	Schematic of the MOT vacuum chamber.	71
3.4	Release and recapture measurement of the MOT temperature.	73
3.5	Layout of the ultrafast pump-probe experiment.	75
3.6	Optical parametric generation.	77
3.7	Experimental layout of the NOPA.	78
3.8	Typical time of flight spectra for REMPI and pump-probe ionization.	81
4.1	REMPI ionization scheme of molecules in the a state.	86
4.2	REMPI spectroscopy of the a state.	88
4.3	Classical oscillation period of wavepackets associated from scattering pairs and bound triplet molecules.	90
4.4	Pump-probe ionization of molecules in the $5S + 5P$ manifold	92
4.5	Atomic and molecular pump-probe signals	94
4.6	Simulation of time and position dependence of the excited-state fol- lowing a pump pulse	97
4.7	Theoretical pump-probe signals using the ionization projection oper- ator.	99
4.8	Demonstration of bound molecules in the excited-state.	101

4.9	Results of simulations of the moving-cut experiment at a range of internuclear separations.	103
4.10	Comparison of best fit population distribution with background molecules and scattering states.	104
5.1	Vacuum chamber design for the new chamber.	114
5.2	Labview control panel	120
5.3	Circuit diagram for the magnetic coils.	123
5.4	Fast switch-on of the magnetic coils.	124
5.5	Laser preparation in the new experiment.	128
5.6	Calculation of trap depth vs. beam waist for the fiber laser.	132
5.7	Layout of Dipole trap optics and demonstration of a $70 \mu\text{m}$ focus.	133
5.8	Absorption imaging	139
5.9	Spectrum of the Probe laser.	140
5.10	Time-of-flight (TOF) temperature measurement.	142
5.11	Optimization of the detuning and current for the MOT.	144
5.12	TOF temperature measurement of the MOT.	144
5.13	Optimization of the duration and current for the cMOT.	145
5.14	Time-of-flight temperature measurement of the optical molasses phase before optimization.	146
5.15	The effect of changing the molasses duration on the final temperature.	147
5.16	TOF measurement of the optical molasses phase after optimization.	148
5.17	The effect of detuning on the final temperature of the optical molasses.	149

5.18	Estimation of the magnetic field gradient required for the magnetic trap.	150
5.19	Optimization of the magnetic field gradient for the magnetic trap.	151
5.20	Measurement of the trapping lifetime in the magnetic trap.	152
5.21	The effect of the stark shift on fluorescence imaging of the MOT.	154
5.22	The effect of the stark shift on absorption imaging of the magnetic trap.	155
5.23	First dipole trap image and setting the focal position.	156
5.24	A sequence of images showing atoms falling out of the magnetic trap and remaining in the dipole trap.	157
5.25	Optimization of the ramp time in the dipole trap loading.	158
5.26	Optimization of the vertical position of the dipole trap.	159
5.27	Horizontal and vertical fits of the dipole trap image.	161
5.28	Simulation results of the TOF mass spectrometer.	163
5.29	Photograph of one of the grids used in the TOF mass spectrometer.	164
5.30	Schematic diagram of the TOF mass spectrometer.	165
5.31	Comparison of theoretical and experimental behavior of the TOF.	166
5.32	Arrival times and ion signal strength in a pulsed TOF spectrometer.	167
7.1	Λ -level system for the Raman quantum memory.	180
7.2	Pulse sequence in the Raman quantum memory.	186
7.3	Beam diagram for the Raman memory experiment.	190
7.4	Raman memory efficiency as a function of control pulse energy.	191

7.5	Storage lifetime of the Raman memory	193
7.6	Single-photon level storage and retrieval in the Raman memory.	194
7.7	Layout of the two-memory interferometer.	197
7.8	Quantum process tomography at short memory times.	206
7.9	Quantum process tomography at 300ns storage time.	208
7.10	Visibility and purity of the memory process as a function of storage time.	209
A.1	The D_2 line in ^{87}Rb	215
A.2	The D_2 line in ^{85}Rb	216
A.3	Relevant molecular potentials for the pump-probe experiment.	217
B.1	Classical oscillation period in the excited state as a function of average vibrational number.	222
B.2	Classical turning points of the vibrational wavepackets in the excited state.	223
B.3	Classical oscillation period in the excited state as a function of inter- nuclear separation.	223
C.1	Technical drawing of the tapered amplifier (TA), top view.	226
C.2	Technical drawing of the TA, front view.	227
C.3	Photograph of the TA module.	228
C.4	Close-up photograph of the TA chip and aspheric lenses.	228
D.1	Bakeout data for the dipole trap apparatus.	231

D.2 Demonstration of the LIAD mechanism.	234
E.1 The D_2 line in cesium.	237

List of Tables

2.1	Summary of the good quantum numbers in Hund's case (a)	16
2.2	Summary of the good quantum numbers in Hund's case (c)	17
2.3	Molecular states of Rb ₂ in Hund's case (a) and (c) basis	30
5.1	NI CompactRIO output channels used in the experiment.	118
5.2	A summary of the experimental procedure for loading the hybrid trap.	160
7.1	Expected measurement outcomes of the 36 polarization measurements.	195
7.2	Waveplate angles for polarization state preparation and analysis. . .	198
A.1	Atomic data of ⁸⁵ Rb and ⁸⁷ Rb	214
A.2	Ground and excited state potentials relevant to the pump-probe ex- periment.	217
A.3	Energy levels of rubidium	218
E.1	Atomic data of cesium.	236

Chapter 1

Introduction

In the 1920s, Albert Einstein predicted that, at low temperatures, a non-interacting bosonic gas would suddenly develop a macroscopic population in its lowest energy level. This remarkable quantum phase transition, known as Bose–Einstein condensation (BEC), was predicted to occur when the atomic separation became comparable to the thermal de Broglie wavelength of the atoms. One of the motivations of early cold atom experiments was the experimental verification of this theory. In 1995 BEC was realised in ^{87}Rb ^[1], ^7Li ^[2] and in ^{23}Na ^[3]. Since the advent of atomic condensates the search for an analogous molecular state has begun. Molecules have inherently more complicated energy levels than atoms because they have three degrees of freedom — translational, vibrational and rotational. The ultimate goal is a sample of translationally cold molecules, in which the experimentalist can control the internal degrees of freedom of the molecule.

The study of the formation of ultracold molecules is motivated by a range of

scientific and technological goals, with successful formation, and manipulation, of ultracold molecules expected to have ramifications in quantum information processing as well as in the study of the fundamental properties of matter. A string of ultracold polar molecules, whose large, permanent electric dipole moment is either aligned, $|0\rangle$, or anti-aligned, $|1\rangle$, with an external electric field represents a promising candidate for a molecular quantum computer. Computational operations can be applied to these molecular qubits by driving transitions from $|0\rangle$ to $|1\rangle$, either directly by microwave transitions or indirectly via stimulated Raman transitions^[4]. Alternatively, one can consider using the rich ro-vibrational structure of molecules to form ‘qudits’, in which more than one bit of quantum information is stored in a single molecule^[5,6]. On a more fundamental level, it is interesting to consider the nature of chemical reactions in the ultracold regime. Many chemical reactions are thermally activated with collisional energy overcoming an activation barrier before the reaction proceeds. At ultracold temperatures the probability of such a collision becomes negligible meaning that most chemical reactions will not occur. The absence of collisional energy in ultracold chemical reactions leaves us free to study collisions in which there is no potential energy barrier. These are of particular interest, for example, in astrochemistry and are thought to play a key role in the reaction between H_2 and H_2^+ (the most common chemical reaction in the universe) and the lengthening of carbon chain molecules in interstellar space^[7]. Ultracold molecules also provide a potential testbed in which to measure the electric dipole moment (EDM) of the electron, d_e . The standard model predicts that d_e is far too small

to detect with current apparatus, however, many extensions to this model predict a larger, detectable value. Hence, the discovery of a significant EDM of the electron would have a profound impact on our understanding of the standard model. The signature of an EDM is a linear Stark-induced energy shift in the presence of an electric field. The use of polar molecules enhances the effective electric field by up to three orders of magnitude over the atomic case due to the polarizability of the molecule^[8], meaning that measurements of d_e with polar molecules are the most sensitive. Currently, the most precise measurement of d_e was made in a molecular beam^[9] but it is hoped that greater sensitivity can be achieved using cold molecules^[10,11].

Standard laser cooling techniques do not work on molecules as they rely upon cycling between two closed energy levels; it is hard to find such a system in the complex molecular structure. Hence, the road to cold molecules is split into two paths — finding methods to cool molecules directly and forming molecules from cold atoms. Directly cooling molecules has the advantage that stable, deeply bound, molecules can be used; hence lower vibrational levels can be accessed. So far, however, it has not been possible to cool molecules directly to quantum degeneracy. Indirect methods such as continuous-wave photo-association or Feshbach resonances have been used to form sub-micro Kelvin molecules from ultracold atoms; however, these methods tend to produce vibrationally excited molecules. Hence indirect cooling techniques have recently focussed on controlling the internal states of an ultracold molecule.

Two different techniques have been demonstrated to successfully transfer molecules

into the vibrational ground state; stimulated Raman adiabatic passage (STIRAP)^[12] and molecular optical pumping^[13]. Complimentary to these two techniques is the idea of ultrafast photoassociation in which broadband laser pulses are used to excite a time non-stationary wavepacket in the excited state. The evolution of this wavepacket could be manipulated by pulse-shaping the excitation laser hence leading to enhanced photoassociation rates. This technique is the avenue explored in this thesis.

1.1 Thesis Overview

Chapter 2 gives an overview of the necessary background required to understand the subsequent chapters. First, a simple model of a diatomic molecule is discussed; during this section, it will become clear why it is not possible to use direct laser cooling techniques, on even this most simple of molecules. Secondly, the basic principles behind laser cooling are introduced. Finally, a summary of the state-of-the-art in cold molecule formation is given.

In Chapter 3 a description of the apparatus used for ultrafast photoassociation experiments is given. This apparatus was inherited by the author from previous experiments and was used to produce the results discussed in Chapter 4.

Chapter 4 describes photoionization and photoassociation experiments conducted in a magneto-optical trap (MOT). In these experiments a narrow-band pulsed laser was used to detect molecules in the triplet ground state in the MOT. The distribution of these molecules indicated that they are formed via photoassociation by

the trapping lasers. Ultrafast pulses were then used to perform time-dependent ionization of ultracold molecules. By observing this signal as a function of detuning from atomic resonance, we were able to infer information about the origin of these molecules. Comparison with the initial distribution indicates that these molecules were photoassociated from the atoms in the MOT as opposed to being molecules which existed before the pulse and were merely excited rather than associated.

Chapter 5 describes the construction of a new cold atom apparatus to replace that used in Chapter 3. In this system, the density of the sample was increased in a hybrid magnetic and optical trap. However, despite these improvements, we were unable to achieve improvements to the results presented in Chapter 4. A summary of the results of the photoassociation experiments and outlook for the future is presented in Chapter 6. In the context of the successes of alternative indirect methods for molecular cooling, such as STIRAP and molecular optical pumping, as well as improvements in direct cooling techniques, it appears that ultrafast photoassociation has fallen behind its competitors. Reasons for this are given, and recommendations for future experiments are made. In the light of this, we begin to consider alternative uses for the cold atom apparatus. Many quantum communication experiments utilize ultracold atoms (see for example references^[14–17]) and it is thought that this is a potential application of the new apparatus. Another experiment within Professor Walmsley’s group has developed a quantum memory based on a Raman interaction between hyperfine ground states in cesium in a warm vapor cell^[18,19]. It would be interesting to think of the extension of this scheme into the ultracold regime where

atom-atom interactions allow manipulation of stored quantum states.

Following the conclusion of the photoassociation experiments, the author joined the Raman quantum memory experiment to work on the memory in the warm ensemble, with an aim towards potentially applying this technology to an ultracold sample of atoms. Polarization encoded information was stored in an interferometric dual-rail memory, one arm storing horizontally polarized light, and the other vertical. By performing quantum process tomography on the system, we were able to demonstrate a process purity of the memory of over 97%. This is discussed in [Chapter 7](#)

1.2 Contribution of the Author

The experiments discussed in the following chapters were all performed in the research group of Professor Ian Walmsley at the University of Oxford. Excited state investigations performed in the old MOT apparatus ([Chapter 4](#)) were performed by the author together with a senior D.Phil. student (David McCabe) under the guidance of Dr Jovana Petrovic. The author is also particularly indebted to B atrice Chatel and Antoine Monmayrant for building the NOPA. Theoretical support to the experimental project was provided by Hugo Martay, most notably in the simulations of the initial state distribution ([Section 4.1.1](#)) and modeling of the pump-probe experiment ([Section 4.1.3](#)).

The construction of the Dipole trap apparatus was performed primarily by the author. Initial assistance was provided by David McCabe and Dr Giuseppe Smirne,

in particular in the development of the magnetic field control. However, from the point of demonstrating a MOT onwards, the experiments were performed by the author alone.

Chapter 2

Background

In this chapter we introduce the key concepts behind the experiments described in subsequent chapters. A simple model for the diatomic molecule is discussed in Section 2.1. Despite the simplicity of the model, we are able to derive the long-range behaviour of homonuclear dimers which has significant implications to photoassociation experiments. We also follow a derivation of the Franck-Condon principle which is key to understanding vibronic transitions. Section 2.3 is a review of conventional atom-cooling techniques including the magneto-optical trap (MOT), magnetic trapping, dipole force trapping and evaporative cooling. Section 2.4 provides a review of techniques for cold molecules: both directly cooling bound molecules (so-called direct cooling) and the synthesis of ultracold molecules from ultracold atoms (indirect cooling). Due to the nature of this thesis, this review is dominated by indirect methods and includes only a brief section on direct cooling. For a more thorough review

of direct cooling methods¹ the reader is directed to section 3.1 of the review article by Carr *et al.*^[20]. Finally, in Section 2.4.3, the concept of ultrafast photoassociation is introduced; this is the method pursued in this work.

2.1 A physical model of a diatomic molecule

In the simplest possible case, we consider a diatomic molecule to be two nuclei, of mass m_1 and m_2 , held together by a chemical bond, modelled by a mass-less spring, as shown in Figure 2.1. The motion of the nuclei can be separated into three types:

- **Translational** — Motion of the entire molecule with respect to a fixed reference.
- **Rotational** — Rotation of the molecule about its centre of mass.
- **Vibrational** — Motion of the nuclei in the atom with respect to their equilibrium positions.

We can decouple the translational motion of the molecule by introducing a centre-of-mass co-ordinate frame. In this picture, the reduced mass of the molecule is

$$\mu = \frac{m_1 m_2}{m_1 + m_2} \text{ [21].}$$

Because of the large mass difference between the electrons and the nuclei ($m_p/m_e = 1836$) we can consider the nuclei to be stationary on the time-scale of electronic motion. This allows us to separate the state of the system into nuclear and electronic components. In the case of ultracold collisions, the energy of a collision is sufficiently

¹As of march 2009

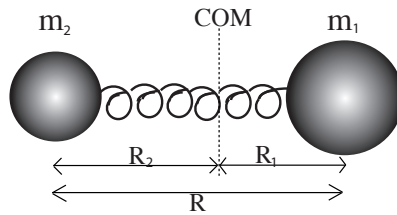


Figure 2.1 A simplified sketch of a diatomic molecule with internuclear separation, R . The nuclei, of mass m_1 and m_2 are at distances of R_1 and R_2 from the centre of mass.

low that we can neglect all states in which the angular momentum is non-zero. Hence we can neglect the rotational contribution to the Hamiltonian^[22]. The molecular wavefunction can, therefore be completely characterised as follows;

$$|\psi_{n,v}^{Mol}\rangle = |\psi_n^e\rangle |\psi_{n,v}^N\rangle, \quad (2.1)$$

this is known as the *adiabatic Born–Oppenheimer approximation*^[23].

With this simple assumption, we can solve the Schrödinger equation separately for the nuclear and electronic motion. First, let us consider the electronic motion, at a fixed inter-nuclear separation, R ;

$$\hat{H}_e |\psi_n\rangle = [\mathbf{T}_e(\mathbf{r}) + \mathbf{V}_{ee}(\mathbf{r}) + \mathbf{V}_{Ne}(R, \mathbf{r})] |\psi_n\rangle = U_n(R) |\psi_n\rangle. \quad (2.2)$$

The vector \mathbf{r} represents the set of electronic co-ordinates. \mathbf{T}_e is the kinetic energy operator of the electrons. The \mathbf{V} terms represent the Coulomb potentials felt by the nuclei and electrons. Just as for atoms, the result is a series of discrete energy levels

depending on the electronic orbitals^[23]. As we vary R , the solutions to this equation trace out a series of curves, $U_n(R)$. These potentials, together with the electrostatic repulsion, completely define the potential energy of the two nuclei, \mathbf{V}_{NN} . The effect of the electrostatic attraction between the electrons and the nuclei, \mathbf{V}_{Ne} , on the nuclear motion is neglected under the Born–Oppenheimer approximation. These potentials are non-trivial to solve, however their general form can be understood by a simple model proposed by Lennard-Jones^[24]. The Lennard-Jones potential consists of the sum of an attractive Van der Waals force (proportional to R^{-6}) and a repulsive Coulomb force ($\sim R^{-12}$);

$$V_{LJ}(R) = U_0 \left(\left(\frac{R}{R_0} \right)^{-12} - 2 \left(\frac{R}{R_0} \right)^{-6} \right). \quad (2.3)$$

As we sum these two together, we get a potential well of depth U_0 located at the equilibrium position, R_0 . A sharp inner edge and a gently sloping outer edge are characteristic of a molecular potential as is shown in Figure 2.2.

Now that we have defined the molecular potentials, we allow the nuclei to vibrate within them. The vibrational motion will be quantized in a series of vibrational energy levels, v , with associated wavefunctions, $|\psi_{n,v}\rangle$. Hence we would like to solve the following Schrödinger equation for nuclear motion;

$$\hat{H}_N |\psi_{n,v}\rangle = [\mathbf{T}_N(R) + \mathbf{V}_{NN}(r)] |\psi_{n,v}\rangle = E_{n,v}(R) |\psi_{n,v}\rangle, \quad (2.4)$$

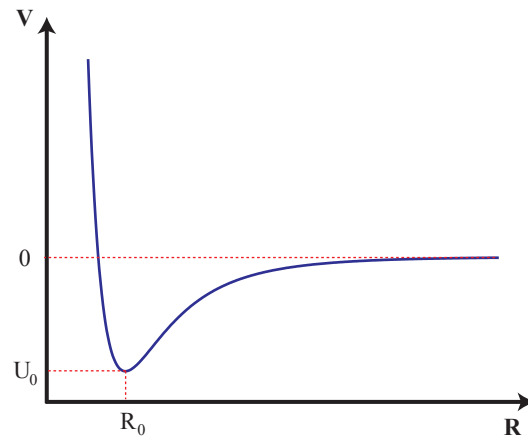


Figure 2.2 The model Lennard-Jones molecular potential exhibiting a potential well of depth U_0 with a minimum at R_0 .

where \mathbf{T}_N is the kinetic energy operator of the nuclei and the subscripts n, v indicate the v^{th} vibrational state in the n^{th} electronic state. As before, solutions to this equation are complex and must be solved numerically; examples of such solutions are shown in Figure 2.3. At the bottom of the well, the potential is often well approximated by a harmonic potential with evenly spaced vibrational energy levels;

$$E_v^{Har} = \hbar\omega_{osc} \left(v + \frac{1}{2} \right). \quad (2.5)$$

However, due to the anharmonicity of the potential, the oscillation frequency, ω_{osc} , decreases with decreasing binding. Hence the vibrational levels are closer together towards the top of the potential, this is clearly evident in Figure 2.3(a).

The vibrational wavefunctions in Figure 2.3(b) are the result of purely quantum-mechanical calculations, yet they, too, can be understood in a classical manner. The probability distribution in R , is given by the modulus squared of the wavefunction

$|\langle \psi_{n,v} | \psi_{n,v} \rangle|^2$. As we can see in Figure 2.3(b), especially in $v = 100$, the wavefunction is largest at the classical turning points of the potential, *i.e.* exactly where we would expect the molecule to spend most time in the simple mass-on-a-spring picture shown in Figure 2.1. Towards the top of the potential well, due to the large anharmonicity of the potential, the outer turning point is much softer than the inner turning point. This leads to asymmetric wavefunctions with population density at the outer turning point significantly larger than the inner. This can be easily understood classically as the atoms spend more time at the outer turning point. This feature of molecular wavefunctions is universal across all states and is crucial when considering vibronic transitions (see Section 2.2.6).

2.2 Hund's coupling cases and molecular notation

The total angular momentum of a molecule, \mathbf{J} , is the resultant of the vector sum of all the different angular momenta in the molecule — electron spin, \mathbf{S} , electron orbital angular momentum, \mathbf{L} and nuclear angular momentum \mathbf{N} . The manner in which these component angular momenta sum is dependent on their couplings to each other, and to the internuclear electric field. Five different coupling regimes are labeled as Hund's cases (a) - (e). All five of these cases are discussed in detail in reference^[23]. For the ultracold collisions relevant to this thesis, we can neglect the effects of the nuclear angular momentum, hence only cases (a) and (c) are relevant.

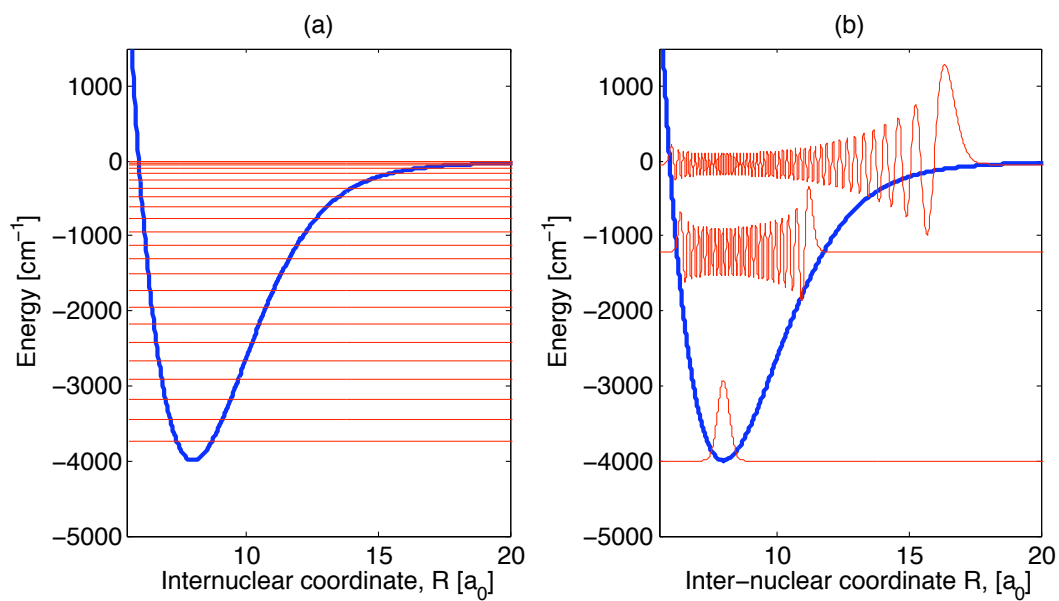


Figure 2.3 (a) Ground singlet ($X^1\Sigma_g^+$) state of the Rb₂ molecule (thick blue) and associated vibrational levels (thin red). For clarity, only every 5th level is plotted. Note the spacing between levels gets smaller at increasing energies due to the anharmonicity of the potential. (b) With increasing energy; $v = 0$, $v = 50$ and $v = 100$ vibrational wavefunctions of the X state. Note that the wavefunctions have maxima at the classical turning points of the molecular potential

Symbol	Definition	Physical quality
Λ	$\Lambda = \mathbf{L} \cdot \hat{\mathbf{R}}$	Projection of the orbital angular momentum onto the internuclear axis
Σ	$\Sigma = \mathbf{S} \cdot \hat{\mathbf{R}}$	Projection of the electron spin onto the internuclear axis
Ω	$\Omega = \Sigma + \Lambda$	Total electronic angular momentum about the internuclear axis

Table 2.1 Summary of the good quantum numbers in Hund's case (a). $\hat{\mathbf{R}}$ is a unit vector along the internuclear axis.

2.2.1 Hund's case (a)

In Hund's case (a), both the electronic spin and electronic orbital angular momentum are strongly coupled to the internuclear electric field. Hence \mathbf{L} and \mathbf{S} precess about the internuclear axis, $\hat{\mathbf{R}}$ and their projections onto the nuclear axis, Λ and Σ respectively, become good quantum numbers. The total angular momentum about the internuclear axis is given by $\Omega = \Lambda + \Sigma$. The relevant quantum numbers for Hund's case (a) are summarised in table 2.1, a vector diagram is shown in Figure 2.4. In the Hund's case (a) basis, molecular states are labeled $^{2S+1}\Lambda_{g/u}^{\pm}$, with the symbols $\Sigma, \Pi, \Delta, \Phi, \dots$ used to denote the quantum number, Λ , in the same way S, P, D, F, \dots are used to denote \mathbf{L} . g/u and \pm indicate the symmetries of the molecular wavefunction. In Hund's case (a), \mathbf{S} can be considered a good quantum number due to its strong coupling to the internuclear axis. Each valence electron has $\mathbf{S} = 1/2$. For a two-spin system, the electron spins can be either parallel, leading to three $\mathbf{S} = 1$ (*triplet* states), or anti-parallel giving a single $\mathbf{S} = 0$ (*singlet* state), where the multiplicity of these states is given by $2S + 1$. The electronic states are labeled, with increasing energy; X, A, B, C, \dots (for singlets) and a, b, c, \dots (for triplets).

Symbol	Definition	Physical quality
\mathbf{J}_a	$\mathbf{J}_a = \mathbf{L} + \mathbf{S}$	Resultant of the electronic spin and orbital angular momentum
Ω	$\Omega = \mathbf{J}_a \cdot \hat{\mathbf{R}}$	Total electronic angular momentum about the internuclear axis

Table 2.2 Summary of the good quantum numbers in Hund's case (c). $\hat{\mathbf{R}}$ is a unit vector along the internuclear axis.

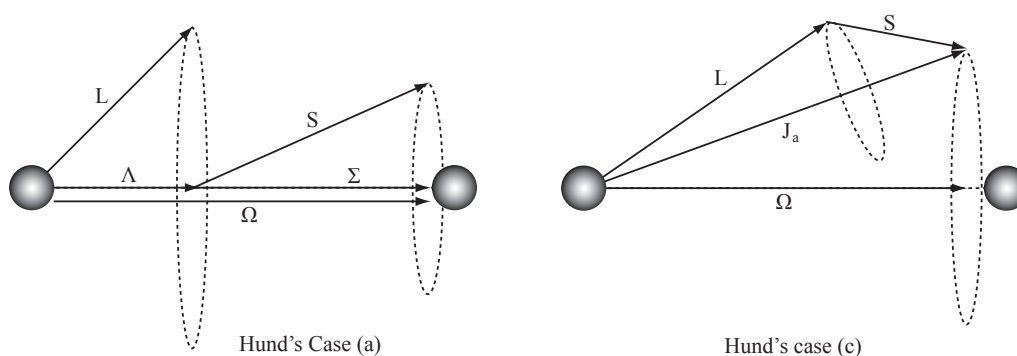


Figure 2.4 Vector diagram of Hund's coupling cases (a) and (c).

2.2.2 Hund's case (c)

In Hund's case (c), the spin-orbit coupling between \mathbf{L} and \mathbf{S} is significantly stronger than the coupling of these properties to the internuclear axis, hence they precess about their resultant, \mathbf{J}_a . In turn, \mathbf{J}_a precesses about the internuclear axis, with a component, Ω , along the internuclear axis. This is summarised in Figure 2.4 and table 2.2. In the Hund's case (c) basis, molecular states are labeled $\Omega_{g/u}^{\pm}$ where $\Omega = 0, 1, 2, \dots$. Typically, Hund's case (a) dominates at shorter internuclear separations and (c) at long-range.

2.2.3 Symmetry properties

For homonuclear molecules, the electronic motion must be unaffected by an exchange of the two nuclei. Hence the molecular wavefunction must remain the same, or change sign when reflected about the centre of mass. States with the former symmetry are known as *gerade* and the latter as *ungerade* (from the German for 'even' and 'odd' respectively). In a diatomic molecule, any plane which passes through both nuclei is a plane of symmetry of the molecule, the electronic wavefunction must remain the same (+) or change sign (-) when reflected about any of these planes. For Σ states these states are non-degenerate and hence are labeled Σ^\pm . For all other states ($\Pi, \Delta \dots$), the $+/-$ states are degenerate and hence are not labeled.

2.2.4 Selection rules

A series of selection rules govern the allowed transitions between molecular states. Assuming a single photon transition in a homonuclear dimer, in Hund's case (a) basis, the following selection rules apply (see section 5.3 of Herzberg^[23] for derivations);

- The component of the electric field parallel to the internuclear axis maintains the orbital angular momentum projection and the perpendicular component changes it by ± 1 . Therefore; $\Delta \mathbf{A} = 0, \pm 1$.
- The total electronic spin must be conserved; $\Delta \mathbf{S} = 0$.
- The inversion symmetry must be changed between initial and target state;

$$g \Leftrightarrow u.$$

- If the state is defined by its reflection symmetry, this does not change in a transition; $\pm \rightarrow \pm$.

It is important to note here that the $g \Leftrightarrow u$ selection rule precludes dipole transitions between vibrational levels in the same molecular potential. Hence, in order to change vibrational states via dipole transitions, one must go via an intermediate state, as discussed below in Section 2.4.2.

Often, the projection of the orbital angular momentum onto the internuclear axis produces allowed molecular transitions where atomic transitions would be forbidden. An example of this is utilized in Section 4.1.1 where molecules are excited from the $a^3\Sigma_u^+$ state asymptotic to $5S$, to the $(2)^3\Sigma_g^+$ state asymptotic to $4D$, despite the $5S \rightarrow 4D$ atomic transition being dipole forbidden.

A good knowledge of the selection rules allows us to distinguish which of the many molecular potentials will play a role in a given experiment. A list of the relevant potentials in the ground and first excited state is given in Table A.2; these potentials are plotted in Figure A.3.

2.2.5 Long-range behaviour

At small internuclear separations, *i.e.* close to the minimum of the potential well, there is significant overlap of the electronic wavefunctions. Hence chemical bonding, the sharing of electrons between nuclei, plays a significant role in shaping the potential landscape of the molecule. This is why the simplistic model portrayed in

Figure 2.2 can never fully recreate a realistic molecular potential. However, with increasing vibrational energy² the nuclei become further and further apart and the simple model becomes more and more accurate and it becomes possible to simply express the long-range potential $\mathbf{V}_{\text{LR}}(R)$ as an expansion in $1/R$;

$$\mathbf{V}_{\text{LR}}(R) = \frac{C_1}{R} + \frac{C_2}{R^2} + \frac{C_3}{R^3} + \frac{C_4}{R^4} + \frac{C_5}{R^5} + \frac{C_6}{R^6} + \dots \quad (2.6)$$

In the case of a pair of oppositely charged ions, the C_1/R term dominates, for one ion and one neutral atom, the C_4/R^4 term dominates³. However, in the case of neutral atoms, we must consider series beginning with C_6/R^6 .

A sketch of a simple electric dipole is shown in Figure 2.5. A dipole is formed by two equal but opposite charges, $+q$ and $-q$, separated by, d . A small test charge, p , sits a distance, R , away from the centre of the dipole. The potential experienced at p is simply the sum of the potentials due to each charge;

$$\mathbf{V}_{\mathbf{d}} = \frac{q}{4\pi\epsilon_0} \left(\frac{1}{|\mathbf{r}_+|} - \frac{1}{|\mathbf{r}_-|} \right) = \frac{q}{4\pi\epsilon_0} \left(\frac{|\mathbf{r}_-| - |\mathbf{r}_+|}{|\mathbf{r}_+|\mathbf{r}_-|} \right). \quad (2.7)$$

In the limit $R \gg d$ then $\mathbf{r}_- - \mathbf{r}_+ = \mathbf{d} \cdot \hat{\mathbf{R}}$ (where $\hat{\mathbf{R}}$ is a unit vector in the direction of R) and $|\mathbf{r}_+||\mathbf{r}_-| \simeq R^2$. The electric dipole moment, \mathbf{p} , is defined by $\mathbf{p} = q\mathbf{d}$, hence;

$$\mathbf{V}_{\mathbf{d}} = \frac{1}{4\pi\epsilon_0} \left(\frac{\mathbf{p} \cdot \hat{\mathbf{R}}}{R^2} \right). \quad (2.8)$$

²Decreasing binding energy.

³The Electric field around the ion, of the form $\mathbf{E} \propto 1/R^2$ induces an instantaneous dipole in the neutral atom whose energy is given by $\mathbf{u} = -\mathbf{p} \cdot \mathbf{E} \propto 1/R^2$.

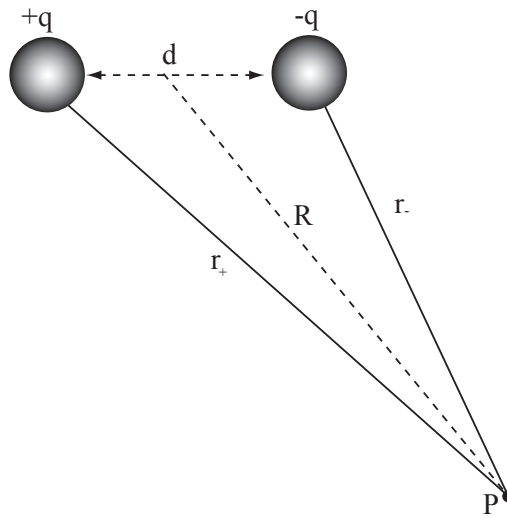


Figure 2.5 An electric dipole with test charge at position P.

Taking the gradient of this potential yields the electric field surrounding the dipole;

$$\mathbf{E}_d = -\nabla V_d = \frac{3\mathbf{p} \cdot \hat{\mathbf{R}} - \mathbf{p}}{4\pi\epsilon_0 R^3}. \quad (2.9)$$

The energy of a dipole in a field is $\mathbf{u} = -\mathbf{p} \cdot \mathbf{E}$ so, two dipoles, separated by a distance R will experience a potential, $\mathbf{V}_{dd}(R)$, of the form;

$$\mathbf{V}_{dd}(R) = -\mathbf{p}_1 \cdot \mathbf{E}_1 = \frac{\mathbf{p}_1 \cdot \mathbf{p}_2 - 3(\mathbf{p}_1 \cdot \hat{\mathbf{R}})(\mathbf{p}_2 \cdot \hat{\mathbf{R}})}{4\pi\epsilon_0 R^3}. \quad (2.10)$$

Very few atoms, either in their ground or excited states, have a permanent electric dipole⁴. However, small fluctuations in the electron density in an atom can lead to a temporary dipole. The electric field produced by this dipole, \mathbf{E}_1 , can be strong

⁴There are exceptions due to degeneracy of excited states.

enough to induce a dipole in a neighboring atom, \mathbf{p}_2 . The attraction between these two dipoles, known as the *van der Waals force*, can lead to molecule formation in even inert elements^[23]. The strength of this induced dipole is proportional to the strength of the field; *i.e.* it is proportional to $1/R^3$. Hence, the van der Waals force potential of two neutral atoms⁵ with respect to each other is;

$$\mathbf{V}_{\text{vdW}} \propto \frac{C_6}{R^6}. \quad (2.11)$$

In the case of homonuclear molecules, the first excited state takes on a very different form. If only one of the atoms is excited, due to the degeneracy of the state, we do not know *which* atom has been excited, hence we can consider each atom to be in a correlated superposition of ground, $|g\rangle$, and excited, $|e\rangle$, states; *i.e.* $|\psi\rangle = |ge\rangle + e^{i\theta}|eg\rangle$. As this superposition evolves, we have a real oscillating dipole moment, hence the potential reverts to the $1/R^3$ dipole-dipole form shown in Equation (2.10). This is discussed in detail by Jones *et al.* in reference^[25]. This difference in long range behaviour is clear in the rubidium dimer, shown in Figure 2.6.

2.2.6 The Franck-Condon principle

In order to manipulate the internal states of the molecule, we need to make transitions between different vibrational states. Often (for example in photoassociation and stimulated Raman adiabatic passage (STIRAP)) this involves a light-assisted

⁵Without a permanent electric dipole.

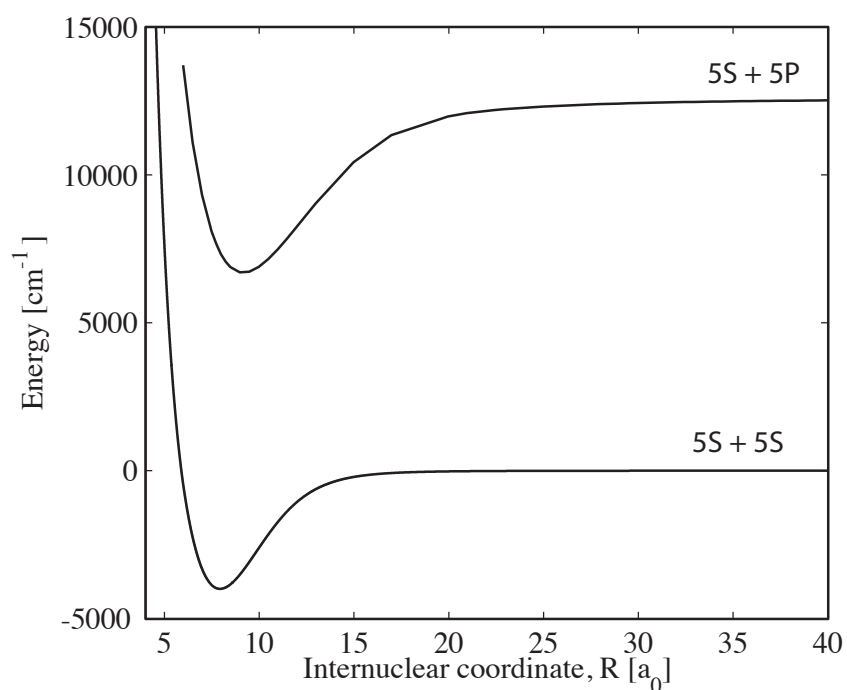


Figure 2.6 The ground (*X*) and first excited (*A*) singlet states in Rb_2 . The *X* has two ground state atoms in the 5*S* state while in the *A* state an excitation to the 5*P* state is exchanged between the atoms. Note the difference in long range behaviour.

transition from the ground electronic state and a second radiative transition (either spontaneous or stimulated) back to a different ground state. To design schemes for controlling the vibrational levels of a molecule we need to understand these processes and what governs their transition strengths. This was first formalised by Franck in 1925^[26], and later transcribed into the wave-mechanical basis in 1928 by Condon^[27]. Together, their work is known as the *Franck–Condon principle*. Both approaches arrive at the same conclusion: that the most intense transitions in a spectrum are those related to vertical transitions (*i.e.* transitions in which the internuclear separation does not change) between turning points in the molecular potentials. However, it is worth examining both methods as Franck's gives the more intuitive view, while Condon's is more rigorous in the quantum mechanical picture.

Franck's analysis is semi-classical; the vibrational *energy* of the nuclei is quantised, however, the *motion* is considered to be purely classical. The nuclear motion is deemed to be slow by comparison with the electronic transition which is considered to be almost instantaneous. It is also assumed that the nuclei cannot pick up much extra kinetic energy due to an electronic excitation. Figure 2.7 (a) shows a pair of arbitrary molecular potentials whose minima occur at the same internuclear separation, R . We assume that the molecule starts in the lowest state, $v'' = 0$ ⁶, and hence has very little kinetic energy. We would like to produce a transition to an excited electronic state; Franck's principle suggests that this transition should not significantly alter the position or kinetic energy of the nuclei. We can see that a tran-

⁶By convention, vibrational levels in the ground electronic state are labeled $v'' = n$ while those in excited states are labeled $v' = n$.

sition from $v'' = 0$ to $v' = 0$ satisfies both of these conditions; the nuclear position is maintained by a vertical transition from A to B, while the kinetic energy is zero at both A and B. However, if we try to excite the molecule to a higher vibrational level ($v' \gg 0$), in order to maintain nuclear position by making a vertical transition (A \rightarrow E) we must gain kinetic energy. The only way we can conserve kinetic energy is to make a transition to one of the turning points (C or D) which involves a large nuclear movement. Hence this transition is extremely unlikely to occur. This is shown in a generalised 2-state system in Figure 2.7 (b); strong transitions are indicated by solid black lines while weak transitions have a dashed line.

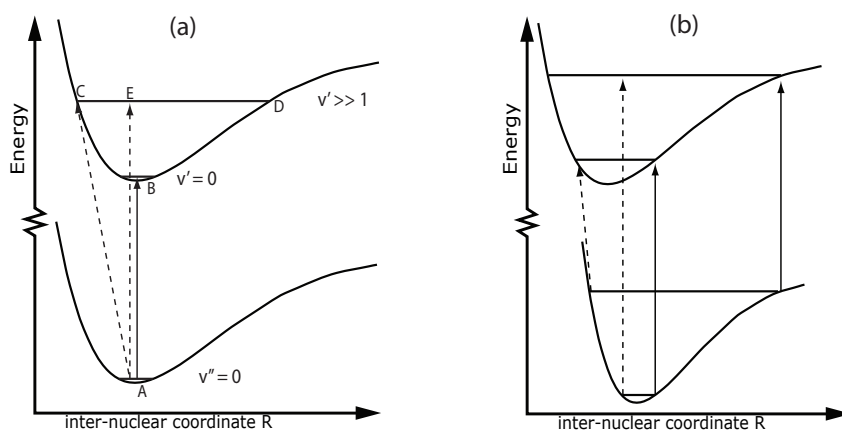


Figure 2.7 A semi-classical illustration of the Franck-Condon principle. Vertical transitions between turning points (solid lines) are likely to occur as kinetic energy and nuclear position are conserved. Other transitions (dashed lines) in which there are large changes in kinetic energy or nuclear position are unlikely.

While the model put forward by Franck is intuitive and, most importantly, fits observed molecular spectra, it does not sit comfortably with a fully quantum mechanical picture in which the nuclear positions are not discrete but rather described

by a wavefunction. In this basis, as the nuclear positions are not well defined, it is hard to consider vertical transitions. Instead we consider a more mathematical approach.

In analogy with the atomic case, the dipole transition moment between two vibrational states, v'' and v' , in different electronic levels, 0 and 1, is given, under the Born–Oppenheimer approximation, by;

$$\langle \psi' | \mathbf{d} | \psi'' \rangle = \langle \psi_{1,v'}^N | \langle \psi_1^e | \mathbf{d} | \psi_0^e \rangle | \psi_{0,v''}^N \rangle, \quad (2.12)$$

where $\mathbf{d} = -e\mathbf{r} \cdot \mathbf{E}$ is the electric dipole operator which can be written as a sum of a part depending on electrons, and another on the nuclei ($\mathbf{d} = \mathbf{d}_e + \mathbf{d}_N$). Hence the dipole transition moment can be re-written as;

$$\begin{aligned} \langle \psi' | \mathbf{d} | \psi'' \rangle &= \langle \psi_1^e | \langle \psi_{1,v'}^N | (\mathbf{d}_e + \mathbf{d}_N) | \psi_{0,v''}^N \rangle | \psi_0^e \rangle, \\ &= \int \int \psi_1^{e*}(R, r) \psi_{1,v'}^{N*}(R) (\mathbf{d}_e + \mathbf{d}_N) \psi_0^e(R, r) \psi_{0,v''}^N(R) dR dr, \\ &= \int \psi_{1,v'}^{N*}(R) \left[\int \psi_1^{e*}(R, r) \mathbf{d}_e \psi_0^e(R, r) dr \right] \psi_{0,v''}^N(R) dR \\ &\quad + \int \psi_{1,v'}^{N*}(R) \mathbf{d}_N \left[\int \psi_1^{e*}(R, r) \psi_0^e(R, r) dr \right] \psi_{0,v''}^N(R) dR. \end{aligned} \quad (2.13)$$

By orthogonality, $\int \psi_1^{e*}(R, r) \psi_0^e(R, r) dr = 0$. Making the assumption that the electronic component of the dipole moment (\mathbf{d}_e) is independent of internuclear separation (see section III.2 of Herzberg^[23] for a discussion of this assumption) gives;

$$\begin{aligned}
\langle \psi' | \mathbf{d} | \psi'' \rangle &= \int \psi_{1,v'}^{N*}(R) \psi_{0,v''}^N(R) dR \times \int \psi_1^{e*}(R, r) \mathbf{d}_e \psi_0^e(R, r) dr, \\
&= \langle \psi_{1,v'}^N | \psi_{0,v''}^N \rangle \langle \psi_1^e | \mathbf{d} | \psi_0^e \rangle.
\end{aligned} \tag{2.14}$$

So we see that the dipole matrix element that we would expect for an atomic transition is multiplied by a factor $\langle \psi_{1,v'}^N | \psi_{0,v''}^N \rangle$. This factor, which is known as the *Franck–Condon factor (FCF)*, is the spatial overlap between the two vibrational levels involved. Hence transitions between vibrational levels are more likely to occur if this overlap is larger.

Figure 2.8 shows the same simple system as illustrated in Figure 2.7(a), but this time with wavefunctions plotted for each vibrational state. This gives a graphical illustration of the FCF derived in Equation (2.12). We can see that there is a strong overlap between $v'' = 0$ and $v' = 0$, hence the FCF is large. However, the overlap between $v'' = 0$ and $v' \gg 1$ is very small hence the weak transition. The illusion of ‘vertical transitions’ can be recovered, in the quantum-mechanical picture, by considering the nature of the vibrational wavefunctions. All of the wavefunctions are largest at the classical turning points, hence the FCF will be largest between vibrational levels with similar turning points, *i.e.* ‘vertical transitions’.

2.2.7 The Rb₂ molecule

Rubidium is an alkali metal with an atomic number of 37. Rubidium exists in two naturally-occurring isotopes ⁸⁷Rb and ⁸⁵Rb. The full electronic configuration is

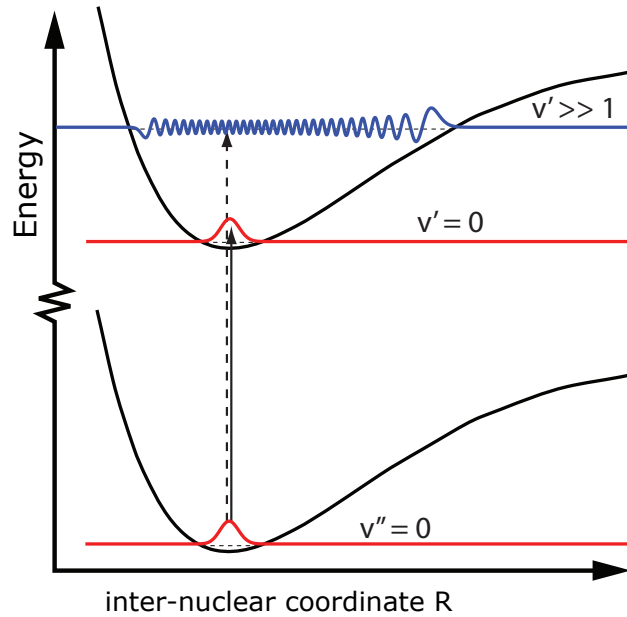


Figure 2.8 A quantum-mechanical illustration of the Franck-Condon principle. The wavefunction overlap between $v'' = 0$ and $v' = 0$ is large so there is a high Franck-Condon factor (FCF). However, the overlap between $v'' = 0$ and $v' \gg 1$ is small, so the FCF is weak.

$1s^2 2s^2 2p^6 3s^2 3p^6 3d^{10} 4s^2 4p^6 5s^2 S_{1/2}$ ^[28] however, in this work, we consider only the behaviour of the single valence electron in the $^2S_{1/2}$ level. The first excited state, 5^2P , is split by fine structure into two levels: $5^2P_{1/2}$ and $5^2P_{3/2}$. Full details of the physical and optical properties of ^{87}Rb and ^{85}Rb can be found in reference papers by Steck^[29,30]. In this thesis we investigate the Rb_2 dimer; below we discuss the molecular potentials related to the ground, $5S$, and first excited, $5P$, states. Further information can be found in Appendix A.

Ground states

The ground states of the Rb_2 molecule are asymptotically connected to the $5S_{1/2}$ atomic ground state. As both valence electrons are in S states, there is no orbital angular momentum; hence $\Lambda = 0$. This leaves us with a pair of Σ states with either singlet or triplet character. As the two electrons are in the same electronic state, the Pauli exclusion principle dictates that their overall wavefunction must be anti-symmetric. This constrains the parity. Hence a singlet state must be *gerade* as the electron spins are anti-parallel and a triplet state must be *ungerade*. Under these constraints the two ground state molecular potentials are $X^1\Sigma_g^+$ and $a^3\Sigma_u^+$. As the orbital angular momentum is zero, it is not relevant to discuss ground state Rb_2 molecules in the Hund's case (c) basis.

Excited states

The lowest-lying excited Rb_2 molecular states are formed from a ground-state $5S_{1/2}$ atom bonding with an excited-state $5P_{1/2,3/2}$ atom. These states have a single quantum of orbital angular momentum, and hence can be described either in Hund's case (a) or (c) basis. At short range, where the molecular bond is strong compared to the fine-structure interaction, Hund's case (a) is appropriate, meanwhile Hund's case (c) basis is used at long range when the fine structure dominates.

In the Hund's case (a) basis, the total electronic orbital angular momentum is $\mathbf{L} = 1$, the projection of which onto the internuclear axis yields Σ or Π potentials. The $\mathbf{S} = 1/2$ electronic spins can be aligned or anti-aligned leading to triplet or

		Singlets	Triplets
Hund's case (a)	<i>gerade</i>	$1\Sigma_g^+ 1\Pi_g$	$3\Sigma_g^+ 3\Pi_g$
	<i>ungerade</i>	$1\Sigma_u^+ 1\Pi_u$	$3\Sigma_u^+ 3\Pi_u$

		$5S + 5P_{1/2}$	$5S + 5P_{3/2}$
Hund's case (c)	<i>gerade</i>	$0_g^+ 0_g^- 1_g$	$0_g^+ 0_g^- 1_g 1_g 2_g$
	<i>ungerade</i>	$0_u^+ 0_u^- 1_u$	$0_u^+ 0_u^- 1_u 1_u 2_u$

Table 2.3 Molecular states of Rb_2 in Hund's case (a) and (c) basis. Some states appear twice in the Hund's case (c) basis as they are degenerate at long range but diverge at short-range.

singlet potentials respectively. The parity is unconstrained by the Pauli exclusion principle, this gives the $2^3 = 8$ different molecular potentials shown in Table 2.3. Taking into account the multiplicity of the triplet states, we have 16 different states.

At long-range, these 16 potentials can be described in the Hund's case (c) basis. As fine structure dominates, these potentials are separated into those asymptotic to either $5P_{1/2}$ or to $5P_{3/2}$. In states connected to $5P_{1/2}$ we have $\mathbf{J}_a = 0$ or 1 so $\mathbf{\Omega}$ is 0 or 1. While in $5P_{3/2}$, $\mathbf{J}_a = 1$ or 2 so $\mathbf{\Omega} = 0, 1$ or 2. These states are shown in Table 2.3.

2.3 Techniques for cold atoms

The discovery of laser cooling in the early 1980s enabled experimentalists to cool neutral atoms into the micro-kelvin regime, far colder than had been previously possible using cryogenic methods, simply by using momentum transfer from a near-resonant laser beam. This discovery, and the subsequent development of related

cooling systems, led to the Nobel prize being jointly awarded to Steven Chu, Claude Cohen-Tannoudji and William Phillips in 1997^[31–33]. Colder temperatures can be achieved by transferring the laser cooled atoms in various non-radiative traps, and performing evaporative cooling. This led to the first observations of Bose–Einstein Condensation (BEC) and further Nobel prizes for Eric Cornell, Wolfgang Ketterle and Carl Wieman in 2001^[1,3]. This section lays out some of the techniques commonly used in cooling atoms, and introduces some of the underlying theory. For a more complete overview of the field, the reader is directed to reference^[22].

2.3.1 Laser cooling of atoms

An atom in a near-resonant laser beam experiences a scattering force, F_{scatt} , which is the rate at which atoms gain momentum by absorbing photons;

$$F_{scatt} = (\text{photon momentum}) \times R_{scatt}. \quad (2.15)$$

Photon momentum is $\hbar k$ and R_{scatt} is the scattering rate given by;

$$R_{scatt} = \frac{\Gamma}{2} \frac{\Omega^2/2}{\delta^2 + \Omega^2/2 + \Gamma^2/4}, \quad (2.16)$$

where the laser is detuned from resonance by an amount $\delta = \omega - \omega_0$, Ω is the Rabi frequency and Γ is the natural linewidth of the transition. The Rabi frequency is related to the intensity of the laser beam by $I/I_{sat} = 2\Omega^2/\Gamma^2$, hence (2.15) can be

re-written as;

$$F_{scatt} = \hbar k \frac{\Gamma}{2} \frac{I/I_{sat}}{1 + I/I_{sat} + 4\delta^2/\Gamma^2}. \quad (2.17)$$

A rubidium atom traveling at 300 ms^{-1} has momentum $p = m_{Rb} \times v = 4 \times 10^{-23} \text{ kg m s}^{-1}$. A photon resonant with the D2 transition in rubidium (780 nm) has momentum $\hbar k = 8.5 \times 10^{-28} \text{ kg m s}^{-1}$. Hence, it is clear that we require several thousand near-resonant photons to stop an atom. However, with a narrow linewidth laser, this is easily achievable and this technique has been used to completely stop a beam of atoms ⁷. It is also key that the atom remains in the same two states throughout these thousands of cycles of absorption and spontaneous emission, hence the necessity for a closed loop with no spontaneous emission to external states (or at least with a second laser to return lost atoms to the cycle).

Optical molasses

A single laser beam can provide slowing in one direction, however, to truly cool a sample, we must slow the thermal motion in all dimensions. This can be achieved by producing 3 orthogonal balanced pairs of counter-propagating laser beams of the same frequency. Symmetrically, this set-up has no net effect on a stationary atom, which is exactly what we want, but the symmetry is broken if an atom is moving towards one beam and away from the other. This produces a differential scattering force, $F_{molasses}$. We consider this problem in one dimension, but it is simple to

⁷The difficulty in this technique is maintaining resonance with the atoms as they slow down and the Doppler shift reduces. This can be done by producing a position-dependent magnetic field which counter-acts the Doppler shift with a Zeeman shift hence maintaining resonance^[33]. These so-called Zeeman slowers are a commonly used source of cold atoms.

extend to three. An atom moving with velocity, v , experiences a Doppler shift, kv , hence the differential scattering force is;

$$F_{molasses} = F_{scatt}(\delta - kv) - F_{scatt}(\delta + kv). \quad (2.18)$$

Assuming a low initial velocity, such that $kv \ll \Gamma$, this can be approximated as

$$F_{molasses} \simeq \left[F_{scatt}(\delta) - kv \frac{\partial F}{\partial \omega} \right] - \left[F_{scatt}(\delta) + kv \frac{\partial F}{\partial \omega} \right], \quad (2.19)$$

$$\simeq -2kv \frac{\partial F}{\partial \omega}, \quad (2.20)$$

$$F_{molasses} = -\alpha v, \quad (2.21)$$

where $\alpha = 2k \frac{\partial F}{\partial \omega}$ is the damping force experienced by an atom moving through the optical molasses. It is this property which led Chu *et al.* to refer to their new technique as optical molasses — as it is analogous to a particle moving through a viscous fluid.

A theoretical limit on the final temperature one can achieve in such an optical molasses can be derived by considering the heating effects of the Brownian motion on atoms continuously absorbing and re-emitting photons in an optical molasses. This limit, known as the Doppler temperature, is given by^[34,35];

$$K_B T_{Doppler} = \frac{\hbar \Gamma}{2}. \quad (2.22)$$

For sodium, this corresponds to $T_{Doppler} = 240 \mu\text{K}$. However, when Lett *et al.*

measured the temperature of their sodium molasses in 1988^[36], they were pleasantly surprised to measure a temperature of $43 \pm 20 \mu\text{K}$ — significantly below the Doppler limit. They were unable to provide a mechanism to explain this discrepancy, but speculated that the two-level model used in the derivation of (2.22) was over-simplistic and that a multi-state model would yield a lower limit. The solution to this problem, called polarisation gradient (or Sisyphus) cooling was provided by Dalibard *et al.*^[37], and is summarised below.

Consider an atom, in the ground state (angular momentum, $J = 1/2$) moving along in a pair of counter-propagating beams near resonant with the transition to the first excited state in the atom ($J = 3/2$). The beams interfere with each other creating a standing wave, in which the polarization depends on the relative phase between the two beams. Hence the polarisation spatially varies from linear, to σ^- , back to linear and then to σ^+ producing a so-called polarisation gradient. As the polarisation varies, so do the energies of the Zeeman sub-states, $M_J = \pm 1/2$, so we have spatially varying energy levels, as shown in Figure 2.9.

As an atom moves along the polarisation gradient it exchanges energy from kinetic to potential and back, but its total energy remains the same. Cooling is achieved by absorption and spontaneous emission. If an atom absorbs a photon towards the top of a ‘hill’ with frequency ω_{abs} and re-emits to the opposite M_J state with frequency ω_{em} , then the kinetic energy converted into climbing the ‘hill’ is lost to the photon. This process has a higher probability than the reverse, hence, over time, the sample is cooled. Sisyphus cooling continues until the atoms do not have

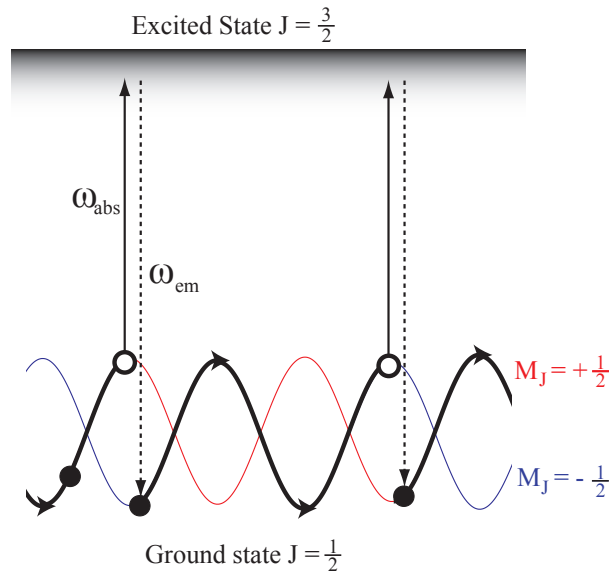


Figure 2.9 Sisyphus cooling method in a polarisation gradient. As the polarisation varies, so do the energies of the M_J energy levels. Energy is dissipated by absorption at the top of one of the ‘hills’, ω_{abs} , and spontaneous emission to the ‘valley’, ω_{em} .

enough energy to climb the hill. Hence, at equilibrium, we reach;

$$k_B T \simeq U_0 \propto \frac{I}{|\delta|}, \quad (2.23)$$

where U_0 is the height of the ‘hill’. U_0 is proportional to the intensity of the laser beams, I , and inversely proportional to the detuning, δ . Hence we can reduce the final temperature by reducing the power of our lasers and increasing the detuning.

Unfortunately, temperature does not decrease indefinitely, the limit is reached when the energy lost by spontaneous emission, U_0 , is balanced out by the recoil

energy. At this limit, we have;

$$k_B T_{recoil} \simeq E_{recoil} = \frac{h^2}{m\lambda^2}. \quad (2.24)$$

For sodium, T_{recoil} is $2.4 \mu\text{K}$, compared to a Doppler temperature of $240 \mu\text{K}$. Typically, temperatures are an order of magnitude higher than this but still significantly below the Doppler limit^[38]. For the polarisation gradient cooling to work, it is vital that the system has no background magnetic fields, the presence of which would produce a Zeeman shift that would nullify the energy shift induced by the polarisation gradient. Hence one must be very careful to nullify stray magnetic fields in the region of the cloud.

Magneto-optical trap

The molasses force is only velocity-dependent and hence the molasses slows atoms down, but does not trap them. However, by the application of a magnetic field gradient, and careful selection of the beam polarisations, it is possible to add a position-dependent force and hence create a trap for cold atoms. This technique, called a magneto-optical trap (MOT), was demonstrated by Chu *et al.*^[39] in 1987.

A MOT is formed by overlapping 3 orthogonal pairs of counter-propagating, red-detuned, laser beams at the centre of a quadrupole magnetic field gradient. This field gradient is typically produced by a pair of magnetic coils in the anti-Helmholtz configuration⁸, this is shown in Figure 2.10 (a). The field gradient induces a Zeeman

⁸The Helmholtz condition is two coils, carrying the same current, separated by their radius; this

shift in the atomic energy levels which is proportional to the distance from the centre. The opposing beams have opposite senses of circular polarisation, such that they excite different M_J states. By choosing the polarisations appropriately with respect to the field gradient, we see that the detuning of the laser decreases with distance from the centre (Figure 2.10(b)). Hence, atoms further from the centre of the field gradient scatter more photons and are returned to the centre and trapped. This is discussed mathematically below.

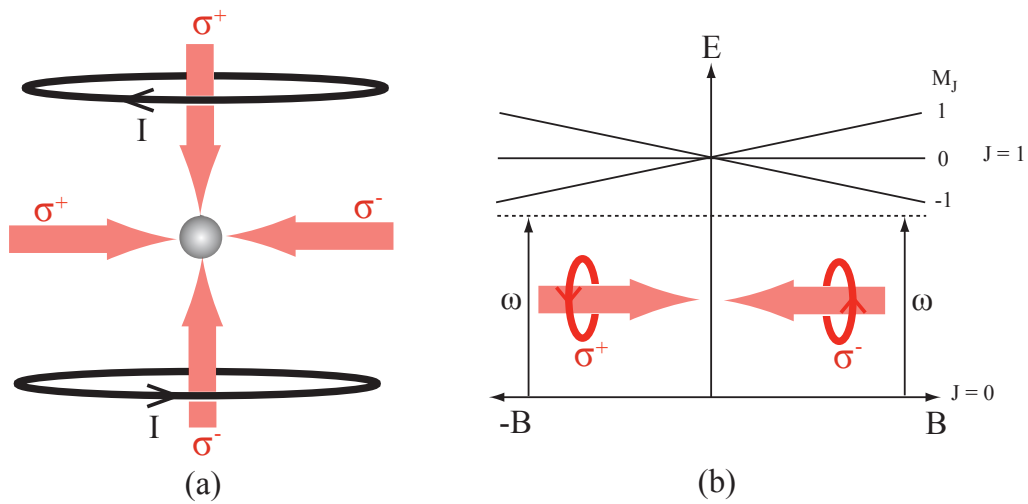


Figure 2.10 (a) A MOT is realised by overlapping 3 counter-propagating pairs of laser beams, with opposite circular polarisation (σ^\pm) at the centre of a magnetic field gradient. A third pair, orthogonal to the two pairs shown, is omitted for clarity. The magnetic field gradient is provided by passing a current through a pair of coils in the anti-Helmholtz configuration. (b) The magnetic field gradient produces a shift in Zeeman energy levels leading to a restoring force towards the centre of the trap.

produces a homogeneous magnetic field between the coils. In the anti-Helmholtz configuration, the current in one of the coils is reversed, producing a quadrupole magnetic field gradient.

The Zeeman shift in a magnetic field, B , is given by;

$$\Delta E = M_J g \mu_B B, \quad (2.25)$$

where g is the Landé g-factor for the transition. Hence the Zeeman shift, at a position, x , in a magnetic field gradient B' is;

$$\Delta\omega = \frac{M_J g \mu_B B' x}{\hbar} \quad (2.26)$$

$$= \beta x. \quad (2.27)$$

Therefore, we can calculate the force experienced by an atom in the MOT in much the same way as for the molasses in (2.28);

$$F_{MOT} = F_{scatt}^{\sigma^+} (\delta - kv + \beta x) - F_{scatt}^{\sigma^-} (\delta + kv - \beta x) \quad (2.28)$$

$$\simeq -2 \frac{\partial F}{\partial \omega} (kv + \beta x) \quad (2.29)$$

$$= -\alpha v - \frac{\alpha \beta}{k} x. \quad (2.30)$$

So we see that the system takes the form of a damped harmonic oscillator providing both cooling and trapping. Initially, MOTs were loaded from pre-slowed atoms, however it was soon demonstrated that a MOT could be loaded directly from a thermal vapor^[40], although only the very slowest atoms in the Maxwell–Boltzmann distribution are captured by the MOT.

2.3.2 Magnetic trapping

As we saw in equation (2.25), the energy of an atom has a dependence on the magnetic field; this can be utilized to trap low-energy atoms in magnetic field minima. The Zeeman energy of an atom in a magnetic field is

$$V = g_F \mu_B m_F |B|. \quad (2.31)$$

It is important to note that the energy depends only on the *magnitude* of the magnetic field and not on its direction; this is because the dipole adiabatically follows the magnetic field as it moves in the potential. Hence, we can trap cold atoms in a simple magnetic field gradient, such as is formed between a pair of anti-Helmholtz coils. States with positive m_F have energy which decreases with decreasing magnetic field and hence are trapped at the zero of a magnetic field gradient. States with zero or negative m_F are not trapped; this is shown in Figure 2.11.

Unfortunately, this simple quadrupole trap is not sufficient to cool atoms towards degeneracy due to the presence of the zero in the magnetic field gradient. When an atom is at zero magnetic field, all m_F states are degenerate, hence there is a chance that the atom will undergo a spin-flip to an un-trapped state. At higher temperatures, this is not a problem as the atoms spend very little time at the centre of the trap, however, as the atoms get colder and denser, they congregate at the zero-point and spin-flips are no longer negligible. All magnetic routes to BEC must overcome this issue, either by a time orbiting potential (TOP) trap^[1], an optical

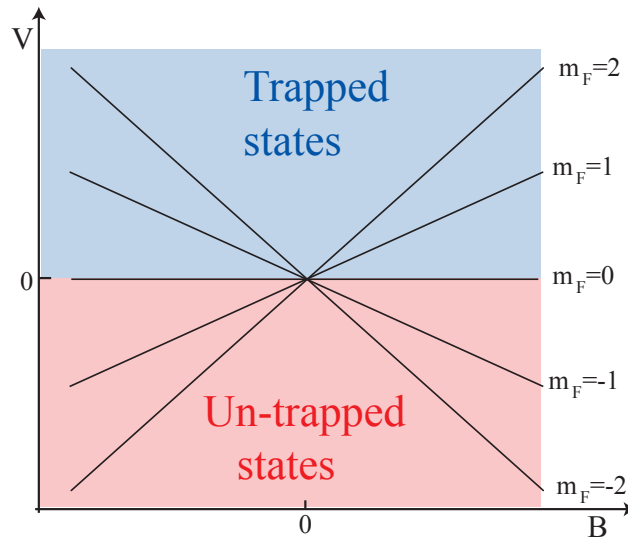


Figure 2.11 Magnetic trapping in a field gradient. States with positive m_F experience a potential, V , which increases with increasing magnetic field, B , and hence are trapped. States with $m_F \leq 0$ are not trapped.

plug^[3] or by adding extra coils to provide an offset^[41].

2.3.3 Dipole trapping

An atom in an intense laser beam experiences two forces: the scattering force and the dipole force. The scattering force dominates close to resonance (*i.e.* $\delta \simeq 0$), however at large detuning the dipole force becomes relevant.

The dipole force due to a laser propagating along z is given by;

$$F_{dipole} = -\frac{\hbar\delta}{2} \frac{\Omega}{\delta^2 + \Omega^2/2 + \Gamma^2/4} \frac{\partial\Omega}{\partial z} \quad (2.32)$$

For far detuned radiation ($|\delta| \gg \Gamma$) and intensity such that $|\delta| \gg \Omega$ this can be

approximated as;

$$F_{dipole} \simeq -\frac{\partial}{\partial z} \left(\frac{\hbar\Omega^2}{4\delta} \right) \quad (2.33)$$

For a full derivation consult chapter 9 of reference^[38]. $\left(\frac{\hbar\Omega^2}{4\delta} \right)$ is the a.c. Stark shift; hence the atom moves in a potential, U_{dipole} , provided by the light shift induced by the presence of the laser field:

$$\begin{aligned} F_{dipole} &= -\nabla \cdot U_{dipole} \\ U_{dipole} &\simeq \frac{\hbar\Omega^2}{4\delta} \equiv \frac{\hbar\Gamma^2}{8\delta} \frac{I}{I_{sat}}. \end{aligned} \quad (2.34)$$

By comparison with the scattering force equation ((2.17)), it is clear why the dipole force is dominant at large detuning. For $\delta \gg \Gamma$ (2.17) becomes;

$$F_{scatt} \simeq \hbar k \frac{\Gamma^3}{2} \frac{I/I_{sat}}{4\delta^2}, \quad (2.35)$$

so we can see that, at large detuning, $F_{scatt} \propto 1/\delta^2$, while F_{dipole} only drops off as $1/\delta$.

For negative detuning ($\omega < \omega_0$), the potential is minimum for maximum intensity, hence the atoms will be trapped in regions of high intensity. Thus cold atoms can be trapped in the focus of a high power laser beam; this has been implemented by several research groups (see reference^[42] for the seminal work in this field).

2.3.4 Evaporative cooling

Once the ultracold atoms are loaded into a non-radiative trap such as a dipole force or magnetic trap, they can be cooled below the Doppler limit by *evaporative cooling*. In the same way that a cup of coffee loses heat as the steam carries energy away, the atoms can be cooled by removing those with the most energy. The atoms initially have a Boltzmann distribution, $N = N_0 e^{-E/k_b T_0}$, with a characteristic temperature, T_0 . We then remove atoms with an energy greater than E_{cut} and allow the atoms to re-thermalize to a new temperature, $T_1 < T_0$. This process is repeated until the desired temperature is reached (or no atoms are left).

In the case of a dipole force trap, this cut is simply performed by lowering the depth of the trap. In a magnetic trap, transitions from trapped to un-trapped states are driven by a radio-frequency source thereby applying a ‘RF knife’ to the potential. Reducing this frequency reduces the height of the cut-off and thereby the depth of the trap.

2.4 Cold molecules

The complex internal structure of molecules makes them substantially harder to cool than atoms, as within the multiple vibrational and rotational energy levels it is very hard to find a closed loop around which to perform laser cooling (see Section 2.3.1). In addition to these technical problems, the vibration and rotation of the molecules raises an interesting question as to whether a molecule with ultracold translational temperature, but with significant rotational and vibrational energy, is

truly ultracold.

Routes to ultracold molecules are split into two paths; direct cooling of bound molecules and molecular synthesis from pre-cooled atoms (indirect cooling). Indirect cooling takes advantage of established laser cooling techniques to reach truly ultracold temperatures, but the species involved are constrained to those which can be laser cooled. At the time of writing, indirect methods have not been used to create anything larger than a diatomic molecule⁹. Direct cooling techniques, by contrast, are widely applicable and have been used to cool a range of large molecules. However, the temperatures reached by these methods are, at best, hundreds of μK and hence are orders of magnitude higher than temperatures achieved by indirect cooling.

The following section summarizes the state-of-the-art in direct and indirect cooling methods, with a necessary emphasis on indirect cooling due to the nature of this thesis. The concept of ultrafast photoassociation is also introduced as a technique complementary to those already in existence.

2.4.1 Direct cooling

A wide range of molecules have been cooled using various techniques. The discussion in this section is necessarily kept brief; for a full review, the reader is directed to section 3.1 of the review article by Carr *et al.*^[20], and references therein. As the molecules are pre-formed the vibrational and rotational energy levels are thermally populated. As the translational temperature of these molecules decreases, collisional

⁹Although recent work in the Innsbruck group has demonstrated the presence of triatomic Feshbach resonances in cesium leading to the possibility of an ultracold sample of Cs_3 in the future^[43]

relaxation reduces the ro-vibrational energy maintaining equilibrium between the internal and external temperature of the molecule.

A common and powerful technique for cooling molecules is buffer gas cooling: a dilute sample of the desired molecule is placed in a cryogenic refrigerant (typically helium) and the molecular sample thermalizes with the refrigerant. Once cooled, a paramagnetic molecule can be trapped in a magnetic trap. This technique has been demonstrated by, among others, Doyle *et al.* [44,45] producing cold CaH molecules at temperatures of around 300 mK. It is hoped that evaporative cooling in such a trap may lead to temperatures in the micro-Kelvin regime, but this has yet to be realized experimentally. Cold molecules can be extracted from a cryogenic bath in the form of a cold molecular beam by using an electrostatic guide; velocity selection is imposed on this beam by introducing curvature to the guide [46,47].

Polar molecules can be cooled in a Stark decelerator; in this technique, an alternating electric field is applied synchronously to a beam of molecules traveling along a decelerator converting kinetic energy to Stark energy and hence cooling the molecules. See, as examples, references [48,49] for deceleration of metastable CO and ground-state ^{174}YbF respectively. Once the beam has been slowed, it can be held in an electrostatic trap. Electrostatically trapped ND_3 and NH_3 at 25 mK were demonstrated by Bethlem *et al.* [50–52].

Recent work in the DeMille group has identified a quasi-closed loop for direct laser cooling of SrF. The main cooling laser acts on the $|X^2\Sigma^+, v'' = 0\rangle \rightarrow |A^2\Pi_{1/2}, v' = 0\rangle$ electronic transition. Due to the highly diagonal Franck–Condon

factors (FCFs), only two repumping lasers are required to return molecules from $v'' = 1$ and 2 to the cooling cycle. The cryogenic beam has been cooled from 50 mK to an estimated 5 mK suggesting 500-1,000 photon scattering events. This is a significant step towards 3-dimensional laser cooling and trapping of SrF, however, because this technique relies upon a peculiarity of the FCFs, it is not generally applicable^[53,54].

2.4.2 Indirect cooling

In the absence of a proven method for direct laser-cooling, to produce ultracold molecules in the micro- and nano-kelvin temperatures regimes, it is necessary to associate molecules directly from ultracold atoms. These molecules are often formed in a high vibrational state due to the nature of the association process. As there is no direct cooling of these molecules, the internal temperature of the molecules cannot equilibrate with the translational temperature meaning, instead, that the experimentalist must devise strategies to produce translationally cold molecules in the desired vibrational state. The following section is a summary of techniques used for the association of ultracold atoms and efforts made towards producing samples in the ro-vibrational ground state.

Continuous-wave photoassociation

Continuous-wave (cw) photoassociation was first proposed by Thorsheim *et al.*^[55]. Consider two ground-state ultracold atoms colliding in the presence of a near-

resonant field; they may absorb a photon forming an excited bound molecule;



Usually, this excited state molecule will decay back to two unbound atoms, re-emitting another photon;



But occasionally the molecule will decay to a bound ground state molecule;



The difference between the two photon energies, $\Delta E = E_{\gamma''} - E_{\gamma}$, corresponds to the binding energy of the resultant molecule. This process has been successfully implemented to form a range of homonuclear^[56–62] and heteronuclear^[63–66] molecules in a magneto-optical trap.

The distribution of vibrational states formed by photoassociation depends on the Franck–Condon (FC) overlaps between the scattering state, $|i\rangle$ and the excited state $|e\rangle$, as well as the overlap between $|e\rangle$ and the final bound molecular states in the ground state, $|f\rangle$. Hence, the population of the ground states are determined by the system, and cannot be chosen by the experimentalist. Figure 2.12 shows generalized molecular potentials in which photoassociation preferentially forms loosely bound molecules. However, in some systems, the molecular structure is such that there is

good two-fold FC overlap between the scattering state and the lowest vibrational state. For example, in the Cs_2 dimer, a fortuitous double-well structure in the excited 1_g potentials leads to a turning point close to the potential minimum of the ground $a^3\Sigma_u^+$ state leading to significant population in $v'' = 0$ [56]. High photoassociation power has been used to overcome poor FC overlap in LiCs and produce an excited state with good overlap with the vibrational ground state [67]. Meanwhile another group has proposed a three-step scheme in RbCs in which atoms are first photoassociated, then transferred to a deeply bound excited state, before stimulated transfer to $v'' = 0$ [63,68–70].

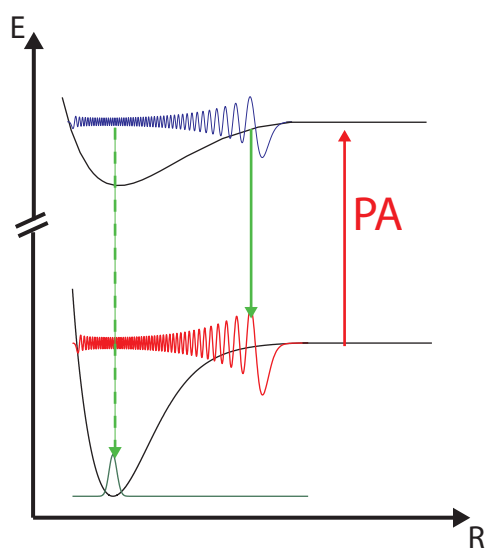


Figure 2.12 Continuous wave photoassociation. A pair of unbound atoms in the ground state absorb a photon (red arrow) to form a bound excited-state molecule. Bound ground-state molecules are formed — albeit with a small probability — by spontaneous emission of a photon of a different frequency (green arrows). In this system, the Franck–Condon factors are such that photoassociation preferentially forms loosely bound (solid green) rather than deeply bound (dashed green) molecules.

Photoassociation has been demonstrated to be a widely applicable technique for producing cold molecules in a range of homonuclear and heteronuclear species. However, due to the nature of the spontaneous decay, an incoherent mixture of vibrational states are formed and centre-of-mass heating is unavoidable. In order to achieve the goal of ultracold molecules in a pure vibrational state, more sophisticated approaches are required. Such techniques are discussed below.

Molecular optical pumping

In 2008, Viteau *et al.* demonstrated a molecular optical pumping scheme in which Cs_2 dimers are stabilized into the $v'' = 0$ ground state with 70% efficiency^[13]. This scheme starts with ultracold Cs atoms in a MOT, a cw photoassociation laser is tuned $\sim 1 \text{ cm}^{-1}$ below the D2 line and excites vibrational states in the 1_g potentials. Internal coupling of these potentials produces a turning point with good overlap to the bottom of the X state. Deeply bound molecules in the $X^1\Sigma_g^+$ potential with $v'' = 0 - 10$ are formed by spontaneous decay via the 0_u^+ states. After this, a series of broadband optical pulses are applied to pump molecules to vibrational states at the bottom of the $B^1\Pi_u$ potential, from where they decay back to the X -state. This re-distributes the molecular population in the different vibrational levels. A simple spectral cut removes all intensity with sufficient energy to excite the $v'' = 0$ state, and hence this state becomes a dark state in the optical pumping. After repeated excitations and spontaneous decays, population gradually accumulates in the ground vibrational state, with $65 \pm 10\%$ of the molecules initially formed by photoassociation

in $v'' = 0 - 10$ remaining in $v'' = 0$. The remaining $\sim 30\%$ are lost by excitation to higher vibrational states. Theoretical modeling suggests that, on average, only 5 cycles are required to transfer a molecule to the ground state; suggesting low centre-of-mass heating¹⁰. A schematic diagram of the molecular optical pumping scheme is shown in Figure 2.13.

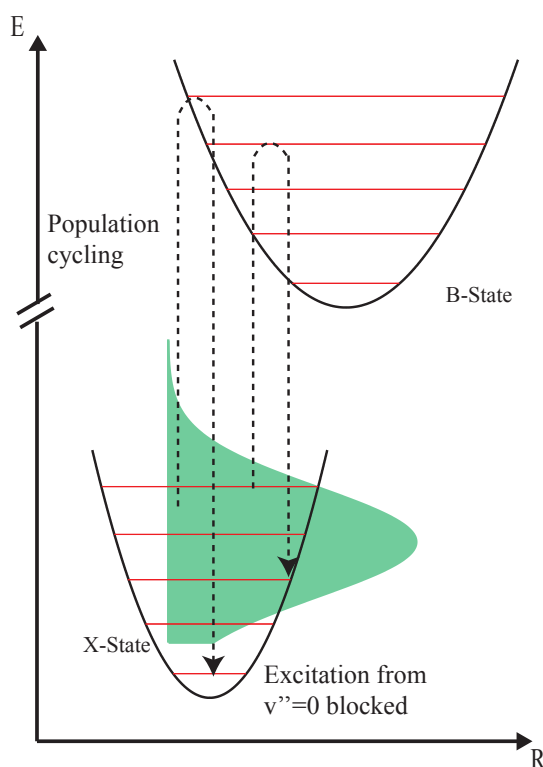


Figure 2.13 Optical cycling scheme demonstrated by Viteau *et al.* in Cs_2 . Population in the vibrational states of the X -state is redistributed by optical pumping, via the B -state, using a broadband laser. Light resonant with $v'' = 0$ is filtered out leading to accumulation of population in the vibrational ground state.

Following the initial experiments, this technique has been extended to produce

¹⁰The fact that the process only saturates after 5000 pulses is explained by the low probability of interaction per pulse.

molecules in $v'' = 1, 2$ and 7 by using active pulse shaping to remove light resonant with the target state^[71]. The technique has also been demonstrated with an incoherent broadband laser diode^[72]. At the time of publishing, this technique was expected to be applicable to a range of ultracold molecules, however, as of September 2011, there has yet to be another publication using this technique. The optical pumping requires molecular population which is already tightly bound due to the fortuitous photoassociation of Cs_2 , and would not work, for example, in Rb_2 where photoassociation forms loosely bound molecules; optical pumping on such a system would require many more cycles and hence significant heating of the sample.

While the relative simplicity of the molecular optical pumping technique makes it an attractive one, the lack of generality is a downside. Also, the centre-of-mass heating limits the temperatures that can be achieved, and its reliance on photoassociation makes it inefficient. Colder samples can be produced, with greater efficiency, using Feshbach resonances and STIRAP, as discussed below.

Feshbach resonances

Although the attractive potential between two atoms takes the form shown in Figure 2.6, the overall macroscopic effect is the same as for hard spherical potentials. Hence we can model an ultracold gas as a cloud of hard spheres each of radius, a . This radius, known as the scattering length, is a key result of *scattering theory* which is discussed at length in textbooks such as Pethick and Smith^[73]. Interestingly, the scattering length is not fixed; it can be tuned by the application of an external field

and be made to take a range of positive and negative values. Positive a corresponds to repulsive interaction while a negative scattering length leads to attractive interactions. A Feshbach resonance occurs at the point where a changes from positive to negative. By sweeping a magnetic field around this resonance we can tune the interaction strength between atoms.

Consider a collision between two unbound atoms in the lowest hyperfine state; the kinetic energy of such a collision is much lower than the difference between this hyperfine state and the next, ΔE . Hence the upper level is closed to the atoms. However, as the atoms approach each other in a collision, the energy of the collision may approach that of one of the bound vibrational states in the upper hyperfine state. Application of a specific magnetic field tunes these two energies into resonance via a differential Zeeman shift; this is the Feshbach resonance. This process is summarised in Figure 2.14. Adiabatically sweeping the magnetic field across a resonance transfers population with good efficiency to the bound molecular state, sweeping in the opposite direction has the opposite effect^[74].

The Feshbach resonance has been used to produce pure molecular samples in BECs of ^{85}Rb ^[75], ^{133}Cs ^[76], ^{87}Rb ^[77] and ^{23}Na ^[78]. However, these samples are very short-lived due to inelastic atom-molecule and molecule-molecule collisions. To increase the lifetime of such a sample, we must hold the molecules in an optical lattice to prevent collisions as demonstrated in reference^[79]. The Feshbach resonance has also been used to form bosonic molecules from pairs of Fermionic atoms. These pairs have much longer lifetimes due to Fermionic suppression of vibrational quenching in

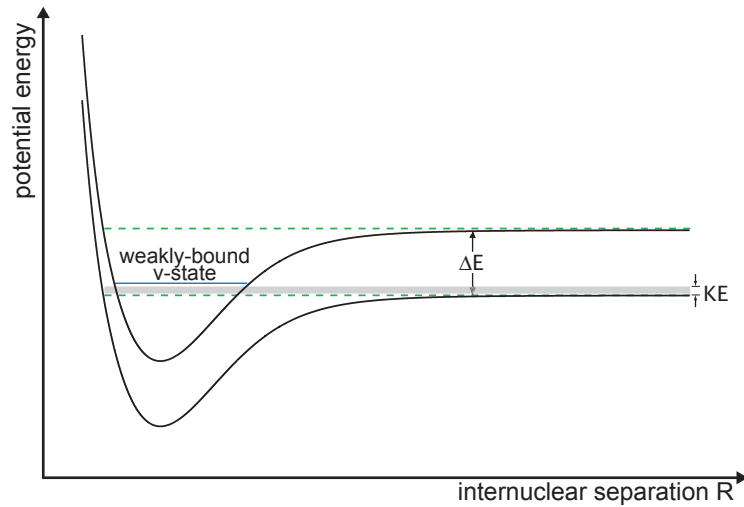


Figure 2.14 Two energy levels of a pair of colliding atoms separated by an energy difference, ΔE . The molecular potentials (solid) and their atomic asymptotes (dashed) are shown. We note that the energy of the colliding atoms is nearly degenerate with a bound state in the upper level. This can be tuned into resonance via an external magnetic field to produce bound molecules.

molecular collisions. This long lifetime enabled the formation of molecular BECs in ^{40}K ^[80] and ^6Li ^[81,82] providing a clear demonstration of molecules which are translationally, but not vibrationally or rotationally, ultracold.

The nature of the Feshbach resonance is such that it can only produce molecules in high vibrational states; the energy difference between the vibrational ground state and the atomic asymptote is typically too large to be brought to degeneracy by application of a magnetic field. The vibrational relaxation employed in direct cooling techniques is not applicable in these schemes as there is no active cooling to dissipate the vibrational energy, therefore collisions between molecules will heat the sample, as observed in references^[75–78]. Hence alternative schemes must be found to reduce the vibrational energy of Feshbach molecules. In reference^[83], Lang *et al.*

use magnetic tuning of the mixing between adjacent molecular states to facilitate radiofrequency transitions between them. Using this technique, they are able to apply 9 transfers of molecular state in a Rb_2 dimer, thereby walking the molecule from a binding energy of $E/h = 24$ MHz to 3.6 GHz. While this is an interesting extension of the Feshbach technique, compared to the 120 THz depth of the X state in Rb_2 , these molecules are not very deeply bound. Greater binding energy can be achieved by using STIRAP, as discussed below.

STIRAP

Stimulated Raman adiabatic passage (STIRAP) is a well established technique for population state transfer in atoms and molecules. For full details of experimental and theoretical consideration, the reader is referred to review articles by Bergmann *et al.* (references^[84–87]). In the most basic instance, STIRAP is the transfer of population from an initial state $|1\rangle$ to a final state $|3\rangle$ via an intermediate state $|2\rangle$. Typically $|1\rangle$ and $|3\rangle$ are different ground states in the system and are long-lived, while $|2\rangle$ is an excited state susceptible to spontaneous decay to states outside the three-level system.

Coupling is strongest when the individual fields are on resonance with $|2\rangle$, but this is not essential. What is critical is that the 2-photon resonance criterion is met *i.e.* that both fields are detuned by an amount Δ from $|2\rangle$. This is shown in Figure 2.15(a). In this case, the coupling of the Stokes and pump fields to the

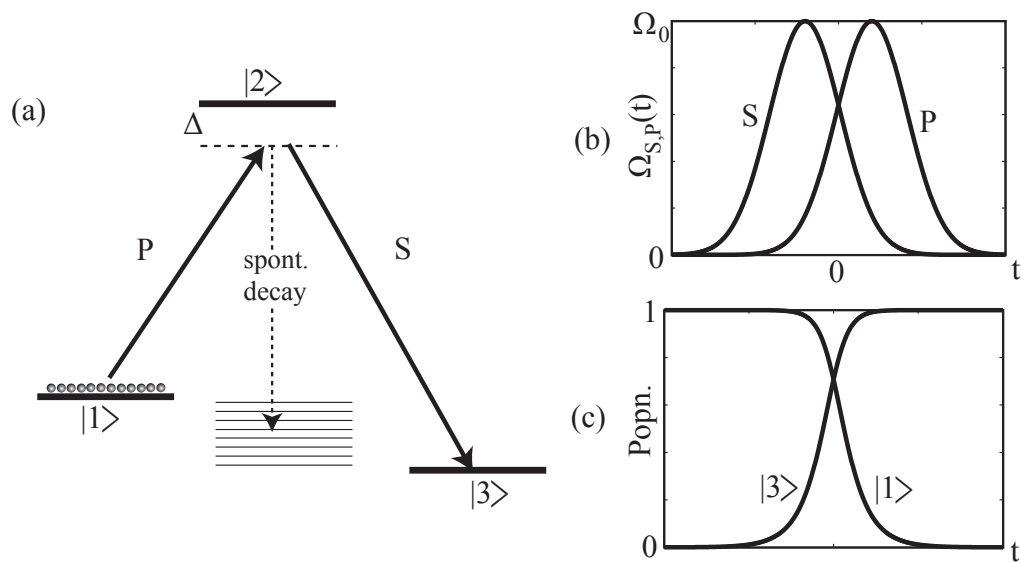


Figure 2.15 (a) Typical level diagram in a STIRAP system. Population is transferred from $|1\rangle$ to $|3\rangle$ by pump (P) and Stokes (S) pulses. In adiabatic following, state $|2\rangle$ is never populated, which avoids spontaneous emission into undesired states. (b) Typical pulse timings for adiabatic following; note the counter-intuitive pulse sequence, with the Stokes arriving before the pump. (c) Population transfer in the ideal case, exhibiting 100% transfer from $|1\rangle$ to $|3\rangle$.

three-level system is described by the Hamiltonian;

$$H(t) = \frac{\hbar}{2} \begin{bmatrix} 0 & \Omega_p(t) & 0 \\ \Omega_p(t) & 2\Delta & \Omega_s(t) \\ 0 & \Omega_s(t) & 0 \end{bmatrix}, \quad (2.39)$$

where the rotating wave approximation has been made. $\Omega_{S,P}(t)$ are the Rabi frequencies of the pulsed control fields. The following linear combinations of $|1\rangle$, $|2\rangle$ and $|3\rangle$ are eigenstates of this Hamiltonian;

$$|a_+\rangle = \sin\theta \sin\phi|1\rangle + \cos\phi|2\rangle + \cos\theta \sin\phi|3\rangle \quad (2.40)$$

$$|a_0\rangle = \cos\theta|1\rangle - \sin\theta|3\rangle \quad (2.41)$$

$$|a_-\rangle = \sin\theta \cos\phi|1\rangle - \sin\phi|2\rangle + \cos\theta \cos\phi|3\rangle, \quad (2.42)$$

with corresponding eigenenergies of;

$$\frac{E^+}{\hbar} = \Delta + \sqrt{\Delta^2 + \Omega_P^2 + \Omega_S^2} \quad (2.43)$$

$$\frac{E^0}{\hbar} = 0 \quad (2.44)$$

$$\frac{E^-}{\hbar} = \Delta - \sqrt{\Delta^2 + \Omega_P^2 + \Omega_S^2}, \quad (2.45)$$

where θ is given by;

$$\tan\theta = \frac{\Omega_p(t)}{\Omega_s(t)} \quad (2.46)$$

and ϕ is a known function of the detunings and Rabi frequencies and is irrelevant

to subsequent discussions. During the STIRAP process, the system adiabatically follows the zero energy eigenstate, $|a_0\rangle$, which has no contribution from the intermediate state, and hence the population is steered into the target state without any spontaneous loss. The adiabatic condition is met using the counter-intuitive pulse sequence shown in Figure 2.15(b). The population transfer—assuming perfect adiabatic transfer—is shown in Figure 2.15(c). In the ideal case of adiabatic following, the state remains in a superposition of $|1\rangle$ and $|3\rangle$ throughout the transfer with no content in $|2\rangle$; this avoids spontaneous losses from the excited state and preserves the purity.

In addition to this pulse sequence, an additional adiabaticity criterion is derived in reference^[84];

$$\Omega_{eff}\Delta\tau > 10, \quad (2.47)$$

where $\Delta\tau$ is the period during which the two pulses overlap and $\Omega_{eff} = \sqrt{\Omega_P^2 + \Omega_S^2}$. Hence, this criterion implies long laser pulses and high Rabi frequencies. However, experimentally, the Rabi frequency is limited by the laser power and by the Franck-Condon overlap of the 3 vibrational states in question. An upper limit is placed on the pulse duration by the time for which the two lasers remain phase coherent.

STIRAP has been used with great success to manipulate the internal state of ultracold molecules formed by Feshbach resonances. An initial proof-of-principle demonstration was performed by Winkler *et al.*^[88] in which molecules in the highest vibrational state of the triplet a state in rubidium (binding energy $h \times 24$ MHz) were coherently transferred to the next highest ($h \times 637$ MHz). The same group later

demonstrated transfer to the lowest vibrational level in the a state^[89]. A sample of ultracold molecules in the vibrational ground state of the ground singlet, X , state was demonstrated in Cs_2 by Danzl *et al.*^[90]; this involved a two-step STIRAP process via $v'' = 73$ to overcome the poor Franck–Condon overlap between initial and target state^[91,92]. Single-step transfer of KRb molecules to the lowest vibrational state in both the triplet and singlet ground states was demonstrated by Ni *et al.*^[93].

STIRAP is a hugely successful technique for controlling the internal states of an ultracold molecule. However, it does rely heavily upon the phase space density of the initial sample. It has been shown that Feshbach efficiency is negligible below a phase space density of 0.1^[94] meaning that STIRAP requires an atomic sample close to quantum degeneracy whereas photoassociation techniques are used to form molecules in a MOT where phase space densities do not exceed 10^{-5} ^[95].

2.4.3 Ultrafast photoassociation

Coherent control is the steering of chemical reactions in a particular direction by application of a tailored optical pulse, or by the specific timing of said pulse. Such techniques have been used to control several chemical processes, for example isomerization^[96] and dissociation^[97,98]. It is suggested that coherent control could be used to manipulate photoassociation interactions to overcome unfavorable Franck–Condon overlaps.

The basic principle of ultrafast photoassociation (UFPA) is as follows; where continuous-wave photoassociation (CWPA) excites unbound scattering pairs at a

single internuclear separation, R , to one bound vibrational level in the excited state, UFPA excites scattering states from a range of R to several vibrational levels. This coherent excitation forms a superposition of vibrational levels — a wavepacket — which is time non-stationary. As the wavepacket evolves in the attractive excited state potential, it moves to shorter R hence increasing the Franck–Condon overlaps with deeply bound ground-state molecules, as shown schematically in Figure 2.16. It is, therefore, predicted that ultrafast pulses would have greater photoassociation efficiency than any of the constituent frequencies on their own.

The initial wavepacket immediately after excitation, $|\Psi_0(R)\rangle$, can be represented as a sum over all the vibrational states, $|\phi_n(R)\rangle$, in the excited state. The amplitude, c_n , of the contribution of each state is governed by the pump spectrum and the Franck–Condon factors of the transition;

$$|\Psi_0(R)\rangle = \sum_n c_n |\phi_n(R)\rangle. \quad (2.48)$$

The evolution of this wavepacket under the time dependent Schrödinger equation is given by;

$$|\Psi(R, t)\rangle = \sum_n c_n e^{i\Delta E_n t/\hbar} |\phi_n(R)\rangle, \quad (2.49)$$

where ΔE_n is the energy splitting between adjacent vibrational energy levels E_n and $E_{(n+1)}$. Hence we can see that, for a harmonic potential with evenly spaced vibrational levels, the wavepacket will remain in phase as all components evolve together. However, in an anharmonic molecular potential, the different components

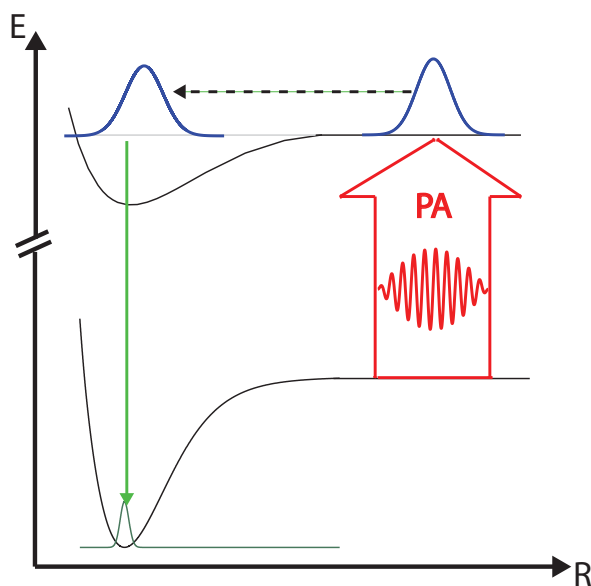


Figure 2.16 A schematic diagram of ultrafast photoassociation. An ultrafast pulse excites a coherent wavepacket in the excited state. As the wavepacket evolves, it moves inwards due to the attractive nature of the potential producing more favourable overlap with deeply bound ground-state molecules.

will evolve at different speeds leading to dephasing of the wavepacket. This problem is exacerbated by producing wavepackets close to the atomic asymptote (where the potential is least harmonic) as we do in these photoassociation experiments.

By applying pulse-shaping techniques^[99] to the pump pulse, one could aim to compensate for the dephasing of the wavepacket caused by the anharmonic potential and produce focussing. The shape of the pump pulse could be altered to provide optimal overlap with a desired molecular state. By combining a programmable pulse-shaper with a measurement of molecular population in the desired state one could implement closed-loop feedback on the shape of the pump to steer population to the desired target state.

Once the excited state wavepacket has been produced, one could either rely upon spontaneous emission to populate the ground state — ‘pump-decay’ — or stimulate the decay with a second, ‘dump’, pulse. Stimulated decay to ground states has been suggested in the CW regime, but this scheme is infeasible as the process is completely reversible meaning that the reverse process — *i.e. photodissociation* — would occur with equal probability. However, in the case of ultrafast pulses, the timing and chirp of the pulses breaks the symmetry of the process making it possible to engineer the pulses such that association is more prominent than dissociation; this makes a single-shot ‘pump-dump’ approach a viable option. However, accumulation over several thousands of pulses, as in the molecular optical pumping scheme, would not be possible.

Ultrafast photoassociation has been the focus of intense theoretical interest for the last 10 years with several proposals being put forward. The inherent difficulty and expense of the experiments proposed has understandably largely tended to necessitate that they focus on more proof-of-principle applications of the more technologically demanding theoretical proposals. The theoretical proposals, and experimental progress, are outlined below.

Theoretical proposals

Pulsed photoassociation was first proposed in 1994 by Machholm *et al.*^[100] in a study of the Na₂ dimer. Various investigations on the effects of wavepacket dynamics in photoassociation followed^[101–103] while Vardi *et al.* were the first to suggest a pump-

dump scheme using a pair of nanosecond pulses^[104]. In 2000, Vala *et al.* realized the potential advantage of applying chirp to the pump pulse and studied the photoassociation of Cs₂ dimers with chirped picosecond pulses^[105], a calculation which was later improved by including a more accurate initial-state distribution^[106,107]. The extension of this proposal to include a ‘dump’ pulse was suggested by Koch *et al.*^[108].

Experimental progress

Experimental implementation of the proposed schemes has been hampered by the absence of a device for picosecond pulse shaping. The picosecond regime represents an awkward challenge for pulse-shaping; the duration of picosecond pulses is too short to be directly shaped in the time-domain, as can be done with nanosecond pulses, while their bandwidth is too small to be shaped in the frequency domain as is done with femtosecond pulses. Despite this, some groups began to investigate the idea of ultrafast photoassociation; either with un-shaped picosecond pulses or with shaped femtosecond pulses.

The first sub-nanosecond photoassociation experiments were performed by Fatemi *et al.* in a sodium MOT using 15 ps pulses^[109]. The bandwidth was sufficient to excite several vibrational levels and hence form an excited-state wavepacket. Population in the excited state was monitored by photoionization from a second pulse arriving a time, τ , later. The sharp rise and slow decay of this population, on a nanosecond timescale, was explained as inward motion of the wavepacket followed

by dephasing. Were this curve to have exhibited a dependence on the chirp of the pump pulse, it would have represented a clear demonstration of the feasibility of coherent control of photoassociation; unfortunately, the technology precluded this.

Pump-decay experiments using chirped femtosecond pulses and ultracold rubidium atoms were performed simultaneously by a Freiburg-Berlin collaboration, and by predecessors of the author in Oxford. Both experiments produced the unexpected result that application of ultrafast pulses *reduced* the population in the $a^3\Sigma_u^+$ ground triplet state rather than enhancing it¹¹. In Oxford, Brown *et al.* compared chirped pulses with transform limited ones and demonstrated that the quenching of the molecular signal is dependent on the chirp^[110–112]. The Freiburg-Berlin experiment demonstrated that the molecular signal could be minimized using coherent control with a closed-loop algorithm acting on a programmable pulse-shaper. These two experiments indicated that the course of these interactions can be manipulated by shaping the pump pulse, and hence opened the door for coherent control experiments in ultracold photoassociation.

Subsequently, the attention switched from the ground state to the excited state. In the next stage of experiments the pump-pulse spectrum overlapped with both the D1 and the D2 line in rubidium; a spectral cut was applied to remove light blue-detuned from the D1 line. Rather than allowing the molecules to decay after the application of the pump pulse, they were ionized directly from the excited state using a second ultrafast pulse in a pump-probe experiment. The hope was

¹¹Background population exists due to photoassociation by trapping lasers.

that these experiments would reveal wavepacket dynamics in the excited state as the pulse durations (~ 100 fs) are significantly shorter than the expected molecular dynamics (~ 10 - 100 ps). The Freiburg-Berlin group observed coherent transients in the molecular signal^[113-116]; the sharp spectral cut produced a long temporal tail in the pulse coherently interacts with the atomic dipole set up by the main body of the pulse. These oscillations are similar to those observed in hot rubidium atoms by Zamith *et al.*^[117], and have nothing to do with molecular wavepacket motion.

The Oxford group, including the author, performed a similar experiment which, due to a much ‘blunter’ cut in the frequency of the pump pulse, was not dominated by coherent transients. Despite this, the sought-after wavepacket dynamics were not observed^[118]. By investigating the dependence of the excited state molecular population on the detuning of the spectral cut, an estimation of the internuclear separation of the wavepacket was obtained and compared to the background molecular population^[119]. The method, and results from these experiments are discussed in chapters 3 and 4 respectively. In an accompanying theoretical work, Martay *et al.* showed that coherent wavepackets should still be observed even if the initial state is an incoherent mixture of bound molecules, such as is produced in a MOT^[120].

Chapter 3

MOT Experiment

Initial ultrafast photoassociation experiments were carried out in a MOT, addressed by an ultrafast titanium:sapphire (Ti:Sa) laser. The details of this apparatus are described in the following Chapter. Rubidium was the chosen element for the experiment as laser-cooling techniques are well established for this species and because the D1 and D2 spectroscopic lines overlap well with the gain bandwidth of the Ti:Sa crystal. The MOT was a simple 3-dimensional trap based on the design demonstrated by Raab *et al.* ^[39].

The MOT was probed by photo-ionization and time-of-flight mass spectroscopy (TOF), whereby molecular ions are distinguished from atomic ions by their larger mass-to-charge ratio. The static ground-state population was interrogated by a nanosecond pulsed dye laser, while dynamic population transfer was probed on the picosecond timescales by pump-probe ionization using ultrafast lasers. The main laser used for photoassociation was a home-built chirped pulse amplification (CPA)

laser which produces ~ 50 fs pulses, centered at 800 nm. Frequency conversion of the ultrafast pulses was achieved in a non-colinear optical parametric amplifier (NOPA).

3.1 MOT

Rubidium has two isotopes, ^{85}Rb and ^{87}Rb ; in this experiment we chose to trap ^{85}Rb . The electronic ground state of ^{85}Rb is $5s$. Fine structure splitting of the $5p$ state produces a pair of excited states, $5p^2P_{1/2}$ and $5p^2P_{3/2}$, giving rise to two distinct spectroscopic lines for rubidium known (for historical reasons) as the D1 (794.97 nm) and the D2 (780.24 nm) lines respectively. The hyperfine structure of the D1 and D2 lines is shown in Figure 3.1. The nuclear spin of ^{85}Rb is $\mathbf{I} = 5/2$ hence the ground $5s^2S_{1/2}$ state is split by hyperfine structure into two levels; $\mathbf{F} = 2$ and $\mathbf{F} = 3$. The $5p^2P_{1/2}$ state has the same electronic angular momentum, and hence the same hyperfine structure, as the ground state. Due to its higher electronic angular momentum, the $5p^2P_{3/2}$ has a greater multiplicity of hyperfine states, containing $\mathbf{F}' = 1 - 4$.

During electronic transitions, the total angular momentum of the atom, \mathbf{F} , can only change by 0 or ± 1 ; we can use this to our advantage for laser cooling. By choosing to cool the atoms with a laser on the D2 line we can excite transitions from $\mathbf{F} = 3$ to $\mathbf{F}' = 4$; once in $\mathbf{F}' = 4$ the atoms have no choice but to decay back to $\mathbf{F} = 3$, hence remaining in a closed loop required for laser cooling. The laser used for the MOT was slightly red-detuned of the $\mathbf{F} = 3 \rightarrow \mathbf{F}' = 4$ transition on the D2 line; this laser is, from now on, referred to as the *cooler*. Due to its

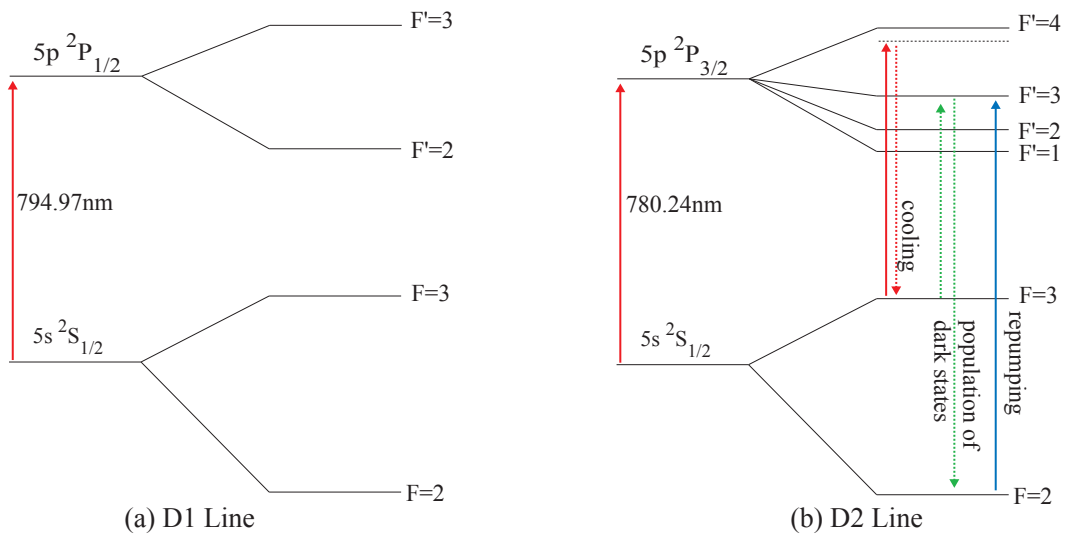


Figure 3.1 Hyperfine structure of the ^{85}Rb D1 and D2 lines. The MOT is constructed with lasers on the D2 line. The cooling laser is red-detuned from the $\mathbf{F} = 3$ to $\mathbf{F}' = 4$ transition to form a closed loop for laser cooling. Atoms lost from this closed loop to the dark $\mathbf{F} = 2$ state are returned by the repumper laser.

detuning from the $\mathbf{F}' = 4$ level, there is a small, but finite chance of the cooler exciting atoms to $\mathbf{F}' = 3$, from where they can decay to $\mathbf{F} = 2$. At this point they would no longer be resonant with the cooler, and hence would be completely lost from the closed loop. As laser cooling requires thousands of iterations of absorption and spontaneous emission, this small probability represents a major loss in MOT loading efficiency. A second laser, the *repumper*, was tuned to the $\mathbf{F} = 2$ to $\mathbf{F}' = 3$ transition to return any lost atoms to the closed loop.

The MOT was produced in a stainless steel vacuum chamber, maintained at a pressure below 10^{-8} mBar. The necessary lasers were frequency stabilized and amplified before being launched into a single-mode fiber and transported to the

MOT chamber. The fiber cleaned up the mode, ensuring that we had a smooth trapping potential, and also decoupled the MOT alignment from the rest of the system. The two halves of the MOT setup; the laser preparation and the vacuum chamber, are described below.

3.1.1 Laser preparation

Both lasers used for the MOT were home-built extended cavity diode lasers. An extended cavity diode laser (ECDL) uses an external cavity to reduce the linewidth of commercially available semiconductor diodes. Using this technique, it is possible to reduce the linewidth of these diodes from several tens of MHz to the sub-MHz regime required for laser cooling experiments¹. An extensive review of the use of diode lasers for atomic physics, including ECDLs, is provided by Wieman *et al.*^[121]. In this case, a grating is used to form the external cavity. The first-order reflection, typically about 10% of the input, is injected back into the laser diode cavity, and wavelength tuning of the laser is achieved by rotating the grating. Sanyo DL7140-201S and Hitachi HL7851-G laser diodes were used for the cooler and repumper lasers respectively

The temperature of the diode is measured by a 10 k Ω thermistor and stabilized using a PID feedback circuit (*Wavelength Electronics* MPT-2500) acting on a peltier element underneath the diode mount. The wavelength of the laser is coarsely set by adjusting the temperature and current to the diode, and fine control is achieved by rotating the grating using a piezoelectric transducer (PZT). Saturated absorption

¹The natural linewidth of the D2 transition in rubidium is 6 MHz^[29].

spectroscopy^[122] was used to monitor the frequency of the laser and, by adjusting the current to the laser diode, and voltage to the PZT, the frequency was locked to a spectroscopic peak using feedback electronics (Oxford Physics CEG Ew1225 laser diode stabilizer).

The cooling laser diode has a maximum output power of 80 mW. Given that it is never possible to have the laser on the correct resonance at maximum output power and a fraction has been removed for frequency stabilization, and more is lost in mode-cleaning in the single mode fiber, typically only ~ 10 mW remains. For this reason, we chose to amplify the cooling light in a master-slave configuration. In this instance the cooler laser was the master and a high-power single-mode laser diode (Roithner Lasertechnik RLT780-150GS) was chosen for the slave diode. At maximum current the slave provided 150 mW. By careful matching of the polarization and spatial mode of the master to that of the slave, the slave ran single mode at maximum power with only ~ 3 mW injection power. The frequency of the slave was monitored with absorption spectroscopy.

The cooler laser was locked to the $\mathbf{F} = 3 \rightarrow \mathbf{F}' = 3$ resonance and then frequency shifted to 15 MHz below the $\mathbf{F} = 3 \rightarrow \mathbf{F}' = 4$ using an acousto-optic modulator (AOM). Similarly, the repumper was locked to the $\mathbf{F} = 2 \rightarrow \mathbf{F}' = [1, 2]$ crossover resonance² and frequency shifted onto resonance by a second AOM. The AOMs also acted as fast (sub μ s) switches allowing us to quickly switch the MOT beams on and off during an experiment. This ensures that all the atoms are in the

²A crossover resonance occurs when the frequency of the laser is exactly half way between one resonance and another. In this instance, one particular velocity class is on one resonance for the probe, and the other for the pump.

ground state before the photoassociation pulses arrive. After the AOMs, both beams are combined on a polarizing beamsplitter (PBS) and launched into orthogonal axis of a polarization maintaining single mode fiber. Following the fiber, we have over 35 mW of power in the cooling beam. A schematic for the layout of the laser preparation is shown in Figure 3.2

3.1.2 The vacuum chamber

The MOT is formed inside a cylindrical vacuum chamber constructed from stainless steel. Eight ports around the circumference, and a further two on each end allow vacuum viewports and other accessories to be attached; all seals are made using all-metal CF flanges. The chamber is maintained at ultra-high vacuum by a *Pfeiffer* TMU 071 P turbomolecular pump backed by a rotary vane roughing pump (*BOC Edwards* E2M1.5). The pressure inside the chamber is monitored by an ion gauge (*Granville Philips* Series 270); however, this is not capable of measuring pressures below 10^{-8} mBar hence only provides an upper bound for the pressure achieved. Rubidium vapor is introduced into the chamber by alkali metal dispensers (*SAES*TM getters); the dispensers contain rubidium chromate (Rb_2CrO_4) and a reducing agent (*St101*®). When a current is applied through the dispensers they heat up starting a reduction reaction which produces rubidium vapor. *St101*® also prevents any stray gases produced in the reduction reaction from contaminating the rubidium vapor. The dispenser produces a reliable yield, as a function of current, which is consistently reproduceable. A diagram of the vacuum chamber is shown in Figure 3.3

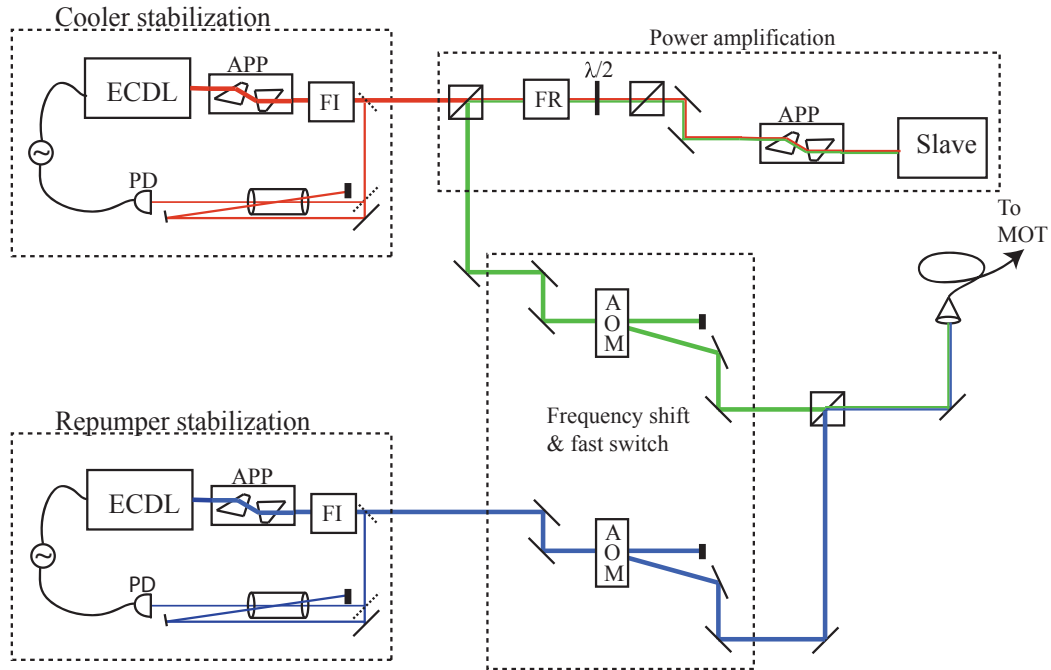


Figure 3.2 Beam diagram of MOT laser preparation. Cooling and repumping light are derived from two separate extended cavity diode lasers (ECDL), the elliptical profile of each is corrected by anamorphic prism pairs (APP) and the lasers are protected from feedback by Faraday isolators (FI). Saturation absorption spectroscopy is measured on a photodiode (PD) and the signal is fed back to locking electronics to stabilize the lasers to a particular spectroscopic resonance. The cooler is injected into a slave laser to amplify the power. The slave output is separated from the cooler by a Faraday rotator (FR) set for 45° rotation and a half-wave plate, also set for 45°, placed between two PBSs. Frequency shifts are applied by acousto-optic modulators (AOMs) to each laser before they are coupled into orthogonal axes of a polarisation maintaining fiber and sent to the MOT.

The cooling and repumping light emerge together from the fiber and are expanded to 6 mm full width half maximum (FWHM); at this point, the cooling laser power was ~ 35 mW and the repumper ~ 3 mW. The beam was split into three

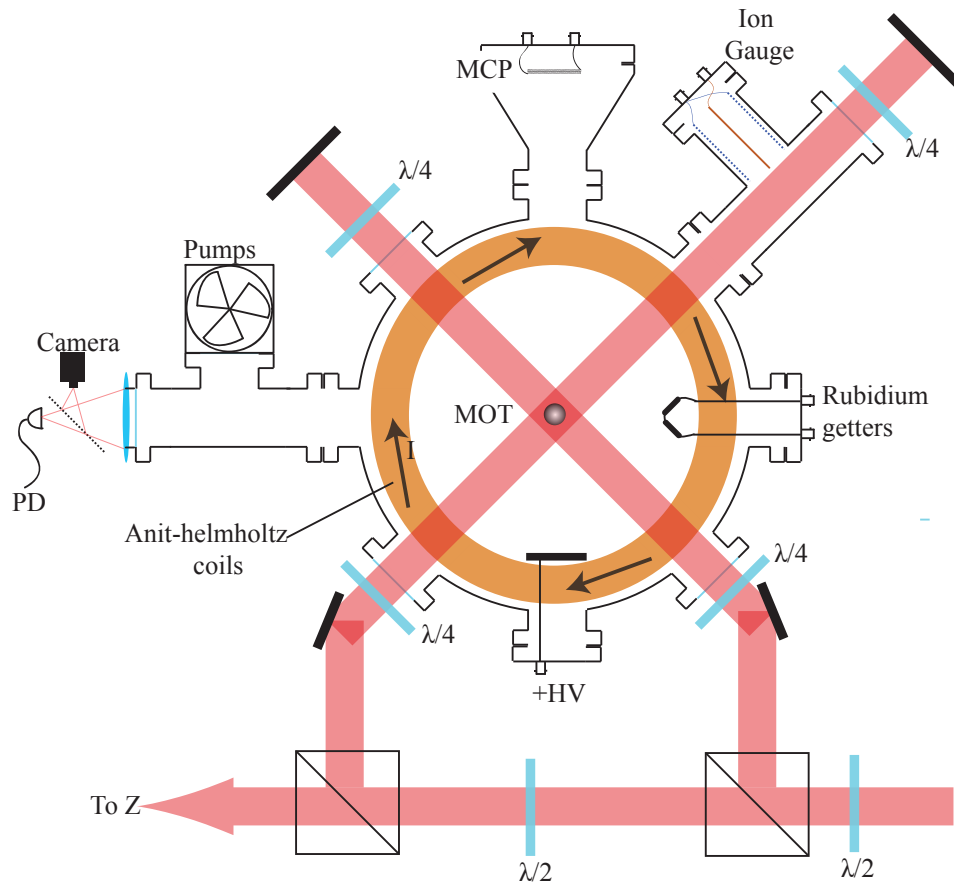


Figure 3.3 Schematic of the MOT vacuum chamber. Ultra-high vacuum is maintained in the chamber by a turbomolecular pump and the vacuum pressure is monitored by an ion gauge. Rubidium vapor is introduced by running a current through rubidium getters. The MOT is formed at the centre of three orthogonal retro-reflected circularly polarised laser beams, the third beam (into/out of page) is omitted for clarity. The centre of the beams coincided with the minimum of a static magnetic field gradient produced by an anti-Helmholtz coil pair. The MOT is imaged by a lens at one of the viewports and monitored by a CCD camera and photodiode (PD). A simple TOF mass spectrometer for ion detection is formed by a high-voltage plate (+HV) situated below the MOT which pushed positive ions towards a Multichannel plate (MCP) detector above the MOT.

with each beam containing equal cooling intensity³. The three beams were sent orthogonally through the centre of the chamber, and then retro-reflected on the other side of the chamber. Quarter-wave retarders ($\lambda/4$) were used to set the correct circular polarizations for the MOT. A pair of coils, with counter-propagating current, containing 80 turns of insulated wire, average diameter 15 cm sat around the circumference of the vacuum chamber, with their centers 15 cm apart; this is a good approximation to the anti-Helmholtz configuration. Care was taken to ensure that the laser beams passed geometrically through the centre of the cell, hence ensuring the centre of their intensities co-incided with the minimum of the magnetic field gradient produced by the coils. Stray magnetic fields were compensated by three pairs of quasi-Helmholtz coils whose axes lay along the three laser beams (these coils are omitted from Figure 3.3 for clarity). The MOT was monitored by a pair of CCD cameras and was also imaged onto a photodiode for characterization.

One can calculate the photon flux on the photodiode by knowing its response function; from this the total luminosity of the MOT can be inferred, by dividing by the solid angle observed by the photodiode. With knowledge of the total laser intensity and detuning, the number of atoms in the MOT can be calculated from this luminosity using the scattering rate (see equation (2.16)); further details of this method can be found in Section 5.5.2. Using this method, we estimated that around 2×10^7 atoms were trapped in the MOT in typical experimental configurations.

The temperature of the MOT was measured by releasing the atoms from the trap

³Due to its orthogonal polarization, the repumper beam was not equally split between the three arms; however, this did not affect the quality of the MOT due to the relative rarity of a photon being scattered from the repumping beam.

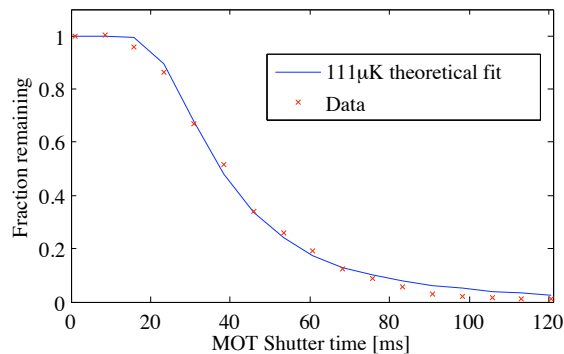


Figure 3.4 Release-and-recapture measurement of the MOT temperature. The measured data points (red crosses) are in good agreement with a theoretical fit function (blue line) calculated with a temperature of $111 \mu\text{K}$ and a capture radius of 6 mm.

and then recapturing them a certain time later. As the recapture time increases, the fraction of the MOT recaptured reduces as the atoms drift out of the capture volume, as plotted in Figure 3.4. By comparison with a theoretical model assuming a spherical capture volume of diameter 12 mm, the temperature was estimated to be $110 \pm 10 \mu\text{K}$. For comparison, the Doppler temperature of rubidium is $230 \mu\text{K}$ (See (2.22)). As the magnetic field gradient in the MOT precludes any sub-Doppler polarization gradient cooling, it is unlikely that this measurement is correct. A more accurate technique for measuring the temperature is discussed in Section 5.5.2.

3.2 Ultrafast lasers

The ultrafast laser used for these experiments is a home-built titanium:sapphire regenerative amplifier CPA system. The CPA produced pulses at a repetition rate of 2 kHz with a pulse energy of $600 \mu\text{J}$, a central wavelength of 790 nm and a FWHM

bandwidth of 18 nm. The spectral phase and pulse duration of the laser was measured using spectral phase interferometry for direct electric field reconstruction (SPIDER)^[123]; this indicated a near transform-limited pulse duration of 53 fs. The majority of the beam was used to pump a NOPA, which produced tunable ultrafast pulses in the region of 480-700 nm^[124]. The NOPA was predominantly used as a probe of population in the $5S + 5P$ state by photoionization, and hence was tuned to 500 nm. At this wavelength, the NOPA typically produced $5 \mu\text{J}$ per pulse with a spectral bandwidth of 15-20 nm FWHM. The pulse duration was measured by intensity autocorrelation to be 390 fs.⁴ The design and operation of the NOPA is detailed below in Section 3.2.1

The remainder of the CPA not used to pump the NOPA passed through a zero-dispersion $4f$ line formed by two 1200 lines/mm diffraction gratings separated by four times the focal length (37.5 cm) of the spherical mirrors. Razor blades were placed in the Fourier plane for spectral shaping, this normally entailed removing light on and above the D1 line (795 nm) to reduce the probability of exciting atomic transitions, while leaving light below the D1 line to excite molecular transitions. The resolution of the spectral shaping was 0.25 nm. With a spectral cut at 795 nm, the pulse duration was measured, by intensity autocorrelation, to be 85 fs. The output of the $4f$ line passed through a variable delay line formed by a retro-reflector on a translation stage before being recombined with the NOPA output on a dichroic mirror. The delay between the two pulses was computer controlled by a motorized

⁴Due to the low power of the NOPA, a long β -barium borate (BBO) crystal was necessary to observe significant second harmonic generation (SHG) which may have artificially increased the measured pulse duration; hence 390 fs must be considered an upper bound on the pulse duration.

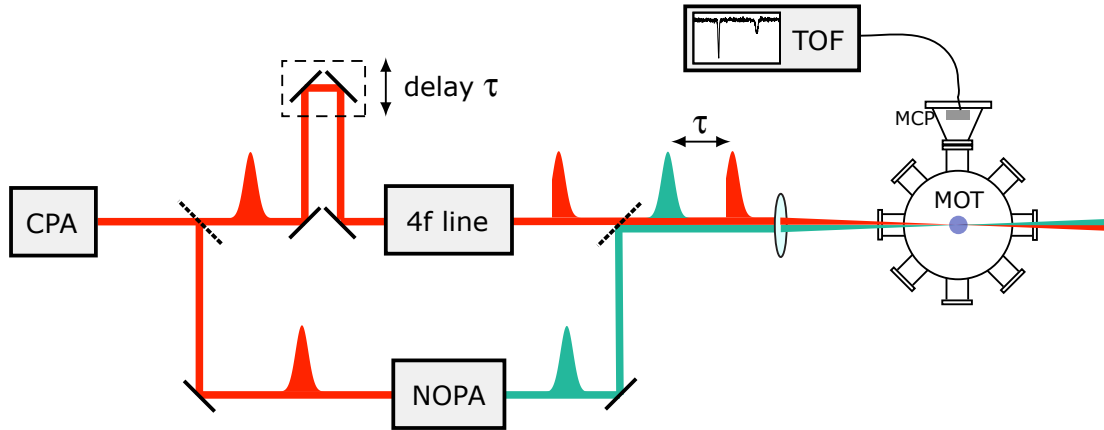


Figure 3.5 Layout of the ultrafast pump-probe experiment. The CPA is split in two; one part pumps a NOPA while the other is spectrally shaped in a 4f line. The two are recombined on a dichroic mirror and focussed onto the MOT.

actuator (Newport LTA-HS) interfaced with a GPIB motion controller (Newport ESP 300). The zero-delay point between the two pulses was found using sum-frequency generation in a BBO crystal. A diagram of the ultrafast laser setup is shown in Figure 3.5

3.2.1 NOPA

Modelocked Ti:sapphire lasers are a common-place source of high-energy ultra-short laser pulses. However, their frequency tunability is limited by the gain bandwidth of the Ti:Sa crystal. Typically, the wavelength is around ~ 800 nm. Due to the high instantaneous peak power of these laser pulses, we can readily use non-linear processes to generate different wavelengths, for example by second harmonic generation

(SHG); ~ 400 nm, or third harmonic generation (THG); ~ 266 nm. However, in order to access a wide range of wavelengths, particularly in the visible, one must use more complex techniques. For this reason we constructed a NOPA to produce the 500 nm required for ionization. The principle and design are discussed below, for a detailed recipe, the reader is directed to papers by Curello *et al.* [124,125].

The NOPA is based on the principle of optical parametric generation (OPG). In OPG, a high intensity pump beam, of frequency ω_p is used to amplify a signal beam (frequency ω_s) inside a nonlinear crystal. As a by-product, a third beam, the idler, is produced at frequency $\omega_i < \omega_s < \omega_p$. Energy conservation dictates;

$$\hbar\omega_s + \hbar\omega_i = \hbar\omega_p. \quad (3.1)$$

The efficiency of conversion is dependent on the conservation of momentum (the so-called *phase-matching* condition);

$$\hbar\mathbf{k}_s + \hbar\mathbf{k}_i = \hbar\mathbf{k}_p, \quad (3.2)$$

where $\mathbf{k}_{s,p,i}$ are the wave-vectors of the associated beams. In a non-linear crystal this phase-matching condition can be tuned by the rotation of the crystal axis with respect to the pump wave-vector, θ . Furthermore, one can tune the phase matching condition by changing the angle, α , between the pump and signal; as shown in Figure 3.6.

Ordinarily the phase-matching condition is highly wavelength-dependent, this

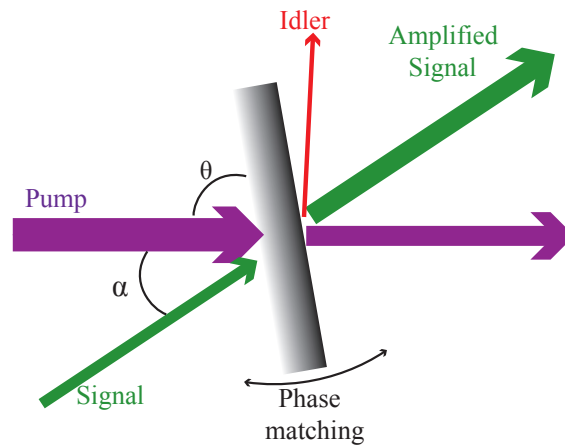


Figure 3.6 Optical parametric generation (OPG). A weak signal beam is amplified by a strong pump beam. The efficiency of this process is determined by the phase-matching condition, which can be modified by rotating the non-linear crystal (θ) and by rotating the beams with respect to each other (α).

precludes ultrashort pulse amplification as some of the spectrum will be phase-matched and other parts not. However, in type I BBO, there exists a “magic angle” of $\alpha = 3.7^\circ$. In this beam geometry, the phase-matching function is flat between 500 and 750 nm allowing simultaneous phase-matching and hence broadband amplification of visible ultrafast pulses⁵.

The NOPA is used to generate ultrafast pulses in the visible regime, hence we require an ultraviolet pump. For this we use the second harmonic of the CPA laser generated in a potassium dihydrogen phosphate (KDP) nonlinear crystal. Due to the high amplification afforded by these ultrashort pulses, only a very weak ‘seed’ pulse is required to see amplification. For this purpose we focus a small fraction of the incident CPA pulse into a sapphire plate to produce a white-light super-continuum.

⁵See figure 17 of Cerullo *et al.* [124] for the relevant phase-matching plots

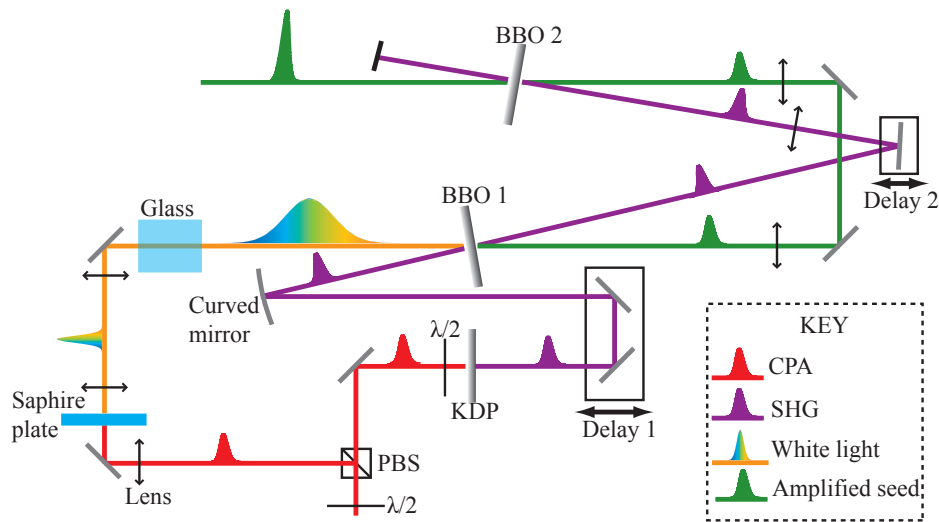


Figure 3.7 Experimental layout of the NOPA. The pump is created by SHG of the incident CPA inside a KDP nonlinear crystal. The seed is produced by super-continuum generation in a sapphire plate producing a chirped white-light beam. The seed is then further chirped by a glass block before being focussed into a BBO crystal (BBO1) with the SHG under the “magic angle” of $\alpha = 3.7^\circ$. The pump produces parametric amplification of the seed only at the frequency which temporally overlaps with the pump. Wavelength tuning is achieved by adjusting the delay between pump and signal (delay 1). A second stage, using a second nonlinear crystal (BBO 2), is employed to boost the output power to $5 \mu\text{J}$.

The white light is inherently chirped due to the generation process, and is further chirped by passing through a glass block. The white light and SHG are focussed into a BBO crystal under the “magic angle”. The SHG is transform limited while the white light is heavily chirped; hence only the fraction of the spectrum which is simultaneous with the SHG pulse is amplified. By tuning the delay between the two pulses, we can achieve tuning of the NOPA wavelength. Figure 3.7 shows the experimental layout of the NOPA.

When the NOPA was first constructed, pulse energies of around $1 \mu\text{J}$ were ob-

served at the desired wavelength. Further amplification was achieved by passing the amplified light through a second crystal along with the residual SHG not used in the amplification, in effect, creating a second NOPA to boost the power. In this two-stage geometry pulse energy was increased to $5 \mu\text{J}$ which was sufficient for the experiment.

3.3 Detection of molecules

Molecules were distinguished from their parent atoms by photoionization and time-of-flight (TOF) mass spectroscopy. In TOF spectroscopy, a sample is ionized by short laser pulses in the presence of an electric field. The electric field accelerates the ions towards a detector; the arrival time of the ions depends on their charge to mass ratio and hence one can distinguish the constituent atoms/molecules in the sample. In our instance, this was relatively simple as we expected only Rb^+ or Rb_2^+ . The design of the mass spectrometer used in this experiment is discussed below.

Due to the relatively low density of molecules in the MOT, one would expect to observe far fewer molecular ions than atomic. However, by careful selection of ionization wavelength, one can choose a multi-photon ionization path which is on-resonant with an intermediate molecular state but off-resonant in the atomic case. This technique, known as resonantly enhanced multi-photon ionization (REMPI), was used to probe the ground state molecular population. Dynamic studies of the excited state population were also performed; for these experiments ultrafast (sub-picosecond) pulses were used in pump-probe configuration.

3.3.1 Time of Flight mass spectrometer

A multi-channel plate (MCP) (Photonis APD HT APTOF) situated above the MOT was used for ion detection. This, in conjunction with a high voltage ‘pushing’ plate beneath the MOT, formed a simple TOF mass spectrometer. This is shown in Figure 3.3; the voltage on the pushing plate was varied between +100 V and +3 kV to vary the sensitivity of detection. A low pushing voltage means a longer TOF which gives the ion cloud more time to expand due to Coulomb forces; this means that the ions hit more channels on the detector and therefore reduces the chance of any given channel saturating. However, a higher pushing voltage means that the ions arrive at the MCP with greater energy leading to more secondary electrons and thereby, in the absence of saturation, a larger signal^[126]. Hence, there exists a trade-off between the two mechanisms which must be optimized for each setup. The ground-state ionization signal was largest at the highest allowed pushing voltage (3 kV) while, for the pump-probe experiment, optimal molecular signals were observed with a pushing voltage of +1.1 kV. Furthermore, it was shown to be beneficial to wait for 3.3 μ s after pump-probe ionization before applying the pushing voltage. This delay, implemented by a high voltage switch box (*DEI PVX4140* pulse generator), caused the small molecular ion cloud to expand in the presence of the large number of atomic ions hence accessing more channels on the MCP without sacrificing arrival energy^[126]. Typical TOF signals for both ground and excited state ionization are shown in Figure 3.8. We can see that the atomic ion signal is much larger in the pump-probe experiment due to the higher peak powers of the ultrafast lasers and

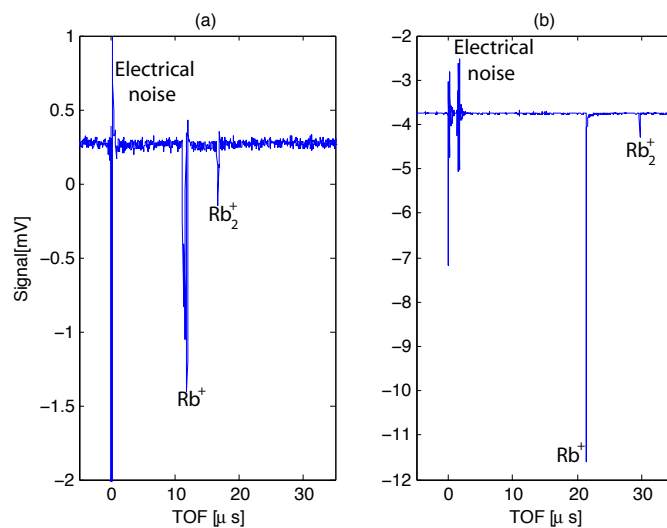


Figure 3.8 Typical time of flight spectra for REMPI (a) and pump-probe (b) ionization. Note the much larger size of the atomic signal in the pump-probe experiment. The difference in arrival times are due to the different pushing voltages applied; 3 kV for (a) and 1.1 kV for (b). The electrical noise in (a) comes from the Q-switching of the pump for the dye laser and, in (b), from the high-voltage switching of the pushing plate.

the fact that ionization is only a two-photon process compared to a three-photon effect in the REMPI scheme.

Chapter 4

Pump-Probe Spectroscopy in a MOT

This chapter presents the results published by McCabe *et al.* in Physical Review A^[119]. Firstly, the initial state of pre-formed molecules in the MOT was characterized using REMPI. Results show that population is spread across the 12 highest vibrational levels with a distribution in good agreement with that suggested by modeling photoassociation by the MOT lasers. Secondly, a pump-probe study of the photoassociation process was performed using a spectrally cut pump pulse and a second ultrafast pulse, delayed by a time, τ , which photo-ionized excited-state population. While the expected wavepacket dynamics were not observed, a clear increase in molecular signal was observed at $\tau = 0$ indicating the presence of excited-state molecules produced by the pump laser. Finally, by detuning the spectral cut from atomic resonance, and observing the decay of molecular signal

compared to atomic ionization, we were able to estimate the internuclear separation at which the wavepacket was formed. Comparison of this internuclear separation with the molecular wavefunctions of the pre-formed molecules, characterized by the initial state spectroscopy, and the unbound scattering state, indicated that photoassociation, rather than excitation of pre-bound molecules, is the dominant process in the pump-probe signal.

4.1 Initial state characterisation

Before conducting an experiment, one must have a clear idea of the conditions under which the experiment is performed; in this instance, this requires a full characterization of our MOT. A simplistic view of the experiment is that pairs of colliding atoms are excited to bound molecular states by the pump pulse, before being ionized by the probe pulse. However, as has been alluded to in previous chapters, a small number of ‘background’ molecules are formed in the ground state by photoassociation with the MOT lasers. These molecules could be excited by the pump laser and hence contribute to the ionization signal. Intuitively, due to the several orders of magnitude difference in the number of atoms and molecules, the effect of the background molecules should be negligible compared to photoassociation. However, every background molecule excited by the pump has a chance to contribute to the molecular ionization signal, whereas only a small fraction of colliding pairs are sufficiently close together to form a bound excited-state molecule. Hence the two signals could be comparable and therefore must both be considered.

4.1.1 REMPI spectroscopy of the a state

A small number of ground-state molecules are spontaneously formed in a MOT via a combination of photoassociation, by the trapping lasers, and three-body collisions. The relative contributions of these two mechanisms are discussed in detail by Caires *et al.*^[127]. This ‘background’ population provides a useful alignment aid for the ionization lasers as molecules are only formed in the densest part of the MOT. However, it is important that we fully characterize the background population as it may contribute to later results. Ground-state molecules may form in either the $X^1\Sigma_g^+$ singlet, or the $a^3\Sigma_u^+$ triplet state. Due to selection rules, the two states can be interrogated separately using different REMPI pathways outlined in references^[128,129].

REMPI detection of the ground-state molecules was implemented using a pulsed dye laser (Sirah Cobra). The pulse duration was 7 ns and the linewidth narrow enough (0.04 nm) to distinguish vibrational levels in the Rb_2 molecule. The MOT lasers were switched off for 1 μs either side of the ionization pulse to ensure that all of the atoms and molecules were in the ground-state before ionization. We were unable to distinguish any X -state molecules but a clear a -state signal was observed using the REMPI scheme outlined in see Figure 4.1^[129].

The REMPI spectrum can be seen in Figure 4.2(a). The frequency of the dye laser is swept across the gain bandwidth of the Pyridine 1 laser dye (680-705 nm) and a series of peaks in the molecular signal are observed. These peaks, spaced by $\sim 50 \text{ cm}^{-1}$, correspond to the REMPI laser being on-resonance with one of the deeply bound vibrational levels at the bottom of the intermediate $(2)^3\Sigma_g^+$ potential.

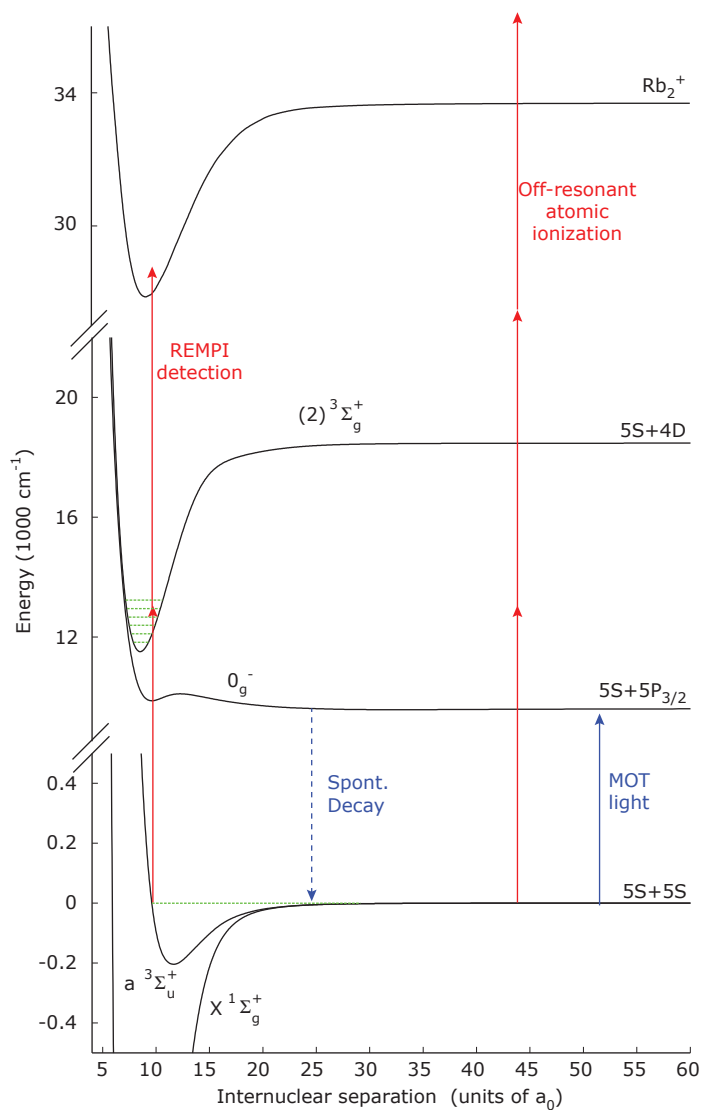


Figure 4.1 REMPI ionization of molecules in the a state. Molecules are resonantly ionized in 2-photon ionization to the Rb_2^+ potential via the $(2) \ ^3\Sigma_g^+$ state asymptotic to $5S + 4D$. The same wavelength provides off-resonant 3-photon ionization of Rb atoms, hence the Rb^+ signal is greatly suppressed. Photoassociation via the 0_g^- potential asymptotic to $5S + 5P_{3/2}$ is proposed as a mechanism for molecule formation.

In addition to the molecular resonances, we also observe large peaks due to REMPI ionization of atoms at particular frequencies, indicated in blue on the plot. At these frequencies, the atomic ionization is so large that it saturates the MCP detector causing ringing which is detected in the TOF window associated with molecular arrival, giving an apparent molecular signal, despite no molecular ions being present. The peak at $14,340\text{ cm}^{-1}$ corresponds to two-photon resonant excitation to the $6D_{3/2}$ and $6D_{5/2}$ states at 697 nm followed by ionization by a third photon. The second peak is due to REMPI via the $8S_{1/2}$ state at 688 nm. See Table A.3 for details of atomic energies and their transition wavelengths. The energies of these transitions are extremely well known, and are used to calibrate the frequency axis of the graph.

Each peak in the REMPI spectrum has an identical structure, an example of which is shown in Figure 4.2(b). The structure is as a result of the distribution of population in the vibrational levels in the a -state. The close spacing of these vibrational levels compared to the intermediate levels in the $(2)^3\Sigma_g^+$ potential suggests that they are near the top of the a state¹. By assuming that the red end of the spectrum represents the top of the molecular potential, the spectrum has been re-plotted in terms of binding energy of the molecule. For comparison, the known positions of the vibrational levels are plotted in vertical blue lines, this shows that the most populated vibrational level is the 9th highest state.

We would like to determine the source of these molecules. Caires *et al.*^[127] put forward two competing mechanisms for molecule formation, photoassociation

¹Recall that molecular energy levels become closer together as we approach the dissociation limit.

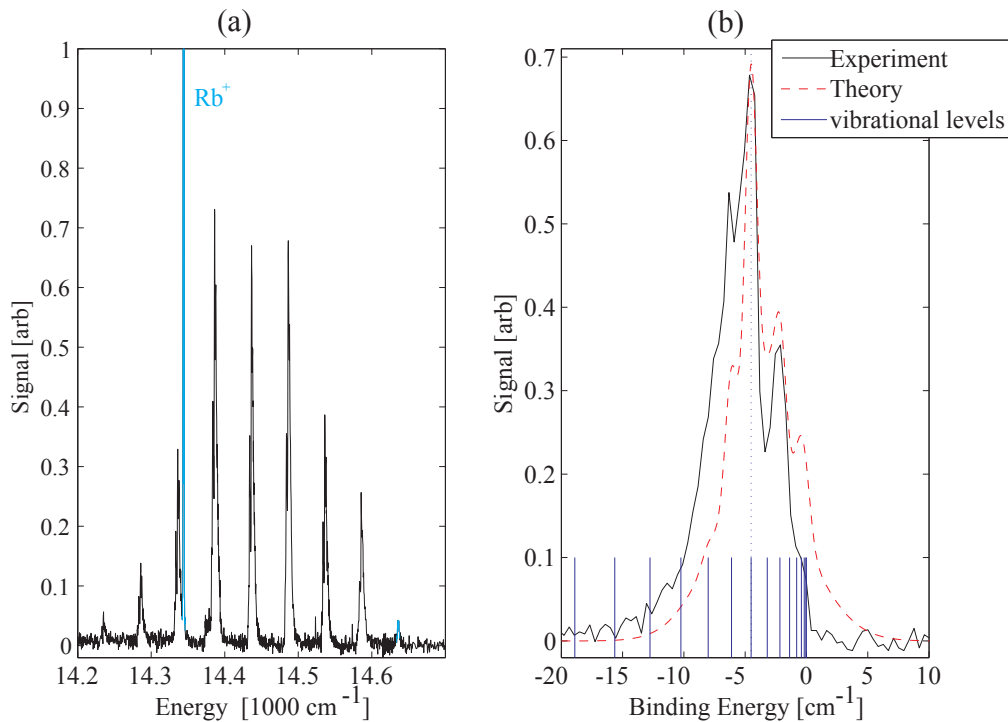


Figure 4.2 REMPI spectroscopy of the a state by 2-photon ionization via the $(2)^3\Sigma_g^+$ potential. **(a)** Rb_2^+ yield as a function of laser frequency. The sharp peaks correspond to vibrational levels in the intermediate potential. Atomic Rydberg resonances (blue) can be observed and are used to calibrate the frequency of the laser. **(b)** A zoom-in on the peak at $14,500\text{ cm}^{-1}$ reveals the population of the vibrational levels in the a state which is in good agreement with theoretical predictions of photoassociation by the MOT lasers.

by the MOT lasers, and three-body collisions. At high trapping laser intensity, photoassociation is thought to be the dominant process so the decay products of this photoassociation were calculated to compare with those observed in the experiment. The calculations were performed by Hugo Martay, details of which can be found in chapter 6 of his thesis^[130]. First an appropriate intermediate state for photoassociation was determined. As the MOT lasers are red-detuned from the $D2$ line,

only states asymptotic to $5S + 5P_{3/2}$ are considered. Secondly, as the a state has *ungerade* symmetry, the intermediate state must be *gerade*. Finally, in order to form bound ground-state dimers, the intermediate potential must be attractive. These three criteria are met only by the 0_g^- and 1_g potentials asymptotic to $5S + 5P_{3/2}$. Vibrational wavefunctions of the a , 0_g^- and 1_g potentials were calculated and the decay products were simulated. A good match was found between the experimental data and the simulation for 0_g^- as shown in Figure 4.2(b). The theoretical spectrum has been convolved with a gaussian to simulate the linewidth of the ionization laser, and its absolute height has been matched with the experimental data, but it is important to note that no other scaling or fitting has been performed.

The importance of the initial state

The importance of knowing the initial state for the pump-probe experiment is demonstrated in Figure 4.3. The classical oscillation period of a wavepacket formed in the excited singlet, $A^1\Sigma_u^+$, potential is plotted as a function of the internuclear separation at which it is created. Because of the favorable Franck–Condon overlaps, we assume that a wavepacket is always created at the outer turning point of the potential (see Figure 4.3(a)). Details of this calculation can be found in Appendix B. Figure 4.3(b) shows the scattering state wavefunction and also the 9th highest vibrational state wavefunction. If we consider a bound initial state, the wavepacket will be formed at $R \simeq 25 a_0$ corresponding to a classical oscillation period of ~ 10 ps, while a wavepacket excited from the final scattering anti-node at $R \simeq 60 a_0$ will os-

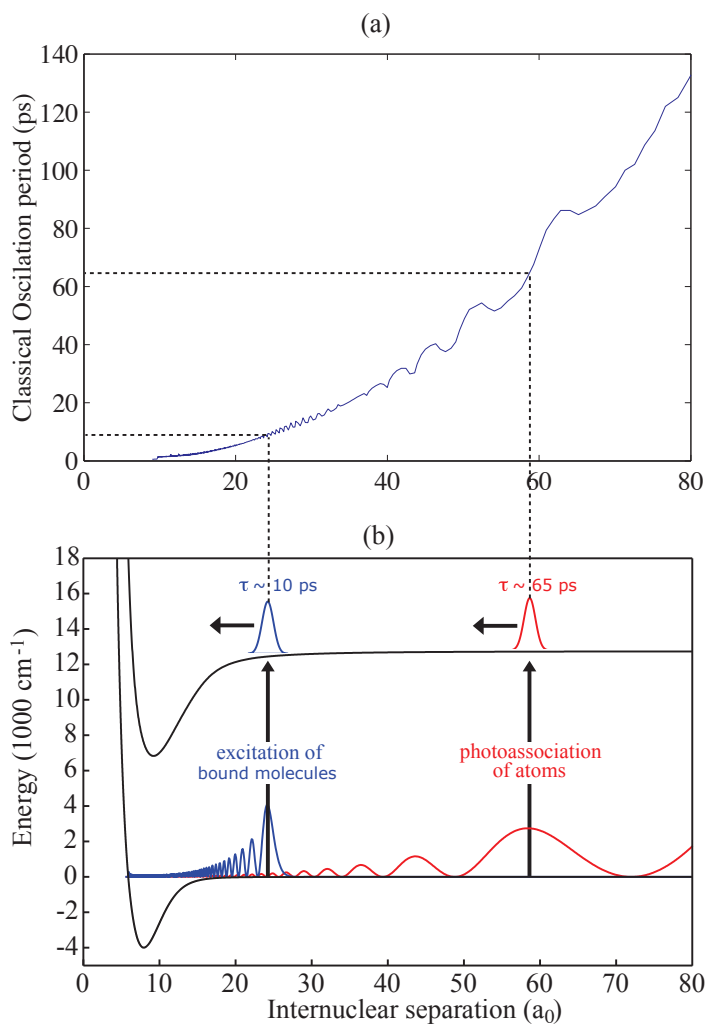


Figure 4.3 (a) the classical oscillation period, τ_{osc} , of the A state is calculated as a function of the outer turning point internuclear separation, R_{OTP} , at which it is created. (b) The wavefunction of the 9th highest triplet vibrational state (blue) is shown along with the scattering state (red). The classical oscillation period of wavepackets excited from these initial states are vastly different; ~ 10 ps for bound triplets and ~ 65 ps for the scattering state.

cillate much slower (~ 65 ps). Hence we can see that our pump-probe experiment would have very different results depending on the initial state.

Summary

In conclusion; the initial state of ‘background’ molecules has been characterized. The molecules seem to reside primarily in the highest 12 vibrational levels with a peak at the 9th as indicated by the vertical dashed line in Figure 4.2(b). Photoassociation via the 0_g^- state is proposed as the most likely mechanism for the formation of this background population; this mechanism is shown in Figure 4.1. In a pump-probe experiment, molecules in the 9th highest vibrational state would be expected to produce wavepacket oscillations with a classical period of ~ 10 ps, as indicated in Figure 4.3.

4.1.2 Pump-probe Experiments

Pump-probe studies of the molecular population in the $5S + 5P$ manifold were performed using the setup described in Section 3.2. In this case, the ‘pump’ pulse was the spectrally cut CPA pulse which excited population to the $5S + 5P$ manifold. The ‘probe’ was the NOPA pulse, tuned to 500 nm, which ionized population in the $5S + 5P$ state. The ionization yield, as a function of the delay, τ , between the two pulses, gave the pump-probe signal. Using this time-dependant ionization, we hoped to observe oscillations of a coherent wavepacket in the excited-state. Figure 4.4(a) shows the relevant molecular potentials and pulse timings for the pump-probe experiment. A sharp spectral cut was applied to the pump pulse to reduce excitation to unbound states, and the probe pulse was also cut blue of 480 nm by an interference filter to reduce resonant ionization of atoms from $5P$. However, despite these

measures, the atomic ionization signal was an order of magnitude larger than the molecular one, simply due the relative abundance of atoms and molecules in the MOT.

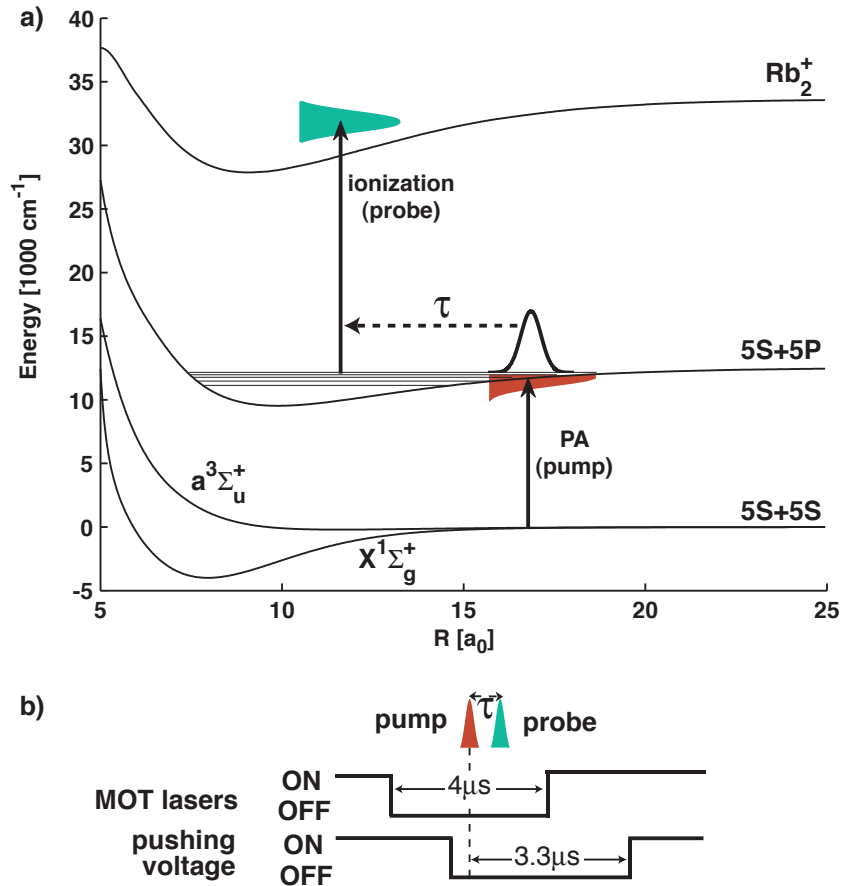


Figure 4.4 Pump-probe ionization of molecules in the $5S + 5P$ manifold. **(a)** The pump pulse (CPA) is spectrally cut to excite molecular states below the $5S + 5P$. The resulting wavepacket is interrogated using time-dependant photo-ionization by the probe pulse (NOPA). **(b)** Timing diagram; the MOT lasers are switched off for $4 \mu\text{s}$ either side of the pulse pair to ensure atoms are in the ground-state. The pushing voltage is switched on $3.3 \mu\text{s}$ after ionization to boost molecular signal (see Section 5.7).

The pump-probe delay was scanned from -50 ps^2 to $+250 \text{ ps}$ and the atomic and molecular ionization yields, as a function of delay, were measured. Both short ($\tau = -10$ – 50 ps) and long ($\tau = -50$ – 250 ps) pump-probe scans were performed in order to search for both fast and slow wavepacket dynamics. A pump-probe scan was taken by moving the motorized translation stage to give the desired pump-probe delay and then averaging 1,000 TOF traces and integrating the atomic and molecular peaks, before moving to the next position. In typical operating conditions for molecular detection, the atomic signal saturates the MCP detector. In order to record pump-probe scans for the atomic signal the bias voltage on the MCP is turned down from 2.3 kV to 1 kV to return the signal to the linear regime, at which point the molecular signal is no longer visible. Unfortunately, this precludes the data from being taken simultaneously. Examples of typical results of a short scan are shown in Figure 4.5; the atomic signal is a single scan while the molecular signals are the average of 6 consecutive scans. In this particular instance, the spectral cut was placed at 795.5 nm which is below the $D1$ line at 794.98 nm ^[29].

Both atomic and molecular pump-probe signals exhibit a clear step at zero pump-probe delay. This indicates that, despite the spectral cut, we still observe atomic excitation to the $5P_{1/2}$ state. The atomic signal at negative delays is due to off-resonant excitation. The atomic signal is more noisy than the molecular as it was only a single sweep whereas the molecular data was the average of 6. The step in the molecular signal indicates that population is being transferred to states asymp-

²Negative pump-probe delay indicates that the probe arrives before the pump.

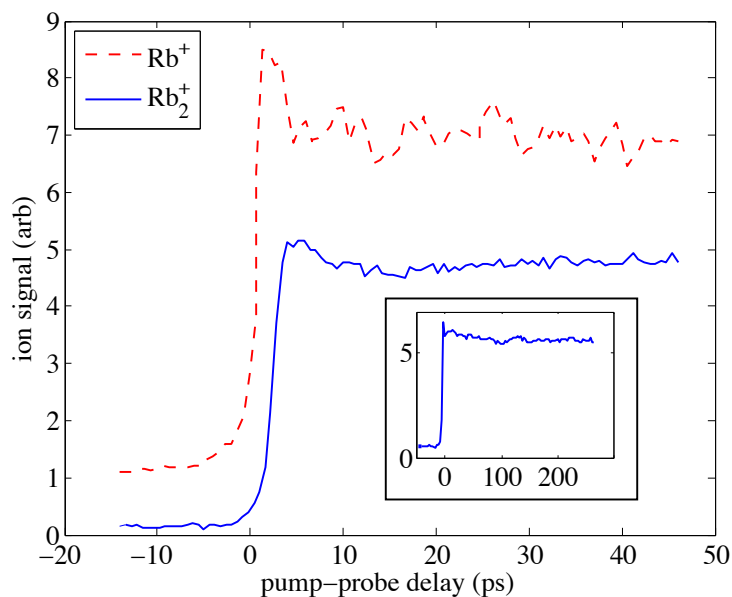


Figure 4.5 Atomic and molecular pump-probe signals taken with the same pump and probe conditions. Both exhibit a step at zero indicating a transfer of population to states asymptotic so $5S + 5P_{1/2}$ (or just to $5P_{1/2}$ in the atomic case). No molecular dynamics are apparent. The atomic signal is more noisy as it is a single scan whereas the molecular signal is the average of 6. **Inset:** A long molecular scan taken from -50–250 ps indicating no dynamics on longer timescales.

otic to $5S + 5P_{1/2}$. The fact that they are detected in the molecular TOF peak indicates that the molecules must be bound in the excited-state, further evidence of bound excited-state dimers is presented in Section 4.1.4. Several pump-probe scans were taken, with a range of spectral cuts, intensities, pump-probe delays and probe wavelengths. None of these displayed any clear oscillations in molecular signal, either from wavepacket motion, or the coherent transients observed by Salzmann *et al.*^[116]. The implications, and potential explanations of this null result are explored in Section 4.2.

4.1.3 Theoretical model of the pump-probe experiment

In parallel to this experimental work, the problem was also analyzed theoretically by Hugo Martay. Full details of the model used can be found in references^[120,130]; the results applicable to the pump-probe study are summarized below. This work represents an effort to approach theoretical modeling from an experimental point of view. The initial state is considered to be an incoherent mixture of atoms and the ‘background’ molecules observed in Section 4.1. The temperature and density of the MOT are considered and the pulses applied to the model were taken directly from the lab spectrometer. The evolution of excited state wavepackets initiated from both bound and unbound ground states was calculated. An attempt to model the ionization process was also included to help model the experiment.

Excited-state evolution

The model prepares population in a chosen ground-state and then applies a spectrally cut pulse at time zero. The population density in the excited state as a function of time and internuclear separation was calculated. The model was initially run using a thermal average of scattering states to match those expected in the MOT however, this was computationally very taxing which led to long calculation times. It was found that choosing any scattering state within this range produced very similar results to the full simulation, but took a fraction of the time³. For simulations of the bound initial state, an incoherent mixture of the first 12 vibrational states

³This can be explained by the similarity of the scattering state wavefunctions at the short internuclear separations required to observe wavepacket oscillations.

in the a state was used, with proportions as indicated in Figure 4.2. All attractive potentials asymptotic to $5S + 5P_{1/2}$ were considered in the excited-state; repulsive potentials were not considered as all light to the blue side of the atomic resonance was removed by the spectral cut.

The calculated excited-state dynamics are shown in Figure 4.6. Dynamics are observed on all three plots; the timescales of these dynamics are shorter for a bound initial state (c) than for an initial scattering state (a,b). The fact that these dynamics are present despite the incoherence of the initial state is a key result of these simulations. The results seem to suggest that dynamics should be present in our system; the issue comes with trying to resolve them with the probe laser. Ideally we would like the probe laser to be highly position sensitive to best resolve the dynamics. However, position selectivity implies a narrow bandwidth and long pulses, hence reducing the temporal resolution of the detection system. Therefore, we would also like to model the ionization step of the pump-probe process to establish whether the oscillations observed in the excited state manifest themselves as a time-dependent ionization signal.

Ionization model

Because of the capacity for the ejected electron to carry away excess energy and momentum, the bound-free electronic transitions involved in photoionization are harder to model compared to bound-bound transitions which can be well explained using the Franck-Condon principle. Hence, in order to estimate the effect of the

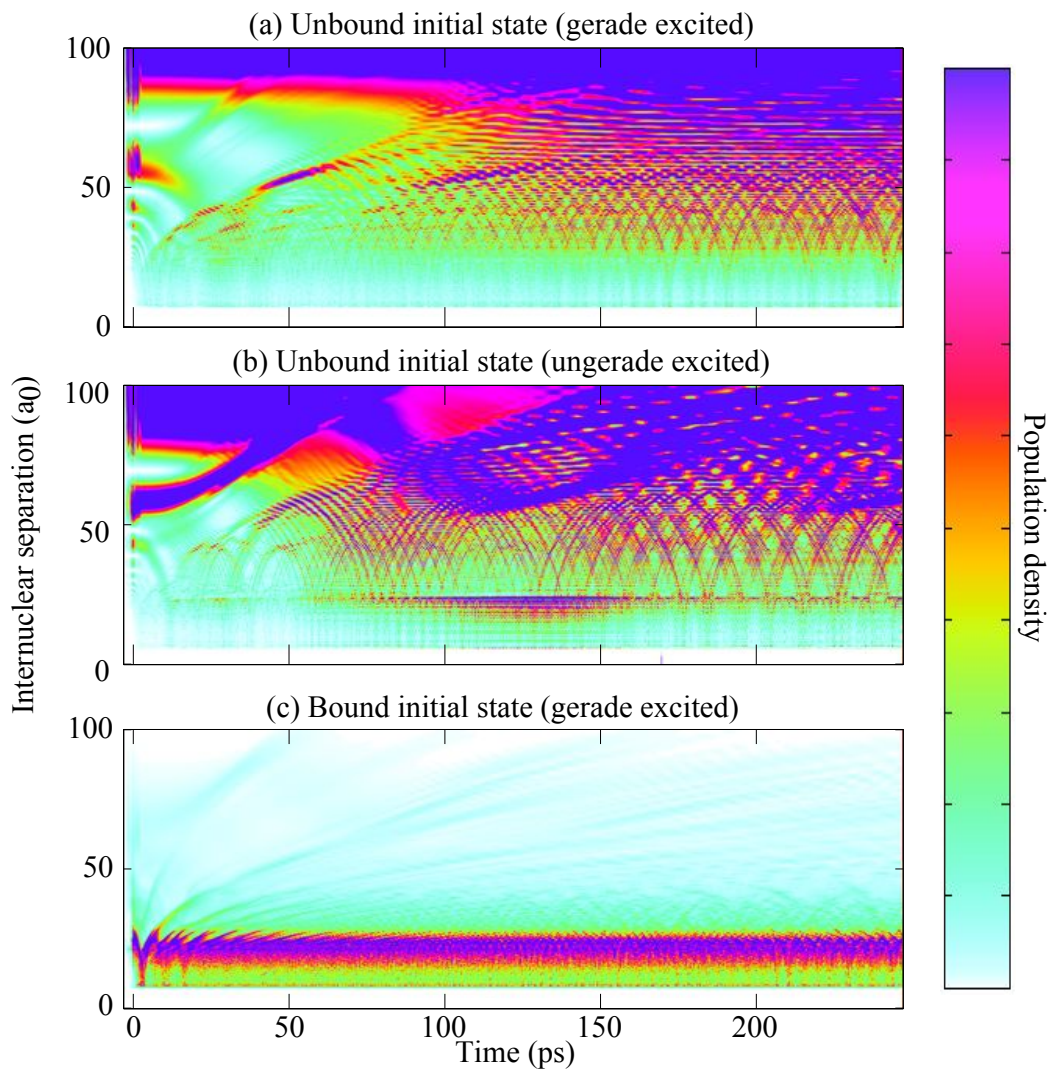


Figure 4.6 Simulation of time and position dependence of the excited-state following a pump pulse. Transitions from an unbound scattering state to both gerade (a) and ungerade (b) excited-states are considered along with a bound initial population (c). Coherent dynamics can be observed on all three plots with faster timescales on the bound initial state due to the shorter internuclear separation.

probe, a crude ionization model was proposed. The model postulates that population will be ionized from a particular excited state provided some of the spectrum is

blue of the ionization threshold. The signal is proportional to the fraction of the spectrum which is blue of the threshold. Mathematically, the contribution from the j^{th} excited-state to the molecular ion signal is proportional to the expectation value of operator;

$$\hat{O}_j(R) = \frac{\int_{\Delta E(R)/\hbar}^{\infty} I(\omega) d\omega}{\int_0^{\infty} I(\omega) d\omega}, \quad (4.1)$$

where the spectrum, $I(\omega)$, is taken from experimental data and ΔE is the position-dependant ionization threshold,

$$\Delta E(R) = V_{ion}(R) - V_j(R). \quad (4.2)$$

$V_{ion}(R)$ is the first molecular potential of the Rb_2^+ ion and $V_j(R)$ is the potential of the j^{th} excited-state. Here we have assumed ‘vertical’ transitions, *i.e.* we are still working under the Franck–Condon principle despite the capacity for the electron to carry away excess energy.

In this model the time-dependent ion signal (as a function of pump-probe delay, τ), is proportional to the expectation value of the total operator, $\hat{O} = \sum_j \hat{O}_j$, acting on the wavepacket, $|\Psi(R, \tau)\rangle$;

$$\text{Signal} \propto \langle \Psi(R, \tau) | \hat{O} | \Psi(R, \tau) \rangle. \quad (4.3)$$

Examples of the simulated signals from both bound and unbound initial states⁴

⁴As above bound states are simulated from the experimental distribution of vibrational levels and the unbound atoms are simulated by a single scattering state.

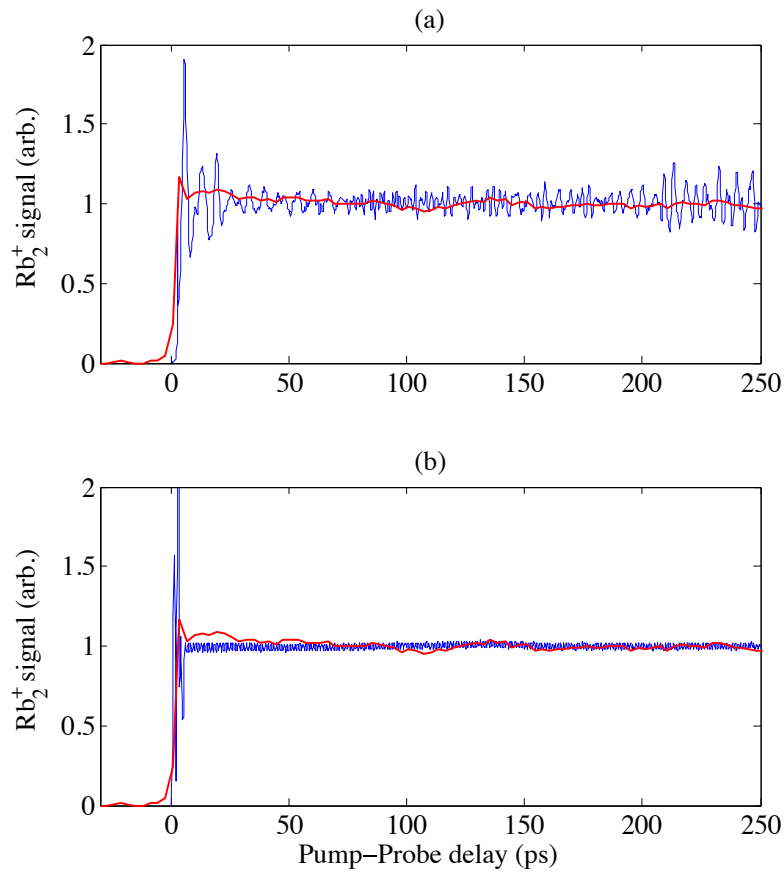


Figure 4.7 Theoretical predictions of the pump-probe signal (blue) are compared to the measured experimental data (red). The predicted ionization signals are derived from the population distributions shown in Figure 4.6 using the ionization operator postulated in the text. Both bound (a) and unbound (b) initial states are considered.

are shown in Figure 4.7, along with an experimental trace for comparison. The signal from the bound initial state displays clear oscillatory behavior (Figure 4.7(a)) with a dominant period of around 5 ps determined by Fourier analysis. The unbound initial state signal contains some initial high frequency oscillations which are attributed to coherent transients during the pulse overlap; however, after these, the plot remains

flat and shows no discernible sign of wavepacket oscillations. Hence it appears that the high-frequency oscillations in the bound initial state data can be resolved using this ionization model, whereas for the unbound initial state, the oscillations are washed out. This can be explained by the internuclear separation of the two populations shown in Figure 4.6. The bound initial state population resides at around $20 a_0$, at which point the molecular potentials have a noticeable gradient (see, for example, Figure 4.4) this means that the threshold ionization frequency varies strongly with internuclear separation. In the unbound initial state, however, the internuclear separation is far greater ($50-100 a_0$), at which point the potentials have flattened out significantly, and hence the ionization frequency is less sensitive to changes in internuclear separation.

4.1.4 Demonstration of bound excited-state dimers

While the pump-probe experiments did not observe any excited-state dynamics, the fact that bound excited-state dimers were formed is an important first step along the road to ultrafast photoassociation. Further information about the nature of the excited-state dimers can be inferred by moving the position of the spectral cut and observing the relative behavior of atoms and molecules, as discussed below.

As we move the spectral cut further away from atomic resonance, we expect the molecular signal to decay, as the Franck–Condon overlap for the excited transition decays. Hence we would like to measure the height of the ‘step’ in the molecular signal as a function of the position of the spectral cut. To do this we choose a fixed

pump-probe delay of ± 40 ps. For a given spectral cut position the molecular signal is taken at both negative, S_- , and positive, S_+ , pump-probe delays and the height of the step, H , is calculated, and normalized, as;

$$H = \frac{S_+ - S_-}{S_+ + S_-}. \quad (4.4)$$

For comparison, the height of the atomic step is also measured with the same laser parameters as the molecular step. As before, it was necessary to reduce the bias voltage of the MCP detector in order to ensure a linear response to atomic ions.

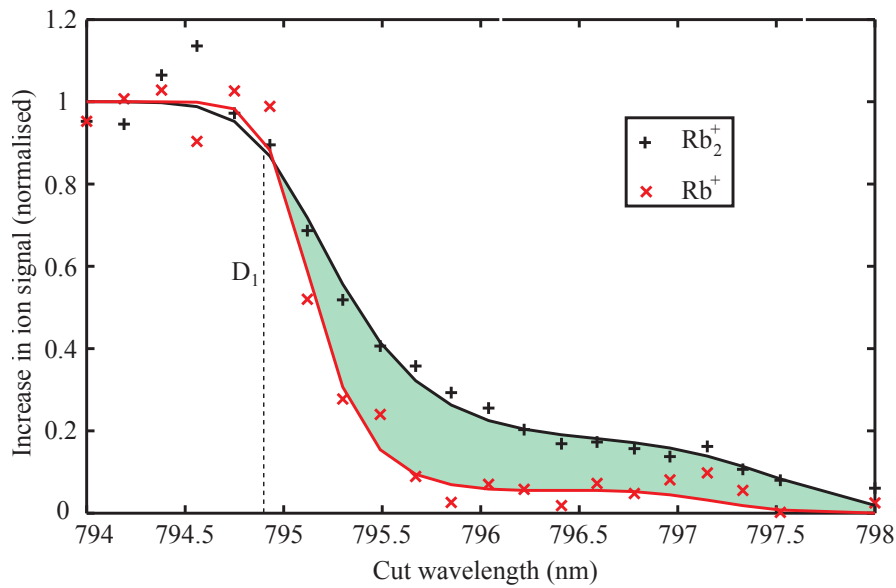


Figure 4.8 Demonstration of bound molecules in the excited-state. The height of the pump-probe ‘step’ was measured for both atoms and molecules at a range of positions of the spectral cut. Both signals are normalised to their maximum value for direct comparison. The molecular signal (black) rolls off more slowly than the atomic (red); the difference between the two curves, shaded in green, indicates the bound nature of the excited-state dimers.

The results of this moving-cut experiment are displayed in Figure 4.8. As we would expect, both signals roll off as the cut moves away from the D_1 line (indicated by vertical dashed line at 794.9 nm). However, the molecules roll off more slowly than the atoms. The difference in the two curves (shaded in green), provides clear evidence that the source of the molecular signal in the pump-probe experiment is bound excited-state dimers rather than pairs of unbound, excited, atoms which are excited to the Rb_2^+ molecular ion potential.

The roll-off of the molecular signal with cut position depends on the difference in energy between the ground and excited states involved in the process, which, in turn, depends on the internuclear separation at which the excitation takes place. The experiment was modeled at a range of internuclear separation by calculating the fraction of population excited at a given internuclear separations given a varying cut position. The ionization step was not modeled but it was assumed that it is independent of internuclear separation, an assumption which is supported by the flat nature of the pump-probe signal. The results of these simulations are displayed in Figure 4.9 along with the experimental data.

At first glance, the experimental data appear to be a poor fit to the theoretical predictions, with the results crossing several of the theoretical lines. However, if we consider that the population is unlikely to reside at a single internuclear separation but rather be spread across a range, then the results become clearer. A gaussian distribution was assumed for the distribution of the internuclear separations of the initial state with the position, R_0 , and full-width-half-maximum, $FWHM$, of the

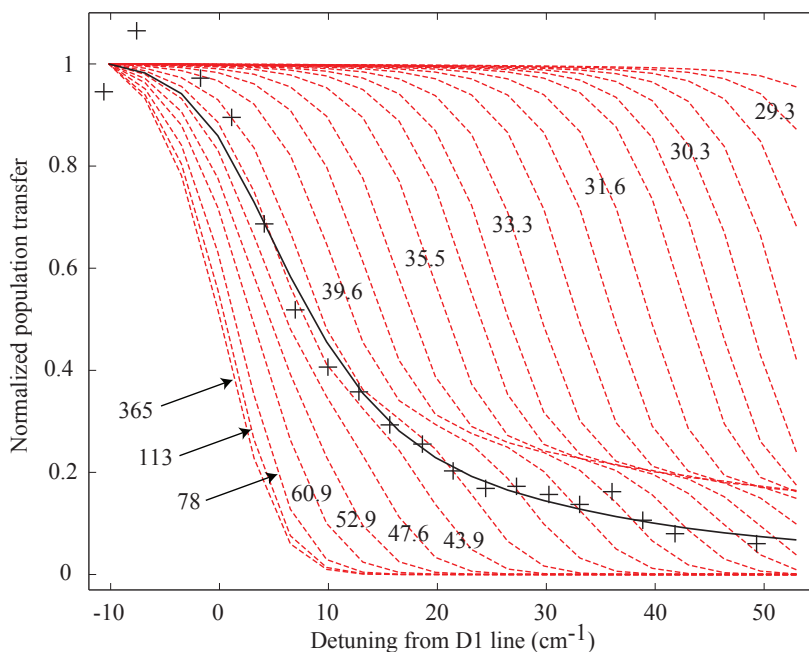


Figure 4.9 Results of simulations of the moving-cut experiment at a range of internuclear separations. The simulation results are shown in dashed red with the corresponding internuclear separation (units of a_0) labeled on some curves. The experimental data (black crosses) is fitted with a distribution of these simulated results (black line) to give an idea of the internuclear separation of the initial population.

gaussian as free parameters. A best-fit analysis of the data with the theoretical curves was performed; the resulting line of best fit is shown in black on Figure 4.9. The parameters which gave the best fit were $R_0 = 47 a_0$ and $FWHM = 29 a_0$. A few other initial state distributions were postulated, but each fit gave similar results, all suggesting that the initial state population resides between $30 a_0$ and $60 a_0$.

Comparison of pump-probe results with the initial state

The inferred initial state population distribution measured with the moving-cut experiment allows us to make assumptions about the origin of the molecules in

the pump-probe signal. The distribution of best fit to the results suggests that the initial state is centered at $\sim 50 a_0$, while the outer turning point of the 9th vibrational state — which is the most populated state in the background molecules — is situated at $24 a_0$. This suggests that the source of the pump probe signal is photoassociation rather than excitation of background molecules. In Figure 4.10, the best fit distribution is plotted along with a scattering state wavefunction and an incoherent sum of the background vibrational states.

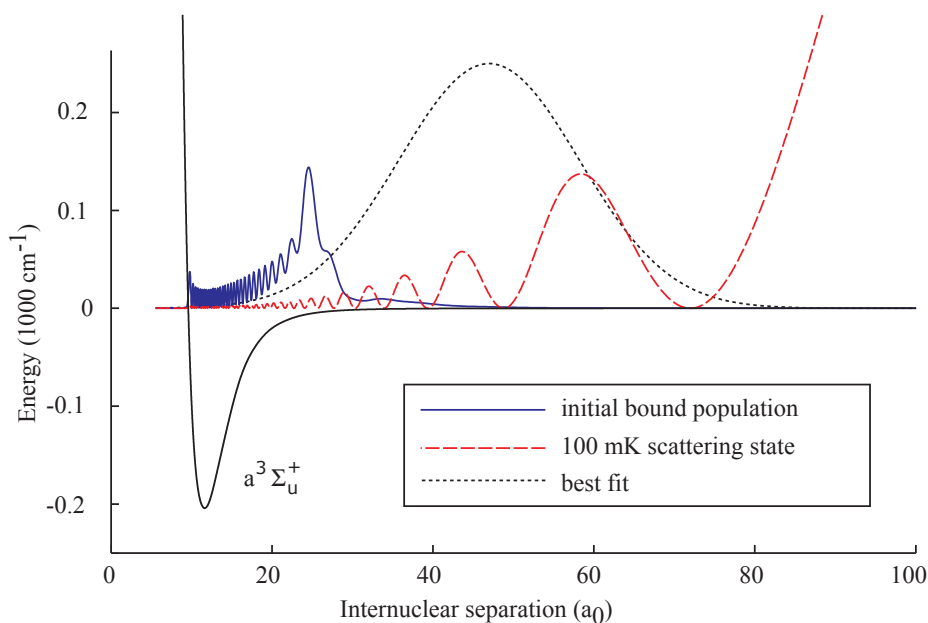


Figure 4.10 The Gaussian best-fit population distribution inferred from the moving-cut experiment (dotted black) is compared with a $100 \mu\text{K}$ scattering state (dashed red) and the background population (solid blue).

The best-fit distribution seems to agree with the scattering state picture of the initial state. Short-range excitation ($R < 25 a_0$) is negligible due to the small wavefunction amplitude of the scattering state, while contribution from long-range

molecules is limited by the detuning of the probe pulse from the Rb^+ asymptote. It is also worth considering that the TOF field produces dissociation of molecular ions below a certain binding energy. For the typical electric fields in the MOT ($\sim 100 \text{ V/cm}$), this binding energy corresponds to a limit of $\sim 100 a_0$ beyond which $\text{Rb}_2^+ \rightarrow \text{Rb}^+ + \text{Rb}$ ^[130]. However, this limit is well beyond the wings of the Gaussian fit, suggesting that long range signal is limited by the probe detuning rather than field dissociation.

In a similar, but less quantitative, way further evidence of the long-range nature of the bound excited state dimers was determined from the choice of ionization wavelength. The atomic ionization threshold from the $5\text{P}_{1/2}$ state is at 474 nm ^[28], the largest molecular ion signal was found when the NOPA was tuned close to this wavelength. Due to the slope of the ionization potential, we would expect short-range molecules to provide ionization signal for wavelengths red-detuned of this resonance. However, red-detuning the NOPA produced a rapid reduction in signal suggesting the long-range nature of the excited state dimers. This experiment is analogous to the spectral-cut experiment but was far more difficult to perform as the wavelength tuning in the NOPA leads to misalignment of the beam and hence results that are not easily comparable from one wavelength to the next.

4.2 Conclusions

The background population of pre-formed molecules in the MOT was characterized using REMPI spectroscopy via the $(2)^3\Sigma_g^+$ state. The distribution of vibrational

levels in the a state was determined to be centred on the 9th highest vibrational level. The photoassociation of ground-state molecules by the MOT lasers was modeled assuming the 0_g^- potential to be the intermediate state. Good agreement was found between experiment and theory, suggesting photoassociation by the MOT lasers as the dominant mechanism in the formation of background molecules.

A pump-probe experiment was performed with the aim of identifying wavepacket dynamics in the excited state. A clear step was observed in the signal at zero delay implying bound excited-state population, however dynamics were not present in the signal, despite a range of parameters being tried. The action of the pump pulse was simulated numerically assuming both an unbound initial state and the bound initial state measured by the REMPI spectroscopy. Results indicated that the population density in the excited state does oscillate for both cases, demonstrating that coherent dynamics should exist, despite the incoherence of the initial state. The bound initial state population oscillates quickly ($\tau_{osc} \sim 5$ ps) and with clear periodic behavior while the unbound initial state evolves slowly with more dephasing of the wavepacket. An ionization operator was proposed to try and map the oscillations in excited state density into an observable that would show up in the experiment. The ionization operator mapped the oscillations from the bound initial state into an oscillating ionization signal, but the more long-range dynamics of the unbound initial state were washed out by the poor position selectivity of the probe at large internuclear separation. Hence the simulations suggest that, while the pump pulse should be creating coherent oscillations, the probe step may not be sensitive to them.

The atomic and molecular signals were monitored as a function of the wavelength of the spectral cut in the pump pulse. By comparison of the two, it was clear that the molecular signal dropped off more slowly than the atomic, demonstrating that the source of the molecular signal was bound excited-state molecules. The moving-cut experiment was simulated at a range of internuclear separations, assuming stationary population. The experimental data were fitted to a Gaussian sum of the resultant curves in order to infer the distribution of internuclear separations in the initial state responsible for the bound molecular signal. The fit indicated that initial population resided around 30-60 a_0 . The outer turning point of the background molecular population observed in the REMPI is at 24 a_0 which suggests that the molecular signal is dominated by photoassociation rather than excitation of bound molecules. The initial state calculation proves that the molecular signal derives from an unbound initial state, and thereby explains the lack of wavepacket oscillations observed in the pump-probe experiment.

4.2.1 Outlook

From the results presented in this chapter, and the previous work on pump-decay schemes in Oxford^[110-112,131] and Germany^[132], it is clear that various technical and scientific hurdles need to be overcome before a strong oscillatory excited-state signal, or even stabilization into the ground state, may be experimentally demonstrated. A major stumbling block is the large internuclear separations involved in the experiment. Working at large R produces several problems. Firstly, the slow variance

of the molecular potentials at long range means that the pump pulse produces an excited-state wavepacket over a large range of internuclear separations. Due to the rapidly varying classical oscillation period at long range⁵, such a wavepacket would very quickly de-focus as different parts evolve at different speeds. A second problem with working at large R is the time taken for population to move towards the centre of the potential; maintaining the shape and focus of a long-range wavepacket on these timescales represents a tough challenge for coherent control techniques. Pump-probe experiments have also proved tough in the long-range regime due to the insensitivity of the probe to position. Hence it is clear that we must move to shorter internuclear separations to improve the prospects for wavepacket observation and, ultimately, pump-dump schemes.

One possibility for short-range dynamic experiments is to use the pre-formed background molecules; simulations in Section 4.1.3 suggest that rapid coherent oscillations of the few-ps timescale should be observable using this setup. However, looking at the theoretical moving-cut curves in Figure 4.9, one would expect the molecular signal due to bound molecules (outer turning point $24 a_0$) to be present well beyond 50 cm^{-1} hence we do not have sufficient detector sensitivity to measure this signal.

A second way to work as shorter internuclear separation is to increase the size and/or the density of the ultracold atom sample. While the overall shape of the moving-cut experiment is believed to be determined by the scattering wavefunction

⁵See appendix B and Figure 4.3(a) for calculations of the classical oscillation period.

and is unlikely to change with an improved atomic sample, a better signal-to-noise ratio may allow us to observe signal at a larger detuning and hence work at shorter internuclear separation. At the time that the above results were taken, work had already begun on a new cold-atom apparatus, details of which follow in chapter 5. In this new apparatus, the atoms will be held in a hybrid magnetic and optical trap; this apparatus offers higher atomic density, which was expected to yield greater photoassociation rates. On top of this, the hybrid trap provides a conservative potential in which to hold any molecules formed by photoassociation (which would not be trapped by the MOT), leading to the potential to accumulate molecules. With these improvements to the system, the search for molecular dynamics continued.

Chapter 5

Construction of the Dipole Trap

Apparatus

At the time the author arrived in Oxford, the cold-atom apparatus described in Section 3.1 was struggling to cope with the demands that the experiment placed upon it. Daily realignment was required to achieve usable molecular signals, while small MOT numbers ($\sim 2 \times 10^7$) meant that signal-to-noise ratio was often a problem. Some improvements were made to the old apparatus; these are outlined in the thesis of David McCabe^[133]. However, it was decided that a complete over-haul of the apparatus was necessary. Work on this, in parallel with the continued work on pump-probe experiments in the old apparatus, began in summer 2007.

A summary of the limitations of the old apparatus lends motivation for the new design, and also provides criteria which the new apparatus must meet. The primary concern is the atomic number and density. The number of atoms trapped

in the old MOT was limited by the low power in the trapping lasers, leading to a prohibitively small capture volume; the new trap must have larger MOT beams and more trapping power. Following the MOT phase, density can be increased and temperature reduced, using a number of techniques including optical molasses, a compressed MOT or a dark SPOT. All of these require computer control of the current in the coils, and the laser detuning and power; in the old apparatus, we did not have the ability to do this. Further increases in density can be achieved by evaporative cooling in a non-scattering trap such as a magnetic trap or a dipole force trap. The bulky vacuum chamber used for the MOT meant that the magnetic coils could not get close to the atoms, therefore very high currents would have been necessary for a magnetic trap. The limited optical access to the MOT also made the implementation of a dipole trap difficult.

Any molecules produced in a MOT are not trapped and hence simply drift out of the photoassociation region. A simple calculation assuming beams focussed to $100\ \mu\text{m}$ and a thermal velocity of $14\ \text{cm/s}$ ¹ indicates a timescale of $\sim 1\ \text{ms}$ for this process. At a repetition rate of $2\ \text{kHz}$ this corresponds to only 2 pulses, making it impossible to accumulate molecules over a sequence of pulses. However, triplet molecules can be trapped in a magnetic trap due to their magnetic moment, and either triplets or singlets can be held in a dipole trap, leading to the possibility of accumulation.

Magnetic traps have a high trapping efficiency due to their large capture volume

¹Corresponding to a temperature of $100\ \mu\text{K}$.

but tend to require long evaporation times, for example, the first BEC observed by Anderson *et al.* required 70 s of evaporation. This places a stringent requirement on the quality of the vacuum and also limits the repetition rate of the experiment. By contrast, all-optical BECs can be produced on timescales below 5 s albeit with fewer atoms due to the poor mode matching between a tightly focussed beam and a large MOT^[134,135]. An elegant solution to this problem, combining both magnetic and optical traps, was presented by Lin *et al.*^[136]. In this scheme, atoms are loaded from a MOT into a hybrid magnetic and optical trap. Evaporation in the magnetic trap loads cold, dense atoms into the dipole trap before reducing the magnetic field gradient to form a hybrid magnetic and optical trap for final evaporation. The key to this approach is that the minimum of the combined potential is located away from the magnetic field centre, hence avoiding degenerate spin-flip losses during evaporation. This technique produces large BECs with a cycle time of 16 s.

While BEC was not necessarily a goal in this experiment, a similar approach was used to load atoms into a dipole trap with the aim of producing a denser atomic medium for photoassociation experiments. It is anticipated that this apparatus may also be utilized for further experiments combining ultrafast lasers with ultracold matter, including, for example, the extension of the Raman quantum memory technique demonstrated by Reim *et al.*^[19] in warm atomic vapor, to an ultracold sample. The apparatus used is described in sections 5.1, 5.3, 5.4 and 5.4.1. The MOT is characterized in Section 5.5.2 and the sequence of loading atoms into the dipole trap is described in Section 5.6.

5.1 Vacuum chamber

Many ultracold atom experiments revolve around a differentially pumped two-chamber design. A MOT is loaded from a high vapor pressure in the first chamber which is connected to a second chamber by a long, thin, pipe. The second chamber (science cell) is usually a small glass cell and is differentially pumped to a much lower pressure. Cold atoms are transported along the pipe to the science cell where the collisional lifetime of a trap is much longer than in the MOT cell.

In this experiment, the necessity to include a TOF spectrometer in the vacuum chamber precludes the use of a glass cell as all the MCP and pushing grids must be placed above and below the MOT as well as a port for the pumps and the rubidium getter. Such a design would be complicated and expensive to make from glass. Instead, an 8 inch, cylindrical, metal chamber was used with 12 ports around its diameter². To avoid adding further complexity to an already large apparatus, the decision was taken to use only a single-chamber design. In order to allow the magnetic coils to get as close to the atoms as possible, re-entrant flanges were designed to fit on each end of the chamber³. A cross-section of the vacuum chamber in Figure 5.1(a) shows the re-entrant flanges and the position of the coils.

In this single-chamber design, it is necessary to dynamically control the partial pressure of rubidium in the chamber as a high pressure is required to load the MOT, while low pressure is necessary during the magnetic/optical trapping phases, to facilitate longer storage times. In systems containing a Zeeman slower, this dynamic

²The vacuum chamber was custom-made by LewVac LLP.

³The re-entrant flanges were manufactured on-site in the Oxford Physics workshop.

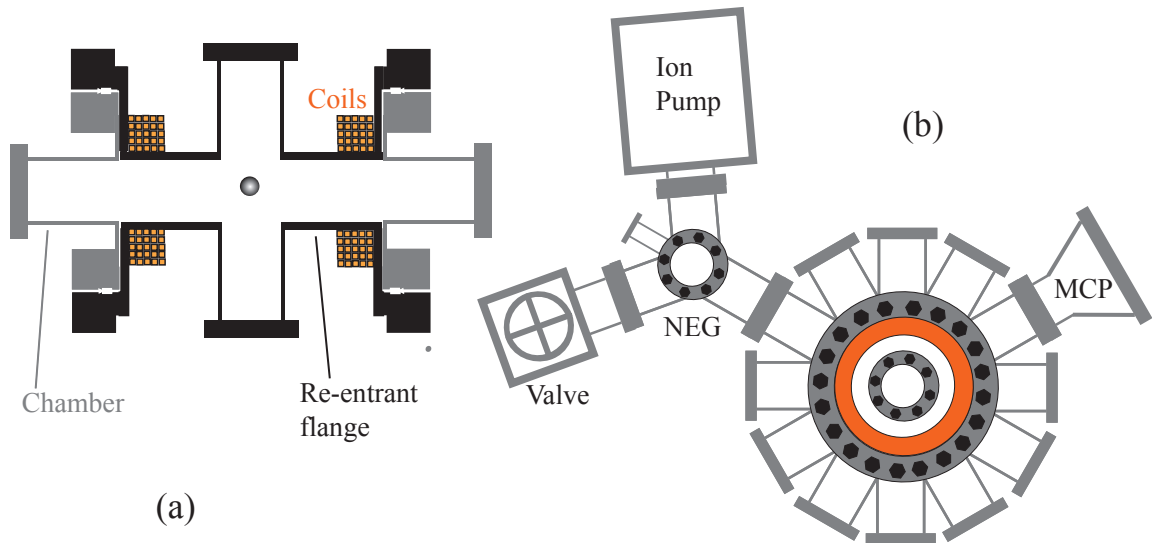


Figure 5.1 (a) A cross-section of the vacuum chamber showing the re-entrant flanges (black) which protrude into the chamber (grey) allowing the magnetic coils (orange) to get as close as possible to the MOT (centre of chamber). (b) a birds-eye-view of the chamber. The 12-port design allows maximum optical access, the vacuum pumps (Ion pump, NEG pump and valve to turbo pump) are all mounted on a custom 5-way adapter to allow optical access through the same port.

control is achieved by simply switching off the slower (see for example, reference^[41]). However, this apparatus does not have a Zeeman slower. Alternatively, one might consider switching the rubidium dispensers on and off; however, the process by which the gas is released is thermal and hence cannot be modulated quickly enough. Another technique, known as light-induced atom desorption (LIAD) has been implemented by several groups for ultracold atom apparatus^[137–140]. The principle behind the LIAD technique is as follows: a conventional source of the alkali metal vapor⁴ is used to fill the chamber, after some time, the vapor is pumped away but

⁴Either a dispenser or an ampule filled with solid metal.

some atoms are adsorbed by the walls of the chamber. At this point, the pressure in the chamber is too low to load a MOT. The pressure can be boosted by the application of a bright light to the cell, this removes atoms from the chamber wall by the process of photodesorption, momentarily increasing the pressure in the cell in order to load a MOT. Once loading is completed, the light is switched off and the atoms are rapidly re-adsorbed onto the chamber walls, reducing the pressure for longer trap lifetimes. This technique was characterized by Klempt *et al.*^[141] showing that ultraviolet wavelengths removed light from the walls most efficiently and suggesting that the LIAD mechanism was equally applicable to stainless steel chambers as to the glass cells previously used.

Before constructing the new cold atom apparatus, the LIAD mechanism was tested in the old MOT. The results of this investigation, shown in appendix D, suggested that LIAD would be suitable for loading the MOT in the new apparatus. However, attempts to replicate these results in the new chamber were met with failure. It was hypothesized that there was insufficient rubidium adhered to the walls of the chamber so attempts to increase the rubidium pressure in the chamber were made, including turning the current to the dispensers up and switching off the ion pump during the coating phase, but still no effect was observed. Hence it was necessary to run the experimental protocol with the rubidium dispensers continuously on. In an effort to reduce the pressure, the current in the dispensers was kept as low as possible, but this constant source of rubidium vapor has a significant detrimental effect on the pressure in the cell and hence was anticipated to cause

problems with the lifetime of the magnetic and dipole trap.

The vacuum chamber was brought down to ultra-high vacuum (UHV) by a turbo-molecular pump backed by a rotary vane pump, but once the desired pressure had been reached, a valve was closed and the turbo pump switched off. Pressure in the chamber was maintained by an ion pump (*Varian* Star Cell 40 L/s) and a NEG pump (SAES CapaciTorr[®]). A custom 5-way adapter allowed all three pumps to be attached to a single port on the chamber, while still allowing optical access. The Y-shape of the adapter minimized the bend in the connection between pump and chamber to increase pumping speed. Rubidium vapor was introduced to the chamber using SAES dispensers mounted on high-current feedthroughs. A sketch of the lay-out of the vacuum chamber is shown in Figure 5.1(b).

5.1.1 Bake-out

When the vacuum system was assembled and leak-tested the turbo pump was switched on, the pressure was monitored using an ion gauge mounted just before the valve which connected the pumps to the system. Once the pressure was below 10^{-6} mbar, the NEG pump was activated and the ion pump switched on. After this the pressure dropped to a steady 10^{-7} mbar. The system was then baked for 6 days at 130°C until the pressure stabilized at 10^{-8} mbar. The chamber was then cooled, making sure to keep the turbo pump $10\text{-}15^{\circ}\text{C}$ cooler than the chamber such that residual gas is preferentially adsorbed on the walls of the pump rather than the chamber. Once the chamber had reached 70°C , the valve to the turbo pump was

closed, at this point the pressure was measured by the ion gauge to be 3×10^{-9} mbar. As the temperature dropped to room temperature, the pressure in the chamber was estimated, by observing the ion pump current, to be below 10^{-9} mbar. A plot of temperature and pressure during the bake-out is shown in Figure D.1.

5.2 Computer control

A typical experimental sequence requires the full control of many parameters including, among others, laser power and frequency, magnetic fields and CCD cameras. It therefore requires the control of many devices using either TTL pulses or precise analog voltages. These devices must be accurately and repeatably controlled on the sub-millisecond timescale. This is achieved using a *National Instruments (NI) CompactRIO-9151* control and acquisition system. The CompactRIO is an external chassis containing a series of input and output modules with imbedded controller and a reconfigurable field-programmable gate array (FPGA)^[142]. The FPGA is essentially a micro-computer which can be re-programmed by the lab computer, but whose operation is entirely separate. An experimental sequence can be programmed in *NI Labview* and then loaded onto the FPGA where it is run. The advantage of the FPGA over conventional PCI cards is that it has a real-time internal clock and hence the timing of the experimental sequence is unaffected by operations on the master computer such as saving data. The CompactRIO chassis contained NI-9263 0-10 V and NI-9265 0-20 mA analog output modules, each capable of processing up to 4 analog outputs simultaneously. We also had a NI-9401 digital input/output

board with 8 channels. This gave a total of 16 outputs from the chassis which were used to control the experiment. The majority of the data for the experiment was taken by oscilloscopes and CCD cameras so the input functions of the CompactRIO were unused. A summary of the analog and digital output channels and their roles in the experiment is show in Table 5.1.

Module	Output	Role
NI-9401 TTL output	DO 0	Unassigned
	DO 1	Helmholtz/Anti-helmholtz switch for magnetic coils
	DO 2	Mechanical shutter for repumper laser
	DO 3	Probe laser AOM on/off
	DO 4	LIAD LEDs on/off
	DO 5	Camera trigger
	DO 6	Ultrafast lasers shutter
	DO 7	Oscilloscope trigger
NI-9263 0-10 V Analog output	AO 0	Unassigned
	AO 1	MOSFET gate voltage
	AO 2	Power supply external voltage control
	AO 3	Power supply external current control
NI-9265 0-20 mA Analog output	AO 0	Master laser AOM RF power
	AO 1	Repumper laser AOM RF power
	AO 2	Master laser AOM RF power frequency
	AO 3	Dipole trap laser AOM RF power

Table 5.1 NI CompactRIO output channels used in the experiment.

The *Labview* interface for the FPGA module was kindly provided by Marcus Gildemeister from Professor Chris Foot's group in Oxford. This excellent piece of software allows the user to split an experimental sequence into sections of varying lengths, within each section one can assign values to each output in order to build up a complete sequence. Each analog channel can be calibrated such that entering

a desired parameter, *e.g.* -47 MHz detuning, produces the correct voltage or current from the analog output (in this instance 2 mA). Furthermore, timing offsets can be applied to the digital outputs to compensate for slow instrument response — for example the finite time taken to close an optical shutter. Sequences and configurations can be saved and recalled to allow several different experiments to be run without having to re-load the program.

5.3 Magnetic coils

In order to get good overlap between the MOT and the magnetic trap, and to reduce the complexity of the experiment, it is prudent to use the same magnetic coils for both. In order to reach the high field gradients required for magnetic trapping, high current must be used. To avoid over-heating of the coils, they must be continuously cooled. To this end, the coils were wound out of 3 mm square profile kapton®-insulated wire with a 2 mm diameter hole running through the core. Water was continuously passed through the core of the wire during operation to keep them cool. With the exception of the coils, the current is carried by welding wire with a 35 mm² profile, which does not require cooling. The current through the coils is constantly monitored using a Hall-sensor around the welding wire.

The hollow-core wire was wound in a former to produce square profile coils, 5 winds per layer, 5 layers in total, although due to the finite distance taken for a the wire to change layer, only 24 winds per coil was possible. The resistance of each coil was measured to ensure that they were identical and contained no shorts between

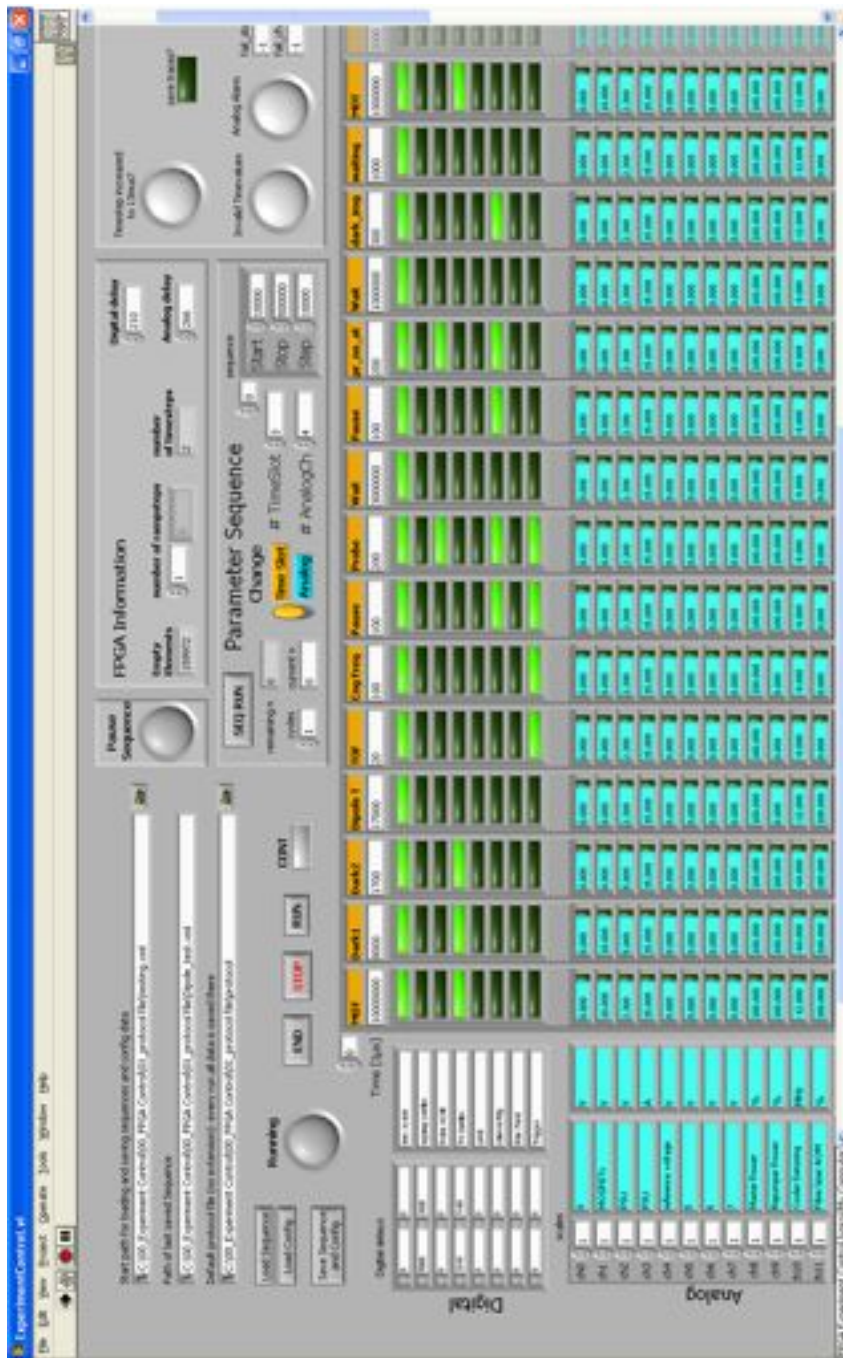


Figure 5.2 Labview control panel.

layers. The outer diameter of the coil was matched to the inner diameter of the re-entrant flanges such that the coils would sit flush against the chamber, as shown in Figure 5.1(a), this ensured that the centre of the field gradient is at the geometric centre of the chamber which simplified alignment of the laser beams.

The power supply (PSU) used to power the coils was a 12kW Xantrex XDC 30-400 with maximum output of 400 A, 30 V. Both current and voltage were externally controlled by analog voltages from the control computer. The PSU was protected from reverse current by a high power diode (*Semikron* SKN 240/04).

5.3.1 MOSFET current control

In order to run the full experimental sequence, one must be able to rapidly switch the magnetic field gradient on and off on the timescales of the motion of the atoms. Assuming a MOT size of 1 mm, and a thermal velocity of 10 cm/s suggests timescales of the order milliseconds; far quicker than the power supply can turn on and off. Instead the current in the coils was switched on and off with banks of metal-oxide-semiconductor field-effect transistors (MOSFETs). The MOSFETs (*STMicroelectronics* STE180NE10) are each specified as being capable of handling up to 180 A, and 5 MOSFETs were wired together in parallel to share the load.

A diagram of the circuit is shown in Figure 5.3. A primary bank of MOSFETs (MF1) was used to control the current to the coils, while four further banks (MF2-5) were opened or closed to switch the coils from Helmholtz to anti-Helmholtz as required. The gate voltage for the MOSFETs is derived from the control computer⁵; to

⁵More details on computer control can be found in Section 5.2.

protect the computer from high current spikes, the circuit was broken by a 1:1 optocoupler module (Oxford Physics CEG J08/112). The gate voltage for the MOSFET banks was referenced to the source, rather than to ground, hence the source voltage was added to the Labview voltage by a series of operational amplifiers in the gate box. The gate box also received a TTL trigger from the Labview (HH/AHH) which opened and closed MOSFETS 2-5 to switch the current direction in coil 2.

Fast switch-on using MOSFETs

By mode-matching the size of the MOT with the tightness of the magnetic trap it was estimated that the magnetic trap would need to run with 70 A in the coils; this parameter was later optimised experimentally (see Section 5.6.5). Hence we would like to minimize the time taken to switch the current from 0 to 70 A. The switch-on time of the current, as measured by the hall sensor, is shown in various situations in Figure 5.4. Initially, 5.4(a), the PSU was simply switched on using its analog input; a time of over 200 ms to reach 70 A is clearly insufficient for our needs. If, instead, the setpoint of the PSU was kept at 70 A and the MOSFETs gate voltage switched from 0 to 10 V then a significantly faster switch-on time of around 100 ms was observed (5.4(b)); however, this is still too slow on the timescale of atomic motion in the MOT. In order to obtain a fast switch-on to 70 A, the PSU current was set much higher and then rapidly turned down; this is shown in 5.4(c) with the PSU initially set to 170 A and then turned down to 70 A as the current reached 70 A, 1.6 ms later. This switch-on time should be sufficient for the experiment, but the subsequent

reduced the effect of the overshoot, as shown in 5.4(d). When the MOSFET gate voltage was at 3.3 V, significant amounts of power were being dissipated, hence we switch back to 10 V after 200 ms to prevent over-heating; this does not present a problem as the overshoot has died down at this point.

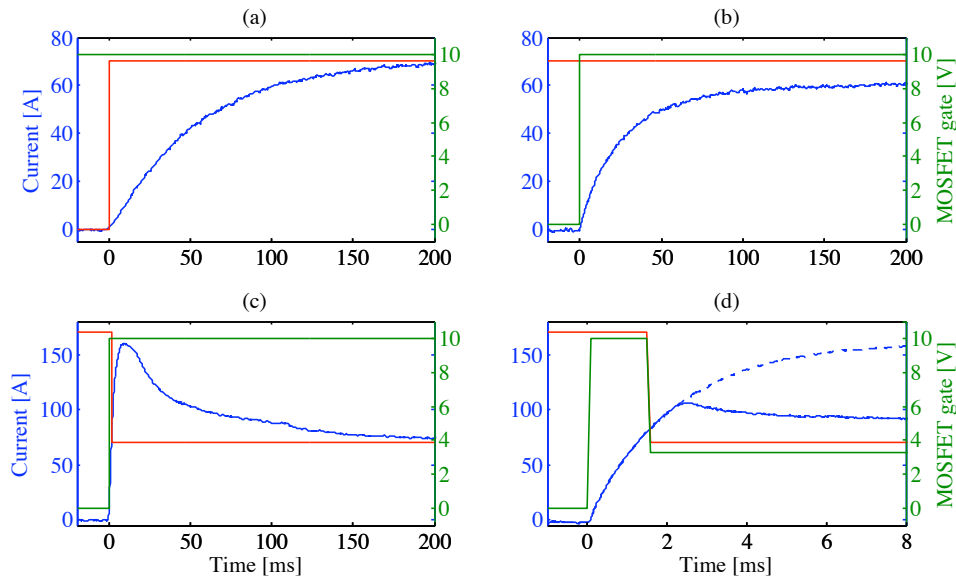


Figure 5.4 Switch-on response of the current in the magnetic coils in various situations. The current is in blue, the PSU setpoint in red and the MOSFET gate voltage in green. **(a)** The PSU is switched on to 70 A. **(b)** The PSU is at 70 A and the MOSFETs are opened at time zero. **(c)** The PSU is initially set to 170 A; the MOSFETs are opened and then the PSU current turned down to 70 A 1.6 μ s later; this produces a fast turn-on to 70 A, but also a huge overshoot. **(d)** Simultaneous with the current being reduced, the MOSFETs gate voltage is turned down to 3.3 V, this ‘catches’ the current before it overshoots and prevents the ringing observed in (c). The dashed blue line indicates the overshoot if the gate voltage remains at 10 V.

5.4 Lasers

5.4.1 Diode lasers

The main lasers for the MOT were a pair of Toptica DL100 extended cavity diode lasers. One was used as the repumper laser, while the other, hereby known as the master, was used as a seed laser to inject a high power tapered amplifier which provided the extra trapping power identified as being a requirement for the new apparatus.

The master laser

The master laser had a maximum output power of 120 mW. The frequency was locked to the $F = 2 \rightarrow F' = [1, 3]$ crossover resonance, which is 211.8 MHz red-detuned from the $F = 2 \rightarrow F' = 3$ cooling transition (see Figure A.1). The frequency was locked using the same saturated absorption spectroscopy and feedback electronics described in Section 3.1.1. The frequency was then shifted closer to resonance by an AOM (*Isomet* 1205-C) in double-pass, with an acoustic frequency of around 100 MHz. The double-pass AOM was set up in ‘cat’s-eye’ configuration^[143] such that a lens of focal length, f , was placed a distance f away from the AOM; the retro-reflecting mirror is a further f behind the lens (see Figure 5.5). In this configuration, the pointing of the beam is independent of the AOM frequency; this allows the detuning of the MOT lasers to be rapidly changed without realignment of the beam — a key requirement for optical molasses and compressed MOT schemes. The MOT was typically run at a detuning of -12 MHz but for optical molasses, the

detuning could be ramped as low as -70 MHz, hence the AOM was optimized for -40 MHz allowing similar power to be available at each detuning. The output of the double-pass AOM was split in two with one path going to seed the tapered amplifier (TA) and the other injection-locking a free-running diode which was used as the probe laser. Typically, less than 2 mW was required to injection-lock the diode, leaving 26 mW available for seeding the TA.

The repumper laser

The repumper laser had a maximum output power of 80 mW. The frequency was locked to the $F = 1 \rightarrow F' = [1, 2]$ crossover resonance which is 78.5 MHz red-detuned from the desired $F = 1 \rightarrow F' = 2$ transition. As the repumper frequency does not need to be dynamically tuned in this experiment, a single-pass AOM is sufficient to tune the frequency to resonance. The 1st order output of the AOM is coupled into a single-mode optical fiber after which 15 mW is available for the MOT. The radio-frequency (RF) source which drives the AOM can be rapidly turned on and off, hence the AOM acts as a fast switch to turn the beam on and off. A mechanical shutter behind the AOM is employed to block any light remaining in the first order.

Probe laser

The probe laser was a free-running diode laser (Roithner LaserTechnik RLT780-150GS) which was temperature tuned to 781 nm. The diode was injection-locked by 1-2 mW of the master beam. The injection and output beams were spatially sepa-

rated by a Faraday rotator between a pair of crossed polarizers. As the probe beam now shares the frequency of the master, it was detuned from resonance, typically by -12 MHz. The frequency was shifted onto resonance by a pair of AOMs⁶ with frequency shifts of 92 MHz and -80 MHz. The second AOM acted as a fast switch to turn on and off the probe beam. The beam was then coupled into a fiber to be transferred to the MOT.

Layout

The diode lasers were frequency-locked and amplified on one end of the table before being transported along the table by optical fibers to the MOT. This decoupled the MOT alignment from the rest of the system, greatly reducing the time spent on day-to-day alignment of the MOT. The experimental layout of the laser preparation is sketched in Figure 5.5. The tapered amplifier setup is discussed below.

5.4.2 The tapered amplifier

After the double-pass AOM, the master laser was the correct frequency for MOT operation, however, the power (26 mW) was insufficient for laser cooling. The power was boosted by amplification in a tapered amplifier (TA) chip (*Eagleyard photonics* EYP-TPA-0780-01000-3006-CMT03). The chip was held in a temperature controlled mount with aspheric lenses for coupling of the seed laser and collimation of the output. Due to the astigmatic nature of the tapered amplifier output, a further cylindrical lens was required to collimate the beam in both dimensions. Full details

⁶AOMs do not operate at frequencies as low as 12 MHz hence two had to be used.

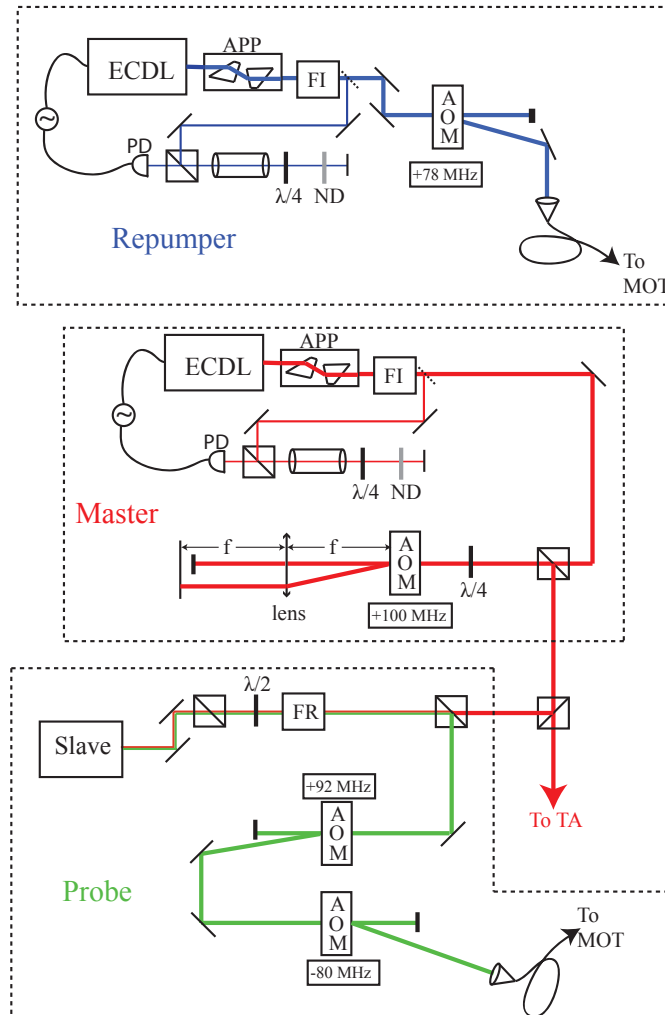


Figure 5.5 A sketch of the layout of the laser preparation. The repumper laser (blue) is frequency stabilized and passes through an AOM before being coupled into a fiber for transport to the MOT. The master laser (red) is also frequency stabilized before entering into a double-pass AOM setup. A lens, of focal length f ensures pointing stability as the frequency changes. The master injects a slave laser (green) which acts as a probe. A pair of AOMs shift the probe onto resonance before it is coupled into a fiber. KEY: ND: neutral density filter; PD: Photodiode; FI: Faraday isolator; FR: Faraday rotator.

of the design of the mount, seed alignment and collimation of the output can be found in Appendix C.

The chip is specified for up to 1 W output, however, with careful alignment of the seed laser, powers of up to 1.1 W were observed. In order to protect the TA from potentially damaging optical feedback, the beam was passed through a 60 dB Faraday isolator. Following the isolator around 800 mW were available for coupling into a single-mode fiber for transportation to the MOT. Due to the highly irregular spatial mode of the TA beam, only 250 mW could be coupled into the fiber. However, this still represents an order-of-magnitude improvement on the output of the AOM, including spatial filtering.

For a well-aligned seed beam, the output power was found to saturate at around 15 mW, however, it was found to be prudent to operate the TA with a higher seed power than this. In the saturated regime, the TA was less susceptible to changes in pointing and power of the master beam; this helped to maintain an even output power, even when the detuning of the laser was adjusted.

5.4.3 Dipole trap laser

Selection of an appropriate laser for optical trapping requires careful consideration.

The main factors involved in this decision are listed below:

- **Wavelength selection** — The wavelength of the laser must be red-detuned from atomic resonance for trapping in regions of high intensity. The laser must also be sufficiently far from resonance such that scattering is minimized. As

we would like to trap molecules in the dipole trap, these considerations are more complicated as we do not know in which internal state the molecules will be. To err on the side of caution, the wavelength would ideally be red-detuned of all molecular resonances.

- **Spatial mode** — To ensure tight focussing for the best possible trap, a single spatial mode is beneficial.
- **Longitudinal modes** — Beating between adjacent frequency modes in the laser produces high-frequency intensity noise which produces heating of the sample. Two solutions exist to this problem; either choosing a single-frequency laser to eliminate this beating, or alternatively, choose a laser with a very large linewidth such that the fluctuations are too fast to be felt by the atoms.
- **Power fluctuations** — Similarly, power fluctuations in the laser produce heating of the sample so a stable laser power is desirable.
- **Trap depth** — The laser should be powerful enough and the focus sufficiently tight, that the trap depth significantly exceeds the temperature of the atoms.

The laser chosen for this experiment was an *IPG photonics* SF Series 30 W fiber laser at 1550 nm; this wavelength is red-detuned of all Franck–Condon point molecular transitions from the X and a state in Rb_2 and hence suggesting that the wavelength selection is appropriate for the experiment. As the laser is delivered by a single-mode fiber, the spatial mode is TEM_{00} . The laser also has exceptionally low linewidth, on the order 20 KHz, and power stability at the 1% level. These

parameters suggest that it would be a good choice for the experiment.

Finally, an estimate of the trap depth must be made. Recalling equation (2.34):

$$U_{dipole} = \frac{\hbar\Gamma^2}{8\delta} \frac{I}{I_{sat}}, \quad (5.1)$$

And re-arranging to express in terms of the beam waist, w_0 , for a fixed power, P_0 of 30 W, the depth of the trap in Kelvin, T_{dipole} , is:

$$T_{dipole} = \frac{U_{dipole}}{k_B} = \frac{\hbar}{k_B} \frac{\Gamma^2 P_0}{4\pi\delta I_{sat} w_0^2}. \quad (5.2)$$

Hence we can calculate the trap depth as a function of beam waist and compare it to the temperature of the atoms. The results are shown in Figure 5.6. With beam waists between 50 and 100 μm , corresponding to trap depths of 100-500 μK , this was determined to be sufficient for the experiment.

The large vacuum chamber limited the focal length of the dipole trap lens to a minimum of 20 cm while a desire to place steering mirrors after the focussing lens imposed further limitations. Ultimately a focal length, F , of 40 cm was chosen. The beam left the fiber with a diameter, D , of 1 mm implying a focus size of:

$$w_0 = \frac{2\lambda}{\pi} \left(\frac{F}{D} \right) = 396\mu\text{m}. \quad (5.3)$$

Evidently, this focus is too large, but if the beam size, D , were increased to 6 mm then we could, theoretically, achieve a beam waist of 66 μm and a trap depth of \sim

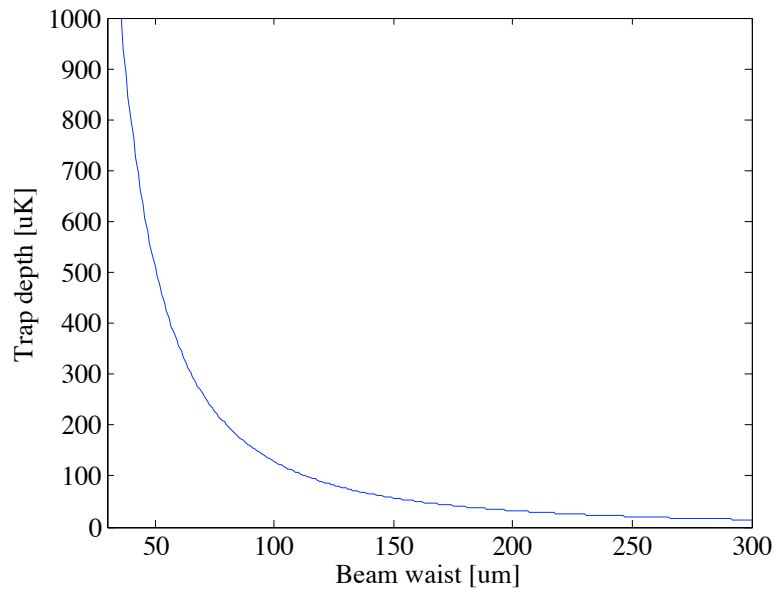


Figure 5.6 Calculation of trap depth vs. beam waist for the 30 W, 1550 nm fiber laser.

300 μK , which was deemed sufficient for the experiment.

In order to rapidly and accurately control the power of the dipole trap laser, the first-order diffraction of an AOM was used⁷. The beam remained small through the AOM in order to avoid clipping the aperture, before being expanded by a 6:1 telescope. The beam was then focussed and steered onto the MOT by a single dielectric mirror. The telescope was formed by a pair of lenses of -5 cm and 30 cm focal lengths. The 5 cm lens was 25.4 mm in diameter, the other two were 50.8 mm. Each lens was anti-reflection coated at 1550 nm. Despite this, great care had to be taken to avoid out-of-the-plane back reflections from the lenses.

⁷Isomet model number M1099-T50L-1550 driven by 6 W 100 MHz RF source (Isomet model number 531C-6). At the large detunings involved in the dipole trap, the frequency shift caused by the AOM is irrelevant.

As an alignment aid, the probe laser was re-directed into an optical fiber and was introduced collinear with the dipole trap beam; as this beam is resonant with the atoms it pushes atoms out of the MOT, producing a clear drop in fluorescence. A sketch of the optics involved in the dipole trap preparation is shown in Figure 5.7.

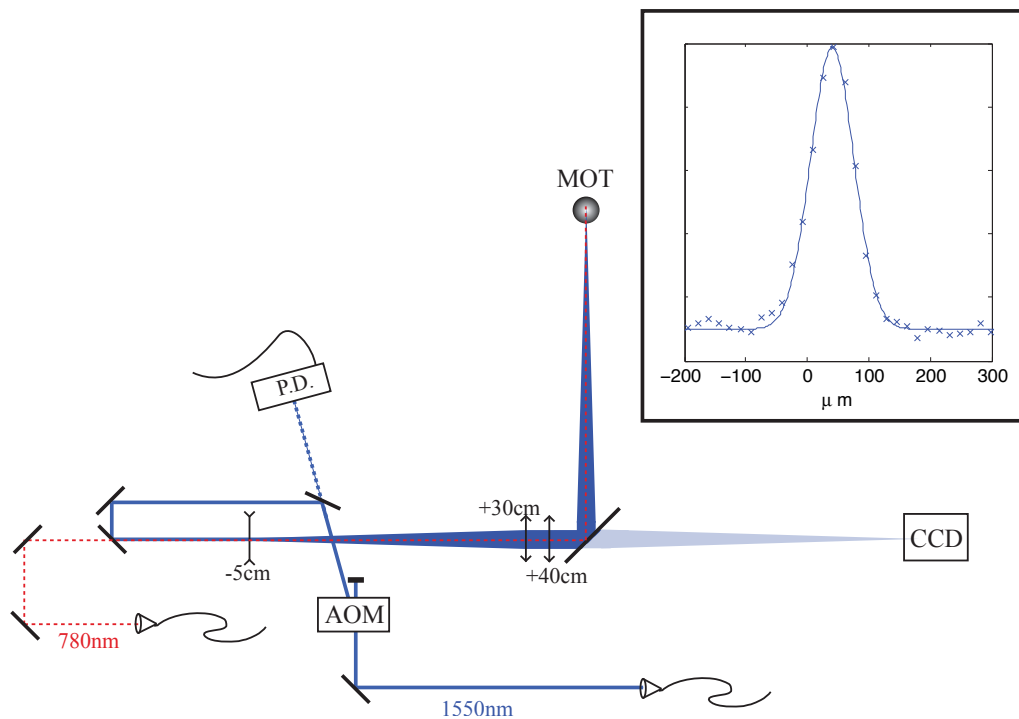


Figure 5.7 Layout of the dipole trap optics. Intensity control of the dipole trap beam was achieved with an AOM; the power through this modulator was monitored by a calibrated photodiode behind one of the mirrors. A 6:1 telescope increased the beam size before it was focussed by a 40 cm focal length lens. A CCD camera behind the final steering mirror measured the beam focus at a position conjugate to the MOT. The minimum focal size was $70\ \mu\text{m}$ as shown in the inset. A resonant probe beam (Red dashed line) was introduced co-linear with the dipole trap for alignment purposes.

The dielectric mirror chosen (*CVI Melles Griot FLM-1550-45-P*) has greater than 99% reflectivity for 45° incidence. This, however, still leaves a significant amount

of power being transmitted by each optic and care must be taken to block each of these transmissions. In certain situations, however, this feature was extremely useful. Firstly, a photodiode was placed on the leak-through power through one of the mirrors; this was used to monitor the beam power. The voltage output on the photodiode was calibrated with a power meter. This avoided the difficulty, and danger, involved with continually measuring a high-power laser beam. Secondly, as the focussing lens was before the final steering mirror, the leak-through beam came to a focus behind the mirror. A CCD camera, with a fluorescent coating to enhance the sensitivity in the infra-red range (*Laser Physics* CamIR¹⁵⁵⁰), was placed at a position conjugate to that of the MOT behind the mirror, in order to measure the beam waist as seen by the atoms. The CCD image was extracted using frame-grabbing software and analyzed in real time using *Matlab*. The image was first adjusted to take the non-linearity of the fluorescent coating into account⁸ and then fitted with a gaussian to extract the beam waist. A minimum beam waist of $70 \pm 2 \mu\text{m}$ was found, which is close to the limit of $66 \mu\text{m}$ calculated using gaussian beam propagation above. A fit of the beam waist is shown in the inset of Figure 5.7.

5.5 MOT alignment and characterization

In order to achieve the best MOT for the experiment, several parameters must be optimized including beam alignment, magnetic field gradient, detuning and magnetic field compensation. Ultimately these parameters are simply optimized to give

⁸Signal \propto input power^{1.41}

the largest number of atoms in the MOT; details of how to calculate this number are given in Section 5.5.2. However, to avoid getting stuck in a local maximum, it is important to carefully align the MOT first so that the parameters are approximately correct before optimization. Details of this alignment procedure are given in Section 5.5.1.

5.5.1 MOT alignment

As the magnetic coils are set into the re-entrant flanges (see 5.3) the centre of the magnetic field gradient is located at the centre of the vacuum chamber. Hence we must also align the MOT laser beams to intersect in the middle of the chamber. This was achieved by placing targets on the viewports and ensuring that each beam struck the centre of both viewports that it passed through. The power in the counter-propagating pairs was adjusted such that opposing beams had equal power, this was done with a power meter.

The fluorescence from the MOT was imaged in all three dimensions by a pair of CCD cameras at 90° to each other. Once the above alignment had been performed, and a moderate field gradient (~ 15 G/cm) applied, the MOT was visible on these cameras. The alignment of the beams was tweaked to give maximum brightness and roundness of the cloud.

Next the stray magnetic fields had to be nulled using the three pairs of Helmholtz coils around the vacuum chamber. The current in the coils was approximately set using a gaussmeter, however, due to the size of the vacuum chamber, it was

impossible to get the head close to the MOT. Hence this had to be optimized *in situ* by observing the atoms. The expansion of the cloud as the magnetic field gradient was turned off was observed on the CCD cameras. In the absence of a magnetic field gradient, the cloud should expand uniformly in all directions, however, stray magnetic fields cause the atoms to move towards the new magnetic minimum. Hence the stray fields were compensated by adjusting the compensation coils for uniform expansion.

5.5.2 MOT characterization

The number of atoms in the MOT can be characterized either by imaging the fluorescence onto a photodiode, or by measuring the absorption of a weak, resonant probe beam. For a MOT, either technique is applicable and each gives similar results, with absorption imaging having the added bonus of spatial resolution, but the disadvantage of having to switch the MOT off for the measurements — *i.e.* fluorescence can be monitored in real-time while absorption imaging is a destructive measurement. For smaller, denser samples such as in a magnetic or dipole trap, illumination by the MOT lasers would destroy the sample so absorption imaging is preferable. The two techniques are discussed below.

Fluorescence measurements

As shown in Section 2.3.1, the MOT scatters photons at a rate:

$$R_{scatt} = N \frac{\Gamma}{2} \frac{I/I_{sat}}{1 + I/I_{sat} + 4\delta^2/\Gamma^2}, \quad (5.4)$$

where N is the number of atoms in the MOT, and all other parameters are as defined in equation (2.17). The intensity, I , was taken to be the sum of the peak intensities of all 6 MOT beams.

The power, P , incident on the photodiode can be inferred from the voltage output, V , load resistance, R , and responsivity ρ . The detection rate, R_{det} , can be derived by dividing the power by the photon energy, E_γ :

$$R_{det} = \frac{P}{E_\gamma} = \frac{V}{\rho R} \frac{\lambda}{hc}. \quad (5.5)$$

The MOT was imaged onto a photodiode by a lens of diameter, d , a distance, D , from the MOT, hence the solid angle seen by the photodiode is:

$$\eta = \frac{\pi(d/2)^2}{4\pi D^2} = \left(\frac{d}{4D}\right)^2. \quad (5.6)$$

Hence, the total number of scattered photons is, $\frac{R_{det}}{\eta}$, and therefore the number of atoms in the MOT is;

$$N = \frac{R_{det}}{\eta R_{scatt}}. \quad (5.7)$$

Applying typical experimental parameters to the above formulae suggests around 7×10^7 atoms in the MOT.

Absorption imaging

A weak probe beam (peak intensity 0.35 mW/cm^2) resonant with the $F = 2 \rightarrow F = 3$ transition was used for absorption imaging. The probe beam was pulsed on for $200 \mu\text{s}$ at a time and was imaged onto a CCD camera (*Sumix SMX-150M*). The probe beam images only atoms in $F = 2$; in order to image atoms in $F = 1$, the repumper was switched on $100 \mu\text{s}$ before the probe.

A 780 nm bandpass filter was placed in front of the camera to eliminate room lights. Also, the camera was triggered by the control software such that the image was only recorded whilst the probe was on; these measures eliminated almost all background from the images. In an imaging sequence first any trapping lasers are turned off then, three images are taken;

1. Image of the probe beam with the atoms; I_{at} .
2. 100 ms later, the atoms have dispersed and an image of the probe beam is taken without any absorption; I_{bg} .
3. Next a background image is taken with the probe beam off; I_{dark} .

The optical density at pixel (i, j) is then calculated as;

$$D_{i,j} = -\ln \left(\frac{I_{at} - I_{dark}}{I_{bg} - I_{dark}} \right). \quad (5.8)$$

Figure 5.8 shows a typical absorption image of a MOT along with the background image and the pixel-by-pixel optical density.

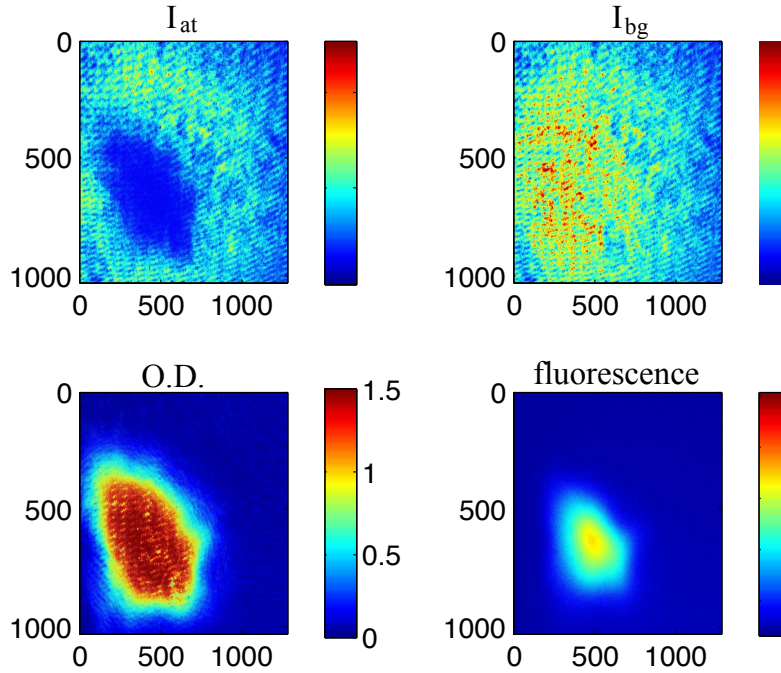


Figure 5.8 Absorption imaging. The optical density, **O.D.** at each pixel is obtained by the log of the ratio of the absorption image, \mathbf{I}_{at} , to the background, \mathbf{I}_{bg} , with a dark image (not shown) subtracted from each. For comparison, the fluorescence signal is also shown.

The pixel size of the SMX-150M is $6.7 \mu\text{m}$ giving an area of $A = 44.9 \mu\text{m}^2$. However, the magnification of the imaging system is 1:1.4, so the effective pixel area is $A' = 23 \mu\text{m}^2$. Hence, the number of atoms in the picture is obtained by numerically integrating the optical density over the image and dividing by the scattering cross-section;

$$N = \frac{A'}{\sigma_0} \sum_{i,j} D_{i,j}. \quad (5.9)$$

Typically, this gave MOT atom numbers of around 9×10^7 , which is in good agreement with the fluorescence measurements.

To confirm that the probe intensity and frequency were appropriately set, the detuning was scanned and the number of atoms calculated at each detuning. The resulting spectrum is shown in Figure 5.9. A Lorentzian fit of the data shows a FWHM of 6.42 MHz, in good agreement with the natural linewidth, suggesting that power broadening was not present. An offset of 1.3 MHz, suggested a miscalibration of the AOM frequency in the Labview code. This was rectified and the resonant frequency used for subsequent measurements.

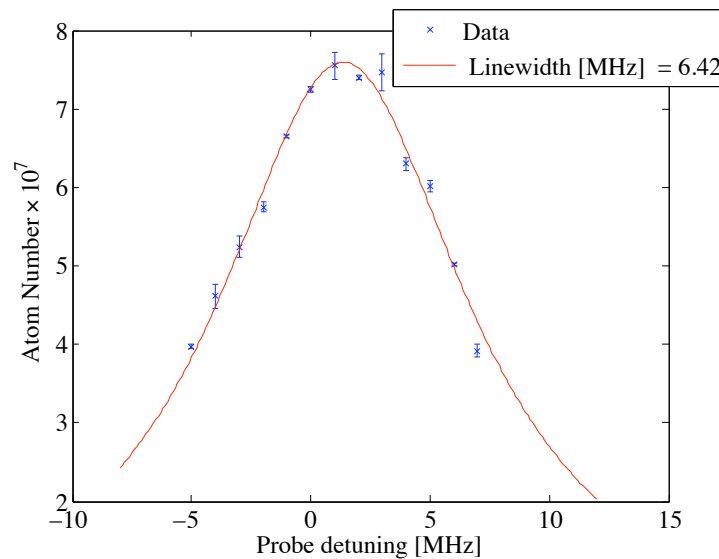


Figure 5.9 Spectrum of the Probe laser shown with a Lorentzian fit of FWHM 6.42 MHz and offset 1.3 MHz.

5.5.3 TOF temperature measurement

The temperature of the cloud can be measured by observing the expansion of the cloud after being released from the MOT. The MOT lasers and magnetic field are switched off at time zero and the cloud is free to expand for a time, τ , after which it is probed by absorption imaging. The cloud's diameter, σ_x is calculated by fitting a gaussian to the absorption image. By measuring the expansion in the cloud from initial, $\sigma_x(0)$, to final, $\sigma_x(\tau)$, size, the temperature can be calculated^[144];

$$\sigma_x^2(\tau) = \sigma_x^2(0) + \frac{k_B T}{m} \tau^2. \quad (5.10)$$

If we measure $\sigma_x(\tau)$ at several different times then fit the resulting points with a model based on (5.10) then we can make a good estimation of the temperature of the cloud. See Figure 5.10 for an example; in this instance the temperature of an optical molasses was measured to be $85 \mu\text{K}$.

If the probe laser is switched on only $20 \mu\text{s}$ ⁹ after the MOT is released then we can measure $\sigma_x(0)$. We can then make a second measurement of the size of the cloud ($\sigma_x(\tau)$) at a large τ ¹⁰ and estimate the temperature using only these two measurements. This is a cruder method for temperature estimation than fitting an entire curve, but requires far fewer measurements making it easy to make several temperature measurements successively. This is useful, for example, when optimizing the experimental sequence.

⁹The minimum time resolution of the FPGA board

¹⁰Typically $\tau = 20 \text{ms}$ was used

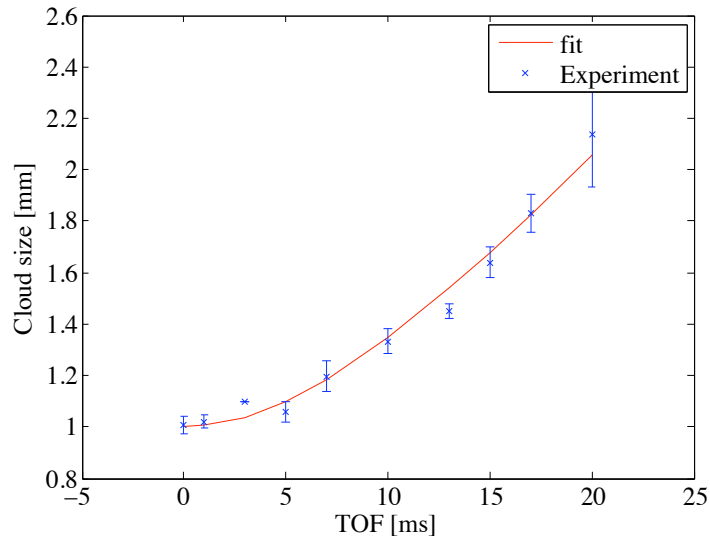


Figure 5.10 Time-of-flight temperature measurement of the optical molasses phase. The fit based on equation (5.10) indicates a temperature of $85 \mu\text{K}$.

5.6 Experimental sequence

The hybrid magnetic-optical trap is a technique that was proposed by Comparat *et al.*^[145] and experimentally demonstrated by the Porto group at NIST, Maryland, to form BECs in ^{87}Rb ^[136]. This technique has been subsequently used to load a crossed dipole trap for a dual-species BEC of ^{87}Rb and ^{133}Cs ^[146]. While BEC was not the aim of this experiment, the relative simplicity of this novel scheme was attractive and hence it was chosen as the method for increasing the density of the sample. The scheme is outlined in the paragraph below before the subsequent sections (5.6.1–5.6.6) describe each step of the loading process in detail.

To load the dipole trap, we initially collect ultracold atoms in the MOT; the density of the MOT is then transiently increased by increasing the field gradient in

a compressed MOT (cMOT) stage. We then enter an optical molasses stage in which the magnetic field gradient is switched off and the atoms undergo polarization gradient cooling (see Figure 2.9). The magnetic field gradient is then rapidly increased to trap the atoms in a magnetic trap. Once the atoms are in the magnetic trap, the dipole trapping beam is switched on and the magnetic field slowly ramped down to the value required to simply levitate the atoms. At this point the atoms are radially confined by the tight focus of the dipole trap beam but, whereas a dipole trap is usually loose in the axial direction, the hybrid trap retains a tight axial geometry due to the residual magnetic field.

5.6.1 MOT

The MOT was roughly optimized as described above (5.5.2), then the detuning of the master laser and the current through the magnetic coils were optimized. The optimization plots are shown in Figure 5.11. A detuning of -12 MHz was chosen and a current of 15 A, corresponding to a field gradient of 10.8 G/cm, proved optimal.

The number of atoms was typically $5 - 8 \times 10^7$. The temperature was measured to be 346 μ K using the time-of-flight (TOF) method, as shown in Figure 5.12.

5.6.2 Compressed MOT

An initial magnetic trapping sequence was programmed into the FPGA with 20 ms of cMOT and 20 ms of optical molasses preceding a rapid switch-on of the magnetic trap to 80 A. This was sufficient to trap $\sim 5 \times 10^6$ atoms in the magnetic trap. The

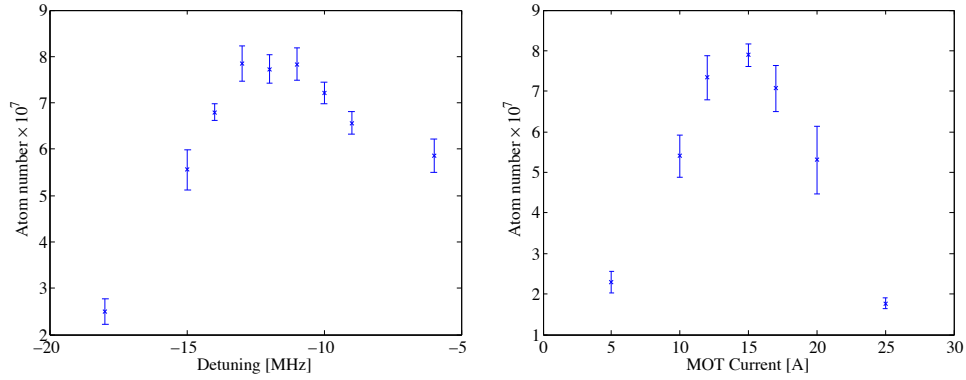


Figure 5.11 Optimization of the detuning and current for the MOT.

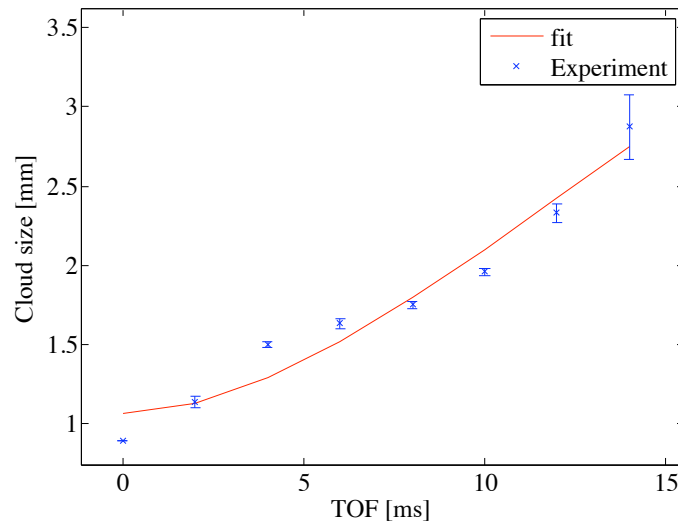


Figure 5.12 Time-of-flight temperature measurement of the MOT. The fit indicates a temperature of $346 \mu\text{K}$.

duration and current of the cMOT stage were optimized with the figure of merit being the number of atoms loaded into the magnetic trap. The optimization graphs are shown in Figure 5.13. A time of 35 ms was chosen along with a current of 30 A,

corresponding to a magnetic field gradient of 21.6 G/cm.

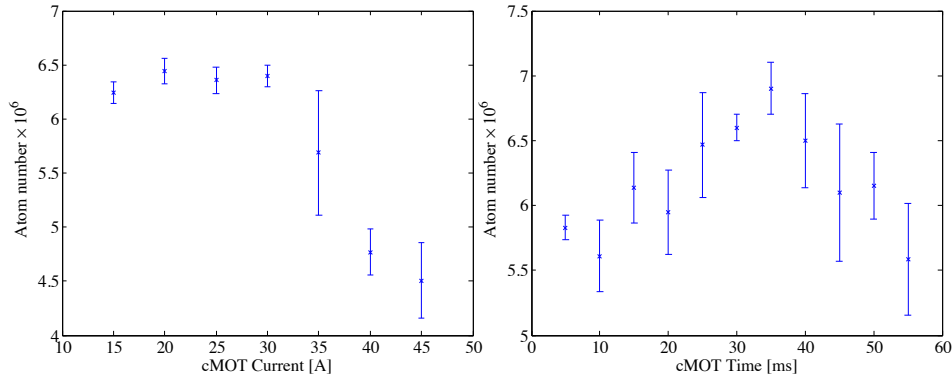


Figure 5.13 Optimization of the duration and current for the cMOT.

5.6.3 Optical molasses

While the importance of an optical molasses phase for sub-Doppler cooling was made clear in Section 2.3, in this scheme the optical molasses is also essential for the fast switch-on of the magnetic trap. As discussed in Section 5.3.1, the response of the current to changes in the setpoint of the PSU is slow. Hence we must close the MOSFETs and overload the PSU current before opening the MOSFETs to achieve a rapid switch-on. While the MOSFETs are closed we are, by necessity, in an optical molasses phase.

As shown in equation (2.23), the final temperature achievable by Sisyphus cooling in an optical molasses is inversely proportional to the detuning. Hence the maximum detuning possible with the AOM driver — -60 MHz — was used for the molasses

phase. Initially a time of 20 ms was chosen as this was shown to be the minimum time required to overload the PSU before switch-on. If the molasses phase was any shorter than this then the switch-on speed of the magnetic trap would be compromised. The temperature of the molasses was shown to be $50\ \mu\text{K}$ using the TOF method (Figure 5.14).

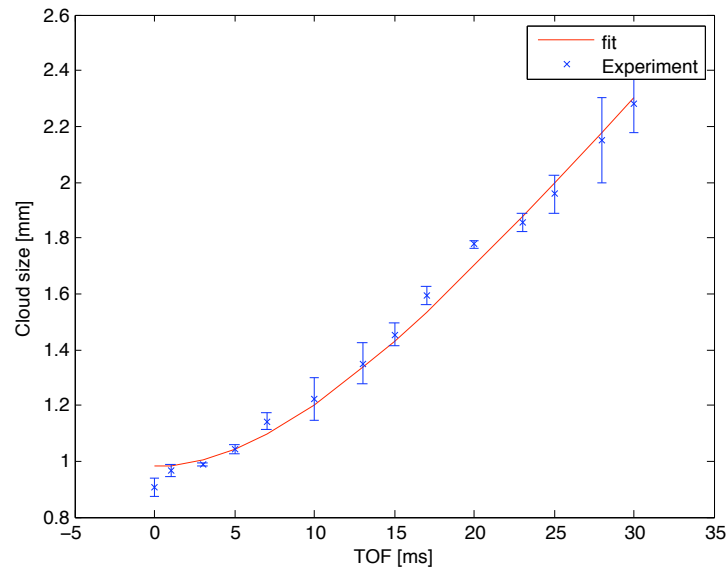


Figure 5.14 Time-of-flight temperature measurement of the Optical molasses phase. The duration was 20 ms and the detuning -60 MHz. The fit indicates a temperature of $50\ \mu\text{K}$.

In order to estimate the effect of changing the duration of this molasses phase, the size of the cloud was measured with $20\ \mu\text{s}$ and 20 ms of TOF expansion at a range of molasses durations. The temperature was estimated by applying the resulting cloud sizes to equation (5.10). The resulting temperature estimates (Figure 5.15) seem to suggest an optimal molasses time of 50 ms so this was chosen. To confirm this choice a full TOF measurement of the temperature was made (Figure 5.16), which

indicated that the molasses temperature had reduced to $30\ \mu\text{K}$.

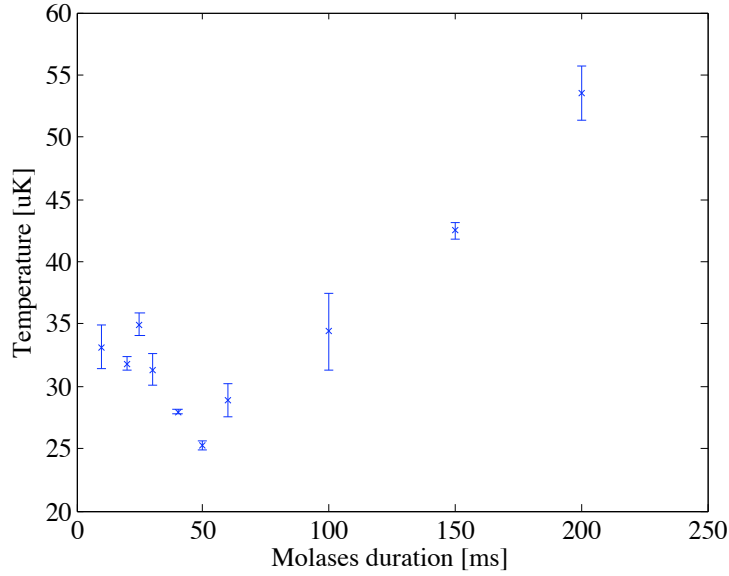


Figure 5.15 Estimation of the temperature at a range of molasses durations, indicating a minimum temperature at 50 ms duration.

As we see in equation (2.23), the final temperature of the molasses phase is proportional to $\frac{I}{\delta}$. In order to confirm that the molasses was operating as expected, the detuning of the master laser was scanned. The temperature after 50 ms of molasses was estimated at each detuning. The power of the laser changed with the detuning, therefore the estimated temperature was plotted against the ratio, $\frac{P}{\delta}$. The resulting graph is shown in Figure 5.17. While the relationship is not quite linear, a clear dependence on detuning is shown, confirming the decision to use the largest possible detuning.

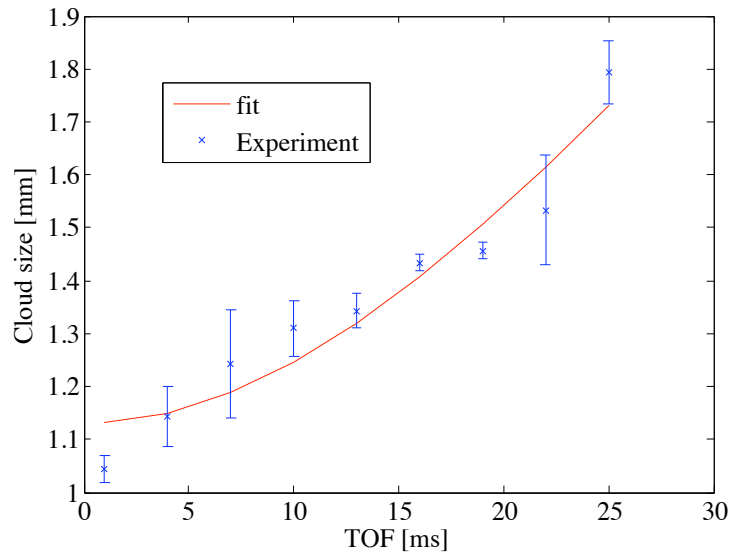


Figure 5.16 Time-of-flight temperature measurement of the Optical molasses phase after optimization of the duration. The duration was 50 ms and the detuning -60 MHz. The fit indicates a temperature of $30 \mu\text{K}$.

5.6.4 Transfer of atoms into $F = 1$

For the final 2 ms of the molasses phase the repumping light was switched off leading to a so-called *dark molasses*. During this time, the atoms were pumped into the lower, $F = 1$, hyperfine state. The efficiency of this process was measured by performing absorption imaging on the cloud both with and without the repumper. With the repumper present, all atoms were pumped into $F = 2$ and are visible in the absorption image. Without the repumper, only those atoms remaining in $F = 2$ after the dark molasses were visible, hence we measure the efficiency of the pumping into $F = 1$ to be over 95%.

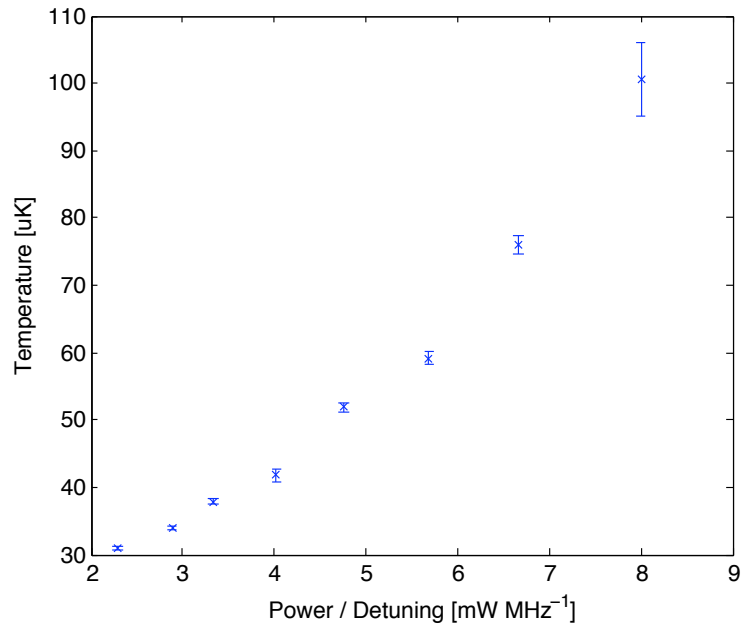


Figure 5.17 The effect of detuning on the final temperature of the optical molasses. Because the power of the laser is dependent on its detuning the temperature is plotted against $\frac{P}{\delta}$.

5.6.5 Magnetic trap

The required magnetic field gradient for the magnetic trap was crudely estimated by equating the depth, ΔU , of the magnetic trap at the edge of the MOT (radius R_{MOT}) to the average energy of an atom in the trap, $k_B T$. This model is sketched out in Figure 5.18. As we can see from (2.31); $\Delta U = g_F \mu_B m_F |B|$. Assuming that the MOT is centered at the minimum of the field gradient, B' , then the magnetic field at the edge of the MOT is $B = B' R_{MOT}$. Equating the trap depth to the

temperature, T_{MOT} , we get;

$$g_F \mu_B m_F B' R_{MOT} = k_B T_{MOT}, \quad (5.11)$$

$$B' = \frac{k_B T_{MOT}}{g_F \mu_B m_F R_{MOT}}. \quad (5.12)$$

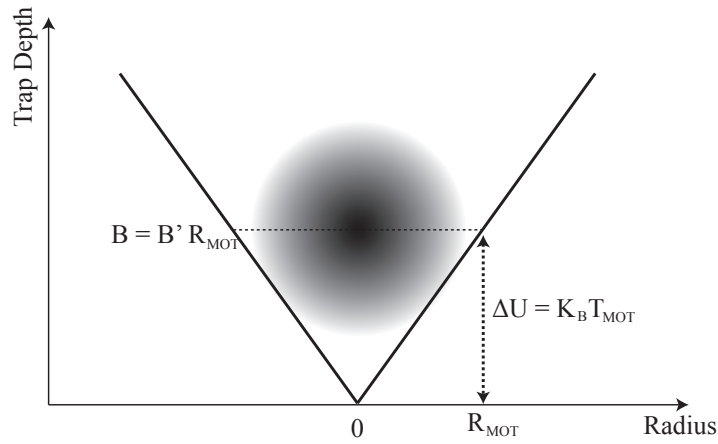


Figure 5.18 Estimation of the magnetic field gradient required for the magnetic trap. The trap depth, ΔU , is equated to the temperature of the MOT, T_{MOT} , at the radius of the mot, R_{MOT} .

A cloud with temperature $100 \mu\text{K}$ and diameter 1 mm was assumed. With $g_f = 1/2$ and, assuming we trap in $F = 1$, this calculation implies a field gradient of 60 G/cm . In our geometry, this corresponds to a current of around 80 A , so this was initially tried. Using this current around 7×10^6 atoms were trapped in the magnetic trap.

The current of the magnetic trap was scanned in order to maximize the number of atoms trapped. The resulting graph is shown in Figure 5.19. This implies an optimal current of 70 A corresponding to 50.4 G/cm . This suggests that, despite

its simplicity, the estimation was reasonably accurate. Using this current, around 1×10^7 atoms were trapped in the magnetic trap.

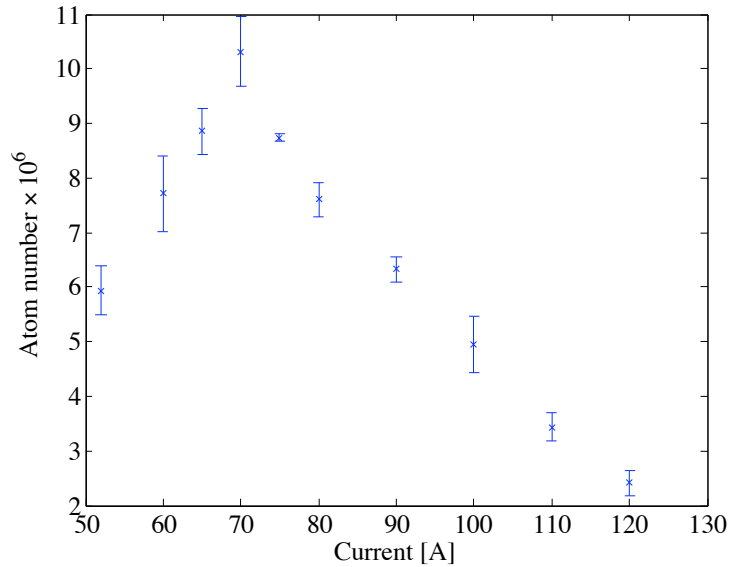


Figure 5.19 Optimization of the magnetic field gradient for the magnetic trap. A current of 70 A (corresponding to 50.4 G/cm) was chosen.

Following concerns over the failure of the LIAD mechanism, it was important to check the lifetime of the magnetic trap. This gives us an indication of the pressure in the chamber which, critically, determines whether evaporation techniques can be used to increase the density of the sample. The number of atoms in the magnetic trap was measured as a function of the hold time and a decaying exponential fit was applied, see Figure 5.20. This fit implied a $1/e$ lifetime of 860 ± 35 ms. Unfortunately, it was clear that this would most likely not be sufficient to perform evaporative cooling techniques as these require slow ramps to allow rethermalization of the atoms. By comparison, the quadrupole trap used in reference^[136] had a lifetime of around

100 s.

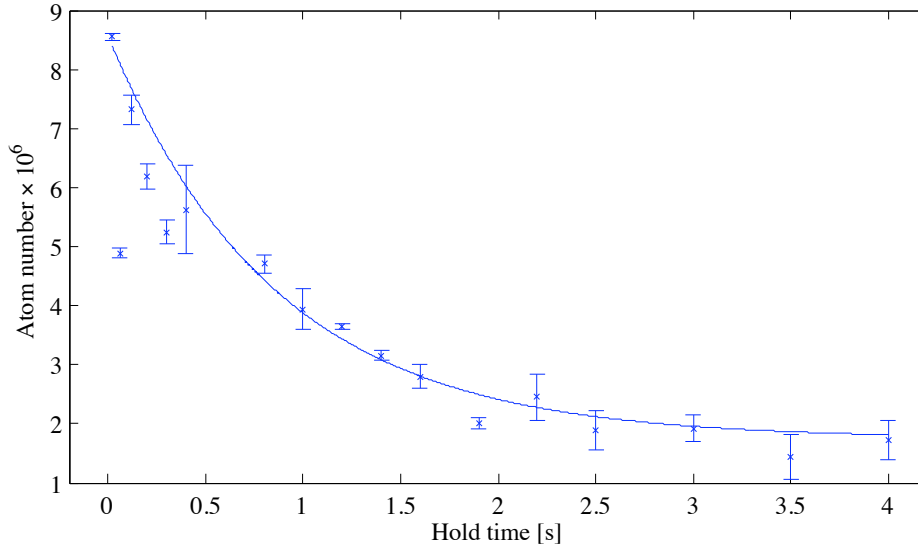


Figure 5.20 Measurement of the trapping lifetime in the magnetic trap. The fit indicates a $1/e$ lifetime of 860 ± 35 ms.

Despite the poor vacuum performance, the decision was taken to continue with the dipole trapping scheme. Improving the vacuum quality would have required a major over-haul of the apparatus most likely to incorporate a double-chamber scheme. This would have required the purchasing and assembling a new vacuum system, as well as potentially more lasers. The time and funds to do this were not available. The poor vacuum pressure precluded evaporative cooling but the formation of a hybrid optical and magnetic trap should still be possible. This apparatus was expected to have significant advantages over a MOT for photoassociation experiments.

5.6.6 Dipole trap

The dipole trap laser was prepared, and focussed to $70\ \mu\text{m}$, as discussed in Section 5.4.3. First the dipole trap laser was overlapped with the re-directed probe beam (hence forth referred to as the *pushing beam*). The pushing beam, being at $780\ \text{nm}$, is much easier to align as it is resonant with the atoms and can easily be seen by conventional CCD cameras and infra-red viewers.

Coarse alignment of the pushing beam was performed with the lenses out. A CCD camera was placed behind the vacuum chamber such that both the MOT and the pushing beam could be imaged. Using this technique, the beam was aligned to the MOT. The MOT was also imaged at an angle orthogonal to the pushing beam so, when the pushing beam was well aligned, distortion of the MOT was obvious. The lenses were then inserted into the beam. To avoid dangerous back-reflections and to preserve the quality of the focus, great care was taken to ensure that the beam passed through the centre of each lens. Once the focussing lens was in, the effect of the pushing beam on the MOT was obvious; a dark stripe was observed where atoms were being pushed out of the trap. This stripe was aligned to the centre of the MOT by moving the final steering mirror.

The origin of the dipole force is the AC stark shift on the atomic energy levels. Hence, in the presence of the dipole trap laser, the cooling and repumping lasers are no longer at the correct frequency. Hence atoms in the region of the dipole trap do not scatter as much light and appear to be dark on a fluorescence image. While this effect is not as obvious as the pushing beam, it is still sufficient to align the dipole

trap beam to the centre of the MOT; see Figure 5.21.

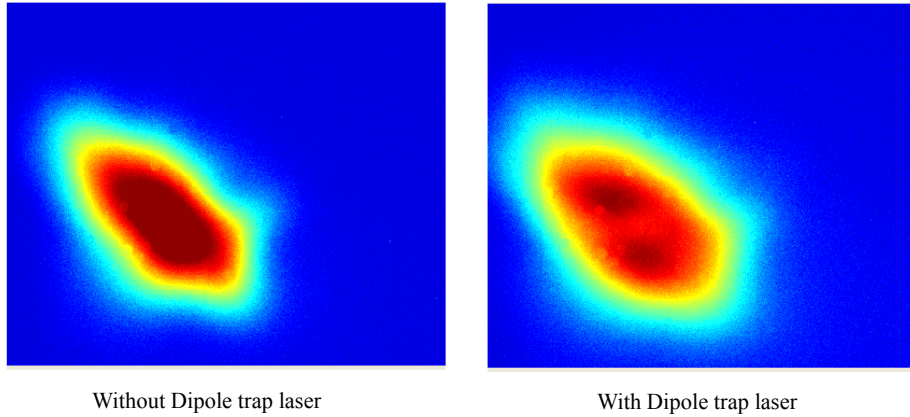


Figure 5.21 The effect of the stark shift induced by the dipole trap on fluorescence imaging of the MOT. The stripe in the image on the right is indicative of the presence of the dipole trap laser.

This effect is also seen during absorption imaging as the absorption is highly sensitive to the resonance frequency. This is shown in Figure 5.22. This technique was used to align the dipole beam to the magnetic trap. While this effect is more sensitive than looking at the fluorescence from the MOT, a magnetic trap is loaded only every 8 seconds, hence the alignment process is slow. Therefore it is prudent to align the dipole trap in stages; first with the pushing beam, then the fluorescence imaging in the MOT, before finally using the absorption image to align to the magnetic trap.

Once this alignment procedure had been performed, we were ready to perform the dipole trap procedure. A magnetic trap was loaded and, simultaneously, the dipole trap beam was switched on. The magnetic field gradient was then reduced from 50.4 G/cm (70 A) to 28.8 G/cm (40 A). As the cloud expands and falls, some

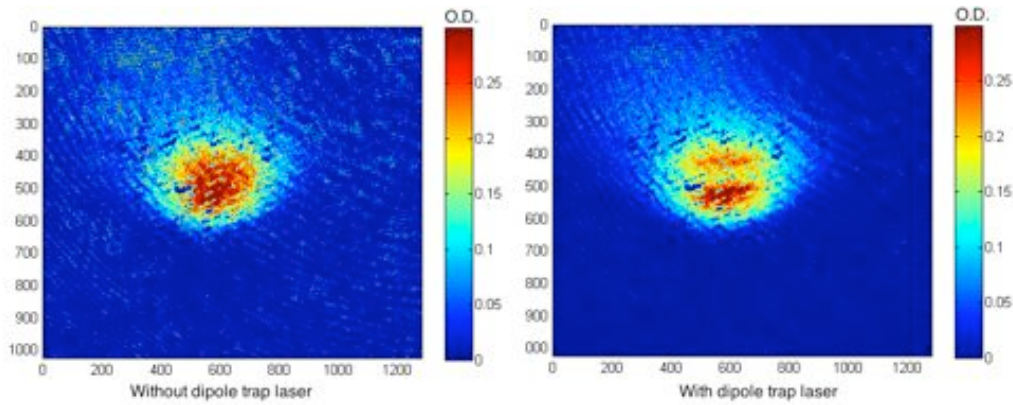


Figure 5.22 The effect of the Stark shift on absorption imaging of the magnetic trap. The colour chart indicates the optical density (O.D.).

atoms remain held in the dipole trap. Figure 5.23(a) shows one of the first observed dipole traps in this system. The absorption image was taken 80 ms after the magnetic trap was released. We can see a long thin dipole trap containing the trapped atoms, with the remnants of the un-trapped atoms falling away below. As we can see, the atoms appear to be ‘pouring’ out of the trap to the right, this is because the axial position of the focus of the dipole trap does not co-incide with the centre of the magnetic field gradient, hence the atoms, which initially reside at the centre of the field gradient, are drawn towards the focus of the laser. This is a similar effect to that which is deliberately used to create atom-lasers^[147].

The position of the focus was adjusted to overlap with the quadrupole field and the ‘atom-laser’ effect disappeared. A sequence of images showing the atoms falling out of the magnetic trap and remaining in the dipole trap is shown in Figure 5.24.

Rather than simply switch the field gradient down, we could slowly ramp it to

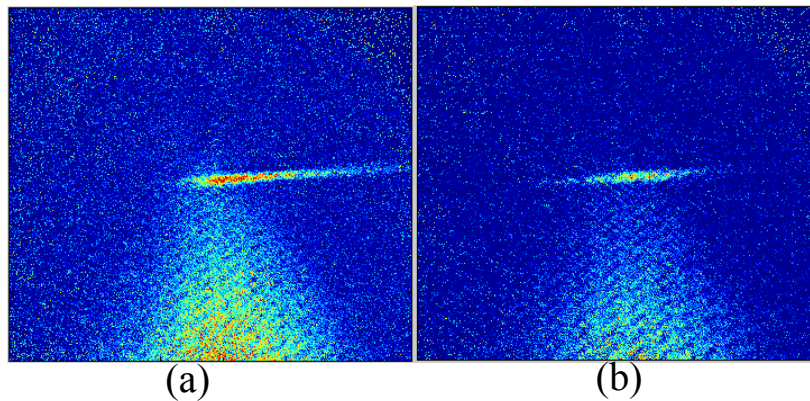


Figure 5.23 (a) One of the first dipole trap images observed in this setup; we can see atoms 'pouring' out of the trap to the right, this is because the focus of the dipole trap does not co-incide with the centre of the magnetic field gradient. (b) The focal position is adjusted to overlap with the quadrupole, hence the atoms remain in the trap. The diffuse clouds of atoms beneath the dipole trap in each picture are the un-trapped atoms falling out of the magnetic trap.

allow more time for the atoms to fall thorough the dipole trap. To test this a series of linear ramps were applied after the magnetic trapping phase. The ramps started at 50.4 and went down to 28.8 G/cm over a variable ramp time, τ_{ramp} . The atoms were then held for a time, τ_{hold} to allow the magnetically trapped atoms to fall away, before being imaged. The atom number for each ramp duration was calculated and plotted in Figure 5.25. In order to eliminate any lifetime effects from this data, the total time, $\tau_{ramp} + \tau_{hold}$, was kept constant at 300 ms. As we can see a maximum appears at $\tau_{ramp} = 70$ ms so this was chosen.

Following this optimization, an important discovery was made. While monitoring the power on the calibrated photodiode, it was noticed that the laser power during the sequence (while the AOM was being pulsed on and off) was only 13 W, compared to 24 W when optimized in steady state. Instead, the AOM alignment was optimized

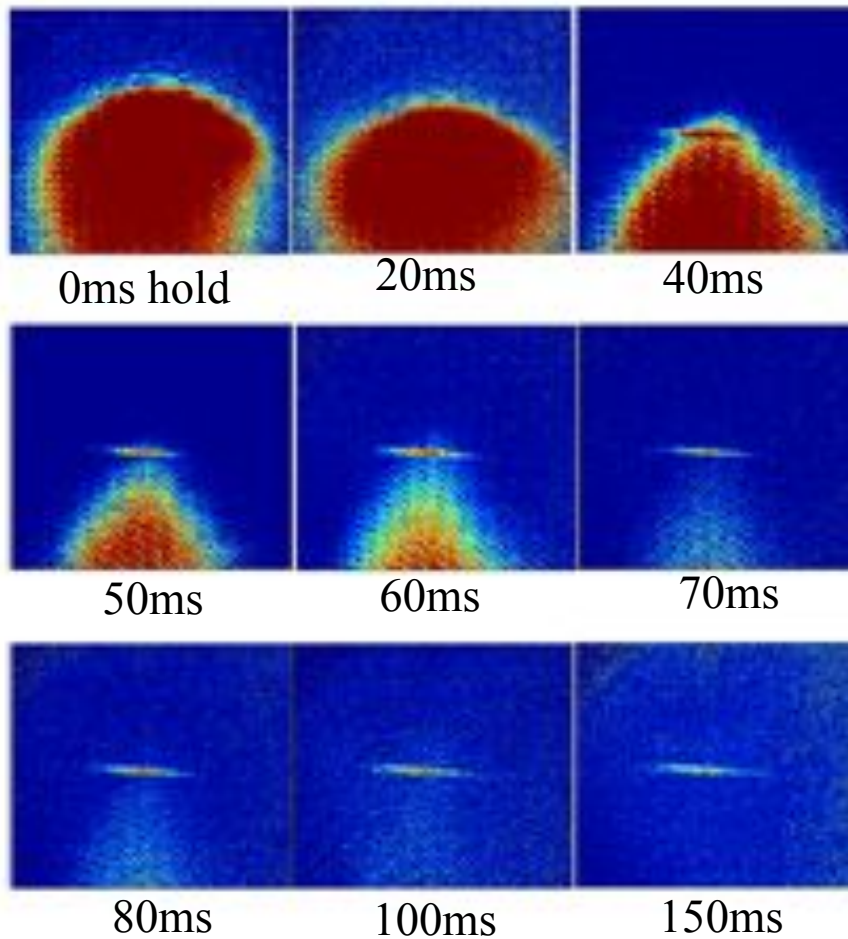


Figure 5.24 A sequence of images showing atoms falling out of the magnetic trap and remaining in the dipole trap. The hold time indicates the time elapsed since the field gradient was reduced to 28.8 G/cm.

while being pulsed to simulate experimental conditions. This utilized the full 24 W for use in the dipole trap. The result was a marked increase in trap number from 8×10^4 to 1.5×10^5 .

Intuitively one would think that maximum dipole trap loading efficiency would occur when the dipole trap strikes the centre of the magnetic trap, as this is where

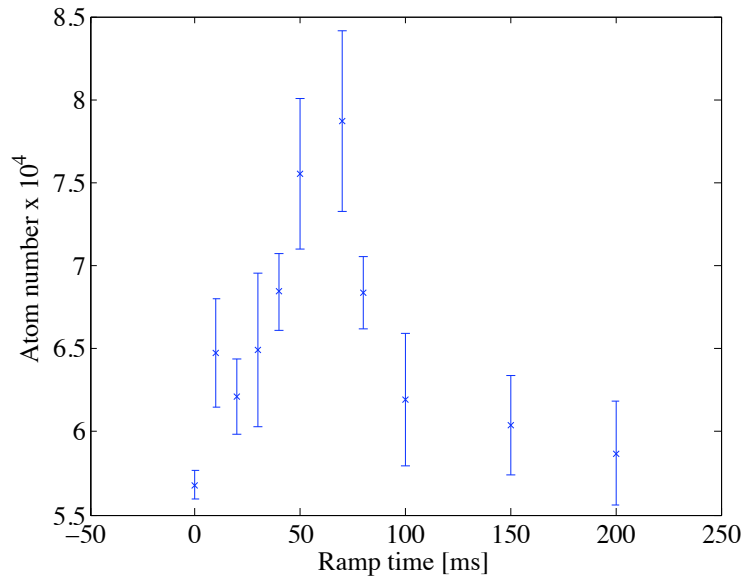


Figure 5.25 Optimization of the ramp time in the dipole trap loading. The magnetic trap was ramped from 50.4 G/cm to 28.8 G/cm over the ramp time before being held. The Dipole trap was imaged 300 ms after the beginning of the ramp.

the atomic density is highest. However, we must also consider that the position of the dipole trap within the magnetic quadrupole affects the tightness of the trapping potential in the axial direction and hence the volume of the trap. Also, as atoms fall out of the magnetic trap through the dipole trap, they may also be trapped, so perhaps a position below the centre would be optimal. To test this, the vertical position of the trap was scanned and the final trap number measured; this is compared with the magnetic trap profile in Figure 5.26. This indicates that optimal loading of the trap occurs when the dipole trap is located around $100 \mu\text{m}$ below the centre of the magnetic trap.

The absorption image of the dipole trap was fitted with a pair of gaussian func-

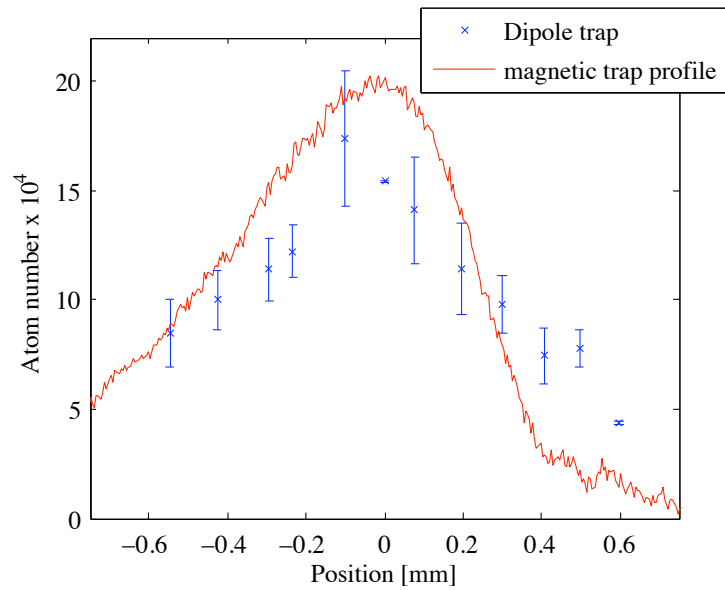


Figure 5.26 Optimization of the vertical position of the dipole trap. For comparison, the vertical profile of the magnetic trap is also plotted indicating that the maximum dipole trap loading occurs when the beam is located slightly below the magnetic trap maximum.

tions to measure its vertical ($64.2 \mu\text{m}$) and horizontal ($448 \mu\text{m}$) size; see Figure 5.27.

We must also consider that the dipole trap is not orthogonal to the probe beam, in fact the angle between the two is only 30° ; hence the true horizontal size of the dipole trap is $(448 \mu\text{m} / \sin 30^\circ) = 896.4 \mu\text{m}$. Assuming a radially symmetric profile, the dipole trap dimensions are therefore $(896 \times 64 \times 64) \mu\text{m}$, implying a peak density of $1.2 \times 10^{11} \text{ atoms/cm}^3$. This is a marked improvement on typical MOT densities of around $9 \times 10^9 \text{ atoms/cm}^3$, but orders of magnitude improvements could be made with evaporative cooling schemes; unfortunately the poor vacuum pressure precluded this.

Stage	Duration	Cooler	Repumper	Detuning	PSU [A]	PSU [V]	MOSFET [V]	Dipole trap	Probe
MOT	8 s	100%	100%	-12 MHz	15 A	2 V	10 V	0%	0%
cMOT	15 ms	100%	100%	-30 MHz	20 A	20 V	10 V	0%	0%
Molases	50 ms	100%	100%	-60 MHz	170 A	20 V	0 V	0%	0%
Dark molases	2 ms	100%	0%	-60 MHz	170 A	20 V	0 V	0%	0%
Overload	550 μ s	0%	0%	-12 MHz	170 A	20 V	10 V	100%	0%
'Catch'	20 ms	0%	0%	-12 MHz	70 A	6.35 V	2.97 V	100%	0%
Load Hybrid	70 ms	0%	0%	-12 MHz	70 \rightarrow 40 A	6.35 \rightarrow 4 V	10 V	100%	0%
Hold	100 ms	0%	0%	-12 MHz	40 A	4 V	10 V	100%	0%
TOF	200 μ s	0%	0%	-12 MHz	0 A	0 V	0 V	0%	0%
Repump	100 μ s	0%	100%	-12 MHz	0 A	0 V	0 V	0%	0%
Probe	200 μ s	0%	100%	-12 MHz	0 A	0 V	0 V	0%	100%

Table 5.2 A summary of the experimental procedure for loading the hybrid trap. The PSU [A (V)] columns correspond to the *setpoint* of the power supply rather than what is measured using the Hall sensor. MOSFET [V] is the gate voltage applied between gate and source of the first MOSFET bank.

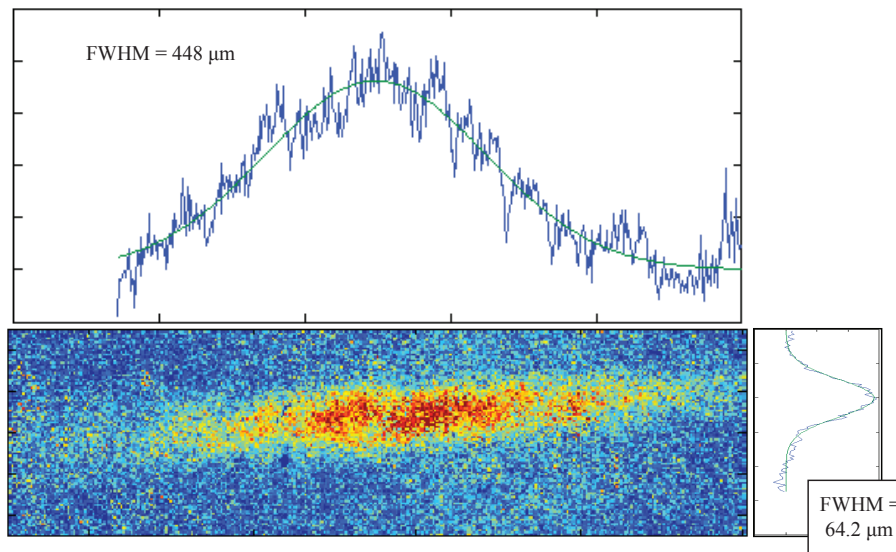


Figure 5.27 Horizontal and vertical fits of the dipole trap image indicating a vertical size of $64\ \mu\text{m}$ and horizontal of $448\ \mu\text{m}$ ($1/e^2$).

5.7 Time-of-flight mass spectrometer.

The time-of-flight (TOF) mass spectrometer was slightly modified for the new apparatus in order to improve the temporal focussing of the ion signal, and hence improve the signal to noise ratio. In 1955, Wiley and McLaren were able to demonstrate a high degree of temporal focussing by using a region of uniform electric field strength followed by a field-free drift region before the detector^[148]. The basic principle is that ions which are positioned closer to the detector arrive in the drift region sooner, but have been accelerated for less time hence are moving slower. Ions positioned further from the detector spend more time in the acceleration region, and hence arrive at the drift region later, but at greater speed. Hence, at some point in the drift region, we obtain temporal focussing. By moving the detector, we can achieve

minimal pulse duration, and hence the highest resolution. As it is often very hard to move the detector, Wiley & McLaren's scheme contained two acceleration regions, of different field strength. By adjusting the ratio of these two fields, the focussing can be adjusted to coincide with the detector.

The geometry of our chamber was the main constraint around which the the new TOF had to be designed. The MOT was situated around 22.5 cm away from the MCP detector. We first considered a basic design in which a single acceleration region is followed by a drift region. The situation was modeled, in one dimension, with the MOT and MCP kept fixed and a pair of grids either side of the MOT moved. The MOT was kept in the centre of the two grids. In the simulation, two molecular ions were placed 1 cm either side of the MOT to simulate an exaggerated spatial distribution of ions. The separation of the two grids was optimized such that the temporal arrival of the two ions coincided at the the MCP. This was found to be at a plate separation of 15 cm, *i.e.* when the second plate is exactly half way between the first plate and the MCP. This result was found to be universal, whatever pushing voltage or MOT–MCP distance was used. A plot showing the simulated trajectories of atomic and molecular ions in the TOF mass spectrometer is shown in Figure 5.28(a). The temporal focussing achieved in the optimized geometry is shown in Figure 5.28(b).

By a fortunate coincidence, the internal diameter of the vacuum chamber was 149.5 mm; hence the separation of the two grids was correct with the grids sat flush with the edge of the chamber. The central grid has to have a high transparency

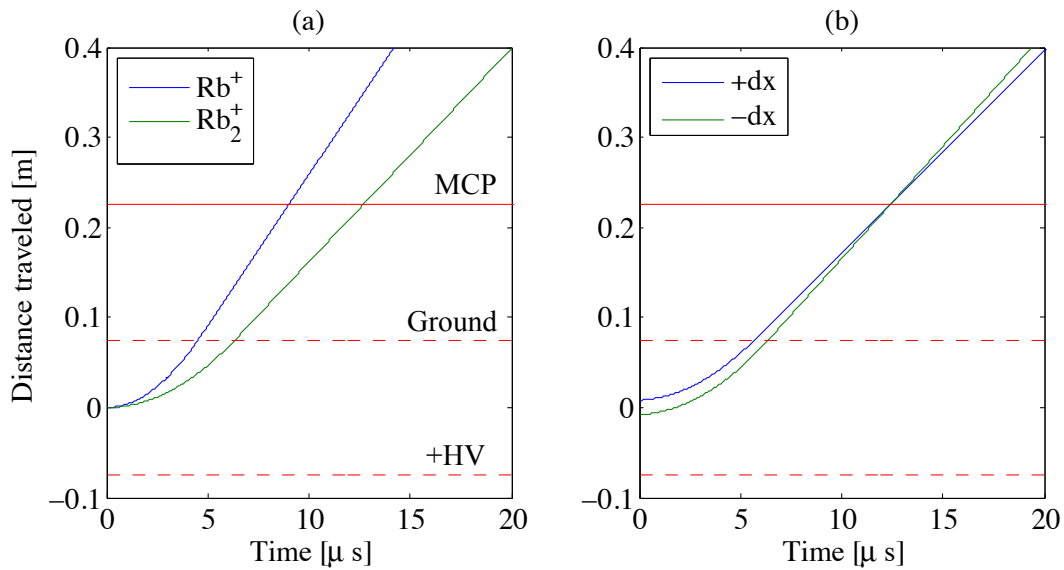


Figure 5.28 Simulation results of the Time-of-flight mass spectrometer consisting of two grids separated by 15 cm; the first at high voltage (+HV = 1 kV) and the other grounded. The MCP detector is placed 15 cm beyond the grounded grid. **(a)** Simulation of both atomic and molecular ions which are simultaneously ionized at time zero. Their temporal separation at the MCP is clearly apparent. **(b)** A pair of molecular ions, separated by 2 cm are simultaneously ionized. The geometry of the optimized system is such that their arrival times at the MCP detector coincide.

in order to allow as many ions through as possible, but also must have as many lines as possible to provide a uniform electric field. Therefore, a very fine stainless steel mesh was used (*Gantois tungsten mesh*, wire thickness: $30\ \mu\text{m}$, wire spacing: $475\ \mu\text{m}$.) This has a transparency of 87% and hence is suitable for the task. The mesh was held between two stainless steel plates (*Kimball Physics inc. SS-PL-B7x7-R750*) which are 1 inch \times 1 inch square with a 0.75 inch diameter clear hole in the middle. The plates were sandwiched together with the mesh in between, the mesh was then pulled tight and clamped at each corner with jewelry clamps. The edges of

the plates were then spot-welded together to hold the mesh, before the clamps were removed again. In order to avoid any chance of the mesh or plate touching the side of the chamber, the excess mesh was trimmed and the corners of the plates snipped as, otherwise, the plate came very close to the edge of the chamber. A photograph of one of the grids, before mounting, is shown in Figure 5.29. The high voltage grid was mounted via a stainless steel post onto a high-voltage feed-through (*Kurt J. Lesker* IFTMG042033). The other, grounded, grid was mounted on an aluminum cylinder which was clamped onto the inside of the chamber. A sketch of the position of the grids in the vacuum chamber is shown in Figure 5.30

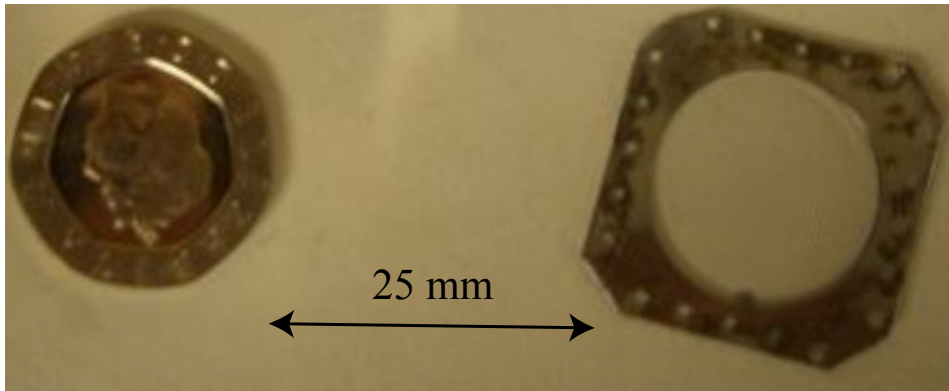


Figure 5.29 Photograph of one of the grids used in the Time-of-flight mass spectrometer. The fine mesh is sandwiched between a pair of stainless steel plates and spot-welded (see indentations in the metal) around the edges.

As an initial test, before attempting to do any ionization experiments in the dipole trap, the TOF was tested by simply ionizing the MOT as in Chapter 3. The CPA was focussed onto the MOT and, with a pushing voltage of 1 kV, the resultant atomic ions were observed on the MCP output. Immediately a problem

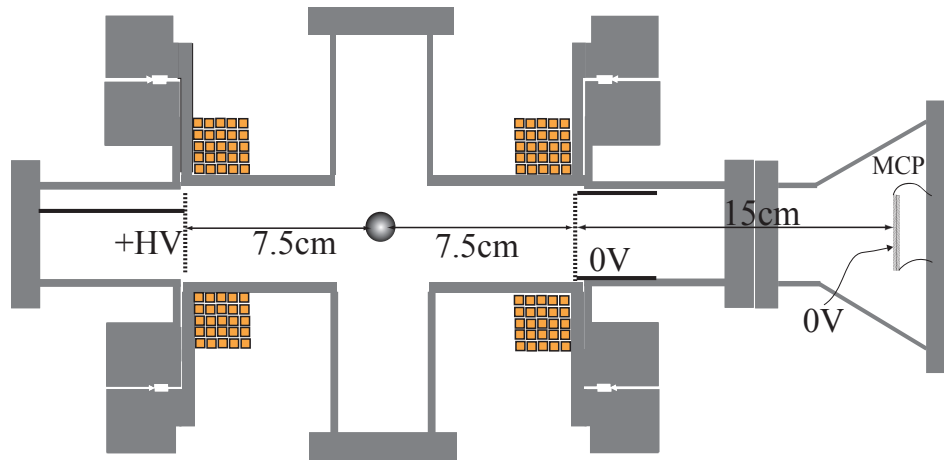


Figure 5.30 A schematic diagram of the TOF mass spectrometer in cross section through the vacuum chamber. An acceleration region is formed between two plates, one at positive high voltage (+HV) and the other grounded, placed 15 cm apart. A further drift region, also of length 15 cm follows the grounded grid, before ions are detected by the MCP. Note the close proximity of the high voltage grid to the grounded walls of the re-entrant flanges.

was observed; the arrival time of the ions ($69 \mu\text{s}$ after the pulse) was significantly higher than predicted by the modeling ($7.34 \mu\text{s}$). The pushing voltage was scanned, and this inconsistency remained, as is shown in Figure 5.31. All the parameters of the system (the voltage, the triggering *etc.*) were checked and double-checked but still this problem remained. Furthermore, the arrival times were significantly longer than those observed in a similar system in the old MOT.

It was postulated that this problem may be caused by the close proximity of the pushing grid to the walls of the chamber (see Figure 5.30). Because the walls are grounded, they cause distortions of the electric field lines and hence it can no longer be considered uniform throughout the acceleration region, as is assumed in

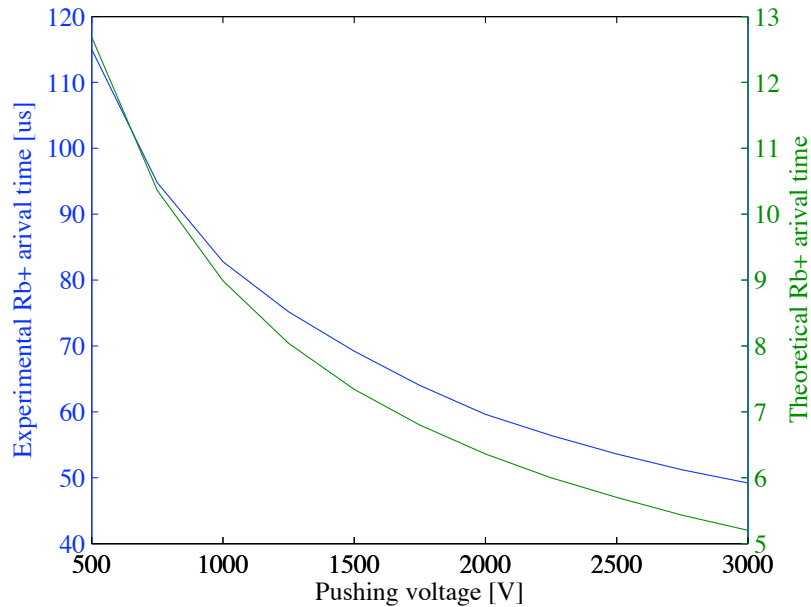


Figure 5.31 Comparison of theoretical and experimental behavior of the TOF. The calculated arrival time of atomic ions (green) is compared to the measured experimental value (blue). A large disparity is found between the two which is consistent at all pushing voltages.

the calculation. In order to test this, a pushing voltage of 3 kV (the largest available on the power supply) was pulsed on for a time after the arrival of the ionization pulse, the size and arrival time of the atomic ion signal as a function of the pulse duration are shown in Figure 5.32. It is interesting to note that increasing the pulse duration beyond $15 \mu\text{s}$ had no effect on the ion signal. The obvious conclusion from this is that the ions are no longer under the influence of the electric field after $15 \mu\text{s}$. It is possible that this represents the time that the ions pass by the grounded grid and that they are decelerated afterwards; however it is far more likely that the electric field lines are being distorted by the walls of the chamber hence the ions enter a quasi field-free region before passing the grid.

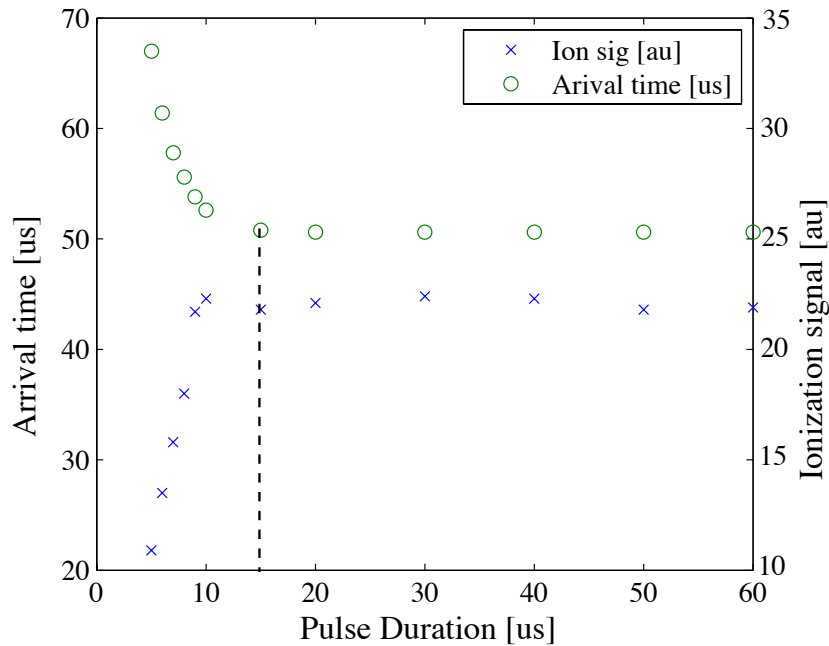


Figure 5.32 A pushing voltage of 3 kV is applied in short pulses. The size (x), and arrival time (o) of the ion signal is measured as a function of the pulse duration. We can see that, beyond $15 \mu\text{s}$ (dotted line), increasing the pulse duration has no effect on the ions.

As well as the long arrival time, it was also noted that the atomic ion signal was significantly lower than for comparable experimental parameters in the old MOT. This can also be explained when considered as part of the same problem; if ions take longer to arrive at the MCP then the cloud will spread out more. Hence the ions will miss the detector surface, hence reducing the signal. Despite these concerns, it was hoped that we may be able to see some molecular ions from the MOT. First, the dye laser was used, tuned to one of the resonances found in Section 4.1; this produced a barely distinguishable atomic signal and no molecular ions. However, it has been shown that ^{87}Rb MOTs do not produce as many background molecules as

those containing ^{85}Rb ^[57,112], so we may not expect to see molecules here anyway. Instead the pump-probe experiment was re-visited; here a step in the atomic signal was visible as we switched from pump-probe to probe-pump delays, but still no molecules were observed. Finally, the frequency of the trapping and repumping lasers were changed such that we could trap ^{85}Rb , and the dye laser was used for ionization, again to no avail. The unfortunate conclusion from this, is that the TOF spectrometer lacks the sensitivity to observe molecular signals.

Out of curiosity, ionization was attempted in the dipole trap using the pump-probe ionization system. The data taking process was slow due to the destructive effect that the excitation pulse had on the dipole trap and the low repetition rate of the re-loading process. Despite this, an observable atomic signal was formed which was dependent on the presence of the dipole beam.

5.8 Summary

In summary a new cold atom apparatus was constructed for the ultrafast photoassociation experiments. The number of atoms in the MOT was improved from 2×10^7 in the old apparatus to 8×10^7 . In addition the 6-beam MOT and improved experimental control facilitated the formation of a compressed MOT and optical molasses stages; these cooling techniques, which simply were not available in the old apparatus, have been fully characterized in the preceding chapter. Furthermore, magnetic and dipole-force traps have been implemented.

These techniques were designed to improve the density of the sample and, thereby,

reduce the internuclear separation of atom pairs in the ultrafast photoassociation experiments. While this was, in part, successful with the dipole trap exhibiting an order-of-magnitude higher density than the MOT, further increases using evaporative cooling were precluded by a poor vacuum pressure. Ionization experiments were performed in the new apparatus, however, despite the presence of an atomic ion signal, no molecular ions were observed. This can be attributed to the close proximity of the grounded chamber walls to the pushing plate which reduces the electric field felt by the ions. This is evident in the long arrival times of the atomic ions compared to predictions calculated for infinite plates.

Though the substantial quantitative optimization procedures described above demonstrated that the new apparatus significantly out-performed its predecessor in a number of key areas, it is clear that the problem with the TOF mass spectrometer must be solved before we can hope to perform meaningful cold molecule experiments in this apparatus. However, in light of the progress of other cold molecule techniques, it was decided not to invest the time and funds in making these improvements, instead alternative uses of this apparatus for future experiments are being considered, details of which are discussed in Chapter 6. The interaction of ultracold matter with ultrafast light remains an interesting area of research and, thanks to this new apparatus, this group is one of the few in the world with access to both technologies.

Chapter 6

Conclusion

The motivation for this thesis, and many others like it, is the formation of truly ultracold molecules: molecules in the ro-vibrational ground state whose translational temperatures are in the μK to nK regime. Laser cooling techniques for atoms have been well established since the mid 1980s, however these techniques, which require millions of cycles of absorption and spontaneous emission, are not generally applicable to molecules as it is almost impossible to find a closed transition within the complex ro-vibrational structure of the molecule¹. Therefore, alternative techniques need to be found. The road to ultracold molecule formation is currently split along two paths. The first approach is to *directly* cool molecules, and the second is to synthesize ultracold molecules from pre-cooled atoms — so called *indirect cooling*.

The direct approach has the advantage of using ‘real’ molecules which are al-

¹The exception to this being SrF in which the DeMille group in Yale have been able to demonstrate laser cooling^[53], however such techniques rely heavily on the Franck–Condon parabola of the system and are rarely applicable to most molecules.

ready deeply bound. During cooling, collisional relaxation in the vibration of the molecule leads to a sample in the vibrational ground state. However, direct cooling techniques have not yet reached the ultracold temperatures that can be readily achieved using laser cooling of atoms. By contrast, the indirect methods are able to easily access the ultracold regime but, as there is no direct molecular cooling mechanism, we do not observe collisional relaxation. Two main methods are used to associate ultracold molecules from pre-cooled atoms; photoassociation and Feshbach resonances. Feshbach resonances always produce a pure sample of molecules in one of the highest vibrational levels, whereas with photoassociation, the bound states are populated by spontaneous decay leading to a mixture of vibrational states. Hence it is important to develop techniques for controlling the internal state of an ultracold molecule. Two successful techniques have been illustrated for controlling the internal states of ultracold molecules and directing them towards the vibrational ground state; STIRAP and molecular optical pumping.

STIRAP has been shown to be a widely applicable technique for producing ground-state ultracold molecules in a range of homo- and hetero-nuclear molecules^[12,89,90,93,149]. In this approach, a sample of loosely bound molecules formed using a Feshbach resonance are coherently transferred to the ground vibrational level via a Raman interaction; this maintains the temperature and purity of the initial sample. Molecular optical pumping starting with photoassociated Cs₂ molecules was demonstrated by Viteau *et al.*^[13]. Following photoassociation, broadband optical pumping was applied to the sample to re-distribute the vibrational levels. By blocking transitions

resonant with $v'' = 0$ they were able to demonstrate accumulation of molecules in the ground state with minimal centre-of-mass heating due to the small average number of cycles required to reach $v'' = 0$. While this technique is both simple and efficient, it relies upon peculiarities in the internal structure of the Cs_2 dimer and as yet, has not been demonstrated in any other molecules.

Complimentary to these two techniques is the concept of ultrafast photoassociation. Whereas conventional photoassociation excites a single vibrational level, a broadband pulse excites a coherent superposition of states producing a *wavepacket*. The evolution of this wavepacket in the excited state potential provides opportunity for Franck–Condon overlap with states which are less accessible with stationary wavefunctions. Application of a well-timed dump pulse can stimulate the transfer of population to bound ground states. Coherent control techniques could be applied to the pulse shape of the pump and, or dump pulse to steer the interaction to a desired state, or superposition of states. This technique has received heavy theoretical treatment^[104–108] but has yet to be demonstrated experimentally.

The complete process of a pump-dump experiment represents a complex experimental challenge, and hence has been broken into pieces. The first piece of this puzzle was tackled by Brown *et al.*^[110,111,131] in Oxford and Salzmann *et al.*^[132] in Freiburg. These two groups investigated the effect of broadband pulses on pre-formed Rb_2 dimers in a MOT. Both observed a reduction of molecular signal that was coherent in nature; *i.e.* that depended on the chirp of the laser pulses. While the reduction of signal was a disappointing result, the coherent nature of the process

lends hope that, with an appropriate dump-pulse we may observe coherent control of the process. The next step in this investigation is to observe the coherent dynamics of the wavepacket oscillations in the excited state; this is a key step before we can consider applying a dump pulse. The search for these dynamics forms the bulk of chapters 3 and 4.

The dynamics of the excited state were investigated by applying a time-dependent ionization pulse delayed with respect to the pump. A clear step in molecular ion signal was observed as the delay was scanned from negative (probe first, then pump) to positive (pump then probe). This was a clear indication that bound molecular population was being created in the excited state. However, there was no indication of the desired dynamics in the excited state. The dependence of the molecular ion signal on the spectrum of the pump pulse was investigated and compared with theoretical results to give an estimation of the initial inter-nuclear separation of the atom-pairs involved in the photoassociation at around 30-60 a_0 . By comparison, the inner turning point of the pre-associated molecules in the MOT is around 25 a_0 , suggesting that the predominant source of excited molecular ions was photoassociation rather than excitation of pre-formed molecules.

Simulations of the population density distribution following the pump pulse suggest that coherent oscillations can be produced from an unbound initial state^[120,130]. However, these oscillations tend to be slow (timescale on the order on 70 ps) and quickly dephase due to the anharmonic nature of the potential. These simulations only predict the population of the excited state, and not the ionization signal. A

simple ionization operator was postulated to model the effect of the probe pulse; the result was to completely wash out the oscillations due to the poor position-sensitivity of a broadband probe at long internuclear separations. This explains the lack of oscillations observed in the pump-probe signal. If, instead of an unbound initial state, we simulate the effect of the pump pulse on the pre-formed molecules in the MOT, whose outer turning point resides at around $24 a_0$ then much faster oscillations (~ 10 ps) are observed. The wavepacket also appears to remain in phase for much longer due to the tighter potential at this point. Furthermore, these oscillations are not washed out by the ionization operator. Hence, in order to produce wavepacket oscillations that may be of use for photoassociation experiments it is clear that we need to operate at shorter internuclear separations. This necessity implies the need to either increase the density of the sample, or to operate with pre-associated molecules.

As these results were being taken, work had already begun on constructing a new cold atom apparatus for the experiment. The construction of the new apparatus, in which atoms are loaded into a hybrid magnetic and dipole force trap, has been outlined in Chapter 5. This trap offered a significant increase in density and the ability to trap molecules as well as atoms, and it was hoped that in this new apparatus we could operate at shorter internuclear separation. However, unfortunately, technical difficulties with the vacuum pressure and mass spectrometer prevented meaningful experiments from being performed. Due to the recent rapid advances in alternative direct and indirect cooling techniques, the decision was taken to abandon the

photoassociation experiments at this point. Despite this, the new apparatus opens exciting possibilities for the combination of ultracold matter with ultrafast light pulses, which are discussed below.

6.1 Outlook

As outlined above, it is essential to create, and observe, molecular wavepackets before we can move forwards towards a true ultrafast photoassociation pump-dump scheme. The indication from the results presented in Chapter 4 is that this is going to be hard to achieve by broadband photoassociation in a magneto-optical trap because of the anharmonic nature of the molecular potentials at large internuclear separations. Increasing the density of the sample and moving towards quantum degeneracy may well yield the desired result; however, if the techniques only work at quantum degeneracy then there is no obvious advantage over the Feshbach resonance and STIRAP techniques. Alternatively, working with pre-formed molecules appears to be a simpler way to reduce the internuclear separation of the initial state. Signal from the bound initial state was not apparent in the rubidium MOT, but if the ultrafast photoassociation was combined with conventional (cw) photoassociation, the signal could become useable.

It is impossible to read this thesis without forming the impression that ultrafast photoassociation is falling behind other indirect cooling methods. STIRAP techniques are producing pure samples of ultracold molecules in their vibrational ground state with near unit efficiency, and the molecular optical pumping scheme

provides a simple yet effective way to accumulate molecules in $v'' = 0$ directly from a MOT. By contrast, the pump-dump ultrafast photoassociation scheme has yet to be experimentally demonstrated; in fact even the intermediate step of demonstrating the requisite wavepacket oscillations has not been achieved.

Because of slow progress in the field and the huge successes of alternative techniques such as STIRAP and molecular optical pumping, it is hard to envisage a scenario in which ultrafast photoassociation becomes a mainstream technique for ultracold molecule formation. Thereby it would be prudent for future ultrafast-ultracold experiments to concentrate on the benefits of ultrafast lasers rather than try to compete with other association techniques. For example, a recent experiment by Goto *et al.* in I_2 molecules has demonstrated quantum interference in the molecular vibrational levels induced by an off-resonant ultrafast pulse^[150]. This result has implications for the use of molecular eigenstates in high speed computation^[151,152]. Experiments are ongoing to try and reproduce this result in the ultracold regime. This is just one example of where ultrafast, ultracold molecular experiments may lead in the future, and is motivation to continue in this challenging, yet promising, field.

While the future of the new cold atom apparatus remains unclear, an exciting avenue to explore would be to combine this apparatus with the burgeoning number of quantum information processing experiments being developed in Professor Walmsley's group. A growing number of quantum memory experiments are utilizing ensembles of ultracold atoms to store quantum information^[14-17]. A quantum

memory based on the Raman interaction in a warm ensemble of cesium atoms has been developed by this group^[18,19,153] and it is thought that this protocol may be extended into the ultracold regime. While an ensemble of ultracold atoms is an inherently more complicated apparatus than a room temperature vapor cell, enhanced storage times as well as the capacity to manipulate stored quantum states via atom-atom interactions makes this idea worth pursuing. With this potential long-term goal in mind, the author joined the Raman quantum memory experiment in order to develop the technology in a warm ensemble, which provides a simpler platform on which to explore ways to store quantum states of light in collective excitations of matter. The results of these experiments are discussed in Chapter 7.

Chapter 7

Raman Quantum Memory

Following the conclusion of the cold molecules experiment, the author joined another experiment within Professor Walmsley's group working on Raman Quantum memories in warm atomic vapors. The concept of an off-resonant atomic quantum memory based on a Raman interaction was first suggested by this group in 2007^[153]. The large detuning from atomic resonance distinguishes this scheme from other atomic quantum memories based on electromagnetically induced transparency (EIT), a resonant effect^[154]. Whereas the storage bandwidth of an EIT memory is limited by the atomic linewidth (typically MHz), the Raman memory circumvents this problem by the creation of a virtual excited state, whose linewidth is determined only by the bandwidth of the control pulse. As we search for ever-increasing data rates, the large bandwidth of this Raman memory is key to allow shorter pulses to be stored. The theory behind the process is briefly introduced in Section 7.1.1; for a more complete picture the reader is directed to the D.Phil thesis of Josh Nunn^[155].

As well as developing the theory, this group has also pioneered the development of an operational Raman quantum memory based on a warm cesium vapor. The memory is capable of storing pulses of 300 ps duration, corresponding to a 1.5 GHz bandwidth. The results achieved in this memory prior to the author's arrival are described in Section 7.2. By necessity, this description is kept short; a far more thorough description of this apparatus and its construction can be found in the D.Phil. thesis of Klaus Reim^[156].

Along with other D.Phil. students, Patrick Michelberger and Tessa Champion, the author developed this memory process to demonstrate the storage of polarization-encoded information in a parallel pair of memories, one storing horizontally and the other vertically polarized light. The memory process was shown to have a purity of over 97%; the experiment, and results, are discussed in Section 7.3.

7.1 The Raman memory protocol

The Raman memory protocol utilizes a two-photon off-resonant process with a weak signal and strong control pulse to map the temporal and spectral structure of the signal pulse onto a collective excitation in an atomic ensemble known as a *spinwave*. The strength of the Raman interaction is increased by the large number of atoms in the ensemble, but the spinwave is delocalized across all atoms in the ensemble. Therefore, despite the extremely weak interaction between a single photon and a single atom, one can still achieve high memory efficiencies.

The energy level diagram of the Raman memory is shown in Figure 7.1 with a

couple of hyperfine or Zeeman levels in the ground state, $|1\rangle$ and $|3\rangle$, coupled via an excited state, $|2\rangle$. Critically both signal and control fields are detuned by an amount Δ from the excited state, $|2\rangle$. This detuning from resonance facilitates the storage of high-bandwidth photons, leading to high time-bandwidth products; an essential parameter as we strive for ever increasing data rates. The only limit on the bandwidth accessible in this memory is the splitting between the two ground-states; this is because the laser must be able to individually address either state $|1\rangle$ or $|3\rangle$. Hence our bandwidth must be significantly less than the hyperfine splitting.

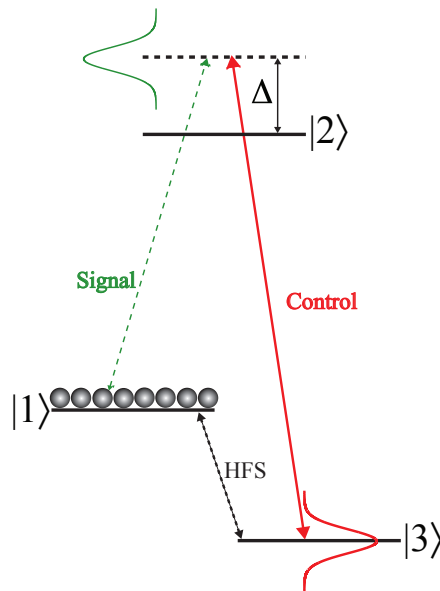


Figure 7.1 A typical Λ -level system for the Raman quantum memory. A pair of hyperfine ground states, $|1\rangle$ and $|3\rangle$, are coupled via a Raman interaction using a pair of laser fields; the signal and the control. The sample is prepared by pumping all the atoms into $|1\rangle$. The signal and control fields are on two-photon resonance with the states $|1\rangle$ and $|3\rangle$ and are detuned by an amount Δ from the excited state, $|2\rangle$. This detuning allows the storage of high-bandwidth laser pulses, provided the bandwidth does not exceed the splitting of the ground states (HFS).

7.1.1 Raman memory theory

Initially we will consider storage of a single photon only, however the memory can, and does, store many thousands of photons simultaneously. The strong control field can be represented classically by the Rabi frequency, $\Omega(\tau)$ ¹. The signal can consist of a single photon, and hence must be described quantum-mechanically by the annihilation operator, $A(\tau, z)$. Likewise, the spinwave is described as a collective coherence of the form;

$$B(\tau, z) \propto \sum_{\beta} |1_{\beta}\rangle \langle 3_{\beta}| e^{-i(\Delta\omega\tau)}, \quad (7.1)$$

where β runs over all the atoms in a thin slice of the ensemble centred at position z and $\Delta\omega = \omega_s - \omega_c$, is the frequency difference between the signal and control fields.

The equations of motion of this system can be calculated from the semi-classical Maxwell-Bloch equations under the slowly varying envelope approximation^[153,157], yielding;

$$\left(\frac{\partial}{\partial z} + \frac{d}{\Gamma} \right) A(\tau, z) = i \frac{\Omega(\tau)\sqrt{d}}{\Gamma} B(\tau, z), \quad (7.2)$$

$$\left(\frac{\partial}{\partial \tau} + \frac{|\Omega|^2}{\Gamma} \right) B(\tau, z) = -i \frac{\Omega^*(\tau)\sqrt{d}}{\Gamma} A(\tau, z), \quad (7.3)$$

where d is the on-resonant optical depth of the ensemble² and $\Gamma = \Delta - i\gamma$ is the complex detuning. γ arises from dephasing processes, including spontaneous emission

¹ τ is the *local* time $\tau = t - z/c$

²The optical depth is defined such that a resonant, monochromatic, weak probe tuned exactly on resonance would be attenuated in intensity by a factor of e^{-2d} .

from the excited state. Analytical solutions to these equations have been calculated by Nunn^[153] and Gorshkov^[158]. The spinwave excitation, in terms of the input signal field, $A_{\text{in}}(\tau)$, is given by;

$$B_{\text{store}}(z) = \int_{-\infty}^{\infty} f(\tau) J_0 \left[2C \sqrt{(1 - \omega(\tau))z} \right] A_{\text{in}}(\tau) d\tau. \quad (7.4)$$

Where C is a key parameter in the system which quantifies the Raman memory coupling which is expressed as^[153];

$$C^2 = \frac{d\gamma W}{\Delta^2}, \quad (7.5)$$

where z has been normalized to the length of the ensemble; *i.e.* $z = 1$ is the exit of memory. Here we have introduced the normalized integrated Rabi frequency of the control pulse, $\omega(\tau) = \frac{1}{W} \int_{-\infty}^{\tau} |\Omega(\tau)|^2 d\tau$, with $W = \int_{-\infty}^{\infty} |\Omega(\tau)|^2 d\tau$ a normalization parameter related to the total energy in the control pulse. $f(\tau) = C e^{iW\omega(\tau)/\Delta} \Omega(\tau) / \sqrt{W}$ is the normalized Stark-shifted Rabi frequency.

Similarly, the read-out signal $A_{\text{out}}(\tau)$ can be calculated to be;

$$A_{\text{out}}(\tau) = f^*(\tau) \int_0^1 J_0 \left[2C \sqrt{\omega(\tau)(1 - z)} \right] B(z) dz. \quad (7.6)$$

Hence the storage efficiency, η_{store} , can simply be calculated as the ratio of the

final number of excited spin waves to the total number of photons in the signal field;

$$\eta_{\text{store}} = \frac{\int_0^1 |B(z)|^2 dz}{\int_{-\infty}^{\infty} |A_{\text{in}}(\tau)|^2 d\tau} \quad (7.7)$$

The total storage and retrieval efficiency can similarly be expressed as

$$\eta_{\text{tot}} = \frac{\int_{-\infty}^{\infty} |A_{\text{out}}(\tau)|^2 d\tau}{\int_{-\infty}^{\infty} |A_{\text{in}}(\tau)|^2 d\tau}. \quad (7.8)$$

It is clear from equations 7.4 and 7.6 that the efficiency of the memory process depends strongly on the coupling parameter, C , which, proportional to the square root of optical depth of the ensemble, \sqrt{d} , and the integrated power in the control field, W , and is inversely related to the detuning, Δ (see (7.5)). Hence, in order to get good memory efficiency, one must have a powerful control field and a high optical density. In his unifying theory paper describing both off-resonant (Raman) and on-resonant (EIT) quantum memories^[158], Gorshkov showed that the memory efficiency is bounded by the optical depth such that $\eta_{\text{tot}} \sim 1 - 2.9/d$. The choice of detuning is less obvious; while it appears that the memory efficiency can be increased by reducing the detuning, one must be careful of avoiding population of the intermediate state, $|2\rangle$, as this leads to spontaneous emission from the excited state.

7.2 The cesium Raman memory

At the heart of the Raman memory is a cesium vapor cell, heated to 60 °C. This system is extremely simple compared to many other quantum memories which rely on, for example, ultracold atoms^[159], cryogenically cooled solids^[160] or single atoms in high-finesse optical cavities^[161]. Furthermore, the off-resonant nature of the Raman memory precludes fluorescence from the excited state; this significantly reduces the noise-floor of the process to allow single photons to be stored and retrieved in the memory.

In the cesium memory, the states $|1\rangle$ and $|3\rangle$ depicted in Figure 7.1 correspond to the $F = 3$ and $F = 4$ hyperfine levels, in the $6^2S_{1/2}$ ground state. The splitting between these ground states is 9.2 GHz, as made famous by the use of cesium atomic clocks to define the SI second^[162]. Atoms are prepared in $|F = 4\rangle$ by optical pumping and are coupled to $|F = 3\rangle$ in a two-photon Raman process involving a weak signal field and a control field. Each laser is typically blue-detuned from the excited state by around 18 GHz. The excited state, $|2\rangle$, in this system is actually a combination of the four hyperfine levels in the $6^2P_{3/2}$ state, but the detuning Δ from this resonance is large enough that they can be considered as a single level. The experimental procedure (Section 7.2.1) and previous results achieved with this apparatus (7.2.2) are discussed below.

7.2.1 Experimental procedure

Pulse preparation

Both signal and control pulses derived from the same laser, a Spectra Physics *Tsunami* Ti:Sa oscillator. The *Tsunami* was configured for long-pulse operation by inserting a birefringent filter in the laser cavity and produced pulses around 300 ps long at a repetition rate of 80 MHz, corresponding to a pulse-pulse separation of only 12.5 ns. To facilitate longer storage times, a Pockels cell was introduced to provide pulse-picking capabilities. The pulse-picker was used to vary the time between read-in and read-out pulses and set the storage time for the memory. The output of the pulse-picker was split into two arms—one to provide the signal field, and the other the control. In order to set the two-photon resonance, the signal field passed through an electro-optic modulator (EOM) driven by a 9.2 GHz radio-frequency (RF) amplifier. We required the red-sideband of the EOM for the signal field so the fundamental and blue sideband were removed by a pair of Fabry–Perot etalons with a free-spectral-range (FSR) of 18 and 36 GHz respectively. Each etalon typically had around 30-40% transmission of the desired sideband and approximately 100:1 extinction at the other frequencies. The RF was switched on to allow the first pulse through into the signal arm before being switched off to allow read-out by the second control pulse. The pulse sequence is shown in Figure 7.2. The signal and control fields were then combined on a PBS and focussed into the cesium cell.

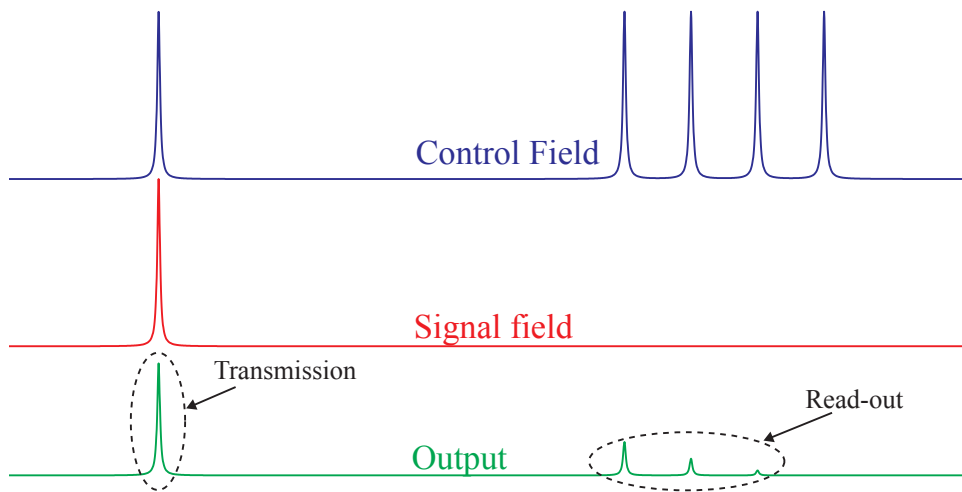


Figure 7.2 Pulse sequence in the Raman quantum memory showing preparation of signal (red) and control (blue) fields as well as the output of the memory (green). A signal pulse is read into the memory by a single control pulse creating a coherence in the atomic ensemble; that which is not read into the memory is transmitted. The atomic coherence is read-out by a series of control pulses; the energy in a single control pulse is not sufficient for 100% efficient readout, hence, after the first read-out, some coherence remains in the ensemble; this can be read-out by subsequent pulses.

The cesium cell

The cesium cell was manufactured by Triad technologies (TT-CS-75-V-Q-CW) and contained a small sample of cesium in 40 Torr of neon buffer gas. The vapor pressure in the cell depends exponentially on the temperature^[163], so in order to increase the vapor pressure, and thereby increase the strength of the light-matter interaction, the cell was heated to 60-70 °C. The temperature of the cell was regulated by a thermocouple and an active feedback system acting on an Ohmic heating tape wrapped around the cell. The wires in the tape were counter-wound to cancel out magnetic fields which would lead to spin-decoherence in the memory. To prevent the heat

from the cell disturbing the rest of the apparatus, it was wrapped in several layers of insulating foam. As the ends of the cell were, by necessity, left open for beam access, they were naturally the coldest parts of the cell and hence cesium is likely to condense on them and block the beams. To prevent this, a small spot in the middle of the cell was cooled by a steady flow of compressed air, this encouraged condensation in this area and kept the windows clean. The temperature of this cold spot was monitored by a second thermocouple and maintained 5-10°C below the rest of the cell.

The neon buffer gas performs a key role in the memory process; the cesium atoms undergo several collisions with the buffer gas leading to a random walk. Hence the atoms remain in the interaction region of the two laser beams for longer, facilitating longer storage times. Neon has no nuclear spin and no electronic spin, hence it has no magnetic moment—crucially, this means that cesium-neon collisions are spin-preserving. This ensures that, despite several collisions with the buffer gas during storage, the atomic coherence is maintained.

Another significant source of loss in the memory was magnetic dephasing of the spinwave in the ensemble. In the presence of a magnetic field, the degeneracy of the Zeeman sub-states is lifted; assuming that the population is initially in an incoherent mixture of different Zeeman levels, each of which precesses at different rates, this will produce decoherence in the memory. To protect the cell from stray magnetic fields, it was wrapped in three layers of μ -metal³, each 120 μ m thick. The μ -metal

³ μ -metal is a nickel-iron alloy, 75% nickel, 15% iron plus copper and molybdenum. Its unusually high magnetic permeability makes it effective at screening magnetic fields

shielding was de-Gaussed using a coil wrapped around the outside of the shielding; an AC current of 5 A is driven through the coils and slowly reduced to zero over a few seconds. This facilitates the re-alignment of the magnetic domains in the metal and improves its shielding.

Detection

The control field is several orders of magnitude brighter than the signal. In fact, if the memory is to achieve the ultimate goal of storing single photons, then the ratio of control-to-signal will be of the order $10^{11}:1$. Hence a major obstacle in detecting weak signal fields is ensuring that the control field is adequately filtered. Much of the filtering was achieved by polarization, as the two fields are orthogonal. However, even the best polarizers only have an extinction ratio of around $10^6:1$, hence the control field still dominates. Therefore, a further three Fabry–Perot etalons were utilized to further filter the signal field.

Following the etalons the signal field transmitted by the memory, along with any read-out, was coupled into a single-mode fiber to be transported to the detector. The single mode fiber provided further spatial filtering of the control field and prevents stray light from scattering into the photodetector. The detector used was a high-speed avalanche photo-detector (*Thorlabs* APD210) with a bandwidth of 1 GHz, rise time of 500 ps and a sensitivity of around 1000 photons/pulse. The speed and sensitivity of this photo-diode make it ideal for measuring the weak pulses used in this experiment. For subsequent experiments down at the single-photon-per-pulse

level, a Perkin Elmer single photon counting module, a time-to-amplitude converter and a multi-channel-analyzer (both Canberra) were used to build up a histogram of photon counts over thousands of experiments.

A simplified diagram of the layout of the optical bench is shown in Figure 7.3

7.2.2 Previous results

The first demonstration of Raman memory was performed by Klaus Reim and co-workers and was reported by Nature photonics in March 2010^[19]. Due to limitations of the Pockels cell driver at the time, the signal was stored and retrieved by successive oscillator pulses limiting the storage time to 12.5 ns. Storage and retrieval efficiencies of up to 30 and 50% respectively were observed leading to an overall read-out efficiency of 15%. Also, the ‘failure’ mode of the memory was transmission of the signal, hence the memory can be considered to be a light-matter beam-splitter whose reflectivity depends on the control pulse. As 12.5 ns is short on the timescale of predicted decoherence mechanisms (atomic motion, magnetic dephasing, collisional spin-flips etc.) it is expected that there should be very little loss in the memory. This was confirmed by applying further read out pulses after the first one to read out all of the coherence from the memory.

The memory efficiency was measured as a function of energy in the write/read pulse; the results are shown in Figure 7.4. The results show an increase in memory efficiency up to the maximum available pulse energy (4.8 nJ); this suggested that greater control field energy, were it available, could produce higher efficiencies.

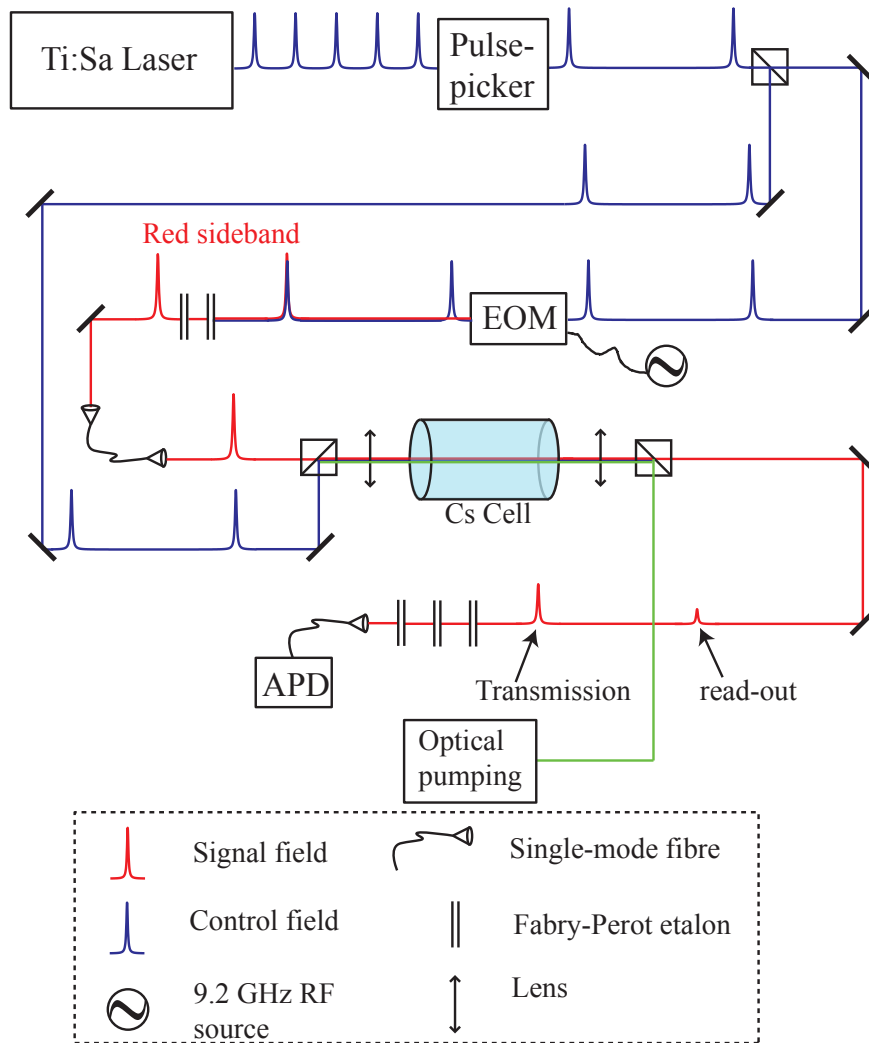


Figure 7.3 Beam diagram for the Raman memory experiment. A train of pulses from the Ti:Sa oscillator is chopped down to a pair of pulses with variable separation by a pulse-picker, the beam is then split in two; one to form the signal field (red), and the other, the control field (blue). A 9.2 GHz red-shifted sideband is added to the signal field with an EOM, the fundamental and blue sideband are filtered by Fabry–Perot etalons. The signal field then passes through a single-mode fiber (SMF) before being combined with the control on a PBS. The two fields are focussed into the cesium cell. After the cell, the control field is filtered out by a polarizer and three further etalons before being coupled into another SMF for transport to the avalanche photo detector (APD).

To demonstrate the coherence between the input and retrieved light, the output of the memory was interfered with some of the signal field which was picked off before the memory and delayed in a 12.5 ns optical delay line. A fringe visibility of 82.7% indicates that the memory is highly coherent. In fact, this visibility is exactly that which is predicted by theory of a perfectly coherent memory where some mode mismatch is introduced by the Stark shift on the retrieved pulse due to the control field^[19].

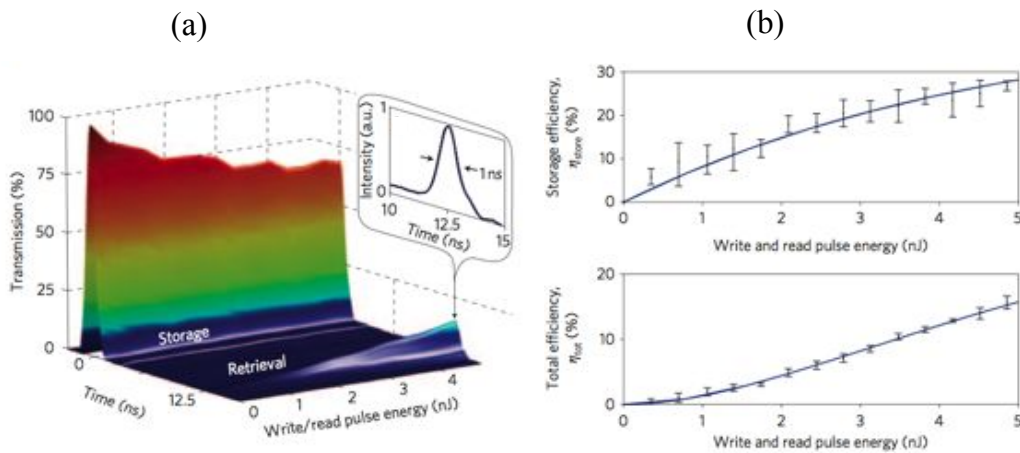


Figure 7.4 Raman memory efficiency as a function of control pulse energy. **(a)** Storage (0 ns) and retrieval (12.5 ns) of the signal field plotted versus the control field energy, as measured by the fast APD. The inset shows that the pulses are shorter than 1 ns indicating a bandwidth in excess of 1 GHz. **(b)** Storage (top) and overall (bottom) efficiency. Figures reproduced with kind permission of K. Reim.

Following the success of the initial demonstration, Reim *et al.* improved their apparatus to enable longer storage times^[18]. Of primary importance was a new high-voltage driver for the Pockels cell which allowed the delay between write and read pulses to be varied continuously⁴ from 100 ns upwards. With the capability for

⁴At least continuously in steps of 12.5 ns

longer storage times, sources of decoherence became apparent. The largest source was re-pumping of atoms in the spin-wave by the optical pumping beam. This was remedied by switching the optical pumping diode laser off during storage using an AOM. It was also found that storage time could be increased by wrapping the cell in a μ -metal shield to suppress stray magnetic fields. Using these techniques, it was possible to demonstrate storage with a half-maximum lifetime of $1.5 \mu\text{s}$ (see Figure 7.5). Assuming magnetic dephasing to be the dominant factor, a theoretical model was fitted to the data with the strength and orientation of the magnetic field treated as free parameters; this suggested a residual field of 0.13 ± 0.05 Gauss consistent with the stray field due to ohmic heaters. Furthermore, retrieval was still observable with $4 \mu\text{s}$ storage time, a figure which is over 10,000 times longer than the pulse duration. As of July 2011, this is the highest demonstrated time-bandwidth product in any quantum memory.

Improvements were also made to the sensitivity of the detector and to the extinction of the control field. As detailed above, these included the purchase of single-photon counting apparatus and inserting etalons after the memory in order to further extinguish the control field leaked by the polarizer. The signal field was attenuated using neutral density filters until significantly less than one detection event per pulse was observed in the input pulse. By backing out the detector efficiency and the transmission through all the etalons, it could be inferred that the input signal field contained, on average, 1.6 photons/pulse and hence is at the single-photon level. Storage and retrieval of these single-photon pulses was demonstrated

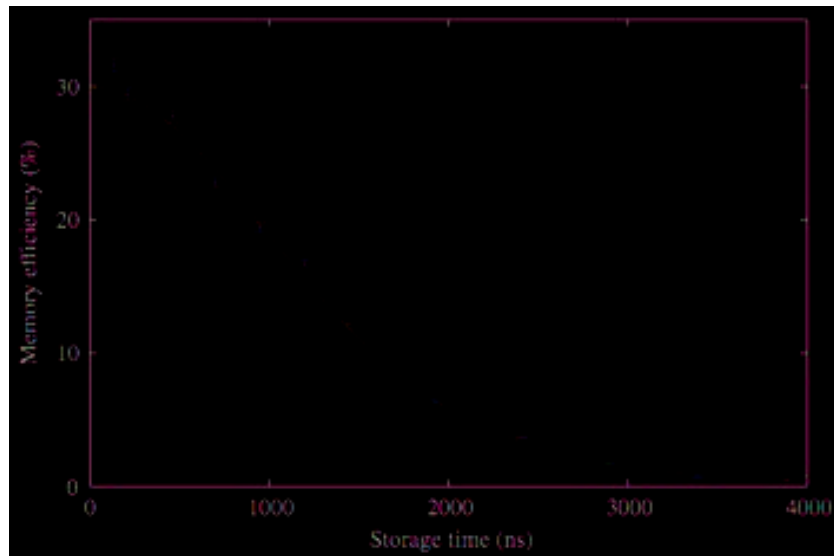


Figure 7.5 Storage lifetime of the Raman memory. The red line is a fit of the data to a theoretical model suggesting a residual magnetic field of 0.13 ± 0.05 Gauss in the cell. Figure reproduced with kind permission of K. Reim.

with a storage time of 775 ns as shown in Figure 7.6. The retrieved signal contained an average of 0.58 photons for every pulse. Background noise measurements with the signal field blocked indicated a noise floor of 0.25 photons/pulse indicating a memory efficiency of around 24% at the single-photon level. The noise floor was measured as a function of optical pumping power and sign (*i.e.* into which level the atoms were being pumped); comparison of this data with theoretical modeling suggested that the origin of the background was spontaneous Raman scattering of the control field^[18].

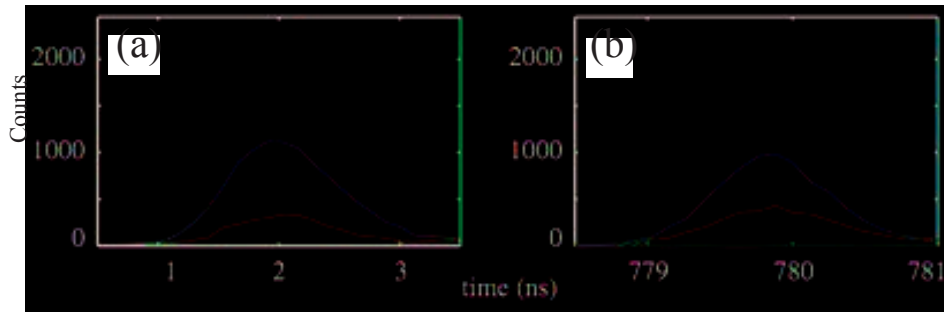


Figure 7.6 Single-photon level storage **(a)** and retrieval **(b)** in the Raman memory. Data is built up in a histogram over 360,000 experiments. The green line is the signal field in the absence of the control, the blue line indicates the transmitted **(a)** and retrieved **(b)** signal field. The noise background with signal field locked (red) indicates, on average, 0.25 photons per pulse background noise. Figure reproduced with kind permission of K. Reim.

7.3 Storage of polarization-encoded information

The results shown above indicate that the Raman memory represents a simple and robust option for the storage of quantum information. Storage and retrieval of GHz bandwidth signals at the single-photon level has been demonstrated with time-bandwidth products larger than have been demonstrated in any other quantum memory. The following section contains details of an effort to store polarization-encoded information in a pair of memories, one storing horizontally polarized light, and the other vertically. When split and re-combined interferometrically, light stored in these two memories should retain the polarization of the input field; this is verified using quantum process tomography (QPT)^[164].

Two-memory interferometer

In order to demonstrate the ability of the memory to store an arbitrary polarization state $\cos\theta|H\rangle + e^{i\phi}\sin\theta|V\rangle$ we prepare 6 polarization states; $|H\rangle, |V\rangle, |D\rangle = \frac{1}{\sqrt{2}}(|H\rangle + |V\rangle), |A\rangle = \frac{1}{\sqrt{2}}(|H\rangle - |V\rangle), |R\rangle = \frac{1}{\sqrt{2}}(|H\rangle - i|V\rangle)$ and $|L\rangle = \frac{1}{\sqrt{2}}(|H\rangle + i|V\rangle)$. Any polarization state on the Poincaré sphere can be constructed from linear combinations of these 6 states, hence demonstrating their storage and retrieval is sufficient to demonstrate full polarization qubit storage.

As the Raman memory is a single mode memory, we cannot store polarization-encoded information in a single memory. Instead, the two orthogonal input modes are mapped onto two quantum memories in an interferometer, one storing $|H\rangle$ and the other $|V\rangle$. After the interferometer, every input state is analyzed in every basis, making a total of 36 measurements. The normalized expected output of each measurement is shown in Table 7.1. The transmitted and retrieved signal field is measured and the comparison of the results of these measurements with the ideal case gives the purity of the quantum process; see Section 7.3.1 for details.

	$ H\rangle_{\text{prep}}$	$ V\rangle_{\text{prep}}$	$ D\rangle_{\text{prep}}$	$ A\rangle_{\text{prep}}$	$ R\rangle_{\text{prep}}$	$ L\rangle_{\text{prep}}$
$ H\rangle_{\text{anal}}$	1	0	1/2	1/2	1/2	1/2
$ V\rangle_{\text{anal}}$	0	1	1/2	1/2	1/2	1/2
$ D\rangle_{\text{anal}}$	1/2	1/2	1	0	1/2	1/2
$ A\rangle_{\text{anal}}$	1/2	1/2	0	1	1/2	1/2
$ R\rangle_{\text{anal}}$	1/2	1/2	1/2	1/2	1	0
$ L\rangle_{\text{anal}}$	1/2	1/2	1/2	1/2	0	1

Table 7.1 Expected normalized measurement outcomes of the 36 polarization measurements. The Polarization is prepared in state $|\Psi\rangle_{\text{prep}}$ and analyzed in state $|\Psi\rangle_{\text{anal}}$.

A diagram of the optical layout for the two-memory interferometer is shown in Figure 7.7. Linear polarization of the signal field was guaranteed by a PBS before a pair of waveplates prepared the polarization in the desired state, $|H\rangle, |V\rangle, |D\rangle, |A\rangle, |R\rangle, |L\rangle_{\text{prep}}$, which was then split into two polarization modes, $|H\rangle$ and $|V\rangle$ by a polarizing beam displacer (PBD). A half-wave plate ($\lambda/2$) flipped the polarization in each arm before a second PBD recombined the two arms hence forming a polarization interferometer. The PBD displaced the horizontally polarized beam by 8 mm compared to the vertical; this is sufficiently close together that both arms could pass easily through the cesium cell. Initially, when data was taken with a storage time of only 12.5 ns, the interferometer was 20 cm long which was sufficient to fit the cell, heater and half-wave plate. However, in order to facilitate longer storage times, magnetic shielding was incorporated around the cell; this necessitated the extension of the interferometer to 35 cm.

The control field was introduced into each arm of the interferometer co-propagating with the signal but with opposite polarization, and the diode laser for optical pumping was introduced counter-propagating. Each beam was focussed separately by lenses placed outside the interferometer. Following the interferometer, the output was analyzed in the six polarization states ($|H\rangle, |V\rangle, |D\rangle, |A\rangle, |R\rangle, |L\rangle_{\text{anal}}$) using a polarizer aligned parallel to the preparation PBS and a pair of calibrated waveplates (see Table 7.2). The signal was then frequency-filtered by the etalons before being coupled into a single-mode fiber for detection.

After the interferometer, a half-wave plate corrected the polarization rotation

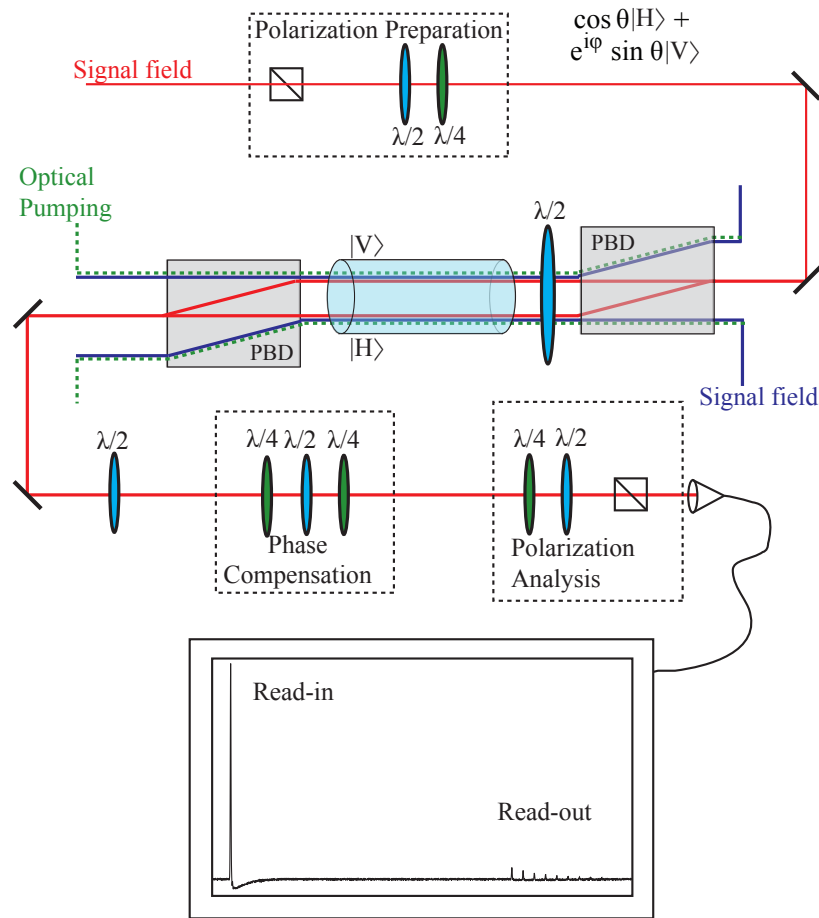


Figure 7.7 Layout of the two-memory interferometer. An arbitrary polarization state, $\cos \theta |H\rangle + e^{i\phi} \sin \theta |V\rangle$, is prepared and split into two arms in a polarization interferometer. The control field and optical pumping laser are introduced along each arm with the orthogonal polarization. The polarization is analyzed with a polarizer and a pair of calibrated waveplates. Phase picked up in the interferometer is compensated by a pair of quarter-wave plates set to $\pm 45^\circ$ sandwiching a half-wave plate. The signal and control field preparation and frequency filtering, as well as the focussing lenses are omitted for clarity. The inset shows a typical memory signal with a single read-in pulse and a multiple read-out chain. In this instance the storage time is 300 ns.

from the waveplate inside the interferometer; hence an input of $|H, V\rangle$ was mapped to an output of $|H, V\rangle$. However, the interferometer produced a phase-shift between

State	$\lambda/2$ angle	$\lambda/4$ angle
$ H\rangle$	0°	0°
$ V\rangle$	45°	0°
$ A\rangle$	22.5°	0°
$ D\rangle$	67.5°	0°
$ R\rangle$	0°	$+45^\circ$
$ L\rangle$	0°	-45°

Table 7.2 Waveplate angles for polarization state preparation and analysis.

$|H\rangle$ and $|V\rangle$ so superposition states such as $|D\rangle$ or $|R\rangle$ were not faithfully reproduced after the interferometer. In order to compensate for this offset, three waveplates were used, two quarter-wave plates sandwiching a half-wave plate. Each quarter-wave plate had its fast axis at $\pm 45^\circ$ to the horizontal such that the combination of the two had no effect on linear polarization. Hence the polarization state is taken around a closed loop on the Poincaré sphere. The topological phase shift, known as Pancharatnam's phase, between the two polarizations is half the solid angle subtended by the loop, and could be adjusted by rotating the central half-wave plate^[165].

While this phase could be compensated, it is important that the phase remained constant throughout a measurement, this means that the interferometer had to remain passively stable, or be actively stabilized. The PBD interferometer was passively very stable as it contained only two elements, and both beams passed through each. However, despite this, it was found to be useful to re-set, or at least re-check, the phase compensation at regular intervals during the course of a measurement. The

inherent stability of the PBD interferometer could be compromised by air currents surrounding the heated cell; to limit these effects the interferometer was encased in plastic tubing.

7.3.1 Quantum process tomography (QPT)

In an ideal quantum memory, the process of storage and retrieval of polarization qubits would be completely unitary; *i.e.* the polarization information would be rotated but would not suffer any decoherence. In the Raman memory, however, there are several potential sources of decoherence including the atoms leaving the interaction region as well as collisional and magnetic dephasing. We have already seen how these affect the lifetime of the memory (Figure 7.5), but what happens to the information remaining in the memory? Does it remain coherent or do non-unitary dynamics lead to loss of polarization information? In order to answer this question, we perform quantum process tomography on the two-memory interferometer described in Section 7.3.

Imagine that the memory is required to store a single qubit with density matrix, ρ . The matrices, $I/\sqrt{2}$, $X/\sqrt{2}$, $Y/\sqrt{2}$ and $Z/\sqrt{2}$ ⁵ provide an orthonormal set of matrices in which to expand the density matrix;

$$\rho = \frac{\text{tr}(\rho)I + \text{tr}(X\rho)X + \text{tr}(Y\rho)Y + \text{tr}(Z\rho)Z}{2}. \quad (7.9)$$

⁵ I, X, Y and Z are the pauli matrices. I is the identity. X corresponds to a bit flip (*e.g.* $|H\rangle \rightarrow |V\rangle$). Y indicates a bit flip with additional phase $\phi = \pi/2$ (*e.g.* $|H\rangle \rightarrow |V\rangle \cdot e^{i\pi/2}$). Z is a phase flip of one of the polarization channels (*e.g.* $|V\rangle \rightarrow |V\rangle \cdot e^{i\pi}$).

Quantities such as $\text{tr}(X\rho)$ correspond to the expectation value of an observable. So if we measure the observable, X , a large number of times, m , we obtain the outcomes $x_1, x_2, x_3, \dots, x_m$, the average of which, $\sum_n x_n/m$, is a good estimate of $\text{tr}(X\rho)$. If we similarly measure $\text{tr}(Y\rho)$ and $\text{tr}(Z\rho)$, we get a very good estimation of the quantum state ρ . This is known as *quantum state tomography* and can, in theory, be easily extended to states containing multiple qubits^[166].

While the measurement of the quantum state is obviously a key requirement in quantum optics, what matters with regard to the memory is to measure the *quantum Process* of storage and retrieval; *i.e.* what happens to the quantum state when it passes through the memory. Non-unitary dynamics in which the density matrix of a quantum state evolves from ρ_{in} to ρ_{out} can be described by a quantum process^[166];

$$\rho_{\text{out}} = \sum_{i,j} \chi_{ij} \Gamma_i \rho_{\text{in}} \Gamma_j, \quad (7.10)$$

where $\chi_{i,j}$ is known as the *process matrix* and contains all the information about the dynamics of the system. $\Gamma_{i,j}$ are orthonormal basis matrices for the density matrix, in our case these are the normalized Pauli matrices as above. The coherence of the quantum process is quantified by the purity $P = \text{tr}(\chi^2)$. For a completely pure process, $P = 1$; purity of less than 1 indicates non-unitary processes in the system. Full characterization of the process matrix is known as *quantum process tomography* (QPT)^[167].

Analyzing the the output of the two-memory interferometer in each of the po-

larization states (H, V, D, A, R, L) is tantamount to performing quantum state tomography for each input state. By preparing the 6 different polarization states, (H, V, D, A, R, L) , we have created a set of states which can be used to describe any state that is input into the memory. Thereby the 36 measurements in all possible combinations of prepared and analyzed polarization states are sufficient to perform a full quantum process tomography and to reconstruct the process matrix of the polarization memory in the $\{I, X, Y, Z\}$ basis^[168]. This reconstruction was performed numerically using an algorithm supplied by Nathan Langford^[167]. The algorithm searches for the most likely solution to the experimental data, but ensures that the resulting matrix is physical. The results of the quantum process tomography performed on the memory are shown below in Section 7.3.2.

7.3.2 Results

Initially, in order to make the interferometer as short as possible, the magnetic shielding was removed from around the cell. This limited the memory storage time to 12.5 ns, however this is sufficient to demonstrate at least a proof-of-principle storage of polarization-encoded information. In addition, it is interesting to investigate whether the purity of the storage and retrieval process is affected by external elements, as this is a key consideration for implementing the memory as part of a large quantum network.

For simplicity, the initial experiments were not performed at the single-photon level but rather were performed using classical weak coherent states containing on

the order of 1000-10,000 photons per pulse. However, these results will also hold for truly quantum single-photon inputs because the counting statistics of single photons passing through a linear optical system always follow the classical behavior^[169]. An obvious example of this being the interference visibility of light attenuated below the single-photon-level^[170]. In order to run this QPT experiment in the fully quantum single-photon regime, the interferometer would have to be modified to include small waveplates in each arm to compensate for the birefringence of the cell. Currently, this birefringence causes a small rotation of the control field polarization leading to significant leakage through the polarization filter; this precludes single-photon level measurements. In addition, the long counting times required to build up single-photon statistics impose strict constraints on the stability of the interferometer.

The PBD interferometer was carefully aligned by overlapping both beams in the far-field; despite this, a small disparity existed in the coupling of each into the single-mode fiber. Hence the coupling stage was adjusted to a point where each field coupled equally to the fiber, ensuring maximal interference visibility. Next the polarization was separately prepared in $|V\rangle$ and then $|H\rangle$ to maximize the memory efficiency in each arm, with all of the control field power directed to the relevant arm. Next the control field power was balanced 50:50 between the two memories and their efficiencies were separately measured. The storage and retrieval efficiencies of each memory were measured again and any slight discrepancies in efficiency were compensated for by adjusting the balance of the control field power to each arm. The balancing of the two memory efficiencies is a vital step because if one polarization

is stored with a greater efficiency than the other, then a superposition state (*e.g.* $|R\rangle$ or $|D\rangle$) will be artificially rotated by the storage and retrieval process. Finally, with the control field blocked, the phase of the interferometer was compensated, as discussed in Section 7.3, by preparing the polarization in $|D\rangle$ and measuring in $|A\rangle$ and rotating the phase waveplate in order to minimize the transmitted field.

Coarse wavelength adjustment of the laser output was achieved by rotating a birefringent filter (bi-fi) situated in the cavity while fine frequency control can be achieved by rotating a Gires–Tournois interferometer (GTI), also situated within the laser cavity. A spectrometer was used to get the wavelength correct while adjusting the bi-fi and then the laser frequency was set to the cesium D_2 line by rotating the GTI and searching for fluorescence in a cell placed in a pick-off of the beam before the Pockels cell. The relative frequency of the laser was monitored by a scanning Fabry–Perot interferometer (SFPI) (*Thorlabs* SA210-8B, Free spectral range 10 GHz) located behind the reference cell. Once the D_2 line was located, the laser frequency was adjusted to the desired detuning using the SFPI to compare the frequency to the resonance. It is essential that this frequency remains stable as the memory performance depends strongly on detuning; the SFPI was not sufficiently stable itself to be used as a reference, and it became tedious to continually turn the GTI to search for the resonance and then re-tune to the desired frequency. Instead, a reference Fabry–Perot etalon was used; the transmission of the etalon was maximised when the desired frequency was found using the SFPI and subsequently monitored during the experiment. A *Labview* code sounded an audible warning if

the transmission falls below a pre-defined threshold; if this happened, the data run was aborted and the frequency manually re-set.

12.5 ns storage time QPT

The memory was set for short storage times by selecting one signal pulse out of a train of nine, the remaining eight were used as read-out pulses, although typically only the first three produced observable signal. The preparation polarization was set, and then analyzed in all 6 polarizations before moving to the next preparation state. The data from the fast APD was read off on a fast oscilloscope (*Lecroy Wavepro 7100*). At each polarization setting, three data sets were taken;

1. V_{sc} — With both signal and control field present; 500 traces, each the average of 20 successive pulse trains.
2. V_s — With only the signal field present; 300 traces, each the average of 20 successive pulse trains.
3. V_c — With only the control field present; 200 traces, each the average of 20 successive pulse trains.

The data from the oscilloscope was read into the computer using a *Labview* script which also controlled a pair of shutters to block the signal and control fields when appropriate. This automation sped up the data-taking process but, unfortunately, no motorized rotation mounts were available so all the preparation and analysis waveplates needed to be set by hand.

The traces were numerically integrated to determine the areas $A_{s,c}^{0,1,2,3}$ in each pulse for each trace. The storage and retrieval efficiencies were calculated as;

$$\eta_{\text{store}} = 1 - \frac{A_{sc}^0 - A_c^0}{A_s^0 - A_c^0}, \quad (7.11)$$

$$\eta_{\text{ret}}^n = \frac{A_{sc}^n - A_c^n}{A_s^0 - A_c^0}, \quad (7.12)$$

where the superscript 0 corresponds to the input pulse and n corresponds to the nth read-out pulse. Typically, the storage efficiency was around $\eta_{\text{store}} = 20\%$; this is lower than observed by Reim *et al.*^[19] because the control field was shared between the two memories. With the multiple read-out pulses, almost all of the coherence was read-out of the memory at these short storage times, with over-all read-out efficiencies of around $\eta_{\text{ret}}^1 = 9\%$, $\eta_{\text{ret}}^2 = 6\%$ and $\eta_{\text{ret}}^3 = 3\%$.

The pulse areas were then averaged and inserted into the QPT algorithm to calculate the process matrix and purity. A process matrix was calculated for the input signal (*i.e.* with the control field blocked), the transmitted signal (the input pulse with some storage), for each of the three readout pulses and also for the total readout (the sum of all three read-out pulses). The calculated process matrices are shown in Figure 7.8. The purity of the input state was calculated as $P_{\text{in}} = 97.9\%$, the transmitted as $P_{\text{trans}} = 98.2\%$ and the retrieval purities were; $P_{\text{ret}}^1 = 99.6\%$, $P_{\text{ret}}^2 = 97.7\%$ and $P_{\text{ret}}^3 = 91.8\%$. The total readout purity was $P_{\text{ret}}^{1,2,3} = 99.8\%$. These high purities suggest that the interferometer is phase stable and that the read-out pulses from the memory are highly coherent with the output.

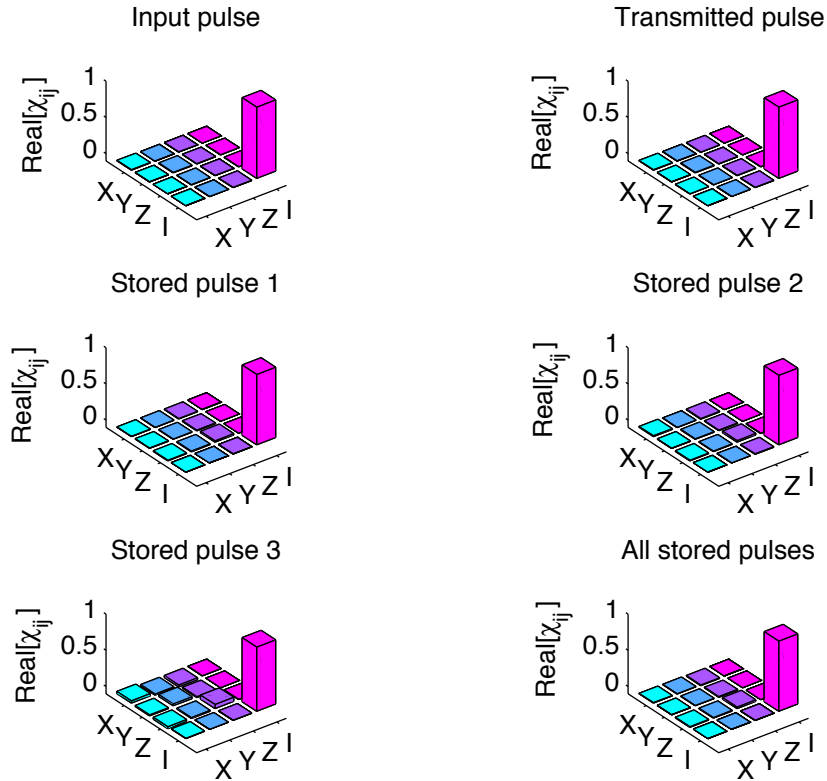


Figure 7.8 Quantum process matrices, χ_{ij} , for the memory process calculated in the Pauli matrix basis set $\{X, Y, Z, I\}$. From top to bottom; the input pulse (purity $P_{\text{in}} = 97.9\%$), the transmitted pulse ($P_{\text{trans}} = 98.2\%$), first, second and third read-out pulses ($P_{\text{ret}}^1 = 99.6\%$, $P_{\text{ret}}^2 = 97.7\%$, $P_{\text{ret}}^3 = 91.8\%$ and the total readout ($P_{\text{ret}}^{1,2,3} = 99.8\%$). Only the real parts of the process matrices are displayed as the imaginary parts are all close to zero.

Quantum process tomography at longer storage times

While the purity of the storage and retrieval process is encouragingly high for the short readout times, it was important to demonstrate this same coherence at longer storage times. As we can see from the lifetime measurement shown in Figure 7.5 the efficiency of the memory decays as we increase the storage time, hence we may

expect that the purity of the process also decreases. To measure this at longer storage times, we first needed to extend the storage time of the memory by adding magnetic shielding around the cell; this also necessitated the lengthening of the interferometer from 20 to 35 cm.

In order to measure the purity of the process as a function of time, we would, ideally, like to vary the the storage time and calculate the process matrix and purity at each time. However, performing a full QPT measurement takes a long time hence, instead, the interference visibility was measured at each storage time. In order to calculate the visibility, we made two measurements; $|A\rangle_{\text{prep}}|A\rangle_{\text{anal}}$ and $|A\rangle_{\text{prep}}|D\rangle_{\text{anal}}$. The pulse areas, A_{AA} and A_{AD} , for each were measured and background subtracted as discussed above and visibility calculated as

$$V = \frac{A_{AA} - A_{AD}}{A_{AA} + A_{AD}}. \quad (7.13)$$

The visibility was measured at 12 storage times between 12.5 ns and 2.5 μ s. These same measurements also provide a lifetime measurement for the memory with the new magnetic shielding if we simply use the $|A\rangle_{\text{prep}}|A\rangle_{\text{anal}}$ data to calculate efficiency as a function of storage time.

For comparison with the visibility measurements, QPT sets were also taken at storage times of 12.5, 300, 700, 1,000 and 1,500 ns to compare the calculated purities with the visibility measurements; for reference the process matrices calculated at 300 ns storage time are shown in Figure 7.9. The resulting data are shown in

Figure 7.10. Figure 7.10(a) shows the visibility and purity of the input and transmitted signal field as a function of storage time. Obviously we do not expect these quantities to change with storage time, however, the high visibilities and purities of the process indicated that the polarization interferometer was stable over the course of all the measurements.

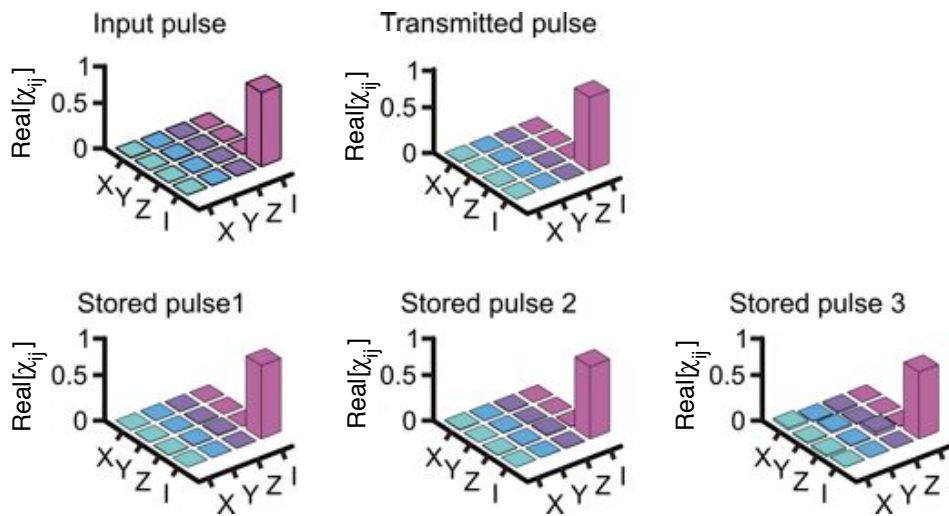


Figure 7.9 Quantum process matrices, χ_{ij} , for 300 ns storage time.

Figure 7.10(b) shows the purity/visibility of the three read-out pulses as a function of storage time along with the lifetime measurement⁶. The lifetime measurement, as expected, decays away with time down to around 20% of its maximum value after $2.5 \mu\text{s}$. By contrast to the efficiency, the visibility remains steadily between 80 and 100% up to around $2 \mu\text{s}$, after which it decreases, probably due to a low signal-to-noise ratio at low memory efficiencies. The purity seems to be in reasonably good agreement with the visibility suggesting that this is a good approx-

⁶These data are only shown for the first read-out pulse, but similar results were observed with the second and third pulses.

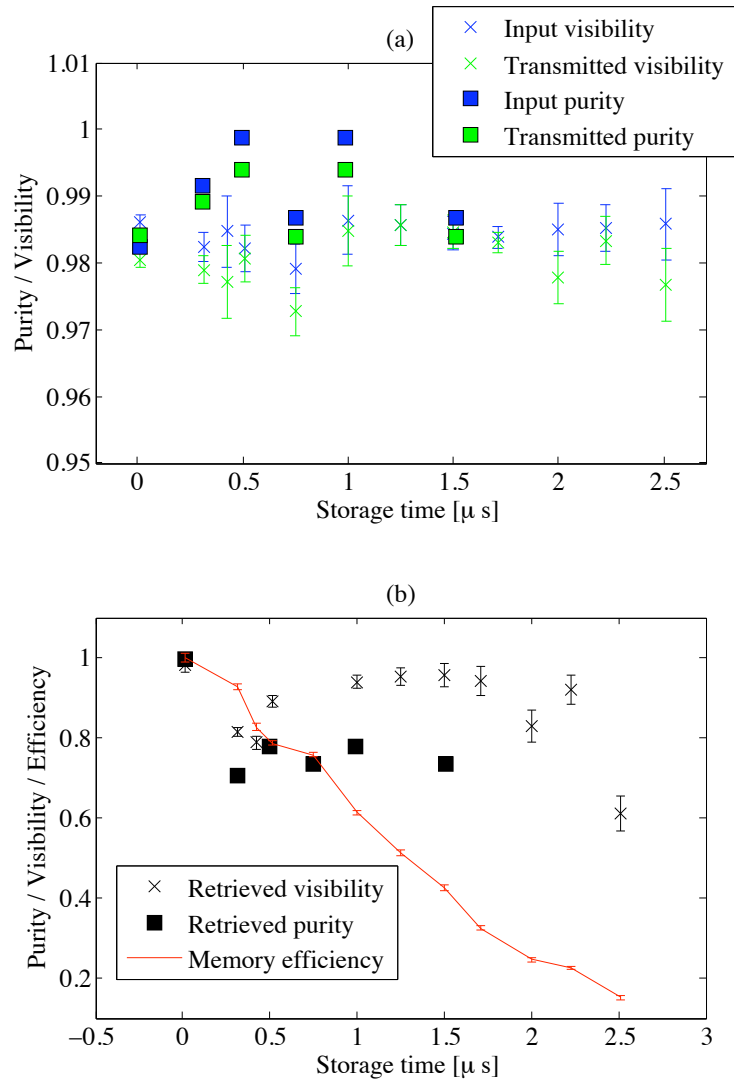


Figure 7.10 Visibility and purity of the memory process as a function of storage time. **(a)** The visibility and purity of the input and transmitted pulses. As expected, these show no dependence on the storage time. The high purity of these pulses indicates that the polarization interferometer remained stable for the duration of the QPT measurement. **(b)** The purity, visibility and efficiency of the first retrieved pulse as a function of storage time. It is important to note that, while the efficiency decays with time, the visibility and purity do not, indicating that the purity of information remaining in storage is unaffected by decoherence.

imation to the purity without having to perform the full QPT measurement. This disparity between the behavior of the efficiency and the visibility is an interesting result suggesting that, although decoherence degrades the efficiency of the memory, the purity of what remains in storage is unaffected.

7.4 Conclusions

Klaus Reim *et al.* have demonstrated a broadband quantum memory based on the Raman interaction in warm cesium vapor^[18,19,156]. The high bandwidth demonstrated in this memory, 1.5 GHz, leads to a huge time-bandwidth product of over 10,000 which, at the time of writing, is the largest value of this key parameter ever demonstrated in a quantum memory. High storage efficiencies of around 30% have been observed and, by applying multiple read-out pulses, the whole coherence can be read out. Furthermore, the off-resonant nature of the Raman interaction almost completely removes the fluorescence background that afflicts EIT based memory schemes in warm vapors and prevents single-photon implementation of EIT based quantum memories^[171,172]. By contrast, Reim *et al.* were able to demonstrate a noise floor of only 0.25 photons/pulse for the Raman memory, indicating that it is a viable option for operating at the single-photon level.

Following on from this work, the author, along with co-workers Partick Michelberger and Tessa Champion, demonstrated the ability of a two-mode memory to store polarization-encoded information. Quantum process tomography (QPT) was performed on the memory — with short storage times of tens of nanoseconds — and

process purity of over 97% was demonstrated. QPT was also performed at longer storage times, while the purities were not as high as 97%, they consistently remained above 80%. The fact that the purity did not decrease with storage time (in fact the highest purity was observed with a storage time of 750 ns) but instead fluctuated, suggests that the stability of the system is at fault rather than something inherent in the memory process.

The interference visibility of a polarization state prepared in the diagonal basis, $\{|D\rangle, |A\rangle\}$, was measured as a function of storage time and appeared to remain constant with storage time. The efficiency, on the other hand, dropped by 80% over the same range. The implication of this result is that the decoherences affecting the efficiency of the memory do not affect the purity of what remains in storage. This is an important result as it has ramifications for the potential use of the memory as part of a quantum network; this suggests that, even for long storage times, and low efficiencies, the memory will not degrade the fidelity of the information stored.

7.5 Outlook

A key step towards showing that the Raman memory will be useful for quantum information processing is to combine it with true single photons. The high bandwidth of the Raman memory makes it possible to think about using parametric down-conversion (PDC) as a source of heralded single photons. While extensive experience of this type of source exists within the group^[173,174], tailoring the bandwidth of such a source to match that of the Raman memory provides a significant

challenge. Once this source is developed, we intend to demonstrate storage and on-demand retrieval of true single photons, a significant milestone which has yet to be demonstrated by any quantum memory. Once the single-photon memory is implemented, we can begin to investigate quantum phenomena in the memory such as entanglement between a single photon and an atomic ensemble, or the entanglement of a pair of atomic ensembles.

Successful demonstration of the storage of exotic quantum states in the Raman memory will allow us to implement our future plans including introducing pulse-routing apparatus to increase multi-photon rates, light-matter Hong–Ou–Mandel interference and the miniaturization of the apparatus for integrated optical circuits. These experiments will reveal the true quantum capability of the Raman memory.

Appendix A

Atomic and Molecular Data of Rubidium

A.1 Atomic data

	⁸⁵ Rb	⁸⁷ Rb
Atomic Number, Z	37	37
Total nucleons, $Z + N$	85	87
Natural abundance	72.17%	27.83%
Atomic mass	84.912 a.m.u.	86.909 a.m.u.
Nuclear lifetime	stable	4.88×10^{10} years
Nuclear spin, \mathbf{I}	5/2	7/2

Table A.1 Atomic data of ⁸⁵Rb and ⁸⁷Rb. Data taken from reference papers by Daniel Steck^[29,30].

The first 20 energy levels of rubidium are shown in Table A.3 along with the ionization limit. For dipole-allowed 1- and 2-photon transitions from the ground

state, the wavelength is shown. A photon has one unit of angular momentum, hence a 1-photon transition changes the angular momentum by $L = \pm 1$ and a 2-photon transition by $L = 0, \pm 2$.

A.2 The D_2 line

The hyperfine structure of the D_2 line in ^{87}Rb and ^{85}Rb are shown in Figure A.1 and Figure A.2 respectively. For ^{87}Rb (^{85}Rb) the MOT transition is $F = 2(3) \rightarrow F' = 3(4)$ and the repumping transition is $F = 1(2) \rightarrow F' = 2(3)$.

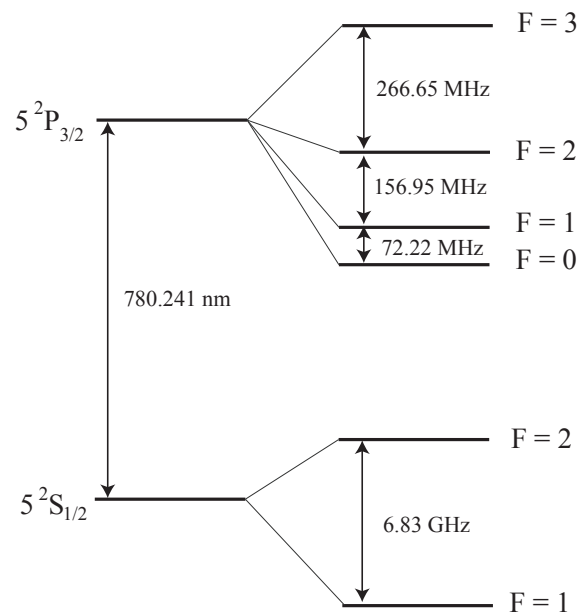


Figure A.1 The D_2 line in ^{87}Rb with hyperfine splitting. Scale is consistent within each electronic state but not with respect to others or to Figure A.2. Data from Steck^[30].

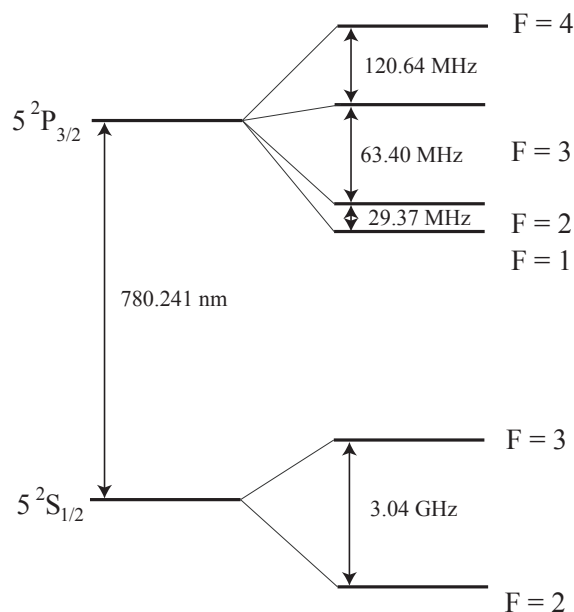


Figure A.2 The D_2 line in ^{85}Rb with hyperfine splitting. Scale is consistent within each electronic state but not with respect to others or to Figure A.1. Data from Steck^[29].

A.3 Rb₂ molecular potentials

The two ground, and 8 excited state potentials relevant to the pump-probe experiment are listed, in Hund's case (a) notation, in Table A.2 and plotted in Figure A.3. The $X^1\Sigma_g^+$ potential is a combination of the short-range spectral study by Seto *et al.*^[175] and the long-range tail from van Kempen *et al.*^[176]. The $a^3\Sigma_u^+$ potential was obtained from the Greene group at JILA^[177,178], and the $A^1\Sigma_u^+$ and $b^3\Pi_u$ potentials were derived from spectroscopy^[179]. The remaining neutral potentials are theoretically calculated by Park *et al.*^[180]. The ionization potential was again theoretically derived, this time by Aymar *et al.*^[181].

		Singlets	Triplets
Ground	<i>gerade</i>	$X^1\Sigma_g^+$	-
	<i>ungerade</i>	-	$a^3\Sigma_u^+$
Excited	<i>gerade</i>	$^1\Sigma_g^+$ $^1\Pi_g$	$^3\Sigma_g^+$ $^3\Pi_g$
	<i>ungerade</i>	$A^1\Sigma_u^+$ $^1\Pi_u$	$^3\Sigma_u^+$ $b^3\Pi_u$

Table A.2 Ground and excited state potentials relevant to the pump-probe experiment.

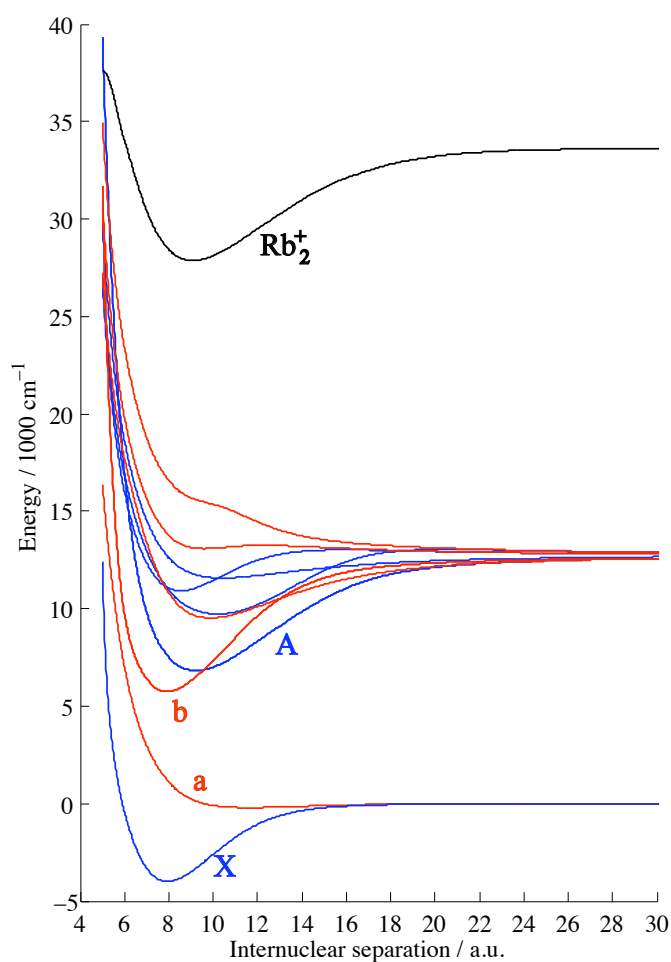


Figure A.3 Relevant molecular potentials for the pump-probe experiment. States with triplet character are plotted in red, while singlets are in Blue. The ionization potential is also included.

configuration	J	Energy [cm ⁻¹]	$\lambda_{1\gamma}$ [nm]	$\lambda_{2\gamma}$ [nm]
4p ⁶ 5s	1/2	0	-	-
4p ⁶ 5p	1/2	12578.95	794.9789132	-
	3/2	12816.55	780.2414769	-
4p ⁶ 4d	5/2	19355.2	-	1033.313885
	3/2	19355.65	-	1033.290075
4p ⁶ 6s	1/2	20132.51	-	993.4181083
4p ⁶ 6p	1/2	23715.08	421.6726057	-
	3/2	23792.59	420.2989073	-
4p ⁶ 5d	3/2	25700.54	-	778.1938867
	5/2	25703.5	-	778.1042098
4p ⁶ 7s	1/2	26311.44	-	760.1257202
4p ⁶ 4f	7/2	26792.09	-	-
	5/2	26792.12	-	-
4p ⁶ 7p	1/2	27835.02	359.2596664	-
	3/2	27870.11	358.8073388	-
4p ⁶ 6d	3/2	28687.13	-	697.1768208
	5/2	28689.39	-	697.121828
4p ⁶ 8s	1/2	29046.82	-	688.5436256
4p ⁶ 5f	7/2	29277.77	-	-
	5/2	29277.79	-	-
4p ⁶ 5g	7/2	29296.2	-	-
	9/2	29296.2	-	-
4p ⁶ 8p	1/2	29834.94	335.1774798	-
	3/2	29853.79	334.9658452	-
4p ⁶ 7d	3/2	30280.11	-	660.4995166
	5/2	30281.62	-	660.4666461
4p ⁶ 9s	1/2	30499.03	-	655.7585387
4p ⁶ 6f	7/2	30627.96	-	-
	5/2	30627.98	-	-
4p ⁶ 9p	1/2	30958.91	323.0087881	-
	3/2	30970.19	322.8911414	-
4p ⁶ 8d	3/2	31221.44	-	640.5854438
	5/2	31222.45	-	640.5646603
4p ⁶ 10s	1/2	31362.33	-	637.707701
Rb ₂ ⁺	-	33690.81	296.8168471	593.6336942

Table A.3 Energy levels of rubidium, neglecting hyperfine structure, along with 1-photon ($\lambda_{1\gamma}$) and 2-photon ($\lambda_{2\gamma}$) transition wavelengths are shown for dipole-allowed transitions from the ground state. Data from Sansonetti^[182].

Appendix B

The Position-Dependence of the Classical Oscillation Period.

Due to the highly anharmonic nature of the molecular potentials, wavepacket motion happens on very different timescales depending on the internuclear separation at which the wavepacket is formed. This has important consequences for the evolution of the wavepacket and the potential for photoassociation, as discussed in Chapter 4. In this appendix, we calculate the classical oscillation period of the A/b pair in the excited state of the Rb_2 molecule as a function of internuclear separation. The result of this calculation is shown in Figure 4.3.

A full theoretical treatment of the wavepacket oscillations in the excited state following an excitation is a very involved process, requiring a complex model. Such a model is not discussed in this thesis, but the interested reader may wish to look at the D.Phil. thesis of Hugo Martay^[130]. However, a feeling for the timescales

involved can be gained by calculating the classical oscillation period of a wavepacket in the excited state.

In much the same way that the period of a Rydberg wavepacket can be estimated by the splitting of energy levels contained within the wavepacket^[183], the classical oscillation period of the wavepacket is here calculated as the inverse of the splitting between vibrational energy levels. The excited state potential used for this model is the A/b pair calculated by Bergeman *et al.*^[179]. The energy of the vibrational eigenstates were calculated by Hugo Martay as part of the model discussed in Section 4.1.3.

In this simple model, it is assumed that the excited wavepacket contains 5 adjacent states, and the period, T_c of wavepacket's oscillation is simply the inverse of the average splitting between the states. This was calculated for each vibrational state as;

$$T_c(v_n) = \frac{4h}{E(v_{(n-2)}) - E(v_{(n+2)})}, \quad (\text{B.1})$$

the results of which are shown in Figure B.1.

Ultimately, we would like to observe the the effect of changing the internuclear separation of the wavepacket excitation on the classical oscillation period; this demonstrates the importance of the initial state, as discussed in Section 4.1. To do this, we first estimate the initial position of a wavepacket by calculating the average point at which the vibrational levels involved cross the molecular potential; these points are shown in Figure B.2.

Finally, the two results are combined to give an estimation of the position-

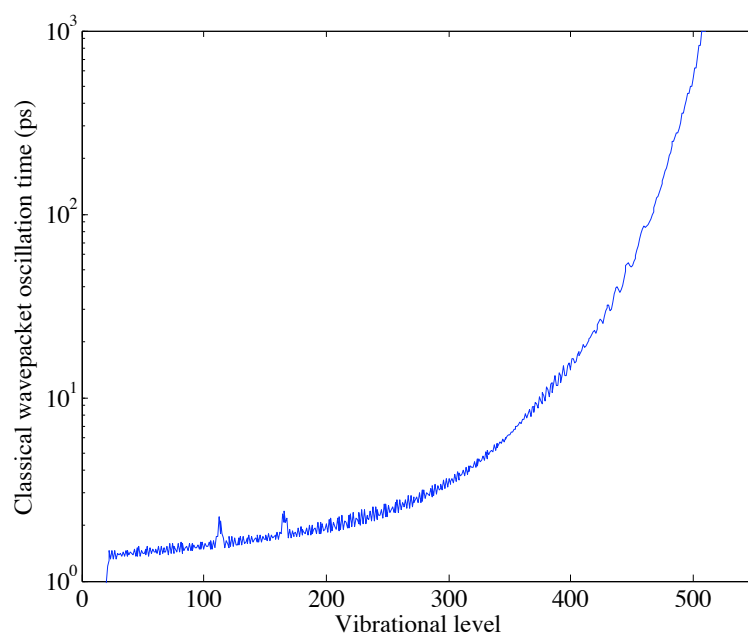


Figure B.1 Classical oscillation period in the excited state as a function of average vibrational number, assuming a wavepacket populating 5 adjacent vibrational levels.

dependence of the classical oscillation period (Figure B.3). The orders of magnitude differences across the molecular potential illustrate the importance of the initial state on pump-probe experiments.

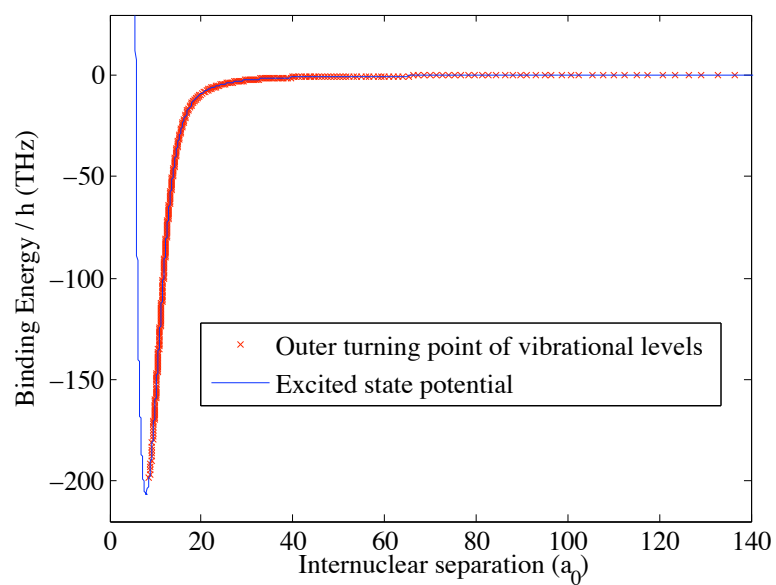


Figure B.2 Classical turning points of the vibrational wavepackets in the excited state.

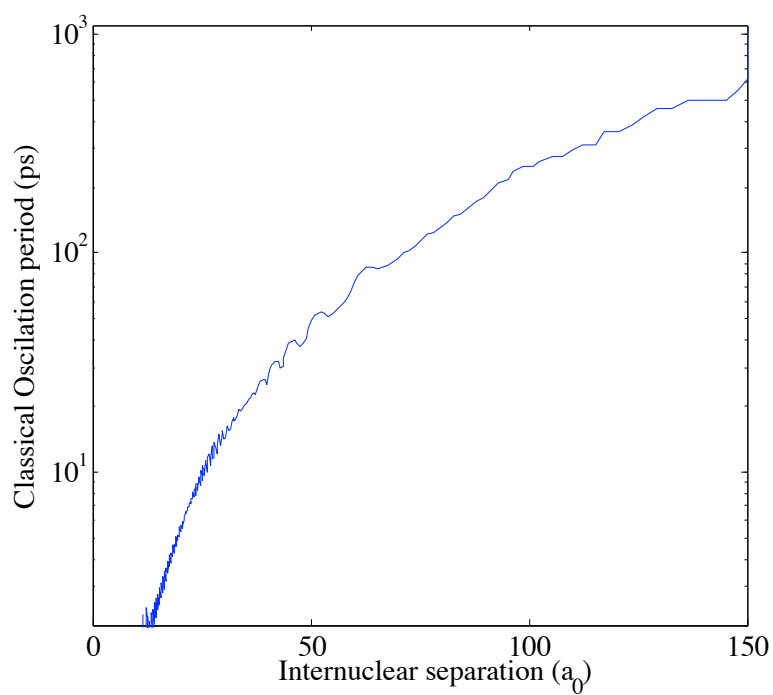


Figure B.3 Classical oscillation period in the excited state as a function internuclear separation.

Appendix C

Design of the Tapered Amplifier

The necessity for high power in the trapping laser in the new cold apparatus motivated the development of a high-powered tapered amplifier (TA) laser. The TA is injection seeded by a frequency stabilized ECDL as discussed in Chapter 5. A tapered amplifier chip was purchased from Eagleyard photonics (EYP-TPA-0780-01000-3006-CMT03-0000). The chip was capable of outputting 1 W of optical power, when appropriately seeded. In order to fully utilize all of this power, it was necessary to mount the chip in a temperature-stabilized mount and to introduce a pair of aspheric lenses for coupling light in to and out of the chip. This device was designed, and built by the author, details of which can be found below.

C.1 Design of the mount

Key to the successful operation of the TA is the choice of appropriate aspheric lenses for coupling the seed laser into the chip and collimating the output. On advice from

Eagleyard, lenses of focal length 6.24 mm and numerical aperture 0.4 were chosen (*Thorlabs C110TME-B*). The short working distance of 3.39 mm placed a stringent requirement on the design of the mount. Sketches of the design of the TA mount are shown in figures C.1 and C.2 as well as photographs in figures C.3 and C.4. The aspheric lenses are held in a hollow lens tube which, in turn, is mounted in a 5-axis fiber launcher (*New Focus 9095*), the fiber launcher offered XYZ control of the lenses position as well as tip and tilt¹. The TA mount is recessed to allow the aspheric lenses to approach the chip to within their working distance.

The TA is anode grounded so the cathode is connected, via a 9-pin D-sub connector for strain relief, to a laser diode driver power supply (*Newport 560 Laser Diode Driver*). The circuit was completed via the mount. The TA chip and the fiber launchers are mounted on a aluminum plate. A pair of Peltier elements (*Melcor CP0.8-127-06L*) are sandwiched between the plate and a large aluminium block whose dual purpose was as a mount and as a heat sink. An AD590 temperature transducer was used to monitor the temperature of the TA mount as close as possible to the chip (see diagrams), this was stabilized by feedback on the current to the Peltier elements using a temperature controller (*Newport 325 Temperature Controller*).

¹In practice the tip and tilt functionalities were not used.

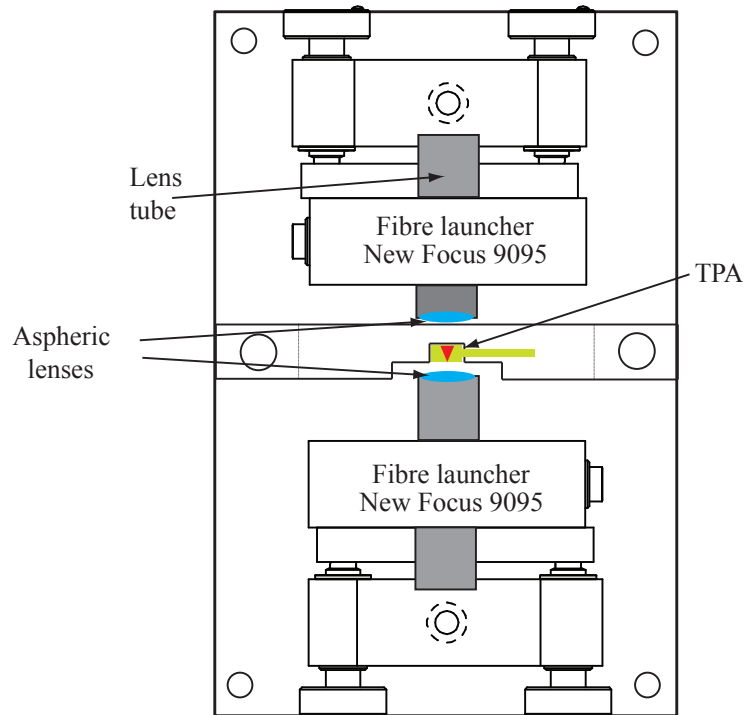


Figure C.1 Technical drawing of the tapered amplifier, top view. The chip (TPA) is mounted centrally with aspheric lenses mounted in fiber launchers allowing coupling of the seed laser and collimation of the output.

C.2 Alignment and collimation

When un-seeded² the tapered amplifier produces significant spontaneous emission in the forwards direction, this light is highly divergent, and attempting to collimate this proved to be a waste of time. However, there was also a small amount of light emitted in the backwards direction; this proved invaluable for aligning the seed laser. The collimation and pointing of the back-propagating spontaneous emission

²It is important not to run the TA on maximum current when unseeded, this can damage the chip. Instead the alignment is performed at around half the specified maximum current.

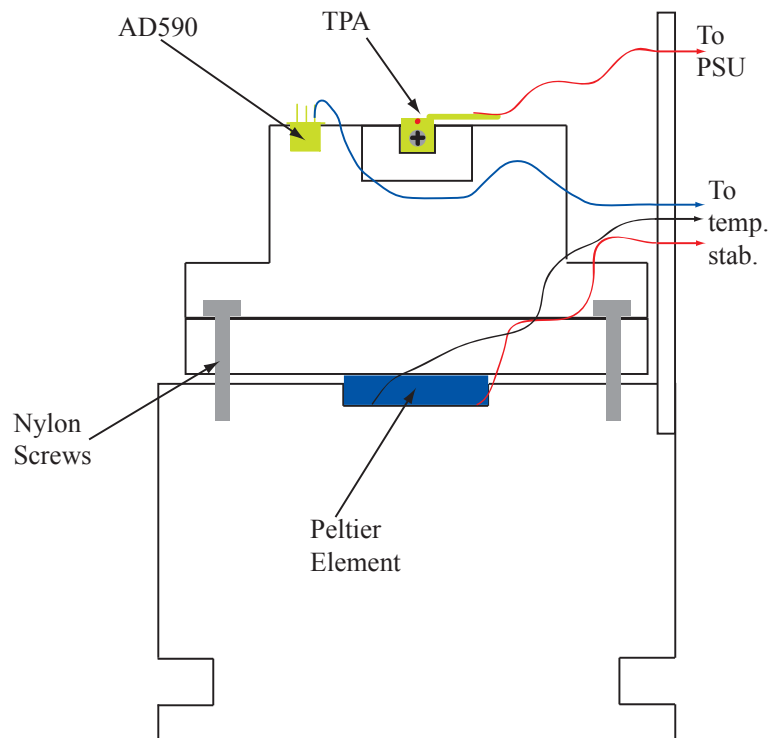


Figure C.2 Technical drawing of the tapered amplifier, front view, the fiber launchers have been removed for clarity. The TPA is mounted on a c-mount which, itself, is mounted in a machined brass block. The brass block is mounted on a plate which is temperature stabilized by a pair of Peltier elements driven by a temperature controller which feeds back on the output of an AD590 temperature transducer.

was adjusted by moving the input lens with the fiber stage until the beam was collimated, horizontal and parallel to the chip, this ensured that the seed could be aligned on-axis with the lens and thereby couple efficiently into the tapered amplifier. The seed laser was spatially overlapped with the spontaneous emission, this was sufficient to produce lasing in the output of the TA, the lasing was obvious due to its higher power and different spatial mode compared to the spontaneous emission. The power of the output was optimized, at low current, by adjusting

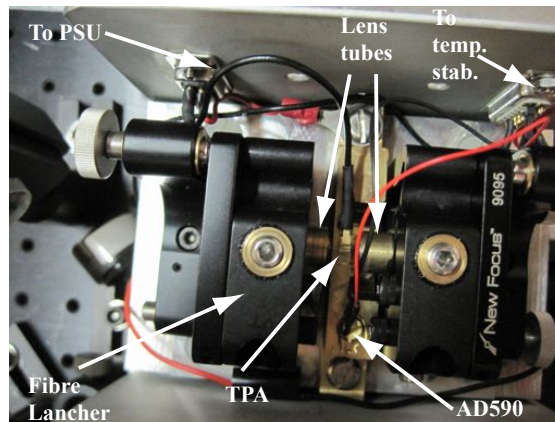


Figure C.3 Photograph of the tapered amplifier module showing a similar view to that sketched in Figure C.1. Note that the chip, AD590 and pelier elements are wired to a 9-pin D-sub connector for strain relief.

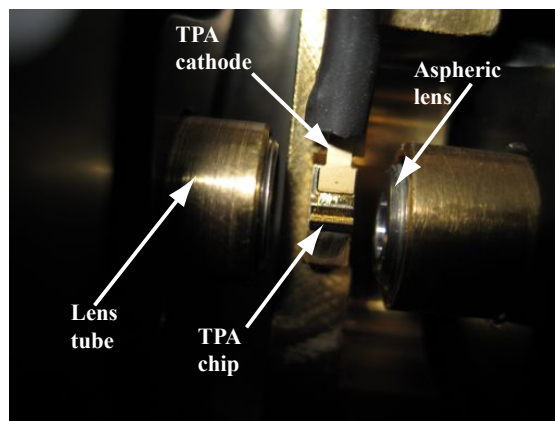


Figure C.4 Close-up photograph of the TA chip and aspheric lenses.

the final two steering mirrors on the seed laser³. The lens was then translated in the Z direction (parallel to the chip) and the power re-optimized using the steering mirrors, this procedure was repeated iteratively to find the optimal focussing of the seed. Finally, the current to the chip was incrementally increased, with the seed

³Optimizing the power by moving the aspheric lens proved to be too sensitive.

coupling optimized at each point, until the maximum current was reached, at this point over 1.1 W of power was observed in the output compared to only 200 mW when unseeded.

Due to the astigmatic nature of the output of the TA, it is only possible to collimate one dimension of the beam — in this case the vertical — using the aspheric lens, the beam is still diverging in the horizontal direction. A cylindrical lens was used to collimate the horizontal dimension of the beam; a range of lenses between 5 and 20 cm focal length were tried in order to maximize the coupling into a single mode fiber, a 10 cm focal length was proven to be optimal. At this point 250 mW was available after the single mode fiber for use in the MOT, only 300 μ W of spontaneous emission was coupled into the fiber, demonstrating that the seeded and spontaneous outputs have different spatial profiles.

Appendix D

UHV Construction

This appendix contains details of the ultra-high vacuum (UHV) preparation for the dipole apparatus. Section [D.1](#) shows the temperature and pressure readings for the bakeout and Section [D.2](#) describes the investigations of the LIAD mechanism performed in the old MOT apparatus to demonstrate the suitability of this scheme for loading the MOT in the new apparatus.

D.1 UHV bake-out

As discussed in Section [5.1.1](#) The UHV apparatus was baked in order to improve the background pressure. Temperature and pressure data for the bake-out are shown in Figure [D.1](#). We can see an obvious increase in pressure corresponding to each increase in temperature as particles are desorbed from the walls, and then the decrease in pressure as the particles are pumped away leading to an overall downwards trend in pressure as the bake-out proceeds. At the end of the bake, the chamber is cooled

leading to a rapid decrease in pressure. The valve to the pumps was closed when the temperature reached 70°C to avoid any contaminants from the pump (which could not be baked) diffusing into the chamber and sticking to the walls. Because of this, we were unable to measure the pressure in the chamber as the temperature fell back to the ambient level. However, by observing the ion pump current we could infer that the final pressure was below 10^{-9} mbar.

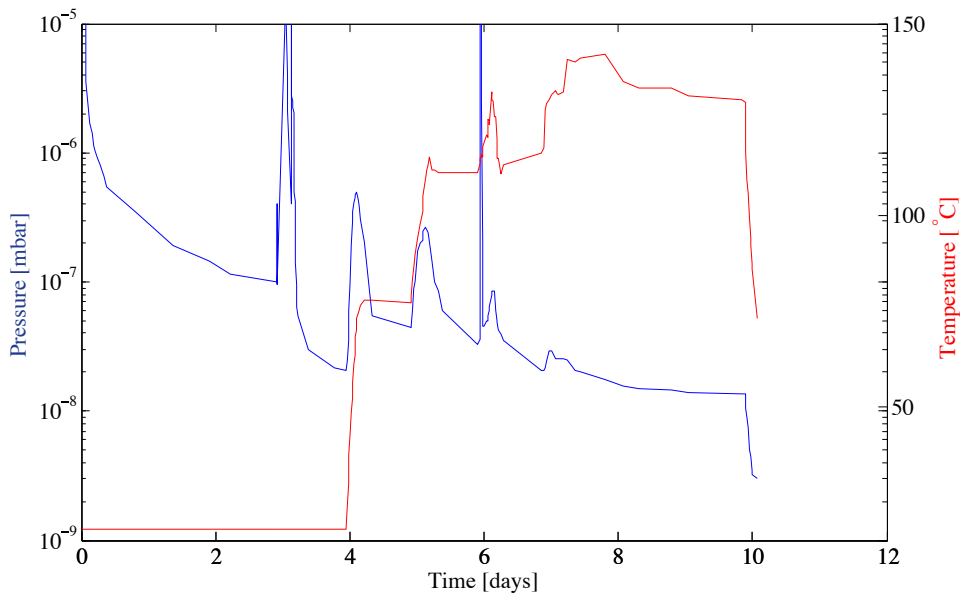


Figure D.1 Bakeout data for the dipole trap apparatus. Spikes in pressure not corresponding to temperature increases are due to the degassing of the vacuum pumps (3 days) and getters sources (6 days).

D.2 Light induced atomic desorption (LIAD)

In July 2007, the MOT experiment had been running daily for over 6 months since the last bakeout, and hence the walls of the chamber were expected to be well coated

with rubidium atoms. Hence this system was used as a test-bed to investigate the LIAD protocol for loading a MOT. The rubidium dispensers were left off overnight to allow the vacuum pumps to remove rubidium vapor from the chamber, the following morning, only a faint MOT was visible on the CCD camera, and the fluorescence could not be detected by the photodiode.

Following the recommendations of Klempt *et al.*^[141], a wavelength of 395 nm was chosen, this provides good photodesorption efficiency, without the safety problems associated with working in the deep UV. A pair of high-power LED arrays (*Roithner Lasertechnik* LED395-66-60-110), each containing 63 separate LEDs, were used to introduce around 480 mW of UV light into the chamber. The current to these diode arrays was switched using a MOSFET to allow TTL control of the output. The light was briefly switched on and the MOT immediately became brighter on the CCD as more atoms were loaded due to the increased vapor pressure. The duration of the pulse of UV light was varied, and the fluorescence of the MOT was monitored, the resulting plots are shown in Figure D.2. We observe saturation of the photodiode while the LEDs are on, once they are switched off, a marked increase in fluorescence indicates that the number of atoms had increased during the LIAD process. If the LEDs were left on for long enough, then the photodiode signal saturated at a voltage corresponding to $\sim 1 \times 10^7$ atoms in the MOT; this number compares favorably with that achieved with the rubidium dispensers switched on. Once the light was switched off, the fluorescence rapidly decayed away showing that the pressure was reduced again. These promising results indicated that the LIAD mechanism had

the potential to act as the source of rubidium vapor in the new experiment.

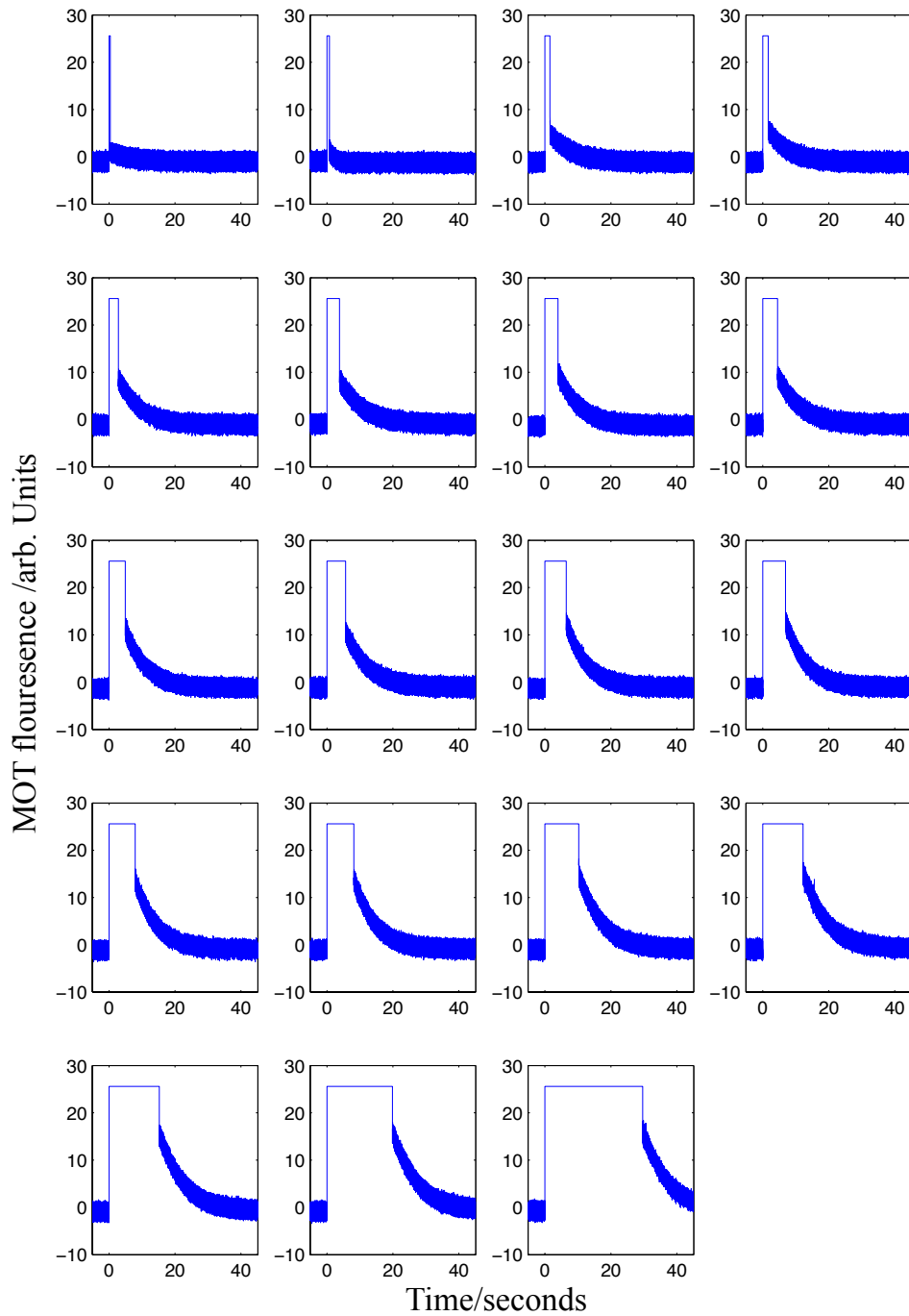


Figure D.2 Demonstration of the LAID mechanism. Two high-power LED arrays are switched on at time zero, and the MOT fluorescence is monitored. The photodiode is saturated by the LEDs leading to the large square-profile features, the width of which indicates the LIAD duration. The increased fluorescence following the LIAD is indicative of the induced increase in the partial pressure of rubidium, while the decay indicates that the pressure rapidly returns to normal after the pulse.

Appendix E

Atomic Data of Cesium

E.1 Atomic data

Cesium has only one stable isotope, ^{133}Cs , this is the only species of relevance to the Raman quantum memory experiment. The relevant atomic data for ^{133}Cs is shown in Table E.1.

Atomic Number, Z	55
Total nucleons, $Z + N$	133
Atomic mass	132.9 a.m.u.
Nuclear lifetime	stable
Nuclear spin, \mathbf{I}	$7/2$

Table E.1 Atomic data of ^{133}Cs . Data taken from reference papers by Daniel Steck^[163]

E.2 The D_2 line

The Raman quantum memory operates close to the D_2 line in cesium, the hyperfine structure of which is shown in Figure E.1. We note that the bandwidth of the laser (1.5 GHz) is significantly smaller than the hyperfine splitting of the ground state (9.19 GHz), demonstrating that the choice of laser, and species, is a good one for this experiment. Typical detuning from resonance of around 16-20 GHz are an order of magnitude larger than the hyperfine splitting in the excited state, making it a safe assumption to neglect this splitting.

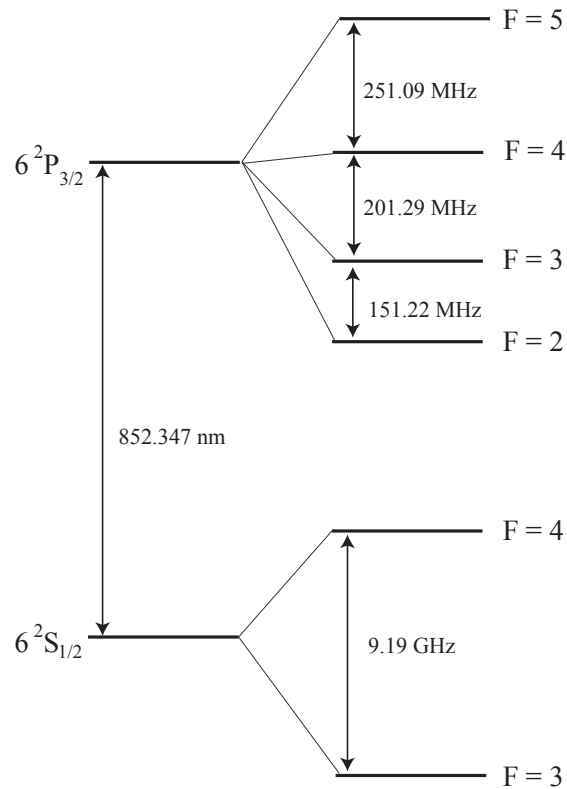


Figure E.1 The D_2 line in cesium with hyperfine splitting. Scale is consistent within each electronic state but not with respect to others. Data from Steck^[163]

Bibliography

- [1] M. Anderson, J. Ensher, M. Matthews, C. Wieman, and E. Cornell, *Observation of Bose–Einstein Condensation in a Dilute Atomic Vapor*, *Science*, **269**, p. 196 (1995). [1](#), [31](#), [39](#)
- [2] C. Bradley, C. Sackett, J. Tollett, and R. Hulet, *Evidence of Bose–Einstein Condensation in an Atomic Gas with Attractive Interactions*, *Phys. Rev. Lett.*, **75**, pp. 1687–1691 (1995). [1](#)
- [3] K. Davis, M. Mewes, M. Andrews, N. V. Druten, D. S. Durfee, D. M. Kurn, and W. Ketterle, *Bose–Einstein condensation in a gas of sodium atoms*, *Physical Review Letters*, **75**, pp. 3969–3973 (1995). [1](#), [31](#), [40](#)
- [4] D. DeMille, *Quantum Computation with Trapped Polar Molecules*, *Phys. Rev. Lett.*, **88**, p. 067901 (2002). [2](#)
- [5] D. Glenn, D. Lidar, and V. A. Apkarian, *Quantum logic gates in iodine vapor using time–frequency resolved coherent anti-Stokes Raman scattering: a theoretical study*, *Molecular Physics*, **104**, pp. 1249–1266 (2006). [2](#)
- [6] Z. Bihary, D. R. Glenn, D. A. Lidar, and V. A. Apkarian, *An implementation of the Deutsch–Jozsa algorithm on molecular vibronic coherences through four-wave mixing: a theoretical study*, *Chemical physics letters*, **360**, pp. 459–465 (2002). [2](#)
- [7] M. Bell and T. Softley, *Ultracold molecules and ultracold chemistry*, *Molecular Physics*, **107**, pp. 99–132 (2009). [2](#)
- [8] D. DeMille, F. Bay, S. Bickman, D. Kawall, D. Krause, S. E. Maxwell, and L. R. Hunter, *Investigation of PbO as a system for measuring the electric dipole moment of the electron*, *Physical Review A*, **61**, p. 052507 (2000). [3](#)
- [9] J. J. Hudson, D. M. Kara, I. J. Smallman, B. E. Sauer, M. R. Tarbutt, and E. A. Hinds, *Improved measurement of the shape of the electron*, *Nature*, **473**, p. 493 (2011). [3](#)
- [10] A. Vutha, O. Baker, W. Campbell, D. DeMille, J. M. Doyle, G. Gabrielse, Y. Gurevich, and M. Jansen, *Search for the electron’s electric dipole moment*

- with a cold molecular beam of ThO*, Bulletin of the American Physical society, **53** (2008). [3](#)
- [11] L. Sinclair, J. Bohn, A. Leanhardt, E. Meyer, R. Stutz, and E. Cornell, *An Electron EDM Search Using Trapped Molecular Ions*, Bulletin of the American Physical society, **52** (2007). [3](#)
- [12] J. Danzl, E. Haller, M. Gustavsson, M. Mark, R. Hart, N. Bouloufa, O. Dulieu, H. Ritsch, and H.-C. Nagerl, *Quantum Gas of Deeply Bound Ground State Molecules*, Science, **321**, p. 1062 (2008). [4](#), [171](#)
- [13] M. Viteau, A. Chotia, M. Allegrini, N. Bouloufa, O. Dulieu, D. Comparat, and P. Pillet, *Optical Pumping and Vibrational Cooling of Molecules*, Science, **321**, p. 232 (2008). [4](#), [48](#), [171](#)
- [14] B. Zhao, Y. Chen, X. Bao, T. Strassel, C. Chuu, X. Jin, J. Schmiedmayer, Z.-S. Yuan, S. Chen, and J. Pan, *A millisecond quantum memory for scalable quantum networks*, Nat Phys, **5**, p. 95 (2009). [5](#), [176](#)
- [15] Y. Chen, S. Chen, Z. Yuan, B. Zhao, C. Chuu, J. Schmiedmayer, and J. W. Pan, *Memory-built-in quantum teleportation with photonic and atomic qubits*, Nature Physics, **4**, p. 103 (2008).
- [16] S. Chen, Y. Chen, T. Strassel, Z. Yuan, B. Zhao, J. Schmiedmayer, and J. W. Pan, *Deterministic and storable single-photon source based on a quantum memory*, Physical Review Letters, **97**, p. 173004 (2006).
- [17] T. Chanelière, D. N. Matsukevich, S. D. Jenkins, S.-Y. Lan, T. A. B. Kennedy, and A. Kuzmich, *Storage and retrieval of single photons transmitted between remote quantum memories*, Nature, **438**, pp. 833–836 (2005). [5](#), [176](#)
- [18] K. Reim, P. Michelberger, K. Lee, J. Nunn, N. Langford, and I. Walmsley, *Single-Photon-Level Quantum Memory at Room Temperature*, Physical Review Letters, **107**, p. 053603 (2011). [5](#), [177](#), [191](#), [193](#), [210](#)
- [19] K. F. Reim, J. Nunn, V. O. Lorenz, B. J. Sussman, K. C. Lee, N. K. Langford, D. Jaksch, and I. A. Walmsley, *Towards high-speed optical quantum memories*, Nature Photonics, **4**, p. 218 (2010). [5](#), [112](#), [177](#), [189](#), [191](#), [205](#), [210](#)
- [20] L. Carr, D. DeMille, R. Krems, and J. Ye, *Cold and ultracold molecules: science, technology and applications*, New J. Phys., **11**, p. 055049 (2009). [10](#), [43](#)
- [21] P. A. Tipler and G. Mosca, *Physics for Scientists and Engineers with Modern Physics*, W. H. Freeman (2007). [10](#)
- [22] H. J. Metcalf and P. V. der Straten, *Laser cooling and trapping*, Springer-Verlag (1999). [11](#), [31](#)

- [23] G. Herzberg, *Spectra of diatomic molecules*, Van Nostrand (1950). [11](#), [12](#), [14](#), [18](#), [22](#), [26](#)
- [24] J. E. Lennard-Jones, *On the Determination of Molecular Fields. II. From the Equation of State of a Gas*, Royal Society of London Proceedings Series A, **106**, pp. 463–477 (1924). [12](#)
- [25] K. Jones, E. Tiesinga, P. Lett, and P. Julienne, *Ultracold photoassociation spectroscopy: Long-range molecules and atomic scattering*, Rev. Mod. Phys., **78**, p. 483 (2006). [22](#)
- [26] J. Franck and E. G. Dymond, *Elementary processes of photochemical reactions*, Trans. Faraday Soc., **21**, pp. 536–542 (1926). [24](#)
- [27] E. Condon, *Nuclear motions associated with electron transitions in diatomic molecules*, Physical Review, **32**, p. 858 (1928). [24](#)
- [28] *National Institute of Standards and Technology (NIST) Physical reference data*, <http://physics.nist.gov>. [28](#), [105](#)
- [29] D. Steck, *Rubidium 85 D line data*, Oregon Center for Optics and Department of Physics, University of Oregon (2008). [28](#), [67](#), [93](#), [214](#), [216](#)
- [30] D. Steck, *Rubidium 87 D line data*, Oregon Center for Optics and Department of Physics, University of Oregon (2001). [28](#), [214](#), [215](#)
- [31] A. Heidmann, C. Salomon, and C. Cohen-Tannoudji, *Cooling atoms with stimulated emission*, Physical Review Letters, **57**, pp. 1688–1692 (1986). [31](#)
- [32] S. Chu, L. Hollberg, J. Bjorkholm, A. Cable, and A. Ashkin, *Three-dimensional viscous confinement and cooling of atoms by resonance radiation pressure*, Phys. Rev. Lett., **55**, pp. 48–52 (1985).
- [33] J. Prodan, A. Migdall, W. Phillips, I. So, and H. Metcalf, *Stopping atoms with laser light*, Physical Review Letters, **54**, pp. 992–995 (1985). [31](#), [32](#)
- [34] V. Letokhov and V. Minogin, *Laser radiation pressure on free atoms*, Physics Reports, **73**, pp. 1–65 (1981). [33](#)
- [35] D. Wineland and W. Itano, *Laser cooling of atoms*, Phys. Rev. A, **20**, pp. 1521–1540 (1979). [33](#)
- [36] P. D. Lett, R. N. Watts, C. Westbrook, W. Phillips, P. Gould, and H. Metcalf, *Observation of atoms laser cooled below the Doppler limit*, Physical Review Letters, **61**, pp. 169–172 (1988). [34](#)
- [37] J. Dalibard and C. Cohen-Tannoudji, *Laser cooling below the Doppler limit by polarization gradients: simple theoretical models*, J. Opt. Soc. Am. B, **6**, pp. 2023–2045 (1989). [34](#)

- [38] C. J. Foot, *Atomic physics*, Oxford University Press (2005). [36](#), [41](#)
- [39] E. Raab, M. Prentiss, A. Cable, S. Chu, and D. Pritchard, *Trapping of neutral sodium atoms with radiation pressure*, *Physical Review Letters*, **59**, pp. 2631–2634 (1987). [36](#), [64](#)
- [40] C. Monroe, W. Swann, H. Robinson, and C. Wieman, *Very cold trapped atoms in a vapor cell*, *Physical Review Letters*, **65**, pp. 1571–1574 (1990). [38](#)
- [41] M. Mewes, M. Andrews, N. V. Druten, D. M. Kurn, D. S. Durfee, and W. Ketterle, *Bose–Einstein condensation in a tightly confining dc magnetic trap*, *Physical Review Letters*, **77**, pp. 416–419 (1996). [40](#), [114](#)
- [42] A. Ashkin, J. Dziedzic, J. Bjorkholm, and S. Chu, *Observation of a single-beam gradient force optical trap for dielectric particles*, *Optics letters*, **11**, pp. 288–290 (1986). [41](#)
- [43] M. Berninger, A. Zenesini, B. Huang, W. Harm, H. C. Nagerl, F. Ferlaino, R. Grimm, P. S. Julienne, and J. M. Hudson, *Universality of the Three-Body Parameter for Efimov States in Ultracold Cesium*, Arxiv preprint arXiv:1106.3933 (2011). [43](#)
- [44] J. Weinstein, R. deCarvalho, T. Guillet, B. Friedrich, and J. Doyle, *Magnetic trapping of calcium monohydride molecules at millikelvin temperatures*, *Nature*, **395** (1998). [44](#)
- [45] J. Doyle, B. Friedrich, J. Kim, and D. Patterson, *Buffer-gas loading of atoms and molecules into a magnetic trap*, *Physical Review A*, **52**, pp. R2515–2518 (1995). [44](#)
- [46] C. Sommer, L. V. Buuren, M. Motsch, S. Pohle, J. Bayerl, P. Pinkse, and G. Rempe, *Continuous guided beams of slow and internally cold polar molecules*, *Faraday Discuss.*, **142**, pp. 203–220 (2009). [44](#)
- [47] L. V. Buuren, C. Sommer, M. Motsch, S. Pohle, M. Schenk, J. Bayerl, P. W. H. Pinkse, and G. Rempe, *Electrostatic extraction of cold molecules from a cryogenic reservoir*, *Physical Review Letters*, **102**, p. 033001 (2009). [44](#)
- [48] H. Bethlem, G. Berden, and G. Meijer, *Decelerating neutral dipolar molecules*, *Physical Review Letters*, **83**, pp. 1558–1461 (1999). [44](#)
- [49] M. Tarbutt, H. Bethlem, J. Hudson, V. Ryabov, V. Ryzhov, B. Sauer, G. Meijer, and E. A. Hinds, *Slowing heavy, ground-state molecules using an alternating gradient decelerator*, *Physical Review Letters*, **92**, p. 173002 (2004). [44](#)
- [50] H. Bethlem, F. Cromptoets, R. Jongma, S. van de Meerakker, and G. Meijer, *Deceleration and trapping of ammonia using time-varying electric fields*, *Physical Review A*, **65**, p. 053416 (2002). [44](#)

- [51] H. Bethlem, G. Berden, A. V. Roij, F. Cromptvoets, and G. Meijer, *Trapping neutral molecules in a traveling potential well*, Physical Review Letters, **84**, pp. 5744–5747 (2000).
- [52] H. Bethlem, G. Berden, F. Cromptvoets, R. Jongma, A. V. Roij, and G. Meijer, *Electrostatic trapping of ammonia molecules*, Nature, **406**, p. 491 (2000). 44
- [53] E. Shuman, J. Barry, and D. DeMille, *Laser cooling of a diatomic molecule*, Nature, **467**, p. 09443 (2010). 45, 170
- [54] E. Shuman, J. Barry, D. Glenn, and D. DeMille, *Radiative force from optical cycling on a diatomic molecule*, Physical Review Letters, **103**, p. 223001 (2009). 45
- [55] H. Thorsheim, J. Weiner, and P. Julienne, *Laser-induced photoassociation of ultracold sodium atoms*, Phys. Rev. Lett., **58**, pp. 2420–2423 (1987). 45
- [56] D. Comparat, C. Drag, B. L. Tolra, and A. Fioretti, *Formation of cold Cs ground state molecules through photoassociation in the pure long-range state*, The European Physical Journal D, **11**, pp. 59–71 (2000). 46, 47
- [57] C. Gabbanini, A. Fioretti, A. Lucchesini, and S. Gozzini, *Cold Rubidium Molecules Formed in a Magneto-Optical Trap*, Phys. Rev. Lett., **84**, pp. 2814–2817 (2000). 168
- [58] A. Fioretti, D. Comparat, A. Crubellier, O. Dulieu, F. Masnou-Seeuws, and P. Pillet, *Formation of Cold Cs₂ Molecules through Photoassociation*, Phys. Rev. Lett., **80**, pp. 4402–4405 (1998).
- [59] T. Takekoshi, B. Patterson, and R. J. Knize, *Observation of cold ground-state cesium molecules produced in a magneto-optical trap*, Physical Review A, **59** (1999).
- [60] A. Fioretti, C. Amiot, C. Dion, O. Dulieu, M. Mazzoni, G. Smirne, and C. Gabbanini, *Cold rubidium molecule formation through photoassociation: A spectroscopic study of the 0_g^- long-range state of $^{87}\text{Rb}_2$* , The European Physical Journal D-Atomic, **15**, pp. 189–198 (2001).
- [61] A. Nikolov, J. Ensher, E. Eyler, H. Wang, W. C. Stwalley, and P. L. Gould, *Efficient Production of Ground-State Potassium Molecules at Sub-mK Temperatures by Two-Step Photoassociation*, Phys. Rev. Lett., **84**, pp. 246–249 (2000).
- [62] F. Fatemi, K. Jones, P. Lett, and E. Tiesinga, *Ultracold ground-state molecule production in sodium*, Physical Review A, **66**, p. 053401 (2002). 46
- [63] A. Kerman, J. Sage, S. Sainis, and T. Bergeman, *Production and state-selective detection of ultracold RbCs molecules*, Physical Review Letters, **92**, p. 153001 (2004). 46, 47

- [64] C. Haimberger, J. Kleinert, M. Bhattacharya, and N. P. Bigelow, *Formation and detection of ultracold ground-state polar molecules*, Physical Review A, **70**, p. 021402(R) (2004).
- [65] M. Mancini, G. Telles, A. Caires, V. Bagnato, and L. G. Marcassa, *Observation of ultracold ground-state heteronuclear molecules*, Physical Review Letters, **92**, p. 133203 (2004).
- [66] D. Wang, J. Qi, M. Stone, O. Nikolayeva, H. Wang, B. Hattaway, S. D. Gensemer, P. L. Gould, E. E. Eyler, and W. C. Stwalley, *Photoassociative production and trapping of ultracold KRb molecules*, Physical Review Letters, **93**, p. 243005 (2004). [46](#)
- [67] J. Deiglmayr, A. Grochola, M. Repp, K. Mörtlbauer, C. Gluck, J. Lange, O. Dulieu, R. Wester, and M. Weidemüller, *Formation of ultracold polar molecules in the rovibrational ground state*, Physical Review Letters, **101**, p. 133004 (2008). [47](#)
- [68] J. M. Sage, S. Sainis, T. Bergeman, and D. DeMille, *Optical Production of Ultracold Polar Molecules*, Physical Review Letters, **94**, p. 203001 (2005). [47](#)
- [69] A. J. Kerman, J. Sage, S. Sainis, T. Bergeman, and D. DeMille, *Production of Ultracold, Polar RbCs Molecules via Photoassociation*, Physical Review Letters, **92**, p. 033004 (2004).
- [70] T. Bergeman, A. Kerman, J. Sage, S. Sainis, and D. DeMille, *Prospects for production of ultracold RbCs molecules*, The European Physical Journal D, **31**, pp. 179–188 (2004). [47](#)
- [71] D. Sofikitis, S. Weber, A. Fioretti, R. Horchani, M. Allegrini, B. Chatel, D. Comparat, and P. Pillet, *Molecular vibrational cooling by optical pumping with shaped femtosecond pulses*, New J. Phys., **11**, p. 055037 (2009). [50](#)
- [72] D. Sofikitis, R. Horchani, X. Li, M. Pichler, M. Allegrini, A. Fioretti, D. Comparat, and P. Pillet, *Vibrational cooling of cesium molecules using noncoherent broadband light*, Physical Review A, **80**, p. 051401(R) (2009). [50](#)
- [73] C. Pethick and H. Smith, *Bose–Einstein condensation in dilute gases*, Cambridge University Press (2002). [50](#)
- [74] T. Köhler and K. Góral, *Production of cold molecules via magnetically tunable Feshbach resonances*, Rev. Mod. Phys., **78**, pp. 1311–1361 (2006). [51](#)
- [75] E. Donley, N. Claussen, S. Thompson, and C. Wieman, *Atom-molecule coherence in a Bose–Einstein condensate*, Nature, **417**, p. 529 (2002). [51](#), [52](#)
- [76] J. Herbig, T. Kraemer, M. Mark, T. Weber, C. Chin, H.-C. Nägerl, and R. Grimm, *Preparation of a Pure Molecular Quantum Gas*, ScienceNew Series, **301**, pp. 1510–1513 (2003). [51](#)

- [77] S. Dürr, T. Volz, A. Marte, and G. Rempe, *Observation of molecules produced from a Bose–Einstein condensate*, Physical Review Letters, **92**, p. 020406 (2004). [51](#)
- [78] K. Xu, T. Mukaiyama, J. Abo-Shaeer, and J. Chin, *Formation of Quantum-Degenerate Sodium Molecules*, Physical Review Letters, **91**, p. 210402 (2003). [51](#), [52](#)
- [79] G. Thalhammer, K. Winkler, F. Lang, S. Schmid, R. Grimm, and J. H. Denschlag, *Long-Lived Feshbach Molecules in a Three-Dimensional Optical Lattice*, Phys. Rev. Lett., **96**, p. 050402 (2006). [51](#)
- [80] M. Greiner, C. A. Regal, and D. S. Jin, *Emergence of a molecular Bose–Einstein condensate from a Fermi gas*, Nature, **426**, pp. 537–540 (2003). [52](#)
- [81] S. Jochim, M. Bartenstein, A. Altmeyer, G. Hendl, S. Riedl, C. Chin, J. H. Denschlag, and R. Grimm, *Bose–Einstein Condensation of Molecules*, Science, **302**, pp. 2101–2103 (2003). [52](#)
- [82] M. Zwierlein, C. Stan, C. Schunck, S. Raupach, S. Gupta, Z. Hadzibabic, and W. Ketterle, *Observation of Bose–Einstein Condensation of Molecules*, Phys. Rev. Lett., **91**, p. 250401 (2003). [52](#)
- [83] F. lang, P. Straten, B. Brandstatter, G. Thalhammer, K. Winkler, P. Julienne, R. Grimm, and J. H. Denschlag, *Cruising through molecular bound-state manifolds with radiofrequency*, Nat Phys, **4**, p. 223 (2008). [52](#)
- [84] K. Bergmann, H. Theuer, and B. Shore, *Coherent population transfer among quantum states of atoms and molecules*, Rev. Mod. Phys., **70**, pp. 1003–1025 (1998). [53](#), [56](#)
- [85] J. Martin, M. Fewell, and K. Bergmann, *Coherent population transfer in multilevel systems with magnetic sublevels. I. Numerical studies*, Physical Review A, **52**, pp. 566–581 (1995).
- [86] B. Shore and K. Bergmann, *Coherent population transfer in multilevel systems with magnetic sublevels. II. Algebraic analysis*, Physical Review A, **52**, pp. 583–593 (1995).
- [87] B. Shore and K. Bergmann, *Coherent population transfer in multilevel systems with magnetic sublevels. III. Experimental results*, Physical Review A, **54**, pp. 1556–1569 (1996). [53](#)
- [88] K. Winkler, F. lang, G. Thalhammer, P. Straten, R. Grimm, and J. H. Denschlag, *Coherent optical transfer of Feshbach molecules to a lower vibrational state*, Physical Review Letters, **98**, p. 043201 (2007). [56](#)

- [89] F. Lang, K. Winkler, C. Strauss, R. Grimm, and J. H. Denschlag, *Ultracold triplet molecules in the rovibrational ground state.*, Phys. Rev. Lett., **101**, p. 133005 (2008). [57](#), [171](#)
- [90] J. Danzl, M. Mark, E. Haller, M. Gustavsson, R. Hart, J. Aldegunde, J. Hutson, and H. Nagerl, *An ultracold high-density sample of rovibronic ground-state molecules in an optical lattice*, Nat Phys, **6**, p. 265 (2010). [57](#), [171](#)
- [91] M. J. Mark, J. G. Danzl, E. Haller, M. Gustavsson, N. Bouloufa, O. Dulieu, H. Salami, T. Bergeman, H. Ritsch, R. Hart, and H.-C. Nägerl, *Dark resonances for ground-state transfer of molecular quantum gases*, Appl. Phys. B, **95**, pp. 219–225 (2009). [57](#)
- [92] J. Danzl, M. Mark, E. Haller, M. Gustavsson, N. Bouloufa, O. Dulieu, H. Ritsch, and R. Hart, *Precision molecular spectroscopy for ground state transfer of molecular quantum gases*, Arxiv preprint arXiv:0811.2374 (2008). [57](#)
- [93] K. K. Ni, S. Ospelkaus, M. de Miranda, A. Pe’Er, B. Neyenhuis, J. Zirbel, S. Kotochigova, P. Julienne, D. Jin, and J. Ye, *A high phase-space-density gas of polar molecules*, Science, **322**, p. 231 (2008). [57](#), [171](#)
- [94] E. Hodby, S. T. Thompson, C. A. Regal, M. Greiner, A. C. Wilson, D. S. Jin, E. A. Cornell, and C. E. Wieman, *Production Efficiency of Ultracold Feshbach Molecules in Bosonic and Fermionic Systems*, Phys. Rev. Lett., **94**, p. 120402 (2005). [57](#)
- [95] C. Townsend, N. Edwards, C. Cooper, K. Zetie, C. Foot, A. Steane, P. Szafrang, H. Perrin, and J. Dalibard, *Phase-space density in the magneto-optical trap*, Physical Review A, **52**, p. 1423 (1995). [57](#)
- [96] G. Vogt, G. Krampert, P. Niklaus, P. Nuernberger, and G. Gerber, *Optimal control of photoisomerization*, Physical Review Letters, **94**, p. 068305 (2005). [57](#)
- [97] B. Sussman, D. Townsend, M. Ivanov, and A. Stolow, *Dynamic Stark control of photochemical processes*, Science, **314**, p. 278 (2006). [57](#)
- [98] R. Levis, G. Menkir, and H. Ritsch, *Selective bond dissociation and rearrangement with optimally tailored, strong-field laser pulses*, Science, **292**, p. 709 (2001). [57](#)
- [99] A. Weiner, *Femtosecond pulse shaping using spatial light modulators*, Review of Scientific Instruments, **71**, pp. 1929–1960 (2000). [59](#)
- [100] M. Machholm, A. Giusti-Suzor, and F. Mies, *Photoassociation of atoms in ultracold collisions probed by wave-packet dynamics*, Physical Review A, **50**, pp. 5025–5036 (1994). [60](#)

- [101] P. Backhaus, B. Schmidt, and M. Dantus, *Control of photoassociation yield: A quantum-dynamical study of the mercury system to explore the role of pulse duration from nanoseconds to femtoseconds*, Chemical physics letters, **306**, pp. 18–24 (1999). [60](#)
- [102] M. Korolkov, J. Manz, G. Paramonov, and B. Schmidt, *Vibrationally state-selective photoassociation by infrared sub-picosecond laser pulses: model simulations for $O + H \rightarrow OH(\nu)$* , Chemical physics letters, **260**, pp. 604–610 (1996).
- [103] U. Marvet and M. Dantus, *Femtosecond photoassociation spectroscopy: coherent bond formation*, Chemical physics letters, **245**, pp. 393–399 (1995). [60](#)
- [104] A. Vardi, D. Abrashkevich, E. Frishman, and M. Shapiro, *Theory of radiative recombination with strong laser pulses and the formation of ultracold molecules via stimulated photo-recombination of cold atoms*, Journal of Chemical Physics, **107**, pp. 6166–6174 (1997). [61](#), [172](#)
- [105] J. Vala, O. Dulieu, F. Masnou-Seeuws, P. Pillet, and R. Kosloff, *Coherent control of cold-molecule formation through photoassociation using a chirped-pulsed-laser field*, Physical Review A, **63**, p. 013412 (2000). [61](#)
- [106] E. Luc-Koenig, R. Kosloff, F. Masnou-Seeuws, and M. Vatasescu, *Photoassociation of cold atoms with chirped laser pulses: Time-dependent calculations and analysis of the adiabatic transfer within a two-state model*, Physical Review A, **70**, p. 033414 (2004). [61](#)
- [107] E. Luc-Koenig, M. Vatasescu, and F. Masnou-Seeuws, *Optimizing the photoassociation of cold atoms by use of chirped laser pulses*, The European Physical Journal D, **31**, pp. 239–262 (2004). [61](#)
- [108] C. Koch, E. Luc-Koenig, and F. Masnou-Seeuws, *Making ultracold molecules in a two-color pump-dump photoassociation scheme using chirped pulses*, Physical Review A, **73**, p. 033408 (2006). [61](#), [172](#)
- [109] F. Fatemi, K. Jones, H. Wang, I. Walmsley, and P. Lett, *Dynamics of photoinduced collisions of cold atoms probed with picosecond laser pulses*, Physical Review A, **64**, p. 033421 (2001). [61](#)
- [110] B. L. Brown, A. J. Dicks, and Ian A Walmsley, *Coherent Control of Ultracold Molecule Dynamics in a Magneto-Optical Trap by Use of Chirped Femtosecond Laser Pulses*, Phys. Rev. Lett., **96**, p. 173002 (2006). [62](#), [107](#), [172](#)
- [111] B. Brown, A. Dicks, and I. Walmsley, *The coherent effect of chirped femtosecond laser pulses on the formation of ultracold molecules in a magneto-optical trap*, Optics Communications, **264**, pp. 278–284 (2006). [172](#)

- [112] B. L. Brown, *Towards Coherent Control of Ultracold Molecule Formation*, PhD. Thesis, University of Rochester (2005). [62](#), [107](#), [168](#)
- [113] F. Eimer, F. Weise, A. Merli, S. Birkner, L. Woste, A. Lindinger, R. Ađanođlu, C. Koch, W. Salzmann, T. Mullins, S. Gotz, R. Wester, and M. Weidemuller, *Spectrally resolved coherent transient signal for ultracold rubidium molecules*, The European Physical Journal D, **54**, pp. 711–714 (2009). [63](#)
- [114] T. Mullins, W. Salzmann, S. Götzt, M. Albert, J. Eng, R. Wester, M. Weidemuller, F. Weise, A. Merli, S. Weber, F. Sauer, L. Woste, and A. Lindinger, *Photoassociation and coherent transient dynamics in the interaction of ultracold rubidium atoms with shaped femtosecond pulses. I. Experiment*, Physical Review A, **80**, p. 063416 (2009).
- [115] F. Eimer, F. Weise, A. Lindinger, W. Salzmann, T. Mullins, S. Gotz, R. Wester, M. Weidemuller, R. Ađanođlu, and C. Koch, *Photoassociation and coherent transient dynamics in the interaction of ultracold rubidium atoms with shaped femtosecond pulses. II. Theory*, Physical Review A, **80**, p. 063417 (2009).
- [116] W. Salzmann, T. Mullins, J. Eng, M. Albert, R. Wester, and M. Weidemüller, *Coherent Transients in the Femtosecond Photoassociation of Ultracold Molecules*, Phys. Rev. Lett., **100**, p. 233003 (2008). [63](#), [94](#)
- [117] S. Zamith, J. Degert, S. Stock, B. D. Beauvoir, V. Blanchet, M. Aziz-Bouchene, and B. Girard, *Observation of coherent transients in ultrashort chirped excitation of an undamped two-level system*, Physical Review Letters, **87**, p. 033001 (2001). [63](#)
- [118] J. Petrovic, D. McCabe, D. England, H. Martay, M. Friedman, A. Dicks, E. Dimova, and I. Walmsley, *A pump–probe study of the photoassociation of cold rubidium molecules*, Faraday Discuss., **142**, pp. 403–413 (2009). [63](#)
- [119] D. McCabe, D. England, H. Martay, M. Friedman, J. Petrovic, E. Dimova, B. Chatel, and I. Walmsley, *Pump-probe study of the formation of rubidium molecules by ultrafast photoassociation of ultracold atoms*, Physical Review A, **80**, pp. 033404–1 (2009). [63](#), [83](#)
- [120] H. Martay, D. McCabe, D. England, M. Friedman, J. Petrovic, and I. Walmsley, *Demonstrating coherent control in $^{85}\text{Rb}_2$ using ultrafast laser pulses: A theoretical outline of two experiments*, Physical Review A, **80**, p. 033403 (2009). [63](#), [95](#), [173](#)
- [121] C. Wieman and L. Hollberg, *Using diode lasers for atomic physics*, Precision Spectroscopy, **62**, pp. 1–20 (2000). [67](#)
- [122] F. Biraben, E. Giacobino, and G. Grynberg, *Doppler-free two-photon spectroscopy of neon*, Physical Review A, **12**, pp. 2444–2446 (1975). [68](#)

- [123] C. Iaconis and I. Walmsley, *Spectral phase interferometry for direct electric-field reconstruction of ultrashort optical pulses*, Optics Letters, **23**, p. 792 (1998). [74](#)
- [124] G. Cerullo and S. D. Silvestri, *Ultrafast optical parametric amplifiers*, Review of Scientific Instruments, **74**, pp. 1–18 (2003). [74](#), [76](#), [77](#)
- [125] G. Cerullo, M. Nisoli, and S. D. Silvestri, *Generation of 11 fs pulses tunable across the visible by optical parametric amplification*, Applied Physics Letters, **71**, pp. 3616–3618 (1997). [76](#)
- [126] S. Kraft, J. Mikosch, P. Staantum, J. Deiglmayr, J. Lange, A. Fioretti, R. Wester, and M. Weidemuller, *A high-resolution time-of-flight mass spectrometer for the detection of ultracold molecules*, Applied Physics B: Lasers and optics, **89**, pp. 453–457 (2007). [80](#)
- [127] A. Caires, V. Nascimento, D. Rezende, V. Bagnato, and L. G. Marcassa, *Atomic density and light intensity dependences of the Rb_2 molecule formation rate constant in a magneto-optical trap*, Phys. Rev. A, **71**, p. 043403 (2005). [85](#), [87](#)
- [128] Y. Huang, J. Qi, H. K. Pechkis, D. Wang, E. E. Eyler, P. L. Gould, and W. C. Stwalley, *Formation, detection and spectroscopy of ultracold Rb_2 in the ground $X^1 \Sigma_g^+$ state*, J. Phys. B: At. Mol. Opt. Phys., **39**, pp. S857–S869 (2006). [85](#)
- [129] J. Lozeille, A. Fioretti, C. Gabbanini, Y. Huang, H. K. Pechkis, D. Wang, P. Gould, E. Eyler, W. Stwalley, M. Aymar, and O. Dulieu, *Detection by two-photon ionization and magnetic trapping of cold Rb_2 triplet state molecules*, The European Physical Journal D, **39**, pp. 261–269 (2006). [85](#)
- [130] H. Martay, *Coherent Control of cold rubidium dimers.*, D. Phil. thesis, University of Oxford (2010). [88](#), [95](#), [105](#), [173](#), [220](#)
- [131] B. Brown and I. Walmsley, *Analysis of some intuitive approaches to the coherent control of state-selected ultracold molecules*, J. Phys. B: At. Mol. Opt. Phys., **39**, p. 51055 (2006). [107](#), [172](#)
- [132] W. Salzmann, U. Poschinger, R. Wester, and M. Weidemuller, *Coherent control with shaped femtosecond laser pulses applied to ultracold molecules*, Phys. Rev. A, **73**, p. 023414 (2006). [107](#), [172](#)
- [133] D. J. McCabe, *The formation of ultracold rubidium molecules using ultrafast photoassociation*, D.Phil. Thesis. University of Oxford (2009). [110](#)
- [134] T. Kinoshita, T. Wenger, and D. S. Weiss, *All-optical Bose–Einstein condensation using a compressible crossed dipole trap*, Phys. Rev. A, **71**, p. 011602(R) (2005). [112](#)

- [135] M. Barrett, J. Sauer, and M. Chapman, *All-Optical Formation of an Atomic Bose–Einstein Condensate*, Phys. Rev. Lett., **87**, p. 010404 (2001). [112](#)
- [136] Y. Lin, A. Perry, R. Compton, and I. Spielman, *Rapid production of ^{87}Rb Bose–Einstein condensates in a combined magnetic and optical potential*, Phys. Rev. A, **79**, p. 063631 (2009). [112](#), [142](#), [151](#)
- [137] A. Vogel, M. Schmidt, K. Sengstock, K. Bongs, W. Lewoczko, T. Schuldt, A. Peters, T. V. Zoest, W. Ertmer, E. Rasel, T. Steinmetz, J. Reichel, T. Könemann, W. Brinkmann, E. Göklü, C. Lämmerzahl, H. Dittus, G. Nandi, W. Schleich, and R. Walser, *Bose–Einstein condensates in microgravity*, Appl. Phys. B, **84**, pp. 663–671 (2006). [114](#)
- [138] S. Du, M. B. Squires, Y. Imai, L. Czaia, R. A. Saravanan, V. Bright, J. Reichel, T. W. Hänsch, and D. Z. Anderson, *Atom-chip Bose–Einstein condensation in a portable vacuum cell*, Phys. Rev. A, **70**, p. 053606 (2004).
- [139] S. Aubin, M. Extavour, S. Myrskog, and L. LeBlanc, *Trapping Fermionic ^{40}K and Bosonic ^{87}Rb on a Chip*, Journal of Low Temperature Physics (2005).
- [140] B. P. Anderson and M. A. Kasevich, *Loading a vapor-cell magneto-optic trap using light-induced atom desorption*, Phys. Rev. A, **63**, p. 023404 (2001). [114](#)
- [141] C. Klempt, T. V. Zoest, T. Henninger, O. Topic, E. Rasel, W. Ertmer, and J. Arlt, *Ultraviolet light-induced atom desorption for large rubidium and potassium magneto-optical traps*, Phys. Rev. A, **73**, p. 013410 (2006). [115](#), [232](#)
- [142] <http://www.ni.com/compactrio/whatis/>. [117](#)
- [143] E. A. Donley, T. P. Heavner, F. Levi, M. O. Tataw, and S. R. Jefferts, *Double-pass acousto-optic modulator system*, Rev. Sci. Instrum., **76**, p. 063112 (2005). [125](#)
- [144] S. Pradhan and B. Jagatap, *Measurement of temperature of laser cooled atoms by one-dimensional expansion in a magneto-optical trap*, Review of Scientific Instruments, **79**, p. 013101 (2008). [141](#)
- [145] D. Comparat, A. Fioretti, G. Stern, E. Dimova, B. L. Tolra, and P. Pillet, *Optimized production of large Bose–Einstein condensates*, Physical Review A, **73**, p. 043410 (2006). [142](#)
- [146] D. J. McCarron, H. W. Cho, D. L. Jenkin, M. P. Köppinger, and S. L. Cornish, *Dual-Species Bose–Einstein Condensate of ^{87}Rb and ^{133}Cs* , arXiv:1102.1576v4, **physics.atom-ph** (2011). [142](#)
- [147] A. Couvert, M. Jeppesen, T. Kawalec, G. Reinaudi, R. Mathevet, and D. Guery-Odelin, *A quasi-monomode guided atom laser from an all-optical*

- Bose–Einstein condensate*, EPL (Europhysics Letters), **83**, p. 50001 (2008). [155](#)
- [148] W. Wiley and I. McLaren, *Time-of-Flight Mass Spectrometer with Improved Resolution*, Rev. Sci. Instrum., **26**, pp. 1150–1157 (1955). [161](#)
- [149] S. Ospelkaus, A. Pe’Er, K. Ni, and J. Zirbel, *Efficient state transfer in an ultracold dense gas of heteronuclear molecules*, Nat Phys, **4**, p. 622 (2008). [171](#)
- [150] H. Goto, H. Katsuki, H. Ibrahim, H. Chiba, and K. Ohmori, *Strong-laser-induced quantum interference*, Nat Phys, **7**, p. 383 (2011). [176](#)
- [151] K. Hosaka, H. Shimada, H. Chiba, H. Katsuki, Y. Teranishi, Y. Ohtsuki, and J. Ohmori, *Ultrafast Fourier Transform with a Femtosecond-Laser-Driven Molecule*, Physical Review Letters, **104**, p. 180501 (2010). [176](#)
- [152] I. Walmsley, *Ultrafast computing with molecules*, Physics, **3** (2010). [176](#)
- [153] J. Nunn, I. Walmsley, M. Raymer, K. Surmacz, F. Waldermann, Z. Wang, and D. Jaksch, *Mapping broadband single-photon wave packets into an atomic memory*, Physical Review A, **75**, p. 011401 (2007). [177](#), [178](#), [181](#), [182](#)
- [154] M. Fleischhauer and M. Lukin, *Quantum memory for photons: Dark-state polaritons*, Physical Review A, **65**, p. 022314 (2002). [178](#)
- [155] J. Nunn, *Quantum Memory in Atomic Ensembles*, D. Phil. Thesis, University of Oxford (2008). [178](#)
- [156] K. F. Reim, *Broadband optical quantum memory*, D.Phil. Thesis, University of Oxford (2011). [179](#), [210](#)
- [157] M. G. Raymer, *Quantum state entanglement and readout of collective atomic-ensemble modes and optical wave packets by stimulated Raman scattering*, J. of Modern Optics, **51**, pp. 1739–1759 (2004). [181](#)
- [158] A. Gorshkov, A. André, M. Fleischhauer, A. Sorensen, and M. Lukin, *Universal approach to optimal photon storage in atomic media*, Physical Review Letters, **98**, p. 123601 (2007). [182](#), [183](#)
- [159] C. Liu, Z. Dutton, C. Behroozi, and L. Hau, *Observation of coherent optical information storage in an atomic medium using halted light pulses*, Nature, **409**, p. 490 (2001). [184](#)
- [160] J. Longdell, E. Fraval, M. Sellars, and N. Manson, *Stopped light with storage times greater than one second using electromagnetically induced transparency in a solid*, Physical Review Letters, **95**, p. 063601 (2005). [184](#)

- [161] X. Maitre, E. Hagley, G. Nogues, C. Wunderlich, P. Goy, M. Brune, J. Raimond, and S. Haroche, *Quantum memory with a single photon in a cavity*, Physical Review Letters, **79**, p. 769 (1997). [184](#)
- [162] M. Lombardi, T. Heavner, and S. Jefferts, *NIST primary frequency standards and the realization of the SI second*, Measure: The Journal of Measurement Science, **2**, pp. 74–89 (2007). [184](#)
- [163] D. Steck, *Cesium D line data*, Oregon Center for Optics and Department of Physics, University of Oregon (1998). [186](#), [236](#), [237](#)
- [164] J. Poyatos, J. Cirac, and P. Zoller, *Complete characterization of a quantum process: the two-bit quantum gate*, Physical Review Letters, **78**, pp. 390–393 (1997). [194](#)
- [165] R. Bhandari and J. Samuel, *Observation of Topological Phase by Use of a Laser Interferometer*, Physical Review Letters, **60**, p. 1211 (1988). [198](#)
- [166] M. A. Nielsen and Isaac L. Chuang, *Quantum computation and quantum information*, Cambridge University Press (2003). [200](#)
- [167] J. O’Brien, G. Pryde, A. Gilchrist, D. James, N. Langford, T. Ralph, and A. White, *Quantum process tomography of a controlled-NOT gate*, Physical Review Letters, **93**, p. 080502 (2004). [200](#), [201](#)
- [168] R. Adamson and A. Steinberg, *Improving quantum state estimation with mutually unbiased bases*, Physical Review Letters, **105**, p. 030406 (2010). [201](#)
- [169] R. Loudon, *The quantum theory of light*, Oxford University Press (2004). [202](#)
- [170] G. Taylor, *Interference fringes with feeble light*, Proceedings of Cambridge Philosophical society, **15**, pp. 114–115 (1909). [202](#)
- [171] S. Manz, T. Fernholz, J. Schmiedmayer, and J.-W. Pan, *Collisional decoherence during writing and reading quantum states*, Phys. Rev. A, **75**, p. 040101 (2007). [210](#)
- [172] M. Hsu, G. Hétet, O. Glöckl, J. Longdell, B. Buchler, H.-A. Bachor, and P. Lam, *Quantum Study of Information Delay in Electromagnetically Induced Transparency*, Physical Review Letters, **97**, p. 183601 (2006). [210](#)
- [173] O. Cohen, J. Lundeen, B. Smith, G. Puentes, P. Mosley, and I. Walmsley, *Tailored photon-pair generation in optical fibers*, Physical Review Letters, **102**, p. 123603 (2009). [211](#)
- [174] P. Mosley, J. Lundeen, B. Smith, P. Wasylczyk, A. U’Ren, C. Silberhorn, and I. Walmsley, *Heralded generation of ultrafast single photons in pure quantum states*, Physical Review Letters, **100**, p. 133601 (2008). [211](#)

- [175] J. Seto, R. L. Roy, J. Vergès, and C. Amoit, *Direct potential fit analysis of the $X^1 \Sigma_g^+$ state of Rb: Nothing else will do!*, *The Journal of Chemical Physics*, **113**, p. 3067 (2000). [216](#)
- [176] E. V. Kempen, S. Kokkelmans, D. Heinzen, and B. Verhaar, *Interisotope determination of ultracold rubidium interactions from three high-precision experiments*, *Physical Review Letters*, **88**, pp. 093201–1 (2002). [216](#)
- [177] N. Klausen, J. Bohn, and C. H. Greene, *Nature of spinor Bose–Einstein condensates in rubidium*, *Physical Review A*, **64**, p. 053602 (2001). [216](#)
- [178] J. B. Jr, J. Bohn, B. Esry, and C. Greene, *Prospects for mixed-isotope Bose–Einstein condensates in rubidium*, *Physical Review Letters*, **80**, p. 2097 (1998). [216](#)
- [179] T. Bergeman, J. Qi, D. Wang, Y. Huang, H. K. Pechkis, E. E. Eyler, P. L. Gould, W. C. Stwalley, R. A. Cline, J. D. Miller, and D. J. Heinzen, *Photoassociation of ^{85}Rb atoms into 0_u^+ states near the $5S+5P$ atomic limits*, *Journal of Physics B: Molecular and Optical Physics*, **39**, pp. S183–S123 (2006). [216](#), [221](#)
- [180] S. Park, S. Suh, Y. Lee, and G. Jeung, *Theoretical study of the electronic states of the Rb_2 molecule*, *Journal of Molecular Spectroscopy*, **207**, pp. 129–135 (2001). [216](#)
- [181] M. Aymar, S. Azizi, and O. Dulieu, *Model-potential calculations for ground and excited states of Rb_2^+ , Cs_2^+ and RbCs^+ ions*, *J. Phys. B: At. Mol. Opt. Phys.*, **36**, p. 4799 (2003). [216](#)
- [182] J. Sansonetti, *Wavelengths, Transition Probabilities, and Energy Levels for the Spectra of Rubidium (Rb I through Rb XXXVII)*, *Journal of physical and chemical reference data*, **35**, pp. 301–421 (2006). [218](#)
- [183] D. Meacher, P. Meyler, I. Hughes, and P. Ewart, *Observations of the collapse and fractional revival of a Rydberg wavepacket in atomic rubidium*, *Journal of Physics B: Atomic*, **24**, pp. L63–L69 (1991). [221](#)